

Surface-Core-Functionalized Polyphenylene Dendrimers in Organic Electronics

**Dissertation zur Erlangung des Grades
“Doktor der Naturwissenschaften”
am Fachbereich Chemie, Pharmazie und Geowissenschaften
der Johannes Gutenberg-Universität Mainz**

Guang Zhang

Geboren in Weifang, China

Mainz, 2015

Dekan: [REDACTED]

1. Berichterstatter: [REDACTED]

2. Berichterstatter: [REDACTED]

Tag der mündlichen Prüfung: [REDACTED]

Die vorliegende Arbeit wurde unter Betreuung durch Herrn [REDACTED]
und [REDACTED] am Max Planck Institut für
Polymerforschung in Mainz im Zeitraum vom [REDACTED]
angefertigt.

Acknowledgements

First of all, I need to thank my supervisor, [REDACTED]. He gave me the opportunity to work in Max Planck Institute for Polymer Research which is a perfect place for me to do research. Without him, all my work here will be impossible. I also thank him for providing me with such interesting topics to work on and many good advices during my PhD study.

Secondly, I need to thank my project leader, [REDACTED]. He helped me a lot in my research with many detailed discussions and valuable advices. I also need to thank him for correcting my manuscripts, thesis and letters.

Thirdly, I need to thank my former supervisor, [REDACTED]. I thank him for recommending me to work here. I also thank him for teaching me how to do organic synthesis and research and thank him for giving many advices and corrections on my dissertation.

I also need to thank my groups members: [REDACTED] who helped me to correct manuscripts, my thesis and gave many advices, [REDACTED] and [REDACTED] who gave me lots of advice to do synthesis and lots of happy time in the lab, [REDACTED] who is such a nice lady and gave me valuable advice on my research and big help to my daily life.

I also want to extend many thanks to my dear reserach collaborators: [REDACTED] [REDACTED] and [REDACTED] for providing considerable support to characterize OLED performances of my materials; [REDACTED] and her students for doing so much sensor measurements on my materials; [REDACTED] [REDACTED] and their students for carring out Perovskite solar cell measurements on my materials.

I also need to thank [REDACTED] for performing so many MALDI-TOF mass measurements, [REDACTED] and [REDACTED] who helped to measure lots of NMRs, [REDACTED]

██████████ who helped to extract single crystal structures, ██████████ who helped to measure many HRMS spectra and ██████████ who helped to measure plenty of photoluminescence spectra.

I also want to thank ██████████ and ██████████ who helped to order all the chemicals for my research, ██████████ who helped to provide all the glasswares and other useful tools for research and ██████████ who is such a nice person and helped to repair my bicycle for several times.

Many thanks go to other group members for their help in research and the happy life we experienced together: ██████████

██████████

██████████

██████████

██████████ and so on.

Lastly, I will thank my family whose always support and understanding are my strongest motivation to get through every challenges.

Dedicated to all the dear people who gave me a hand in my life!

Table of Contents

Chapter 1 Introduction and Motivations.....	1
1.1 Dendrimers-a short overview	1
1.1.1 Synthetic approaches of dendrimers	2
1.1.2 Dendrimer classifications.....	3
1.2 Synthesis of polyphenylene dendrimers.....	4
1.3 Properties of polyphenylene dendrimers.....	6
1.4 Introduction of OLEDs, chemical sensors, PSCs and NGNs.....	8
1.4.1 Introduction of OLEDs and development of fluorescent blue emitters	8
1.4.2 Phosphorescent emitters.....	12
1.4.3 Chemical sensors.....	16
1.4.4 Perovskite solar cells.....	18
1.4.5 Nanographene network	21
1.5 Motivations	24
1.5.1 Motivations for new fluorescent dendrimers for OLEDs.....	24
1.5.2 Motivations for new phosphorescent materials for OLEDs.....	26
1.5.3 Motivations for new dendrimer-based fluorescence sensors	27
1.5.4 Motivations for dendrimer-based hole transporting materials in Perovskite solar cells	27
1.5.5 Motivations for new dendrimer precursors for nanographene networks	28
Literature.....	28
Chapter 2 Pyrene-Based Polyphenylene Dendrimers for Blue OLEDs.....	34
2.1 Peripheral-TPA PYPPDs	34
2.1.1 Synthesis of Peripheral-TPA PYPPDs.....	34
2.1.2 Characterization of dendrimers	36
2.1.3 Photophysical properties	40
2.1.4 Electrochemistry	41
2.1.5 Device performances.....	42
2.2 Synthesis of first-generation PYPPDs with other peripheral chromophores	47
2.2.1 Synthesis of new dendrimers	49
2.2.2 Photophysical properties	51
2.2.3 Electrochemistry	53

2.2.4 Device performances.....	55
2.3 Synthesis of PYPPDs with two kinds of peripheral chromophores	59
2.3.1 Synthesis of peripherally-bipolar PYPPDs	60
2.3.2 Structural characterizations of the new CPs and dendrimers	61
2.3.3 Photophysical properties	65
2.3.4 Electrochemistry	66
2.3.5 Device performances.....	67
2.4 Summary	69
Literature.....	70
Chapter 3 Iridium-Complex-Based Polyphenylene Dendrimers as Phosphorescent Emitters	71
.....
3.1 Synthesis of (dfppy) ₃ Ir-based materials	71
3.1.1 Synthesis of Ir-complex monomers	72
3.1.2 Photophysical properties of Ir-complex monomers	76
3.1.3 Electrochemistry of Ir-complex monomers.....	77
3.1.4 Synthesis of (dfppy) ₃ Ir -based polyphenylene dendrimers	78
3.1.5 Photophysical properties	83
3.2 (dpbic) ₃ Ir-based polyphenylene dendrimers	87
3.2.1 Synthesis of dendrimers	88
3.2.2 Photophysical properties	91
3.3 Summary	94
Literature.....	95
Chapter 4 Polyphenylene Dendrimers in Chemical Sensors	97
4.1 Sensitivities of PYTPA and PYTPAG2 to explosives and metal ions.....	97
4.1.1 Fluorescence quenching of dendrimer solutions to TNT	97
4.1.2 Fluorescence quenching of dendrimer solutions to metal ions	98
4.1.3 Fluorescence quenching of PYTPAG2 thin films to metal ions	102
4.2 Electropolymerized (EP) thin films of PYTPAG2 for chemical sensors.....	105
4.2.1 Fabrication of EP films	105
4.2.2 EP films as chemical sensors	107
4.3 Summary	113
Literature.....	114
Chapter 5 PYPPDs as Hole Transporting Materials in Perovskite Solar Cells.....	116

5.1 Introduction.....	116
5.2 Device fabrications and performances.....	118
5.3 Summary.....	124
Literature.....	124
Chapter 6 Synthesis of Nanographene Networks by Electrochemistry.....	126
6.1 Bithiophene-functionalized dendrimers for NGNs.....	126
6.1.1 Synthesis of dendrimers.....	126
6.1.2 Photophysical properties.....	129
6.1.3 Electrochemical properties and Formation of NGNs.....	129
6.1.4 Characterizations of nanographene network.....	132
6.1.5 Conductivity measurements.....	136
6.2 Synthesis of α -sexithiophene-functionalized PPDs.....	137
6.2.1 Dendrimer synthesis.....	137
6.2.2 Photophysical properties.....	141
6.2.3 Electrochemical properties.....	142
6.3 Summary.....	143
Literature.....	144
Chapter 7 Summary and Outlook.....	146
Literature.....	149
Chapter 8 Experimental Part.....	150
8.1 Materials and methods.....	150
8.2 Synthetic procedures.....	153
8.2.1 Synthesis of blue fluorescent dendrimers (Chapter 2).....	153
8.2.2 Synthesis of iridium-complex-based polyphenylene dendrimers (Chapter 3).....	166
8.2.3 Synthesis of oligothiophene-functionalized dendrimers (Chapter 6).....	174
Literature.....	181
List of Publications.....	182

Index of Abbreviations

CP	2,3,4,5-tetraphenylcyclopentadienone
CV	cyclic voltammetry
DCM	dichloromethane
DFT	density functional theory
DNT	2,4-dinitrotoluene
EL	electroluminescence
EML	emitting layer
EP	electropolymerized
EPR	electron paramagnetic resonance
EQE	external quantum yield
ETL	electron transporting layer
FD	field desorption
FMO	frontier molecular orbital
FRET	Förster resonant energy transfer
GPC	gel permeation chromatography
HBC	hexabenzocoronene
HOMO	highest occupied molecular orbital
HPB	hexaphenylbenzene
HTL	hole transporting layer
ITO	Indium tin oxide
LUMO	lowest unoccupied molecular orbital
MALDI-TOF	matrix-assisted laser desorption ionization-time of light

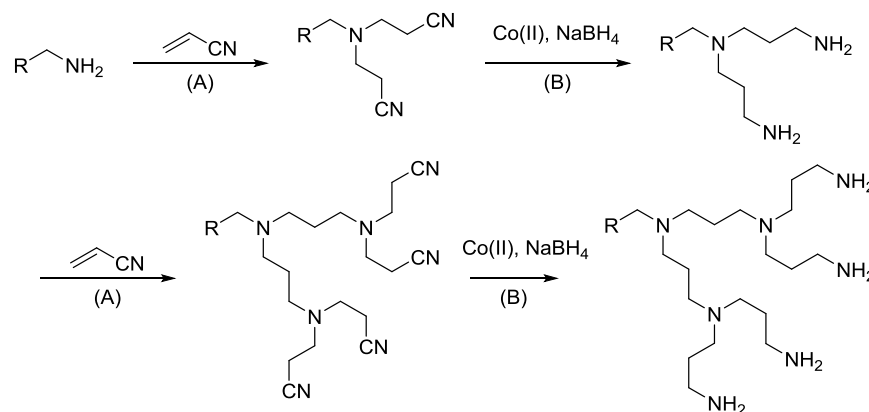
MLCT	metal-to-ligand charge transfer
NGN	nanographene network
OLED	organic light emitting diode
PAH	polycyclic aromatic hydrocarbon
PCE	power conversion efficiency
P3HT	poly(3-hexylthiophene)
PLQY	photoluminescence quantum yield
PPD	polyphenylene dendrimer
PSC	Perovskite solar cell
rt	room temperature
TADF	thermally activated delayed fluorescence
TBAF	tetrabutylammonium fluoride
TBAPF ₆	tetrabutylammonium hexafluorophosphate
TIPS	triisopropylsilyl
TIPSE	triisopropylsilylethynyl
THF	tetrahydrofuran
TMS	trimethylsilyl
TNT	2,4,6-trinitrotoluene
TPA	triphenylamine
VBE	valence band energy
UV-vis	Ultraviolet-visible (absorption spectroscopy)

Chapter 1 Introduction and Motivations

In this thesis, five topics will be included: there are dendrimer-based fluorescent blue emitters for organic light emitting diodes (**OLEDs**) (chapter 2), dendrimer-based phosphorescent emitters for **OLEDs** (chapter 3), dendrimer-based chemical sensors (chapter 4), dendrimer-based hole transporting materials for Perovskite solar cells (chapter 5) and nanographene networks by electrochemistry (chapter 6). The materials utilized are all polyphenylene dendrimers. As a result, in this chapter, dendrimers will be introduced first and then **OLEDs**, chemical sensors, Perovskite solar cells and nanographene networks will be described individually. Lastly, motivations will be given.

1.1 Dendrimers-a short overview

Dendrimers are important members in the macromolecular family nowadays, first reported by Fritz Vögtel and his coworkers in 1978.^[1] They showed the synthesis of a branched-triisopropylamine-based macromolecule starting from a primary amine, which reacted with acrylonitrile via Michael addition to give a dinitrile which was then reduced into a diamine by cobalt(II) salt and sodium borohydride. The repeated Michael addition and reduction process resulted in a macromolecule with regular branching. In their paper, they first called this kind of branched structure a cascade molecule. This kind of dendrimer was later developed into a commercial product called **POPAM** (Scheme 1.1).^[2]



Scheme 1.1: Synthetic route for the first reported dendrimer.

“Dendrimer” as a word for this specific kind of macromolecule was first provided by Tomalia in 1985 for first-time synthesizing branched polyamidoamines (**PAMAM**)^[3] and this word became popular in scientific reports since the 1990s. It originates from a Greek word δένδρον, or dendron, meaning “tree”. So a dendrimer means a tree-like macromolecule with regular, repeated branching, exact molecular structure, precise molecular weight and monodispersity. In general, a dendrimer consists of three parts: the core, scaffold and surface structure (Figure 1.1). The core is the center of the molecule. It connects

with a given number of branches which are called dendrons. Each dendron is composed of a given number of branching units (the scaffold) and surface groups. The number of the branches determines the scale of a dendrimer and the generation. The increasing rates of branches and surface moieties grow exponentially with the number of generations. The nature of peripheral functional groups, which extend to the surroundings, has an essential influence on the chemical and physical properties of the dendrimer.

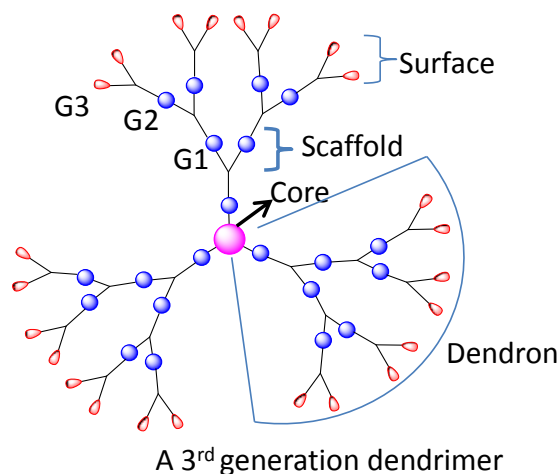


Figure 1.1: General structure of a third generation dendrimer.

1.1.1 Synthetic approaches of dendrimers

The synthesis of dendrimers generally includes two types of reactions: dendritic growth and activation of peripheral groups. In general, there are two approaches to afford a dendrimer: divergent and convergent (Figure 1.2).^[4] The divergent way, e.g. the synthesis of the first dendrimer (Scheme 1.1) or **PAMAM** mentioned above, normally starts with a small functional molecule with the reactive groups, called the core. The core reacts with well-designed building blocks, containing one reactive focal point and some functional groups which can be transformed into new reactive sites by activation or deprotection for controlled and generation-by-generation dendritic growth, to make the first-generation dendrimer (G_1). This process is called dendritic growth. The G_1 dendrimer will then undergo an activation process to expose the reactive sites on its surface and the second-generation dendrimer (G_2) could be formed after the second-stage dendritic growth. With repeated growth and activation steps, higher-generation dendrimers could be achieved rather easily in principle. However, reality is more complicated. With each growth step, the number of the reactive sites on the dendrimer is exponentially increased. This means the reaction time required for synthesis of G_n will also increase exponentially relative to G_{n-1} . It will be very time-consuming for synthesis of very big dendrimers as can be imagined. In addition, there are strong steric-shielding effects for bigger dendrimers, which cause significant problem to ensure every surface-active site to react with the building blocks. For example, for the flexible dendrimers, there are the problems of surface groups bending into the interior of the dendrimer, which will make them unable to react with the building blocks. This is consistent with the so-called

dense-core theory.^[5] For the rigid dendrimers, there is the problem of reduced surface space for each active point after each generation growth, which is also called dense-shell concept.^[6] As a result, there usually exist structural defects with some unreacted active sites when making higher generation dendrimers by the divergent approach.^[7]

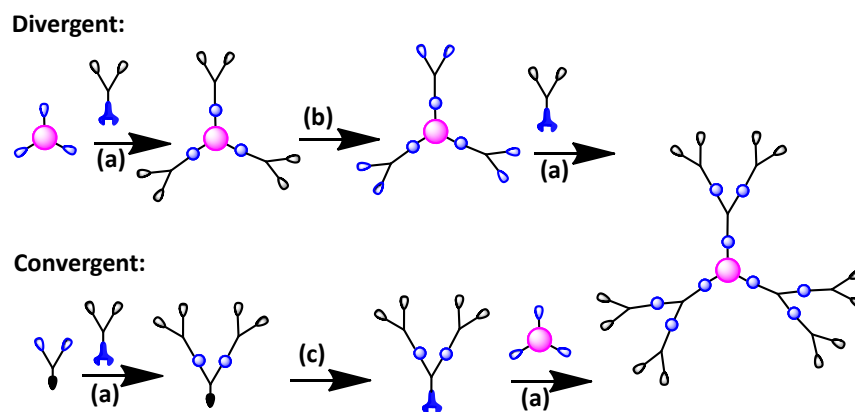


Figure 1.2: Divergent and convergent pathways for synthesizing dendrimers. (a) Dendritic growth; (b) Activation of peripheral groups; (c) Activation of the focal point.

The convergent approach, introduced by Hawker and Fréchet in 1990 for the synthesis of poly(arylether) dendrimers (Figure 1.2), on the other hand, applies a reverse growth process as compared with the divergent one.^[8] It usually starts with a building block with the focal point protected. Its reactive points will react with a focal-activated building block to form a bigger building block or dendron. This process is also called dendritic growth. The activation and growth processes can be repeated to generate the desired building block which will react with a core unit to give birth to the dendrimer. This method comparing with the divergent approach has some advantages. For example, the synthesis of a dendron is easier than that of a dendrimer due to the smaller size of the former. As a result, the relative number of structural defects in the dendron is lower using this method. However, with increasing dendron size, it also suffers from low reaction efficiency with the core due to steric hindrance. As a result, this method usually could not be applied for making higher-generation dendrimers.

1.1.2 Dendrimer classifications

Nowadays there are many different kinds of dendrimers.^[4] Based on the flexibility of their backbones, they can generally be divided into flexible and rigid dendrimers. Regarding flexible dendrimers (Figure 1.3), besides **POPAM**,^[2,9] **PAMAM** is currently widely used in research. For example, it is applied for drug delivery into cells and gene therapy (e.g. siRNA delivery) due to its high water solubility, high drug loading capacity, and good biocompatibility.^[10] It is also commercially available.^[11] Another well-known, water-soluble dendrimer is called **Arborol** which contains amido, ether and hydroxyl groups. This dendrimer was first reported by Newkome and his coworkers in 1985.^[12] The poly(aryl ether) dendrimer, also called Fréchet-type dendrimer is another famous one in this class.^[13]

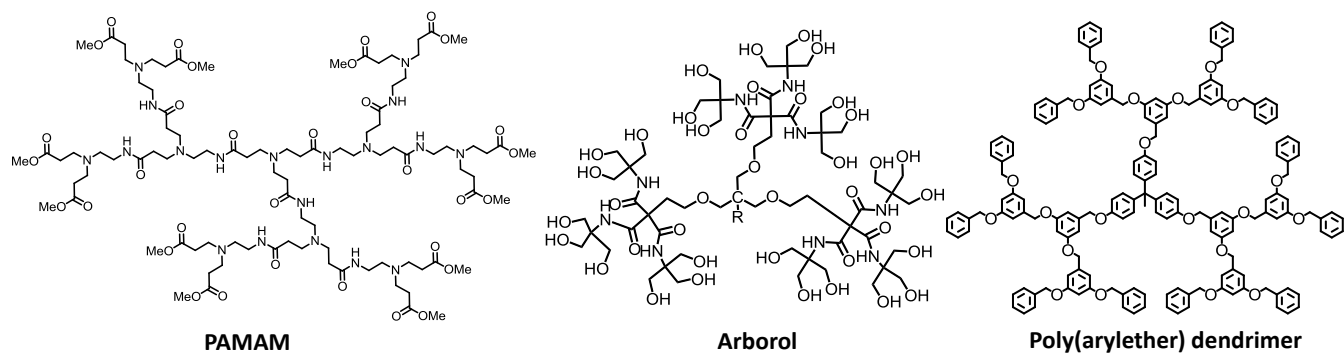


Figure 1.3: Examples of flexible dendrimers.

Rigid dendrimers are shape-persistent and topologically well-defined and allow precise arrangements of functional groups. In 1990, the first rigid dendrimer, i.e. a polyphenylene dendrimer based on 1,3,5-trisubstituted benzenes was reported by Miller and his coworkers using a convergent approach and the Suzuki coupling reaction (Figure 1.4).^[14] In 1991, Hart and his coworkers reported the synthesis of an iptycene-type dendrimer in which phenyl rings were connected by bicyclo[2.2.2]octanes.^[15] Within the same year, Moore and his coworkers reported the convergently synthesized 1,3,5-triethynylbenzene-based polyphenylacetylene dendrimer by Sonogashira coupling.^[16] The Müllen-type dendrimers or polyphenylene dendrimers (**PPDs**), which were also frequently used as the precursors of nanographenes, were first reported in 1997.^[17]

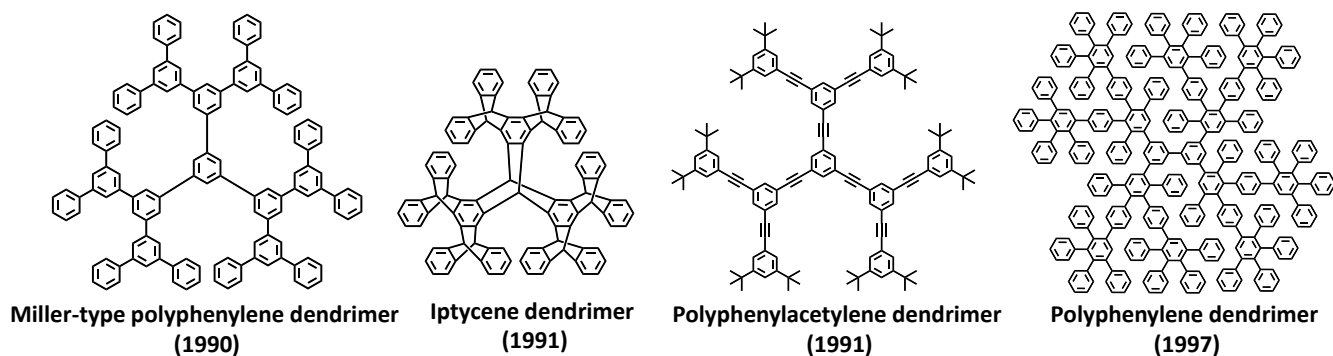


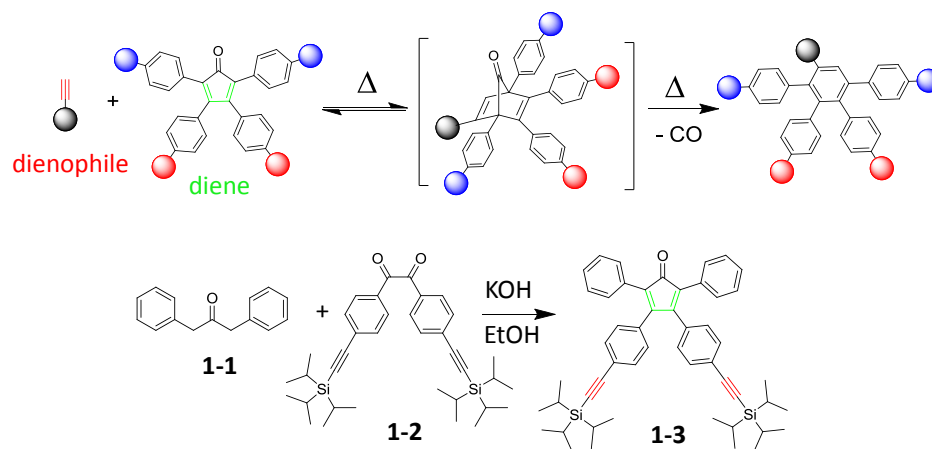
Figure 1.4: Examples of rigid dendrimers.

In the following sections, **PPDs** will be introduced specifically, including synthetic method, intrinsic properties and applications in versatile fields.

1.2 Synthesis of polyphenylene dendrimers

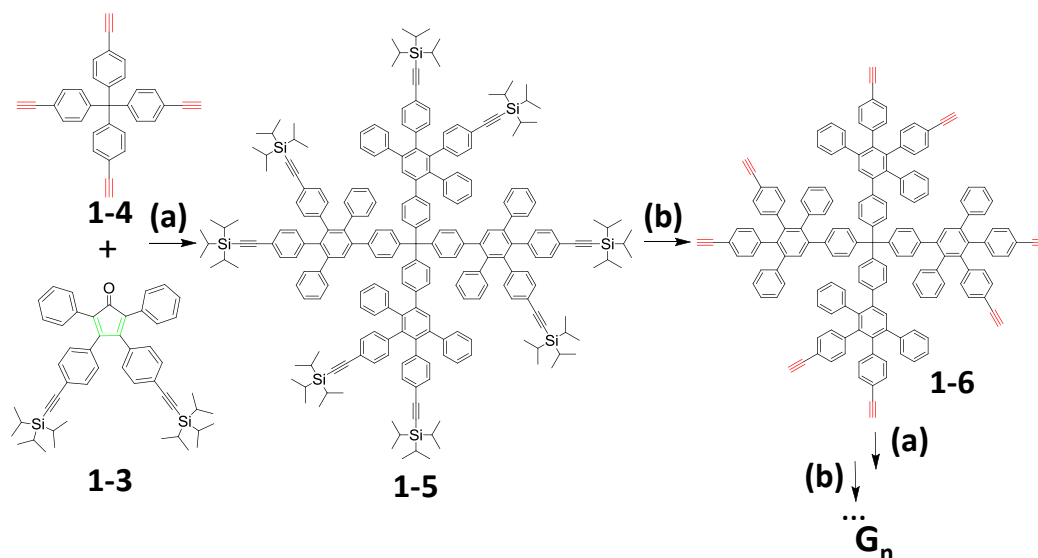
PPDs are prepared based on two essential reactions with nearly no side products and high yields. The dendritic growth step is a [4+2] Diels-Alder cycloaddition. The activation step is the desilylation of triisopropylsilyl (TIPS) substituted alkynes. The Diels-Alder reaction occurs between a 2,3,4,5-tetraphenylcyclopentadienone (the diene) and a functionalized ethynyl moiety (dienophile), a reaction first introduced by W. Dilthey in 1933^[18] (Scheme 1.2, top). Under heating, a norbornadien-7-one

intermediate is reversibly generated via cycloaddition.^[19] However, the reaction is driven forward at high temperature, e.g. 140 °C, when one equivalent of carbon monoxide is extruded, together with the formation of a new phenylene ring or the generation of a polyphenylene dendron while synthesizing **PPDs**. To synthesize higher generation **PPDs**, an AB₂ building block can be introduced, which is 2,5-diphenyl-3,4-bis[4-(triisopropylsilylethynyl)phenyl]cyclopentadienone (**1-3**) (Scheme 1.2, bottom). It contains a diene subunit for the Diels-Alder reaction and two CC triple bonds as potential dienophiles which are protected by bulky TIPS groups. Compound **1-3** is synthesized by Knoevenagel condensation reaction between 1,3-diphenylacetone (**1-1**) and 4,4'-bis(triisopropylsilylethynyl)benzil (**1-2**). This reaction was widely used to make many kinds of functional 2,3,4,5-tetraphenylcyclopentadienones (**CPs**) for **PPDs** with targeted purposes and usually high yields of products were received.^[20]



Scheme 1.2: Representative Diels-Alder reaction between alkyne and CP (top) (note: the colored balls represent functional groups) and synthesis of AB₂ building block (**1-3**) (bottom).

Most often, **PPDs** are synthesized by a divergent approach. Taking the tetraphenylmethane-based dendrimer as an example (Scheme 1.3), the first-generation triisopropylsilylethynyl(TIPSE)-functionalized **PPD** (**1-5**) is obtained after cycloaddition between the ethynyl-functionalized tetraphenylmethane (**1-4**) and 4 equivalents of **CP** (**1-3**). This reaction usually takes place in *o*-xylene solution by heating up to 140 °C and may take 24 hours. To grow higher-generation dendrimers, the peripheral ethynyl groups of dendrimer **1-5** are activated by tetrabutylammonium fluoride (TBAF) and dendrimer **1-6** could be produced in nearly quantitative yield. After that, dendrimer **1-6** will undergo repeated dendritic growth and activation steps to afford higher-generation dendrimers. In addition, a convergent approach to synthesize **PPDs** was also reported by Müllen, et al. in 1999.^[21]



Scheme 1.3: Synthetic route for tetraphenylmethane-based **PPDs**. (a) o-xylene, 140 °C; (b) TBAF, THF, rt.

1.3 Properties of polyphenylene dendrimers

First, **PPDs** are rigid and shape-persistent relative to other dendrimers.^[22] The scaffolds of **PPDs** are polyphenylenes directly linked without any highly flexible components. This renders polyphenylenes quite rigid with little backfolding along the radial directions. This is supported by the extensively explored poly(p-phenylene)s which are rigid and rod-like with the persistence lengths up to 20 nm (around 46 phenylene rings).^[23] The rigidity and shape persistence of **PPDs** has been confirmed by small angle neutron scattering (SANS) experiments which suggest that **PPDs** are true dense-shell examples with end groups exhibiting no backfoldings.^[24] In addition, atomic force microscopy (AFM) studies have shown that a single **PPD** molecule on a mica surface has a height which is consistent with the size of a single dendrimer molecule calculated by the molecular dynamics method. Paused force mode AFM demonstrated that **PPDs** exhibited high stiffness and low adhesion properties.^[25] Solid state NMR research also demonstrated that there existed strong intramolecular steric constraints inside of **PPDs** due to the rigidity of the dendrimers.^[26]

Second, **PPDs** are globular and three-dimensional. Due to the high intramolecular constraints among phenylene rings, the spatial structures of **PPDs** are tunable based on the shape of the core and the dendron positioning. For example, a biphenyl core leads to a dumbbell-shaped dendrimer while a tetrahedral tetraphenylmethane core affords a globular dendrimer. This has been studied with theoretical calculations.^[27] In addition, higher-generation dendrimers tend to adopt more globular configurations. As depicted in Figure 1.5, the crystal structure of hexaphenylbenzene-based, first-generation **PPD** vividly shows its three-dimensional geometry.^[28] The dihedral angles ($\sim 80^\circ$) between the central phenylene ring and its nearby six phenylene groups and the highly twisted polyphenylene dendrons (torsion: $\sim 50^\circ$) induce a propeller-like configuration. The globular nature of **PPDs** prompts special

properties compared with their linear counterpart, i.e. poly(p-phenylene)s. One big difference is the much higher solubilities of **PPDs** in common organic solvents, e.g. DCM, THF and toluene due to the greatly reduced intermolecular interactions in globular **PPDs**, contrary to the linear analogues. This phenomenon has been studied by Miller and his coworkers by comparing the solubilities of 1,3,5-trisubstituted benzene-based polyphenylene dendrimers with some p-phenylene oligomers, e.g. dendrimer-G2 (Figure 1.4, left) (solubility: 120 g/l in toluene) vs. p-tetraphenyl (0.12 g/l).^[29] Fréchet and his coworkers reached a similar conclusion by comparing polyarylether dendrimers and their linear counterparts.^[30] This increased solubility makes **PPDs** easier characterized by various techniques, e.g. NMR spectroscopy, MALDI-TOF mass spectrometry, UV-vis absorption and photoluminance spectroscopy and cyclic voltammetry. The ease of characterization and processing provides **PPDs** with opportunities in many applications, e.g. solution-processed, organic-light-emitting diodes (**OLEDs**)^[31] and solution-bottom-up synthesis of nanographenes.^[17b, 32]

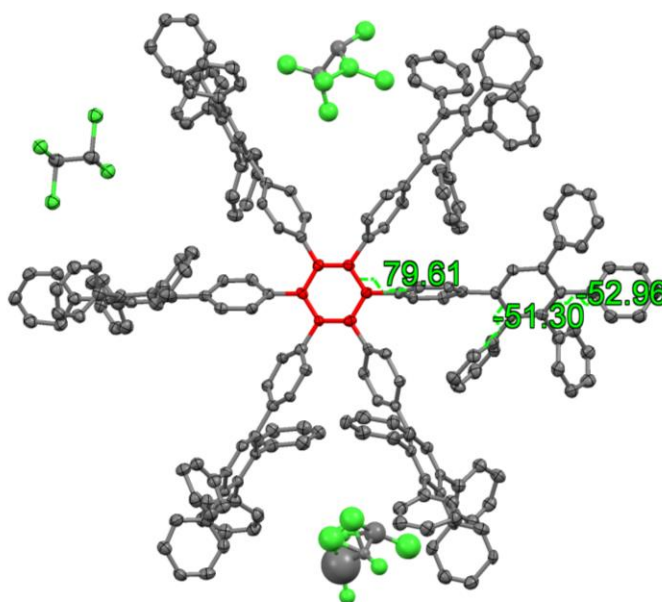


Figure 1.5: Single crystal structure of hexaphenylbenzene-based, first generation **PPD**. (the green species are the solvent molecules).^[28]

Third, PPDs have voids inside. As depicted in Figure 1.5, solvent molecules are encapsulated stably inside the dendrimer molecule or within the cavities between two nearby molecules. This property has prompted the application of **PPDs** as hosts and chemical sensors to detect guest molecules.^[33]

Fourth, PPDs allow site-specific functionalizations. The rigid and shape-persistent globular **PPDs** could be functionalized in the core, scaffold and surface (Figure 1.6). All three positions in **PPDs** are spatially separated and precisely defined and, as a result, multifunctional materials could be designed and applied to many different areas. For example, isolating a light-emitting moiety at the core enhances its photoluminance quantum yield (PLQY) by excluding aggregation-induced fluorescence quenching

and could be applied in many fields, e.g. **OLEDs**.^[31a, 31c, 34] Surface functionalization determines the physical properties of the dendrimers, e.g. the solubility. For example, by introducing sulfonic acid groups on the surface of **PPDs**, water soluble **PPDs** were synthesized to serve as drug-delivery agents into cells.^[20c, 35] Attaching some polar moieties in the scaffold, e.g. pyridine creates host sites that encapsulate polar guest molecules in **PPDs** and also allow their detections.^[33c] Additionally, core-surface functionalized **PPDs** have been applied in single-molecule spectroscopy with efficient surface-to-core energy transfers.^[36]

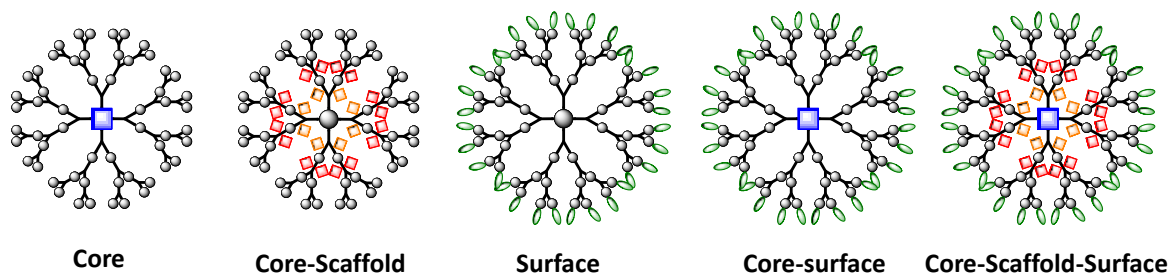


Figure 1.6: Some different functionalization styles of **PPDs**.

Having briefly described how **PPDs** were employed in many different areas, their applications in **OLEDs**, chemical sensors, Perovskite solar cells (**PSCs**) and nanographene networks (**NGNs**) will be introduced in more detail in the following part.

1.4 Introduction of **OLEDs**, chemical sensors, **PSCs** and **NGNs**

1.4.1 Introduction of **OLEDs** and development of fluorescent blue emitters

Nowadays, light emitting diode (**LED**)-based products, i.e. **LED** flat panels and **LED** lighting are widely used in everyday life around the world. **LEDs** are changing our world day-by-day due to their much higher efficiency in light output than the traditional lighting sources (Figure 1.7), e.g. the incandescent bulbs and as a result considerable amount of energy can be saved.^[37]

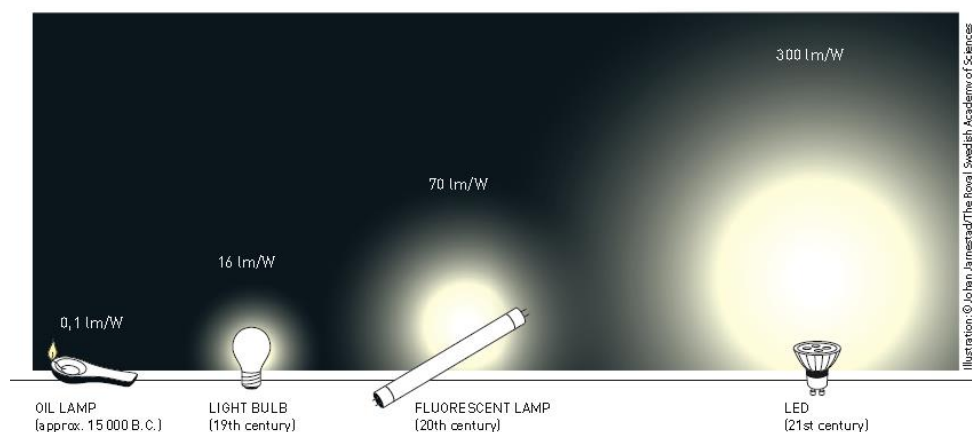


Figure 1.7: Lighting efficiency comparison of four generations of lighting sources.^[38]

OLED-based displays and lighting are considered to be the next generation products. Their advantages include high flexibility, low cost and low energy consumption. The flexibility is probably the most distinctive property based on their organic compositions. It makes products bendable and paves the way to novel applications which are impossible for inorganic materials, e.g. the curved **OLED** flat panels commercialized by LG and Samsung.^[39]

Even though **OLED**-based products have been commercialized, there are still challenges, such as the development of highly efficient, deep blue **OLEDs**, which is still a field with intense research interests. In general, a colorful flat panel display requires three basic colors, i.e. red, green and blue. White **OLED** (**WOLED**) for lighting requires these three as well or a combination of blue and yellow. As a result, blue light-emitting material is necessary for both displays and lighting. So far, red- and green-emitting organic materials are well-developed with high performance. But the blue ones are still far behind, due to their low efficiencies, poor color purities and shorter life time. This is partly because of higher energy required for blue light emission compared with the other colors.^[40]

The simplest **OLED** structure is just composed of cathode/emitting layer (**EML**)/anode, called a single-layer device (Figure 1.8).^[41] However, a single layer device is not able to collect enough holes and electrons for a high performance as proven by **LEDs** and **OLED** results.^[37, 42] To increase the accumulation of both holes and electrons in the **EML** and enhance the light output as a result, introducing more layers is needed, e.g. separate hole transporting layer (**HTL**) and electron transporting layer (**ETL**). They work as the bridges between the electrodes and the emissive layer to help holes and electrons hop into **EML** efficiently due to their proper HOMO and LUMO levels.^[43]

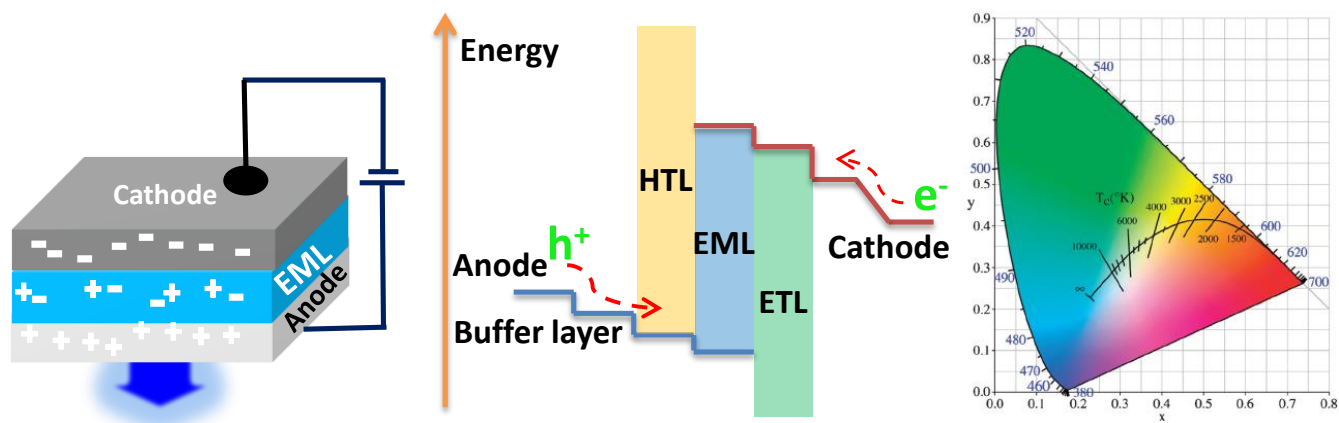


Figure 1.8: Single-layer **OLED** structure (left), energy diagram of three-layer device (middle) and CIE chromaticity diagram (right).^[40b]

There are several parameters commonly used to characterize **OLED** performances. They are:

- luminance: the luminous intensity per unit area and expressed as candela per square meter (cd/m^2);
- current efficiency: evaluates the device efficiency and means the amount of light generated per ampere (cd/A);
- onset voltage: the potential, at which light is first detected;
- 1931 Commission Internationale d'Eclairage (CIE) chromaticity coordinates (x, y): defines a specific color by x and y in the coordinate (Figure 1.8) which shows that blue light locates in the region of ($x \leq 0.2$, $y \leq 0.2$) and for deep blue, the y value should be even less than 0.1;
- external quantum efficiency (EQE): evaluates the device efficiency in percentage and relates the amount of light emitted from the device to the amount of input energy;
- power efficiency: denotes the efficiency as well and represent the luminous intensity per unit watt of power (lm/W).

Nowadays, organic blue-light-emitting materials generally include small molecules, polymers and dendrimers. Depending on the emission mechanisms, they are classified as traditional fluorescent materials (emit only singlet excitons), phosphorescent materials (emit both singlet and triplet excitons) and thermally activated delayed fluorescence (**TADF**) materials (emit singlet excitons and excitons from triplet upconversions). Small molecules have received considerable attention due to their simple molecular structures. Recently, some examples were reported and displayed pure blue or deep blue emission with high efficiencies (Figure 1.9). For example, Adachi et.al reported donor-acceptor-donor type molecules with **TADF** properties, i.e. bis[4-(9,9-dimethyl-9,10-dihydroacridine)phenyl]sulfone (**DMAC-DPS**) which reached an EQE of 19.5% with pure blue emission (CIE_{xy}= 0.16, 0.20)^[44] and bis[4-(3,6-di-tertbutylcarbazole)phenyl]sulfone (**DCAB-DPS**) which demonstrated a deep blue emission with an EQE of 9.9%.^[45] However, there are drawbacks of these materials, i.e. the costly and time-consuming device fabrications due to the UHV deposition method and complicated multiple-layer devices.^[46]

Polymer-based blue emitters, e.g. polyfluorenes (**PFs**)^[47] have the advantage of cost-effective solution processing, e.g. spin coating and ink-jet printing. So far, several efficient blue-emitting polymers were reported. For example, the fluorene-dibenzothiophene-S,S-dioxide-based copolymer (**PPF-3,7SO20**)^[48] exhibited a maximum current efficiency of 6 cd/A with CIE coordinates of (0.16, 0.19) (Figure 1.9) and a pyrene- and triphenylamine (**TPA**)-based copolymer (**PpyrTPA**) in a statistical ratio showed a current efficiency of 1.42 cd/A with a maximum luminance of 16540 cd/m^2 ,^[46] in addition, one copolymer with 4 different components (**CP-ABCD**) reached a current efficiency of 9.7 cd/A with CIE coordinate of (0.14, 0.13) in a two-layer device.^[49] However, polymer materials still suffer from poor performance reproducibility due to their polydisperse properties.

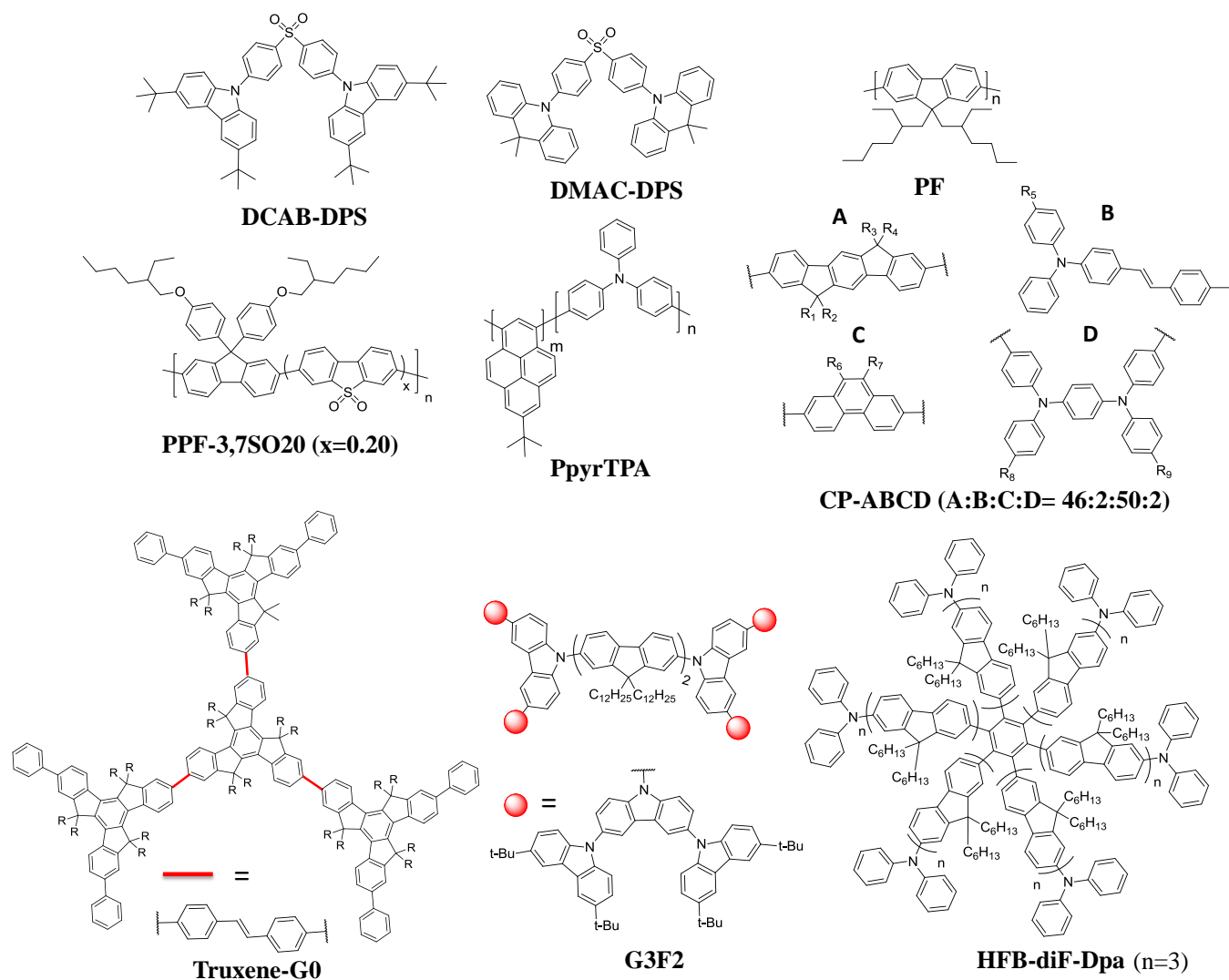


Figure 1.9: Examples of small-molecule, polymer and dendrimer-based blue-light-emitting materials for **OLEDs**.

Dendrimers, in comparison with polymers, have well-defined structures and precise molecular weights, which guarantees their high reproducibility in applications. In addition, dendrimer-based materials enable solution-processed film deposition due to their weak crystallization tendency. Moreover, the possibility of site-specific functionalizations at well-defined points for rigid dendrimers paves the way to multifunctional materials. As a result, dendritic materials have received considerable attention in **OLEDs**. So far, some dendrimer-based materials were reported as efficient emitters in devices (Fig 1.9). For example, the star-shaped, 1,2-diphenylvinylene-bridged truxene-based material (**truxene-G0**) reached an efficiency of 5.3 cd/A with deep blue emission ($\text{CIE}_{x,y}$: 0.155, 0.086),^[50] and an extended carbazole-dendronized, bifluorene-centered dendrimer (**C3F2**) showed a current efficiency of 3.79 cd/A with deep blue emission ($\text{CIE}_{x,y}$: 0.17, 0.11) and strong luminance of 19184 cd/m^2 ,^[51] in addition, the oligofluorene-based and peripheral-**TPA** dendrimer (**HFB-diF-Dpa**) demonstrated a current efficiency of 6.99 cd/A and deep blue emission ($\text{CIE}_{x,y}$: 0.154, 0.136) in a two-layer device.^[52]

PPDs have been applied in both fluorescent and phosphorescent light-emitting materials in OLEDs based on their shape-persistent architectures which enable generation-by-generation and core-scaffold-surface selective functionalizations and their good solubilities in organic solvents, e.g. THF and toluene, facilitating solution-process device fabrications. For instance, Qin et al. reported some polytriphenylene dendrimers, e.g. **TPG2** (Figure 1.10), exhibiting blue emission due to the high torsion angles between neighboring triphenylenes, but poor luminance in devices with the highest value of 300 cd/m^2 .^[31a] Later, a blue emitter, pyrene was placed at the core (Figure 1.10, **PYG2**) and the PLQY was increased significantly due to the effective protection of the core by the surrounding bulky dendrons.^[31b] Further, a new PPD with its surface functionalized with good hole transporting moieties, i.e. TPAs (Figure 1.10, **PYGTPA**) demonstrated both high PLQY and effective hole transport ability. Thus, in a two-layer device, a luminance of 1400 cd/m^2 and an overall current efficiency of 0.26 cd/A were achieved, partly due to the reduced hole injection barrier from the anode.^[31b] Accordingly, the specific surface and core functionalizations seems open the way to high-performance PPDs in blue OLEDs with simple device configurations.

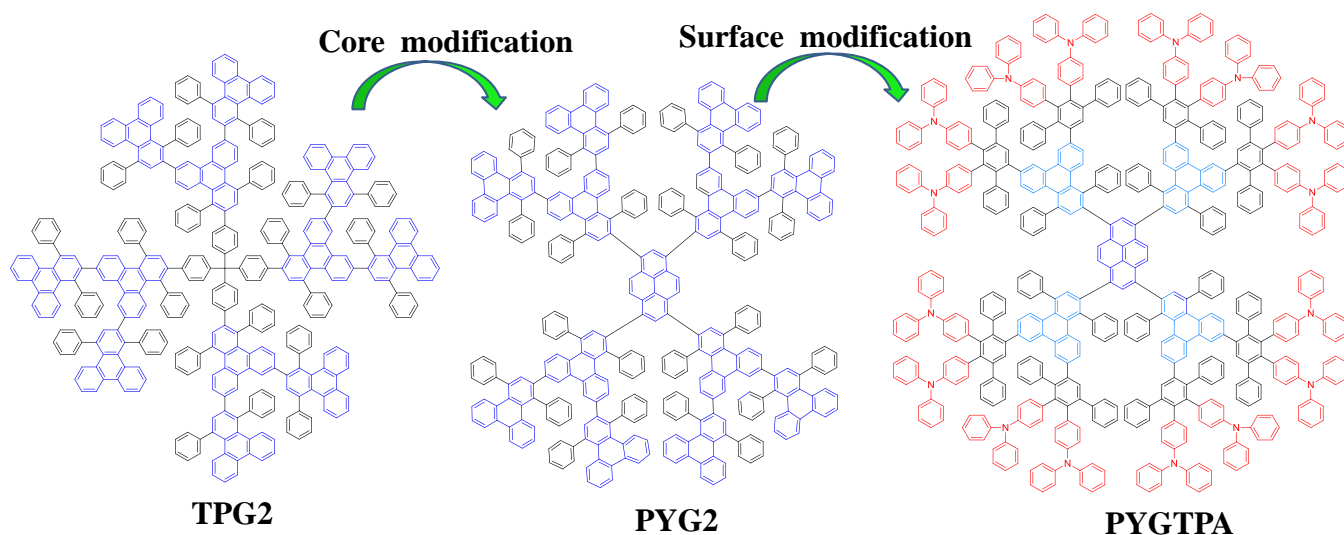


Figure 1.10: Examples of PPDs for blue OLEDs.

1.4.2 Phosphorescent emitters

Traditional organic light-emitting materials, e.g. pyrene or anthracene-based molecules are fluorescent emitters. In devices, excitons are formed in singlet and triplet states with a ratio of 1:3 as determined by quantum spin statistics.^[53] However, these materials only emit from singlet excitons in devices and the triplet ones taking up 75% of the total undergo non-emissive decay, e.g. heat. As a result, the maximum internal efficiency of traditional fluorescent emitters is only 25% theoretically, corresponding to the maximum external efficiency around 5% considering only around 20% of light can be emitted from the conventional planar layered OLED configuration.^[54] This is detrimental in practical applications.

However, there are strong triplet emitters at ambient conditions, most commonly iridium (Ir) and platinum (Pt) complexes due to effective spin-orbital couplings induced by the heavy metal atoms in the organometallic compounds.^[55] Their devices have been developed magnificently since the first report by Forrest and Thompson as well as their co-workers in 1998.^{[56],[40a, 54, 57]} Phosphorescent emitters could acquire much higher efficiency than fluorescent ones because they emit from both singlet and triplet excitons in devices. As a result, triplet emitters could reach an internal quantum efficiency of 100%, corresponding to an external quantum efficiency of around 20% due to the around 20% light extraction efficiency of conventional planar layered **OLED** structure.^{[54, 56, 58][59]} Significant device improvements were achieved so far and **OLEDs** based on red, green and blue triplet emitters all reached 20% EQEs (Figure 1.11). In 2008, Meerheim et al. reported that iridium(III)bis[2-methyldibenzo-(f,h)quinoxaline](acetylacetonate) (**Ir(MDQ)₂(acac)**) as a red emitter reached an EQE of 25.5% with CIE_{xy} (0.66, 0.34).^[60] For green emitters, Kido et al. elucidated that a fac-tris(2-phenylpyridine)iridium (**Ir(ppy)₃**)-based device gave an efficiency of 27% at luminance of 100 cd/m².^[61] In addition, iridium(III)bis(4,6-difluorophenylpyridinato-N,C^{2'}) picolinate (**FIrpic**) as a popular sky blue emitter reached an EQE of 26%, reported by Kido et al.^[62] Moreover, for pure blue triplet emitters, i.e. bis[(3,5-difluoro-4-cyanophenyl)pyridine]iridium picolinate (**FCNIrpic**) which demonstrated a 25.1% EQE with CIE_{xy} (0.14, 0.18) and a planar Pt(II) complex (**PtON7**) which obtained a 23.7% EQE with CIE_{xy} (0.14, 0.15).^[63] Even though, highly efficient and pure blue phosphorescent **OLEDs** have been reported, their life time is still much lower than red and green ones.^[64]

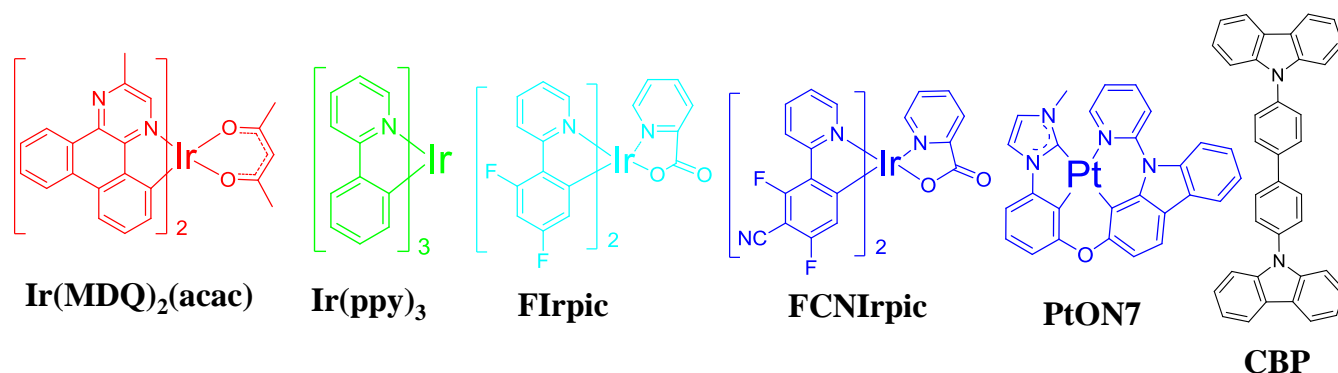


Figure 1.11: Examples of red, green, sky blue and pure blue triplet emitters reaching 20% EQE in **OLEDs** and 4,4'-bis(N-carbazolyl)-1,1'-biphenyl (CBP) (a host material).

The neat films of triplet emitters are prone to undergo severe self-quenching.^{[65], [66]} Therefore, the emitters, also called dopants, are usually incorporated into a matrix to ensure high PLQYs. The matrix composed of host materials, e.g. CBP (Figure 1.11) has the function of charge transport and energy transfer to the dopants.^[58a, 67] However, these small-molecule-based devices still suffer from expensive UHV fabrication and inhomogeneous distribution of the dopants in the matrix. Dendrimers can overcome these problems based on their good film formation and generation-by-generation site-specific

functionalization. In a rigid and structurally well-defined dendritic molecule, the core can be a phosphorescent emitter, while the surface is functionalized with host moieties. Thus, the ratio between the hosts and dopants and their positions are accurately controlled in a dendritic structure.^[43a, 68] There has been considerable attention on dendrimer-based phosphorescent emitters, especially the green and red ones since the pioneering work of Samuel and Burn et al. in 2001.^{[69] [70]}

PPDs have been reported as phosphorescent green and red emitters by Qin et al. (Figure 1.12).^[31c, 34] **Ir(ppy)₃**-based **PPDs** up to the fourth generation were synthesized using the divergent method. Interestingly, the peak emissions of these dendrimers in solutions were at around 516 nm which was close to the bare **Ir(ppy)₃** (λ_{em} : ~508 nm),^[71] suggesting that the attachment of the polyphenylene dendrons did not change the emission wavelength considerably. A two-layer device without doping revealed a maximum current efficiency of 21.9 cd/A and a 6.1% EQE for **GIrG3** (Figure 1.12).^[34] This notable performance was attributed to the effective protection of the core by the bulky dendrons to ensure a high PLQY. In addition, fac-tris(2-benzo[b]thiophenylpyridyl)iridium(III) (**Ir(btp)₃**) as a red phosphorescent emitter was placed in the core to make red **PPD** emitters, e.g. **RIrG2** (Figure 1.12). Pure red color emissions from these dendrimers were demonstrated in **OLEDs**.^[31c]

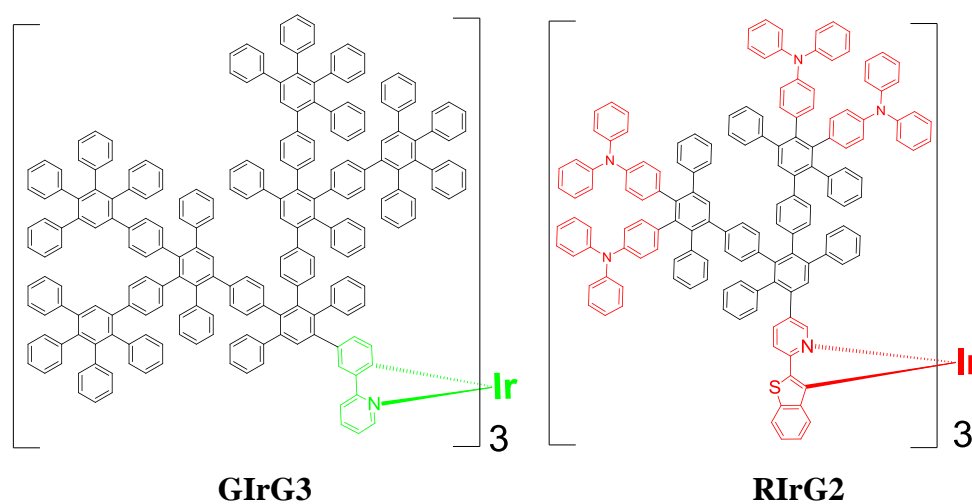


Figure 1.12: Examples of green and red phosphorescent **PPD** emitters.^[31c, 34]

There were very few blue phosphorescent dendrimers reported, however and they all suffered from low color purity or poor efficiencies or both (Figure 1.13, Table 1.1).^[72] Accordingly, it is worthwhile to develop high-performance, dendrimer-based blue-phosphorescent emitters.

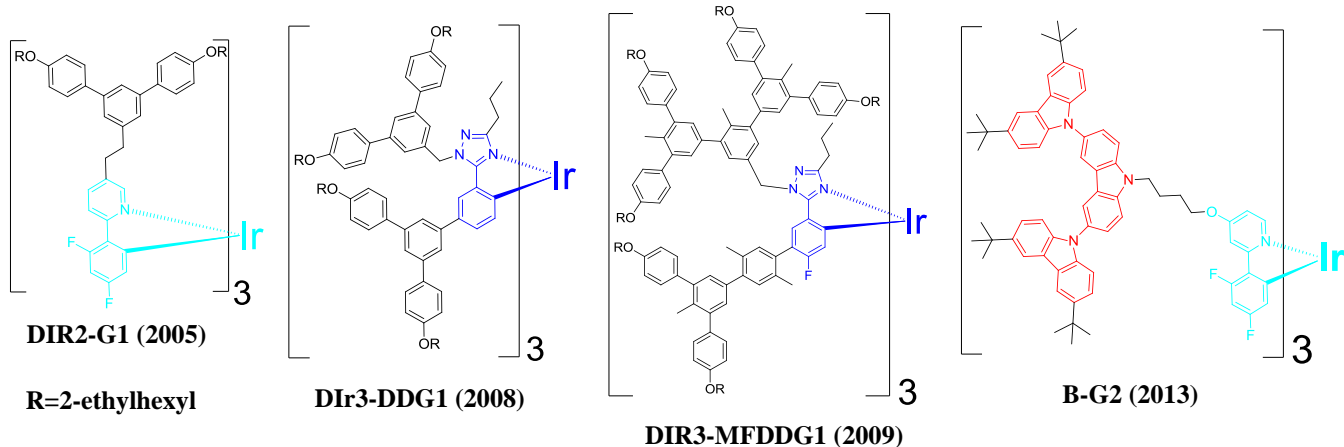


Figure 1.13: Examples of blue-phosphorescent dendrimers.^[72]

Table 1.1: Device performance of blue phosphorescent dendrimers.^[72]

	DIR2G1	DIR3-DDG1	DIR3-MFDDG1	BG2
η (cd/A)	-	-	5.4	31.3
EQE	3.8	7.9	95	15.3
L_{\max} (cd/m ²)	1500	5000	100	6800
CIE (x, y)	-	0.18, 0.35	0.16, 0.17	0.16, 0.29

So far quite a few blue triplet emitters have been reported and most of them are iridium complexes,^[40a, 54, 57a] e.g. the sky blue **FIrpic**^[73], [bis(4,6-difluorophenylpyridinato-N,C^{2'})] [tetrakis(1-pyrazolyl)borate]iridium(III)(**FIr6**)^[74], tri(4,6-difluorophenylpyridinato-N,C^{2'})iridium(III) ((**dfppy**)₃Ir)^[72d, 75], and the pure blue tri(4,6-difluoro-5-cyano-phenylpyridinato-N,C^{2'})iridium(III) (**FCNIr**),^{[76],[77]} fac-tris(2',6'-difluoro-2,3'-bipyridinato-N,C^{4'})iridium(III) ((**dfppy**)₃Ir)^[78] (Chart 1). Due to (**dfppy**)₃Ir's pure blue emission with high PLQY, it is desired to select it as the core of **PPD** to make new **PPD**-based blue light emitting materials. To the best of my knowledge, devices using this kind of emitter have appeared in patents^[79] but no one has reported its incorporation into a dendritic structure. Therefore, it is interesting to utilize this emitter in **PPDs** and this work will be introduced in Chapter 3.

	Firpic	FIr6	(dfppy) ₃ Ir	FCNIr	(dfppy) ₃ Ir
λ_{\max} (PL)(nm)	470, 494	460, 487	468, 480	448, 476	438, 463
PLQY at rt	0.42	0.73	0.43	-	0.71
CIE(x, y)	0.17, 0.34	0.16, 0.27	0.15, 0.29	0.14, 0.16	0.14, 0.12

Chart 1: Common Ir-complex-based blue emitters and their photophysical properties.

The emissions of dendrimers, on the other hand, can also be applied for chemical sensors. Therefore this topic will be introduced in the following part.

1.4.3 Chemical sensors

Currently, there is a strong demand for good chemical sensors as sensitive detectors for explosives, because the terrorist's activities are very common issues concerning people's life nowadays and traditional detection methods are costly and not durable.^[80] For example, trained dogs are commonly used for detecting explosives and are very effective, but they need long time of training and their service time is limited due to inhalation of the poisonous explosives.^[81] The major explosives nowadays are nitro-rich compounds, e.g. 2,4,6-trinitrotoluene (TNT) and 2,4-dinitrotoluene (DNT).^[82] These two compounds are still the major components in landmines today.^[80c, 83] Initially, some conjugated polymers were found to have strong selectivity towards explosives with significant fluorescence quenching of the polymer solutions or thin films when in contact with the explosives (Figure 1.14, compound **1-7** to **1-10**), due to photo-induced electron transfer from the donor (the conjugated polymer) to the acceptor (the explosive).^[80b, 80c, 82, 84] As depicted in Figure 1.15, the former usually has a higher LUMO level than the latter and a spontaneously exothermic donor-to-acceptor electron transfer will occur if their LUMO difference is bigger than the binding energy of the exciton in the polymer after excitation.^{[80c], [85]}

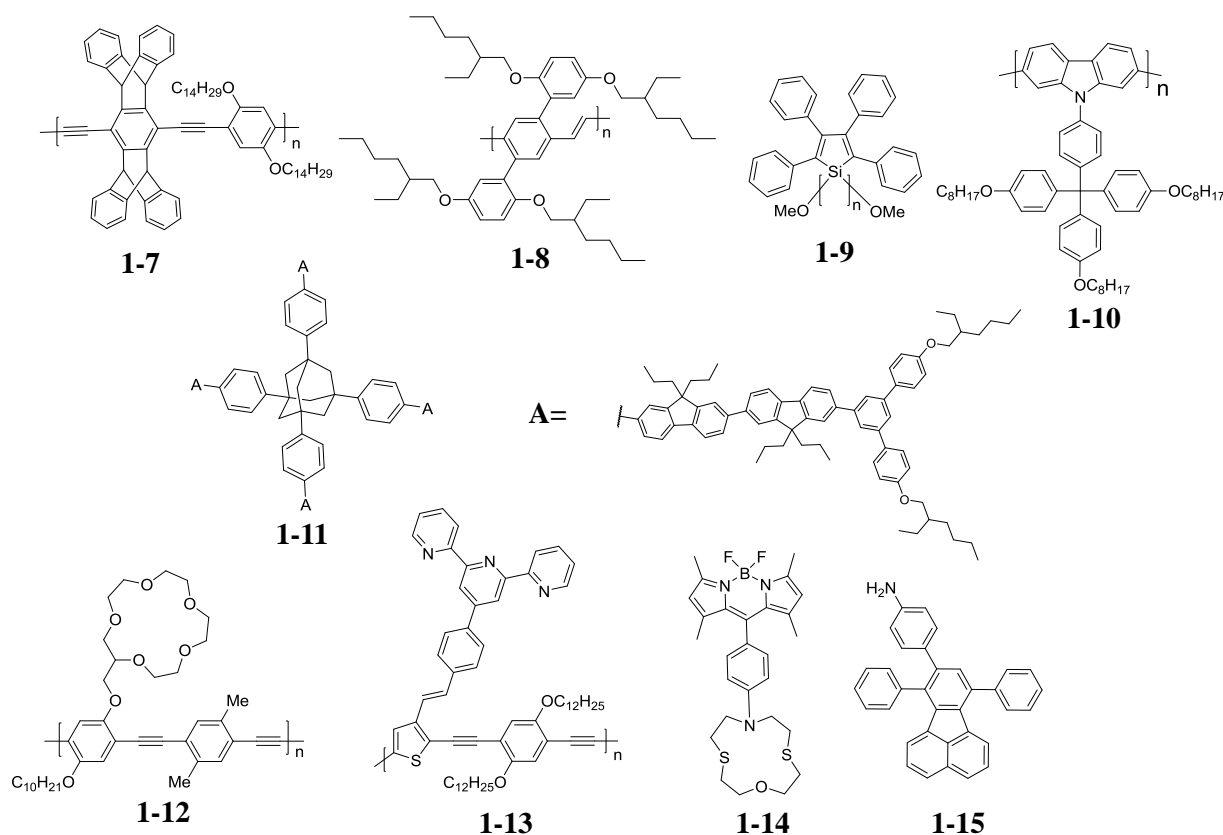


Figure 1.14: Examples of fluorescent chemical sensors for detecting explosives (top and middle) and metal ions (bottom).

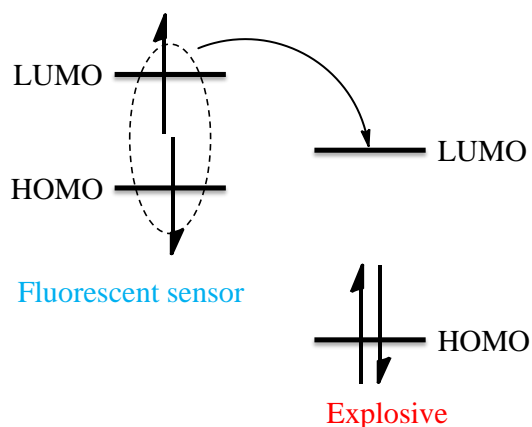


Figure 1.15: Photo-induced electron transfer process from the donor to the acceptor.

In addition, the detection of metal ions is important in that their occurrence in water, soil and in vivo is essential for the health of all living species on earth.^[86] For example, Hg^{2+} , Pb^{2+} and As^{3+} could cause disorders of the central nerve system of animals and Cu^{2+} , Cd^{2+} , Hg^{2+} , Pb^{2+} may affect the kidney or liver.^[87] Also, Fe^{3+} as an indispensable element in cytochromes, oxygen-binding molecules and many enzymes in organisms could easily induce tissue damage and many diseases in human body.^[88] Organic molecules could work as fluorescence sensors which are fast responding, possess a high sensitivity and selectivity and are available at low cost towards discrimination of metal ions.^[89] The mechanism for detection depends on the composition of the material and could rely on photo-induced electron transfer,^[90] the formation of non-emissive metal-organic complexes,^[91] or ion-induced aggregation.^[92] There have been lots of studies based on conjugated polymer and small molecule materials for ion detection (Figure 1.14, compound **1-12** to **1-15**).^[90, 92-93] Investigations in this field are still popular nowadays.^[94]

Even though polymers have gained success in detecting explosives and metal ions, there are still drawbacks: their low reproducibility due to their polydispersity and considerable synthetic efforts to prevent the polymers from close inter-chain interactions.^[85] Rigid dendrimers with monodisperse properties and three-dimensional structures could avoid those problems and dendrimer-based chemical sensors have received some attention recently (Figure 1.14, compound **1-11**).^[85, 95]

Shape-persistent **PPDs** have abundant voids within the molecule. As a result they could absorb organic vapors favorably.^[33b, 33d] In addition, **PPDs** with a good emitter in the core could have high PLQYs. These characteristics make them ideal candidates as fluorescence-quenching sensors. For this purpose, **PPDs** were not explored before, although some were applied to detect the explosive, triacetone triperoxide (**TATP**) (Figure 1.16, dendrimer **1-16** to **1-18**) but were based on quartz crystal microbalance mechanism.^[33a, 33c]

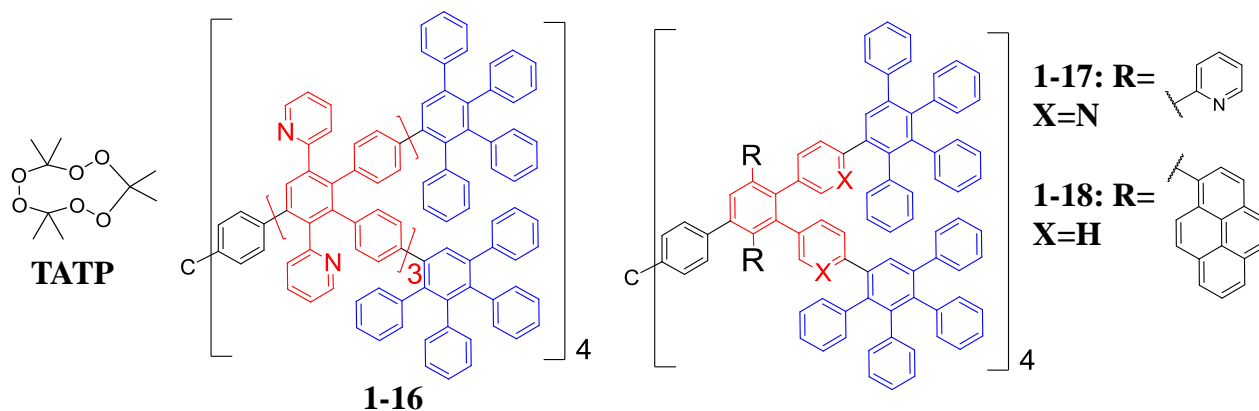


Figure 1.16: PPDs for TATP detections.^[33a, 33c]

Peripheral-TPA functionalized PPD, i.e. **PYGTPA** demonstrated effective hole transporting properties by reducing hole injection barrier in **OLEDs**. Therefore, PPDs with good hole transporting moieties in the periphery could work as hole transporting materials (**HTMs**) in Perovskite solar cells which will be introduced in the following part.

1.4.4 Perovskite solar cells

Nowadays, developing highly-efficient and cost-effective solar cells has become one of the most important tasks in the world because of swift developments in industry and technology, the expansion of the world's population, serious environmental problems caused by the excessive combustion of fossil fuels and the cleanliness and high abundance of solar energy. Silicon-based solar cells were developed long ago and exhibited high efficiencies, however, they suffered from costly purification process and manufacturing. With the invention of organic solar cells (**OSCs**), worldwide applications become possible due to the cheap organic materials and cost-effective fabrication of devices by solution processing, e.g. spin coating and inkjet printing. The first generation **OSC** with a donor-acceptor heterojunction structure could reach power conversion efficiency (PCE) of 11.5% by now with a three-junction device architecture.^[96] Dye-sensitized solar cells (**DSSCs**) represented the second generation **OSC** which employed a dye dispersed on the surface of colloidal semiconductors to generate and transport charges. The highest PCE of **DSSCs** is 13% so far.^[97] Recently, Perovskite solar cells (**PSCs**) have received intense investigations among the photovoltaic community because much higher efficiencies have been obtained.^[98] The first report of **PSC** was in 2009, with a PCE of 3.8%.^[99] Within 6 years, the PCE reached 20.1% in 2015.^[100] The significant improvement in efficiency within such a short time is astonishing, suggesting a bright future of **PSCs** for highly efficient and cost-effective applications. It also reflects some special properties of Perovskite compared with pure organic materials, e.g. poly(3-hexylthiophene) (**P3HT**).

Perovskite is a crystalline material with a general molecular composition of ABX_3 where A and B are cations and X is an anion. It could be purely inorganic, e.g. $CsPbX_3$ or organic-inorganic hybrid which is

currently of strong interest, e.g. $\text{CH}_3\text{NH}_3\text{PbX}_3$ (X=Cl, Br, or I). The crystal structure of a Perovskite was first reported by the Danish scientist Christian Møller in 1952.^[101] Cubic, tetragonal or orthorhombic lattice structures are adopted depending on composition. For example, Figure 1.17 shows a typical lattice with A, e.g. a methylammonium group locating in the central void formed by 8 surrounding octahedral units which consist of corner-halide atoms (symbol X) and a central metal atom (symbol B).^[102]

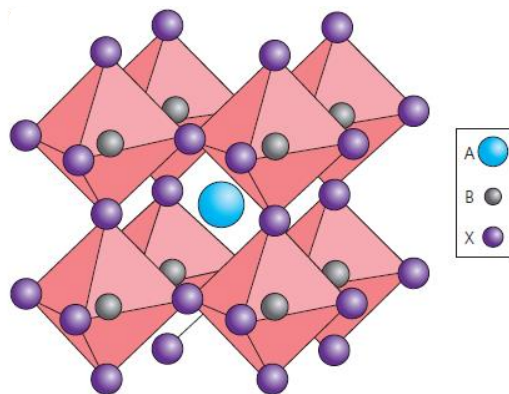


Figure 1.17: Crystal structure of perovskite with the general chemical formula ABX_3 .^[98c]

The organic-inorganic-hybrid Perovskites have several characteristics which should contribute to the obtained high PCEs. First, they harvest a large range of sun light, for example, $\text{CH}_3\text{NH}_3\text{PbI}_3$ absorbs between 350 nm and 800 nm with high absorbance, ensuring sufficient excitons generated in the device.^[103] Second, in contrast to pure organic materials, e.g. **P3HT**, Perovskites can split excitons by themselves due to the very low exciton binding energies (~ 0.030 eV), similar to silicon materials which could generate free charge carriers; this is attributed to the partially-organic and partially-inorganic structure of Perovskite.^[104] Third, high charge carrier mobilities (hole mobility ~ 7.5 $\text{cm}^2/\text{V}\cdot\text{s}$ and electron mobility ~ 12.5 $\text{cm}^2/\text{V}\cdot\text{s}$) were detected in this kind of material, thus enhancing charge transport efficiency in devices.^[104] In addition, it is solution processable, which significantly reduces the device fabrication costs.^[105]

The device structures of **PSCs** currently generally include two kinds: mesoscopic type and planar type. The mesoscopic structure, which has been first applied in **PSCs**, is similar to the architecture of **DSSCs** and is introduced here.^[105a, 106] As depicted in Figure 1.18, the light-absorbing Perovskite is spin-coated on a mesoporous and wide-bandgap semiconductor, i.e. TiO_2 which works as the scaffold and electron transport channel. Electrons are generated in Perovskites under light irradiation and are transported from TiO_2 into the transparent conducting oxide (**TCO**), i.e. the anode (e.g. fluorine-doped tin oxide) and the external circuit. At the same time, the oxidized Perovskite is reduced by its top layer, the hole transporting material (**HTM**), e.g. poly(triarylamine) (**PTAA**) which is then neutralized by the electrons coming through the external circuit and the cathode (back contact), e.g. gold and silver. This process is

also called hole transport. As a result, the photovoltaic device completes a whole charge circuit.^[107] In addition, a thin compacted TiO₂ layer between TCO and mesoporous TiO₂ is used to break direct contact between the Perovskite layer which also works as hole transporter in the device and TCO to prevent the holes and electrons from recombination. Recently, planar device architectures are becoming popular, which are simpler due to the absence of mesoporous TiO₂ layer.^[108] In this case, Perovskite functions as both hole and electron transporter because of its high charge carrier mobilities as mentioned above.

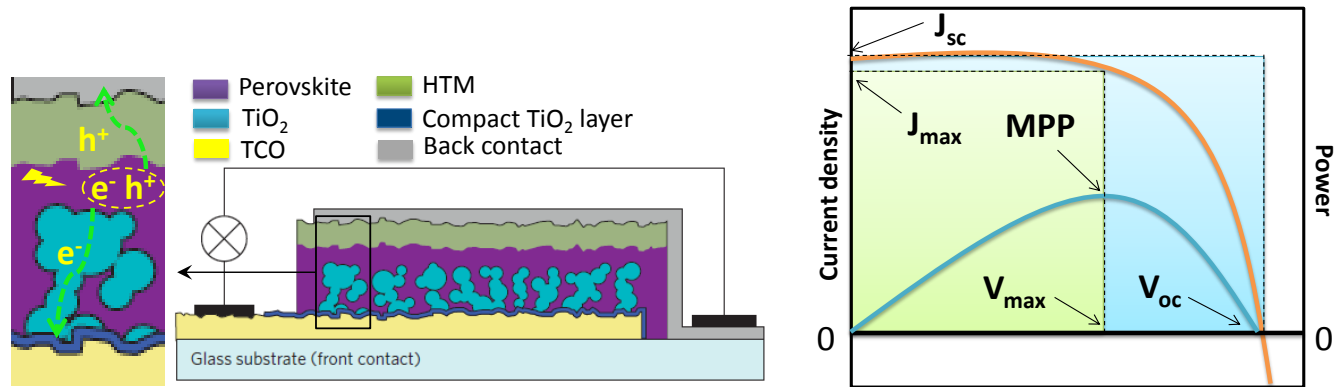


Figure 1.18: Mesoscopic device architecture of PSCs (left) and a typical J-V curve under illumination (orange line) and power curve (blue line) (right).^[98d]

To evaluate a photovoltaic device, it is usually characterized by a current density–voltage (J-V) curve (Figure 1.18, right), which is obtained by applying an external potential under illumination of the device.^[107] Several important parameters to characterize the device performance include PCE, the open-circuit potential (V_{oc}), the short-circuit photocurrent (J_{sc}) and the fill factor (FF). PCE refers to the fraction of incident power (P_{in}) converted into electrical power (P_{el}); V_{oc} is the potential at which the current is reduced to zero; J_{sc} is the current density when the external potential is zero. In addition, from the output power-voltage curve (Figure 1.20 right, blue curve), a maximum power point (MPP) is obtained. The current density and voltage which are directly related to MPP are referred to as J_{max} and V_{max} respectively. FF is defined as the ratio between the product of J_{max} and V_{max} and the product of J_{sc} and V_{oc} , which is also the ratio between the green area and the blue area. PCE and FF can be expressed by the following equations:

$$PCE = \frac{P_{el}}{P_{in}} = \frac{J_{max} \times V_{max}}{P_{in}} = \frac{J_{sc} \times V_{oc} \times FF}{P_{in}} \quad \text{Equation 1}$$

$$FF = \frac{J_{max} \times V_{max}}{J_{sc} \times V_{oc}} \quad \text{Equation 2}$$

PPDs with oligothiophenes in the peripheral could form nanographene-based and oligothiophene-bridged 3-dimensional networks by electrochemistry, which will be introduced in the following part.

1.4.5 Nanographene network

Graphene is a single layer subunit of graphite with a C-C sp^2 hybridized 2D geometry (Figure 1.19). Its preparation was first reported in 2004 by Geim and Novoselov, both of whom won the noble prize in physics in 2010 for their contributions to graphene. Graphene and graphene-related materials are very active research fields nowadays due to graphene's superb properties than other materials,^[109] e.g. exceptionally high electron mobility ($2.5 \times 10^5 \text{ cm}^2/\text{V}\cdot\text{s}$),^[110] very high thermal conductivity (above 3000 W/mK),^[111] extremely high strength ($\sim 130 \text{ GPa}$),^[112] and high transparency (optical absorption: $\sim 2.3\%$).^[113] Graphene was thought as a promising candidate for future integrated circuits by replacing the currently used silicon materials.^[114] However, it suffers from no turn-off in transistors due to its zero bandgap.^[115] As a result, its nano-stripe analogues, graphene nanoribbons (**GNR**) have attracted massive attention because they could be semiconductors with open bandgaps (Figure 1.19).^[116] **GNRs** are roughly divided into zigzag and armchair type based on their edge structures (Figure 1.19). Zigzag **GNRs** were predicted to be used in spintronics, partially due to the easy formation of radicals at its edges.^[117] Armchair or mixed armchair-zigzag **GNRs** behave as semiconductors with real bandgaps which are tunable by the width of the **GNR**.^[118] Currently, armchair **GNRs** have been synthesized in solutions and by a surface-assisted method in two steps: first, formation of polyphenylene precursors and second, intramolecular cyclodehydrogenation (Scheme 1.4).^[118a, 119] In addition, surface-assisted synthesis of the first zigzag **GNR** was reported by Müllen and Fasel et al. recently.^[120]

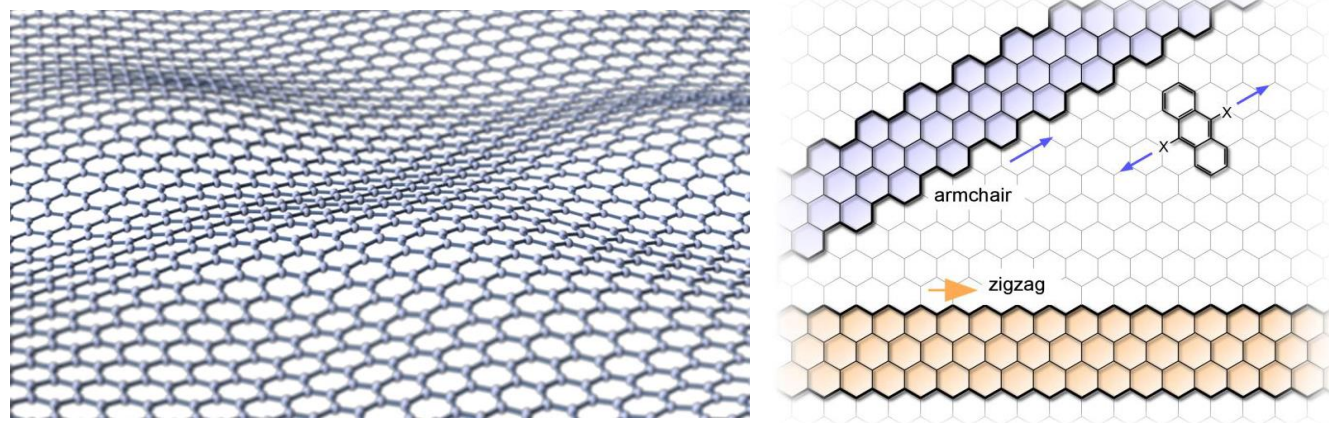
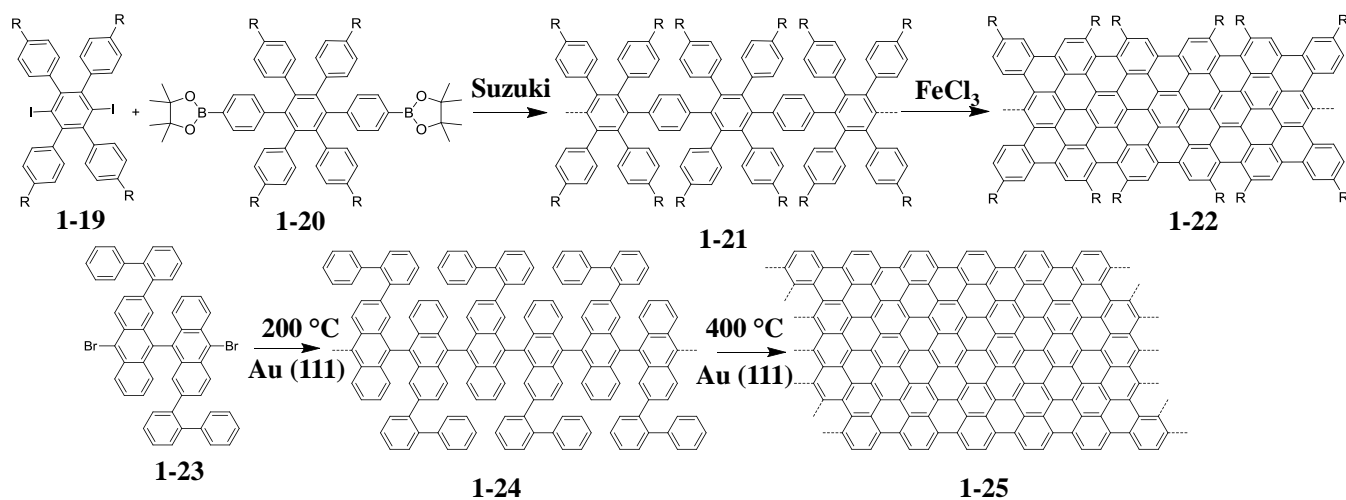


Figure 1.19: Schematic picture of graphene (left) and graphene nanoribbons (right).^[120]



Scheme 1.4: Synthetic routes for armchair **GNRs**.^[118a, 119]

Another member of graphene-related materials is nanographene which is nanosize, extended polycyclic aromatic hydrocarbons (**PAHs**) (Figure 1.20). Since the report on the synthesis of hexabenzocoronene (**HBC**) from hexaphenylbenzene (**HPB**) by Müllen et al. in 1995,^[121] nanographenes, e.g. **C60**,^[122] **C96**,^[123] **C132**^[17b] and **C222**^[17c] have been extensively synthesized from **PPDs** in solutions by cyclodehydrogenation with some oxidant, e.g. FeCl_3 (Figure 1.20).

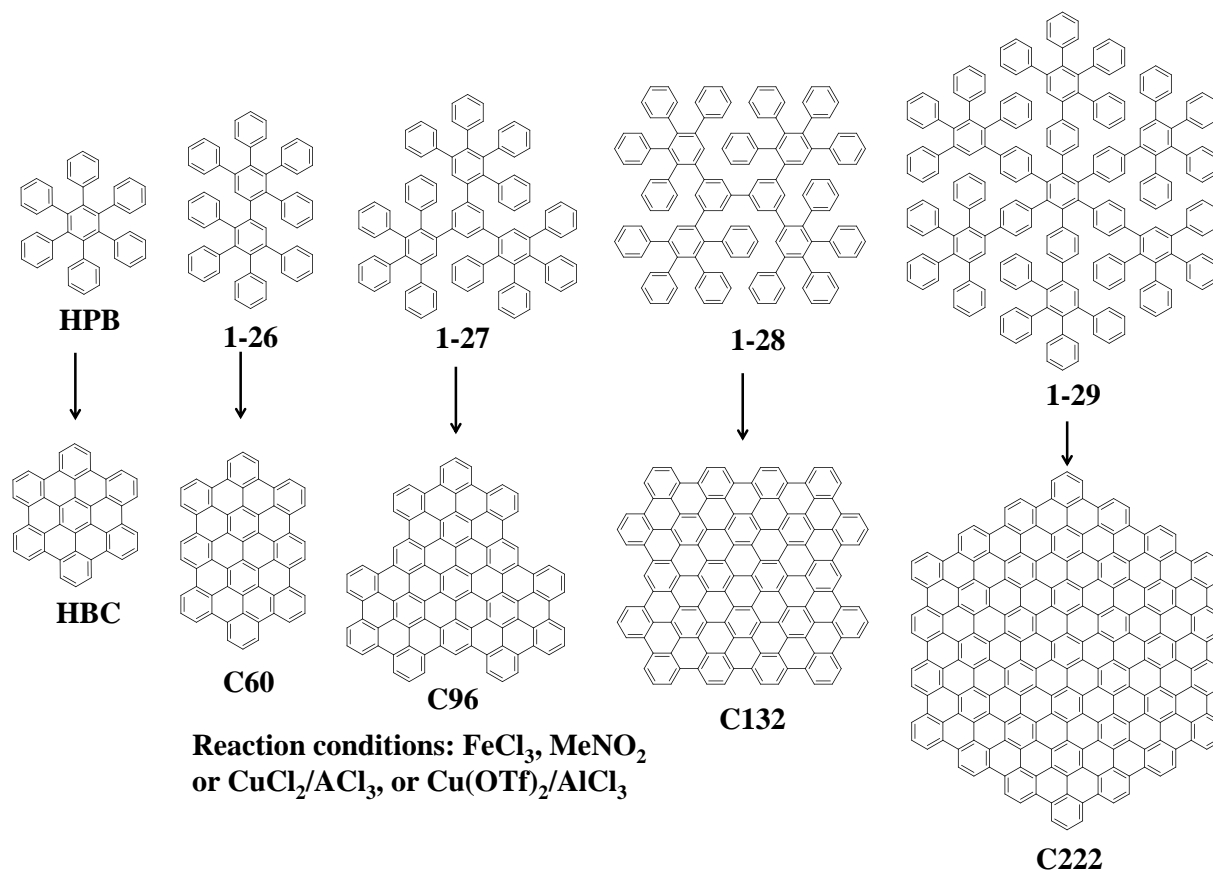
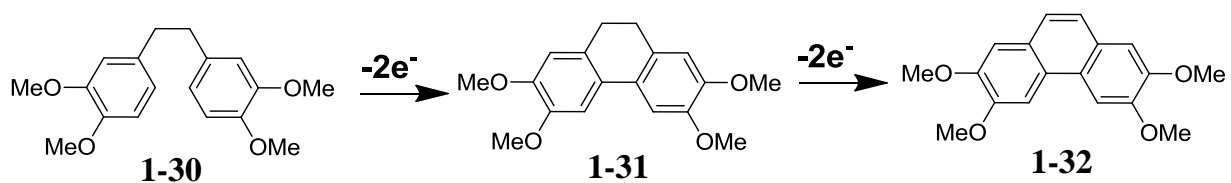


Figure 1.20: Synthesis of **HBC**, **C60**, **C96**, **C132** and **C222**.^[17b, 17c, 121-123]

Besides using oxidants, e.g. FeCl_3 to promote the cyclodehydrogenation of **PPDs**, electrochemistry is another option. The phenyl rings in **PPDs** are oxidized into their radical cations by anodic oxidation and intramolecular couplings could occur between radicals or through radical attacking the unoxidized moieties. In 1970, Ronlan and Parker reported the first case of phenyl-phenyl cyclodehydrogenation by electrochemistry.^[124] In their work, 3,3',4,4'-tetramethoxybibenzyl (**1-30**) was first transformed into 2,3,6,7-tetramethoxy-9,10-dihydrophenanthrene (**1-31**) which was finally oxidized into 2,3,6,7-tetramethoxyphenanthrene (**1-32**) after losing four electrons in total (Scheme 1.5). In addition, in 2015, Ma et al. reported the synthesis of HBC from HPB by electrochemistry and the product was well characterized by mass spectrometry, Raman and IR spectroscopy.^[125]



Scheme 1.5: Synthetic routes for compound **1-32** by electrochemistry.^[124]

In 2005, Müllen et al. reported the synthesis of a nanographene-based and sexithiophene-bridged, 3-dimensional network structure, called a nanographene network (**NGN**).^[126] As depicted in Figure 1.21, the synthesis started from a terthiophene-functionalized **PPD** (**1-33**) by CV and the formation of a **NGN** occurred via two steps: first, intermolecular couplings between terthiophene segments started under a low voltage, e.g. 1 V; second, by sweeping at a higher potential, e.g. 1.7 V, the oxidations of phenyl groups were initiated, followed by cyclodehydrogenation and eventually a **NGN** was procured. With the formation of the **NGN**, the conductivity was increased dramatically and a value of 0.13 S/cm was reported.

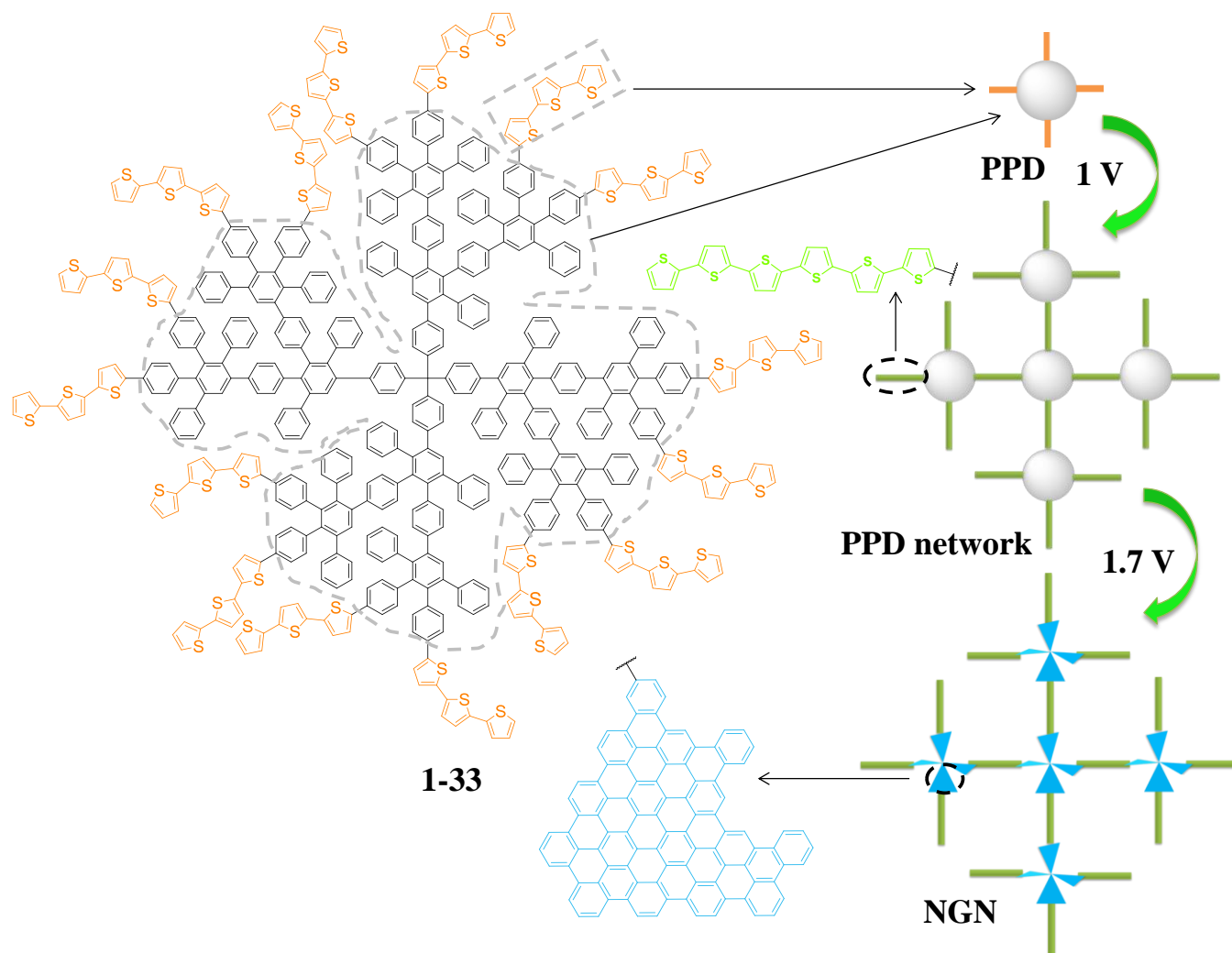


Figure 1.21: Formation of a NGN by electrochemistry.

1.5 Motivations

1.5.1 Motivations for new fluorescent dendrimers for OLEDs

As introduced previously, pyrene-based **PPDs** (**PYPPDs**) exhibited high PLQYs and peripheral-**TPA**-functionalized **PYPPD**, i.e. **PYGTPA** was proved to improve the **OLED** performance markedly by reducing the hole injection barrier.^[31b] Triphenylene moieties in **PYGTPA** were regarded as energy transfer agents between **TPAs** and the core. However, it is well known that direct surface-to-core energy transfer could occur. In addition, the introduction of triphenylene in the scaffold of the dendrimer increased the synthetic efforts significantly. Therefore, we designed new surface-core-functionalized **PPDs**. **Chapter 2** (part one) will describe my synthetic efforts on new dendrimers (Figure 1.22) and their **OLED** performances. First, **PYTPA** would be synthesized to compare with **PYGTPA** in device performances. It could be synthesized in much fewer steps and it could have efficient surface-to-core energy transfer due to the pronounced overlap between the emission of **TPA** and the absorption of the core. In addition, **PYTPAG2** would be prepared in comparison with **PYTPA** and evaluate the size effect of dendrimers on device performances. Moreover, **PYDTPA** with extended **TPAs** in the

periphery would be obtained to estimate the size effect of peripheral chromophores (**PCs**) on device performances.

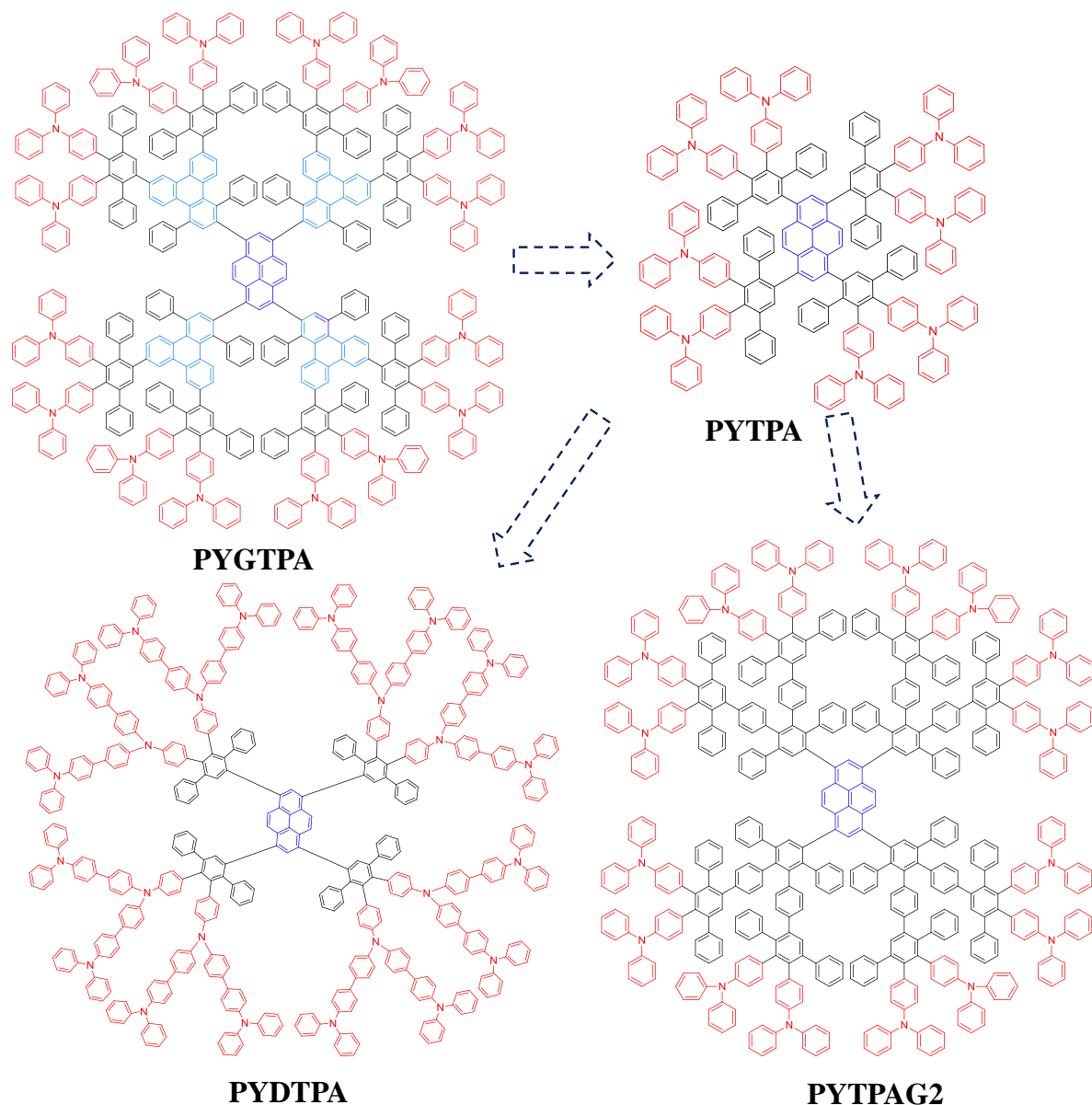


Figure 1.22: Molecular structures of new **PYPPDs**.

In addition to **TPA**, other chromophores e.g. 9-phenylcarbazole (**CAB**)^[127] and 1-naphthyl-N,N-diphenylamine (**NPA**)^[128] as hole transporting moieties and 2-(4-biphenyl)-5-(4-tert-butylphenyl)-1,3,4-oxadiazole (**PBD**)^[43b, 129] as electron transporting fragment could be employed as the **PCs** of **PYPPDs** to reduce the charge injection barriers in **OLEDs**, which has not been investigated before. It is interesting to see how they will influence the **OLED** performances. As depicted in Figure 1.23, **Chapter 2** (part two) will describe my synthetic efforts on new dendrimers and their device performances.

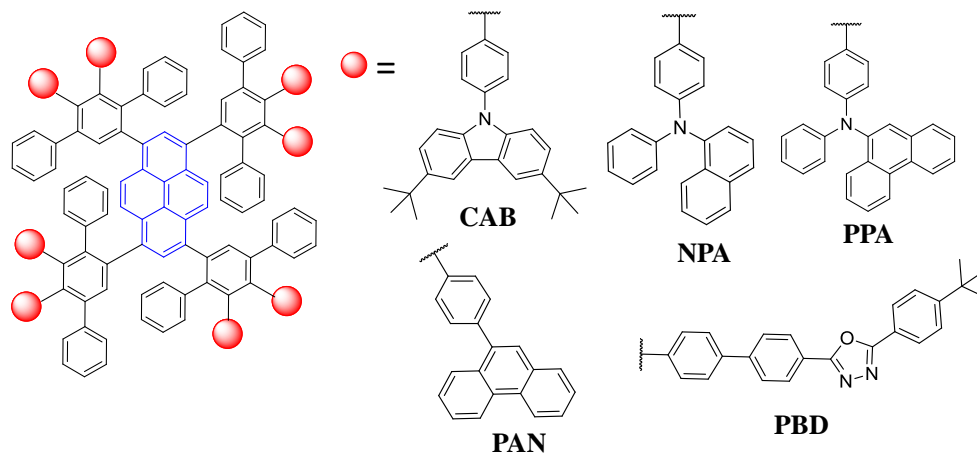


Figure 1.23: Molecular structures of **PYPPDs** with novel surface chromophores.

Moreover, to further improve the charge transport properties of the dendrimers and as a result, to reduce charge injection barriers in devices, it is advisable to utilize both hole and electron transport moieties in one molecule which has been done extensively in small molecules,^[130] polymers^[131] and dendrimers.^[132] Therefore, it is worthwhile to place both hole and electron transport moieties at the surface of a **PYPPD** to compare the devices with **PYPPDs** with a single kind of **PCs**, which has not been done before. As depicted in Figure 1.24, **Chapter 2** (part three) will describe my synthetic efforts on the bipolar dendrimers and their **OLED** performances.

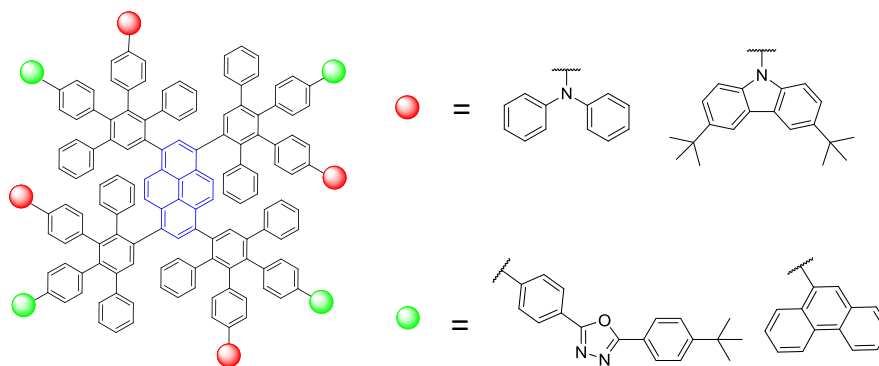


Figure 1.24: Structures of **PYPPDs** with bipolar surfaces.

1.5.2 Motivations for new phosphorescent materials for OLEDs

As mentioned in the phosphorescent emitter part, blue phosphorescent dendrimers are much less developed than small molecules. In addition, blue phosphorescent **PPDs** have not been reported yet. **Chapter 3** will describe my synthetic efforts for blue phosphorescent **PPDs**. As depicted in Figure 1.25, **(dfppy)₃Ir** as an efficient and pure blue phosphorescent emitter was selected as the core. The surface was functionalized with carbazoles and could reduce the charge injection barrier. In addition, **PCs** could transfer the triplet excitons to the core effectively due to the higher triplet energy of 9-phenylcarbazole

(3.04 eV)^[127b] than the core (2.83 eV)^[78], if the conjugation effects between the core and polyphenylene dendrons are not considered.

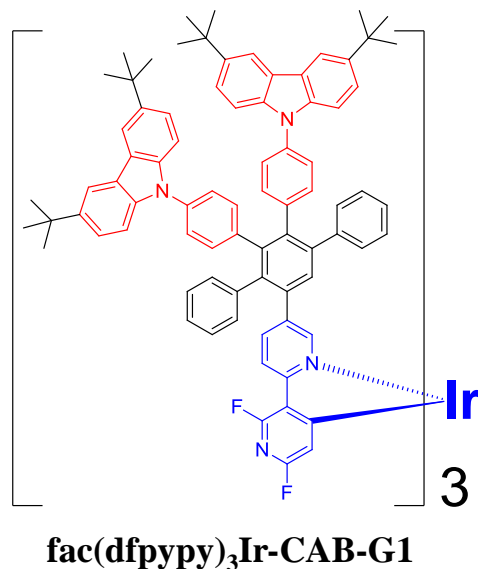


Figure 1.25: Molecular structure of a new **PPD** as a phosphorescent emitter.

1.5.3 Motivations for new dendrimer-based fluorescence sensors

As described in the chemical sensor part, dendrimers for detecting explosives and metal ions are less investigated than polymers and the former have some advantages, i.e. monodispersity and capability to accommodate guest molecules. In addition, **PPDs** have not yet been utilized to detect explosives or metal ions by a fluorescence quenching mechanism. In **Chapter 4**, two **TPA**-functionalized **PYPPDs**, i.e. **PYTPA** and **PYTPAG2** (Figure 1.22) have been selected as chemical sensors to detect explosives and metal ions for the first time. The reasons for choosing them are their high PLQYs from the core which could interact with the explosives, e.g. TNT to quench the emission and their peripheral **TPAs** which could chelate with metal ions, e.g. Fe³⁺ and interrupt surface-to-core energy transfer. Their detecting performances will be described and discussed in detail.

1.5.4 Motivations for dendrimer-based hole transporting materials in Perovskite solar cells

According to the introduction of **PSCs**, very high efficiencies have been achieved in **PSCs**. However, still lots of studies are needed to develop high performance and stable devices for practical applications. For example, **HTMs** for **PSCs** are being actively investigated. **PYPPDs** with hole transporting moieties in the periphery have demonstrated their abilities to reduce hole injection barrier in devices. Therefore, this kind of dendrimers can be applied as **HTMs** in **PSCs**, which has not been studied before. In **Chapter 5**, three **PYPPDs** (Figure 1.26) were employed as **HTMs** in **PSCs** for the first time and their performances in devices will be described and discussed.

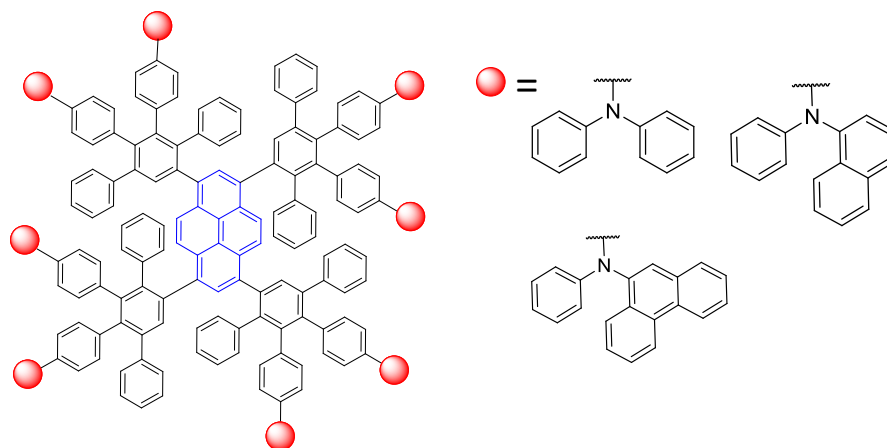


Figure 1.26: Molecular structures of **PYPPDs** as **HTMs** in **PSCs**.

1.5.5 Motivations for new dendrimer precursors for nanographene networks

As described in the nanographene network part, it is worthwhile investigating more **NGNs** because of their intriguing conductivity properties which might be an important addition to the conducting mechanisms of organic metals, not just confined to linear conducting polymers. In addition, with the severe interests in graphene-related materials nowadays, **NGN** as a member of the graphene family could show promise in versatile applications.^[109] Chapter 6 will describe my synthetic efforts on new dendrimers for new **NGN** preparations. As depicted in Figure 1.27, 1,3,5-benzene-based **PPDs** with oligothiophenes (i.e. α -bithiophene and α -sexithiophene) in the periphery were selected as the precursors of new **NGNs**. The reason for selecting them is that they could form **NGNs** with planar C96 nanographenes and oligothiophene bridges which should form better conjugation systems than the one mentioned before.

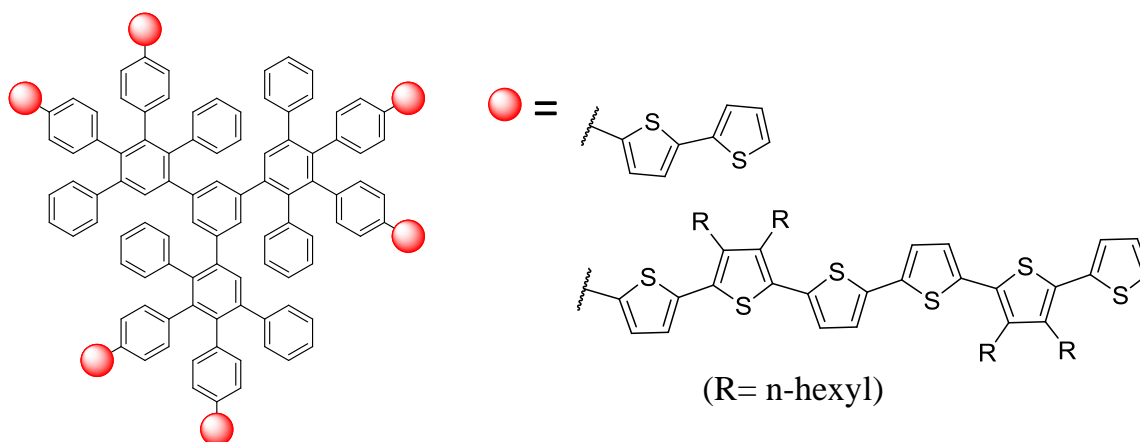


Figure 1.27: Molecular structures of new oligothiophene-functionalized **PPDs**.

Literature

- [1] E. Buhleier, W. Wehner, F. Vogtle, *Synthesis-Stuttgart* **1978**, 155-158.
- [2] E. M. M. Debrabandervandenberg, E. W. Meijer, *Angewandte Chemie-International Edition in English* **1993**, 32, 1308-1311.

- [3] D. A. Tomalia, H. Baker, J. Dewald, M. Hall, G. Kallos, S. Martin, J. Roeck, J. Ryder, P. Smith, *Polym J* **1985**, *17*, 117-132.
- [4] M. Sowinska, Z. Urbanczyk-Lipkowska, *New J Chem* **2014**, *38*, 2168-2203.
- [5] R. L. Lescanec, M. Muthukumar, *Macromolecules* **1990**, *23*, 2280-2288.
- [6] P. G. Degennes, H. Hervet, *J Phys Lett-Paris* **1983**, *44*, L351-L360.
- [7] A. W. Bosman, H. M. Janssen, E. W. Meijer, *Chem Rev* **1999**, *99*, 1665-1688.
- [8] C. J. Hawker, J. M. J. Frechet, *J Am Chem Soc* **1990**, *112*, 7638-7647.
- [9] a) F. Vogtle, S. Gestermann, C. Kauffmann, P. Ceroni, V. Vicinelli, V. Balzani, *J Am Chem Soc* **2000**, *122*, 10398-10404; b) J. Aumanen, V. Lehtovuori, N. Werner, G. Richardt, J. van Heyst, F. Vogtle, J. Korppi-Tommola, *Chem Phys Lett* **2006**, *433*, 75-79.
- [10] a) R. Esfand, D. A. Tomalia, *Drug Discov Today* **2001**, *6*, 427-436; b) R. B. Kolhatkar, K. M. Kitchens, P. W. Swaan, H. Ghandehari, *Bioconjugate Chem* **2007**, *18*, 2054-2060; c) K. M. Kitchens, A. B. Foraker, R. B. Kolhatkar, P. W. Swaan, H. Ghandehari, *Pharm Res* **2007**, *24*, 2138-2145; d) C. Liu, X. X. Liu, P. Rocchi, F. Q. Qu, J. L. Iovanna, L. Peng, *Bioconjugate Chem* **2014**, *25*, 521-532; e) X. X. Liu, C. Liu, J. H. Zhou, C. Chen, F. Q. Qu, J. J. Rossi, P. Rocchi, L. Peng, *Nanoscale* **2015**, *7*, 3867-3875.
- [11] Aldrich,
<http://www.sigmaaldrich.com/catalog/search?term=PAMAM&interface=All&N=0&mode=match%20partialmax&lang=de®ion=DE&focus=product>.
- [12] G. R. Newkome, Z. Q. Yao, G. R. Baker, V. K. Gupta, *J Org Chem* **1985**, *50*, 2003-2004.
- [13] a) C. J. Hawker, J. M. J. Frechet, *J Chem Soc Chem Comm* **1990**, 1010-1013; b) T. H. Mourey, S. R. Turner, M. Rubinstein, J. M. J. Frechet, C. J. Hawker, K. L. Wooley, *Macromolecules* **1992**, *25*, 2401-2406; c) M. Kawa, J. M. J. Frechet, *Chem Mater* **1998**, *10*, 286-296; d) D. L. Jiang, T. Aida, *Nature* **1997**, *388*, 454-456; e) P. B. Rheiner, D. Seebach, *Chem-Eur J* **1999**, *5*, 3221-3236; f) D. L. Jiang, T. Aida, *J Am Chem Soc* **1998**, *120*, 10895-10901.
- [14] T. M. Miller, T. X. Neenan, *Chem Mater* **1990**, *2*, 346-349.
- [15] K. Shahlai, H. Hart, *J Org Chem* **1991**, *56*, 6905-6912.
- [16] a) J. S. Moore, Z. F. Xu, *Macromolecules* **1991**, *24*, 5893-5894; b) Z. F. Xu, J. S. Moore, *Angewandte Chemie-International Edition in English* **1993**, *32*, 1354-1357.
- [17] a) F. Morgenroth, C. Kubel, K. Mullen, *J Mater Chem* **1997**, *7*, 1207-1211; b) F. Morgenroth, E. Reuther, K. Mullen, *Angewandte Chemie-International Edition in English* **1997**, *36*, 631-634; c) C. D. Simpson, J. D. Brand, A. J. Berresheim, L. Przybilla, H. J. Rader, K. Mullen, *Chem-Eur J* **2002**, *8*, 1424-1429.
- [18] W. Diltthey, W. Schommer, O. Trosken, *Ber Dtsch Chem Ges* **1933**, *66*, 1627-1628.
- [19] M. Hanack, F. Massa, *Tetrahedron Lett* **1977**, 661-664.
- [20] a) T. T. T. Nguyen, D. Turp, D. P. Wang, B. Nolscher, F. Laquai, K. Mullen, *J Am Chem Soc* **2011**, *133*, 11194-11204; b) D. Turp, M. Wagner, V. Enkelmann, K. Mullen, *Angew Chem Int Edit* **2011**, *50*, 4962-4965; c) R. Stangenberg, I. Saeed, S. L. Kuan, M. Baumgarten, T. Weil, M. Klapper, K. Mullen, *Macromol Rapid Comm* **2014**, *35*, 152-160.
- [21] U. M. Wiesler, K. Mullen, *Chem Commun* **1999**, 2293-2294.
- [22] D. Turp, T. T. T. Nguyen, M. Baumgarten, K. Mullen, *New J Chem* **2012**, *36*, 282-298.
- [23] a) G. Petekidis, D. Vlassopoulos, P. Galda, M. Rehahn, M. Ballauff, *Macromolecules* **1996**, *29*, 8948-8953; b) S. Vanhee, R. Rulkens, U. Lehmann, C. Rosenauer, M. Schulze, W. Kohler, G. Wegner, *Macromolecules* **1996**, *29*, 5136-5142; c) B. Fuckel, G. Hinze, G. Diezemann, F. Nolde, K. Mullen, J. Gauss, T. Basche, *J Chem Phys* **2006**, *125*.
- [24] S. Rosenfeldt, N. Dingenouts, D. Potschke, M. Ballauff, A. J. Berresheim, K. Mullen, P. Lindner, K. Saalwachter, *J Lumin* **2005**, *111*, 225-238.
- [25] H. Zhang, P. C. M. Grim, P. Foubert, T. Vosch, P. Vanoppen, U. M. Wiesler, A. J. Berresheim, K. Mullen, F. C. De Schryver, *Langmuir* **2000**, *16*, 9009-9014.
- [26] M. Wind, K. Saalwachter, U. M. Wiesler, K. Mullen, H. W. Spiess, *Macromolecules* **2002**, *35*, 10071-10086.
- [27] P. Brocorens, E. Zojer, J. Cornil, Z. Shuai, G. Leising, K. Mullen, J. L. Bredas, *Synthetic Met* **1999**, *100*, 141-162.
- [28] R. E. Bauer, V. Enkelmann, U. M. Wiesler, A. J. Berresheim, K. Mullen, *Chem-Eur J* **2002**, *8*, 3858-3864.
- [29] T. M. Miller, T. X. Neenan, R. Zayas, H. E. Bair, *J Am Chem Soc* **1992**, *114*, 1018-1025.
- [30] K. L. Wooley, J. M. J. Frechet, C. J. Hawker, *Polymer* **1994**, *35*, 4489-4495.

- [31] a) T. S. Qin, G. Zhou, H. Scheiber, R. E. Bauer, M. Baumgarten, C. E. Anson, E. J. W. List, K. Mullen, *Angew Chem Int Edit* **2008**, *47*, 8292-8296; b) T. S. Qin, W. Wiedemair, S. Nau, R. Trattnig, S. Sax, S. Winkler, A. Vollmer, N. Koch, M. Baumgarten, E. J. W. List, K. Mullen, *J Am Chem Soc* **2011**, *133*, 1301-1303; c) T. S. Qin, J. Q. Ding, M. Baumgarten, L. X. Wang, K. Mullen, *Macromol Rapid Comm* **2012**, *33*, 1036-1041.
- [32] a) J. S. Wu, Z. Tomovic, V. Enkelmann, Y. Mullen, *J Org Chem* **2004**, *69*, 5179-5186; b) Z. Tomovic, M. D. Watson, K. Mullen, *Angew Chem Int Edit* **2004**, *43*, 755-758.
- [33] a) D. Lubczyk, C. Siering, J. Lorgen, Z. B. Shifrina, M. Mullen, S. R. Waldvogel, *Sensor Actuat B-Chem* **2010**, *143*, 561-566; b) M. Schlupp, T. Weil, A. J. Berresheim, U. M. Wiesler, J. Bargon, K. Mullen, *Angew Chem Int Edit* **2001**, *40*, 4011-+; c) D. Lubczyk, M. Grill, M. Baumgarten, S. R. Waldvogel, K. Mullen, *Chempluschem* **2012**, *77*, 102-105; d) M. Brutschy, R. Stangenberg, C. Beer, D. Lubczyk, M. Baumgarten, K. Mullen, S. R. Waldvogel, *Chempluschem* **2015**, *80*, 54-56.
- [34] T. S. Qin, J. Q. Ding, L. X. Wang, M. Baumgarten, G. Zhou, K. Mullen, *J Am Chem Soc* **2009**, *131*, 14329-14336.
- [35] R. Stangenberg, Y. Z. Wu, J. Hedrich, D. Kurzbach, D. Wehner, G. Weidinger, S. L. Kuan, M. I. Jansen, F. Jelezko, H. J. Luhmann, D. Hinderberger, T. Weil, K. Mullen, *Adv Healthc Mater* **2015**, *4*.
- [36] a) R. Gronheid, J. Hofkens, F. Kohn, T. Weil, E. Reuther, K. Mullen, F. C. De Schryver, *J Am Chem Soc* **2002**, *124*, 2418-2419; b) T. Weil, T. Vosch, J. Hofkens, K. Peneva, K. Mullen, *Angew Chem Int Edit* **2010**, *49*, 9068-9093.
- [37] S. Nakamura, *Angew Chem Int Edit* **2015**, *54*, 7770-7788.
- [38] LED, http://www.nobelprize.org/nobel_prizes/physics/laureates/2014/popular-physicsprize2014.pdf
- [39] a) OLED-LG, <http://www.oled-info.com/lg-oled>; b) O. Samsung, <http://www.oled-info.com/samsung-oled>.
- [40] a) K. S. Yook, J. Y. Lee, *Adv Mater* **2012**, *24*, 3169-3190; b) G. M. Farinola, R. Ragni, *Chem Soc Rev* **2011**, *40*, 3467-3482.
- [41] J. H. Burroughes, D. D. C. Bradley, A. R. Brown, R. N. Marks, K. Mackay, R. H. Friend, P. L. Burn, A. B. Holmes, *Nature* **1990**, *347*, 539-541.
- [42] a) C. Adachi, M. A. Baldo, S. R. Forrest, S. Lamansky, M. E. Thompson, R. C. Kwong, *Appl Phys Lett* **2001**, *78*, 1622-1624; b) M. A. Baldo, S. Lamansky, P. E. Burrows, M. E. Thompson, S. R. Forrest, *Appl Phys Lett* **1999**, *75*, 4-6; c) D. F. O'Brien, M. A. Baldo, M. E. Thompson, S. R. Forrest, *Appl Phys Lett* **1999**, *74*, 442-444.
- [43] a) S. C. Lo, P. L. Burn, *Chem Rev* **2007**, *107*, 1097-1116; b) A. P. Kulkarni, C. J. Tonzola, A. Babel, S. A. Jenekhe, *Chem Mater* **2004**, *16*, 4556-4573.
- [44] Q. S. Zhang, B. Li, S. P. Huang, H. Nomura, H. Tanaka, C. Adachi, *Nat Photonics* **2014**, *8*, 326-332.
- [45] Q. S. Zhang, J. Li, K. Shizu, S. P. Huang, S. Hirata, H. Miyazaki, C. Adachi, *J Am Chem Soc* **2012**, *134*, 14706-14709.
- [46] R. Trattnig, L. Pevzner, M. Jager, R. Schlesinger, M. V. Nardi, G. Ligorio, C. Christodoulou, N. Koch, M. Baumgarten, K. Mullen, E. J. W. List, *Adv Funct Mater* **2013**, *23*, 4897-4905.
- [47] D. Neher, *Macromol Rapid Comm* **2001**, *22*, 1366-1385.
- [48] H. Liu, J. H. Zou, W. Yang, H. B. Wu, C. Li, B. Zhang, J. B. Peng, Y. Cao, *Chem Mater* **2008**, *20*, 4499-4506.
- [49] S. Nau, N. Schulte, S. Winkler, J. Frisch, A. Vollmer, N. Koch, S. Sax, E. J. W. List, *Adv Mater* **2013**, *25*, 4420-4424.
- [50] L. Wang, Y. Jiang, J. Luo, Y. Zhou, J. H. Zhou, J. Wang, J. Pei, Y. Cao, *Adv Mater* **2009**, *21*, 4854-+.
- [51] P. Moonsin, N. Prachumrak, S. Namuangruk, S. Jungstittiwong, T. Keawin, T. Sudyoasuk, V. Promarak, *J Mater Chem C* **2014**, *2*, 5540-5552.
- [52] C. Liu, Q. Fu, Y. Zou, C. L. Yang, D. G. Ma, J. G. Qin, *Chem Mater* **2014**, *26*, 3074-3083.
- [53] M. A. Baldo, D. F. O'Brien, M. E. Thompson, S. R. Forrest, *Phys Rev B* **1999**, *60*, 14422-14428.
- [54] L. X. Xiao, Z. J. Chen, B. Qu, J. X. Luo, S. Kong, Q. H. Gong, J. J. Kido, *Adv Mater* **2011**, *23*, 926-952.
- [55] H. Yersin, *Wiley-VCH* **2008**.
- [56] M. A. Baldo, D. F. O'Brien, Y. You, A. Shoustikov, S. Sibley, M. E. Thompson, S. R. Forrest, *Nature* **1998**, *395*, 151-154.
- [57] a) W. Y. Wong, C. L. Ho, *J Mater Chem* **2009**, *19*, 4457-4482; b) H. Sasabe, J. Kido, *Chem Mater* **2011**, *23*, 621-630.

- [58] a) C. Adachi, M. A. Baldo, S. R. Forrest, M. E. Thompson, *Appl Phys Lett* **2000**, *77*, 904-906; b) C. Adachi, M. A. Baldo, M. E. Thompson, S. R. Forrest, *J Appl Phys* **2001**, *90*, 5048-5051.
- [59] N. C. Greenham, R. H. Friend, D. D. C. Bradley, *Adv Mater* **1994**, *6*, 491-494.
- [60] R. Meerheim, R. Nitsche, K. Leo, *Appl Phys Lett* **2008**, *93*.
- [61] S. J. Su, T. Chiba, T. Takeda, J. Kido, *Adv Mater* **2008**, *20*, 2125-+.
- [62] S. J. Su, E. Gonmori, H. Sasabe, J. Kido, *Adv Mater* **2008**, *20*, 4189-+.
- [63] a) S. O. Jeon, S. E. Jang, H. S. Son, J. Y. Lee, *Adv Mater* **2011**, *23*, 1436-1441; b) X. C. Hang, T. Fleetham, E. Turner, J. Brooks, J. Li, *Angew Chem Int Edit* **2013**, *52*, 6753-6756.
- [64] Y. F. Zhang, J. Lee, S. R. Forrest, *Nat Commun* **2014**, *5*.
- [65] a) D. L. Dexter, J. H. Schulman, *J Chem Phys* **1954**, *22*, 1063-1070; b) H. Z. Xie, M. W. Liu, O. Y. Wang, X. H. Zhang, C. S. Lee, L. S. Hung, S. T. Lee, P. F. Teng, H. L. Kwong, H. Zheng, C. M. Che, *Adv Mater* **2001**, *13*, 1245-1248.
- [66] a) Y. Kawamura, J. Brooks, J. J. Brown, H. Sasabe, C. Adachi, *Phys Rev Lett* **2006**, *96*; b) J. Kalinowski, W. Stampor, J. Mezyk, M. Cocchi, D. Virgili, V. Fattori, P. Di Marco, *Phys Rev B* **2002**, *66*; c) S. Reineke, K. Walzer, K. Leo, *Phys Rev B* **2007**, *75*.
- [67] a) F. I. Wu, P. I. Shih, Y. H. Tseng, G. Y. Chen, C. H. Chien, C. F. Shu, Y. L. Tung, Y. Chi, A. K. Y. Jen, *J Phys Chem B* **2005**, *109*, 14000-14005; b) M. Ikai, S. Tokito, Y. Sakamoto, T. Suzuki, Y. Taga, *Appl Phys Lett* **2001**, *79*, 156-158; c) G. F. He, M. Pfeiffer, K. Leo, M. Hofmann, J. Birnstock, R. Pudzich, J. Salbeck, *Appl Phys Lett* **2004**, *85*, 3911-3913.
- [68] P. L. Burn, S. C. Lo, I. D. W. Samuel, *Adv Mater* **2007**, *19*, 1675-1688.
- [69] a) J. M. Lupton, I. D. W. Samuel, M. J. Frampton, R. Beavington, P. L. Burn, *Adv Funct Mater* **2001**, *11*, 287-294; b) J. P. J. Markham, S. C. Lo, S. W. Magennis, P. L. Burn, I. D. W. Samuel, *Appl Phys Lett* **2002**, *80*, 2645-2647.
- [70] a) S. C. Lo, T. D. Anthopoulos, E. B. Namdas, P. L. Burn, I. D. W. Samuel, *Adv Mater* **2005**, *17*, 1945-+; b) R. N. Bera, N. Cumpstey, P. L. Burn, I. D. W. Samuel, *Adv Funct Mater* **2007**, *17*, 1149-1152; c) T. D. Anthopoulos, M. J. Frampton, E. B. Namdas, P. L. Burn, I. D. W. Samuel, *Adv Mater* **2004**, *16*, 557-+; d) X. B. Xu, X. L. Yang, J. Zhao, G. J. Zhou, W. Y. Wong, *Asian J Org Chem* **2015**, *4*, 394-429; e) J. Q. Ding, J. Gao, Y. X. Cheng, Z. Y. Xie, L. X. Wang, D. G. Ma, X. B. Jing, F. S. Wang, *Adv Funct Mater* **2006**, *16*, 575-581; f) W. W. Tian, C. Yi, B. Song, Q. Qi, W. Jiang, Y. P. Zheng, Z. J. Qi, Y. M. Sun, *J Mater Chem C* **2014**, *2*, 1104-1115; g) G. J. Zhou, W. Y. Wong, B. Yao, Z. Y. Xie, L. X. Wang, *Angew Chem Int Edit* **2007**, *46*, 1149-1151.
- [71] T. Sajoto, P. I. Djurovich, A. B. Tamayo, J. Oxgaard, W. A. Goddard, M. E. Thompson, *J Am Chem Soc* **2009**, *131*, 9813-9822.
- [72] a) S. C. Lo, R. N. Bera, R. E. Harding, P. L. Burn, I. D. W. Samuel, *Adv Funct Mater* **2008**, *18*, 3080-3090; b) S. C. Lo, R. E. Harding, C. P. Shipley, S. G. Stevenson, P. L. Burn, I. D. W. Samuel, *J Am Chem Soc* **2009**, *131*, 16681-16688; c) S. C. Lo, G. J. Richards, J. P. J. Markham, E. B. Namdas, S. Sharma, P. L. Burn, I. D. W. Samuel, *Adv Funct Mater* **2005**, *15*, 1451-1458; d) D. B. Xia, B. Wang, B. Chen, S. M. Wang, B. H. Zhang, J. Q. Ding, L. X. Wang, X. B. Jing, F. S. Wang, *Angew Chem Int Edit* **2014**, *53*, 1048-1052; e) S. C. Lo, R. E. Harding, E. Brightman, P. L. Burn, I. D. W. Samuel, *J Mater Chem* **2009**, *19*, 3213-3227.
- [73] a) R. J. Holmes, S. R. Forrest, Y. J. Tung, R. C. Kwong, J. J. Brown, S. Garon, M. E. Thompson, *Appl Phys Lett* **2003**, *82*, 2422-2424; b) J. S. Swensen, E. Polikarpov, A. Von Ruden, L. Wang, L. S. Sapochak, A. B. Padmaperuma, *Adv Funct Mater* **2011**, *21*, 3250-3258.
- [74] a) J. Li, P. I. Djurovich, B. D. Alleyne, M. Yousufuddin, N. N. Ho, J. C. Thomas, J. C. Peters, R. Bau, M. E. Thompson, *Inorg Chem* **2005**, *44*, 1713-1727; b) A. Wada, T. Yasuda, Q. S. Zhang, Y. S. Yang, I. Takasu, S. Enomoto, C. Adachi, *J Mater Chem C* **2013**, *1*, 2404-2407.
- [75] A. B. Tamayo, B. D. Alleyne, P. I. Djurovich, S. Lamansky, I. Tsyba, N. N. Ho, R. Bau, M. E. Thompson, *J Am Chem Soc* **2003**, *125*, 7377-7387.
- [76] K. S. Yook, S. O. Jeon, C. W. Joo, J. Y. Lee, *Org Electron* **2009**, *10*, 170-173.
- [77] S. O. Jeon, K. S. Yook, C. W. Joo, J. Y. Lee, *Adv Funct Mater* **2009**, *19*, 3644-3649.
- [78] S. J. Lee, K. M. Park, K. Yang, Y. Kang, *Inorg Chem* **2009**, *48*, 1030-1037.
- [79] a) M. ZHOU, P. Wang, J. Zhang, L. liang, China, **2012**, p. 16; b) M. ZHOU, P. Wang, J. Zhang, L. liang, in *CN 103571454 A*, China, **2014**.

- [80] a) https://en.wikipedia.org/wiki/List_of_terrorist_incidents,_2015; b) C. P. Chang, C. Y. Chao, J. H. Huang, A. K. Li, C. S. Hsu, M. S. Lin, B. R. Hsieh, A. C. Su, *Synthetic Met* **2004**, *144*, 297-301; c) J. S. Yang, T. M. Swager, *J Am Chem Soc* **1998**, *120*, 11864-11873.
- [81] A. W. Czarnik, *Nature* **1998**, *394*, 417-418.
- [82] S. J. Toal, W. C. Troglor, *J Mater Chem* **2006**, *16*, 2871-2883.
- [83] Y. Liu, R. C. Mills, J. M. Boncella, K. S. Schanze, *Langmuir* **2001**, *17*, 7452-7455.
- [84] H. R. Nie, G. N. Sun, M. Zhang, M. Baumgarten, K. Mullen, *J Mater Chem* **2012**, *22*, 2129-2132.
- [85] H. Cavaye, A. R. G. Smith, M. James, A. Nelson, P. L. Burn, I. R. Gentle, S. C. Lo, P. Meredith, *Langmuir* **2009**, *25*, 12800-12805.
- [86] G. Aragay, J. Pons, A. Merkoci, *Chem Rev* **2011**, *111*, 3433-3458.
- [87] a) B. L. Vallee, D. D. Ulmer, *Annu Rev Biochem* **1972**, *41*, 91-&; b) J. W. Hamilton, R. C. Kaltreider, O. V. Bajenova, M. A. Ihnat, J. McCaffrey, B. W. Turpie, E. E. Rowell, J. Oh, M. J. Nemeth, C. A. Pesce, J. P. Lariviere, *Environ Health Persp* **1998**, *106*, 1005-1015; c) T. Partanen, P. Heikkila, S. Hernberg, T. Kauppinen, G. Moneta, A. Ojajarvi, *Scand J Work Env Hea* **1991**, *17*, 231-239.
- [88] N. C. Andrews, *New Engl J Med* **2000**, *342*, 364-364.
- [89] a) J. F. Zhang, Y. Zhou, J. Yoon, J. S. Kim, *Chem Soc Rev* **2011**, *40*, 3416-3429; b) H. N. Kim, Z. Q. Guo, W. H. Zhu, J. Yoon, H. Tian, *Chem Soc Rev* **2011**, *40*, 79-93.
- [90] Z. X. Li, L. F. Zhang, X. Y. Li, Y. K. Guo, Z. H. Ni, J. H. Chen, L. H. Wei, M. M. Yu, *Dyes Pigments* **2012**, *94*, 60-65.
- [91] Z. X. Li, L. F. Zhang, W. Y. Zhao, X. Y. Li, Y. K. Guo, M. M. Yu, J. X. Liu, *Inorg Chem Commun* **2011**, *14*, 1656-1658.
- [92] J. Kim, D. T. McQuade, S. K. McHugh, T. M. Swager, *Angew Chem Int Edit* **2000**, *39*, 3868-+.
- [93] a) L. J. Fan, Y. Zhang, C. B. Murphy, S. E. Angell, M. F. L. Parker, B. R. Flynn, W. E. Jones, *Coordin Chem Rev* **2009**, *253*, 410-422; b) A. P. de Silva, H. Q. N. Gunaratne, T. Gunnlaugsson, A. J. M. Huxley, C. P. McCoy, J. T. Rademacher, T. E. Rice, *Chem Rev* **1997**, *97*, 1515-1566; c) R. Martinez-Manez, F. Sancenon, *Chem Rev* **2003**, *103*, 4419-4476; d) P. J. Jiang, Z. J. Guo, *Coordin Chem Rev* **2004**, *248*, 205-229; e) J. L. Bricks, A. Kovalchuk, C. Trieflinger, M. Nofz, M. Buschel, A. I. Tolmachev, J. Daub, K. Rurack, *J Am Chem Soc* **2005**, *127*, 13522-13529.
- [94] a) Z. H. Xiang, C. Q. Fang, S. H. Leng, D. P. Cao, *J Mater Chem A* **2014**, *2*, 7662-7665; b) P. Li, Y. Zhao, L. Yao, H. R. Nie, M. Zhang, *Sensor Actuat B-Chem* **2014**, *191*, 332-336; c) A. Balamurugan, H. Lee, *Macromolecules* **2015**, *48*, 3934-3940; d) X. C. Xu, C. O. Trindle, G. Q. Zhang, L. Pu, *Chem Commun* **2015**, *51*, 8469-8472.
- [95] a) G. Vamvounis, P. E. Shaw, P. L. Burn, *J Mater Chem C* **2013**, *1*, 1322-1329; b) G. Q. Tang, S. S. Y. Chen, K. H. Lee, A. Pivrikas, M. Aljada, P. L. Burn, P. Meredith, P. E. Shaw, *Appl Phys Lett* **2013**, *102*.
- [96] C. C. Chen, W. H. Chang, K. Yoshimura, K. Ohya, J. B. You, J. Gao, Z. R. Hong, Y. Yang, *Adv Mater* **2014**, *26*, 5670-+.
- [97] S. Mathew, A. Yella, P. Gao, R. Humphry-Baker, B. F. E. Curchod, N. Ashari-Astani, I. Tavernelli, U. Rothlisberger, M. K. Nazeeruddin, M. Gratzel, *Nat Chem* **2014**, *6*, 242-247.
- [98] a) G. Hodes, *Science* **2013**, *342*, 317-318; b) R. F. Service, *Science* **2014**, *344*, 458-458; c) M. A. Green, A. Ho-Baillie, H. J. Snaith, *Nat Photonics* **2014**, *8*, 506-514; d) M. Gratzel, *Nat Mater* **2014**, *13*, 838-842.
- [99] A. Kojima, K. Teshima, Y. Shirai, T. Miyasaka, *J Am Chem Soc* **2009**, *131*, 6050-+.
- [100] W. S. Yang, J. H. Noh, N. J. Jeon, Y. C. Kim, S. Ryu, J. Seo, S. I. Seok, *Science* **2015**, *348*, 1234-1237.
- [101] C. K. Moller, *Nature* **1958**, *182*, 1436-1436.
- [102] a) C. H. Li, X. G. Lu, W. Z. Ding, L. M. Feng, Y. H. Gao, Z. G. Guo, *Acta Crystallogr B* **2008**, *64*, 702-707; b) T. Baikie, Y. N. Fang, J. M. Kadro, M. Schreyer, F. X. Wei, S. G. Mhaisalkar, M. Graetzel, T. J. White, *J Mater Chem A* **2013**, *1*, 5628-5641.
- [103] J. Cao, Y. M. Liu, X. J. Jing, J. Yin, J. Li, B. Xu, Y. Z. Tan, N. F. Zheng, *J Am Chem Soc* **2015**, *137*, 10914-10917.
- [104] C. S. Ponseca, T. J. Savenije, M. Abdellah, K. B. Zheng, A. Yartsev, T. Pascher, T. Harlang, P. Chabera, T. Pullerits, A. Stepanov, J. P. Wolf, V. Sundstrom, *J Am Chem Soc* **2014**, *136*, 5189-5192.
- [105] a) H. S. Kim, C. R. Lee, J. H. Im, K. B. Lee, T. Moehl, A. Marchioro, S. J. Moon, R. Humphry-Baker, J. H. Yum, J. E. Moser, M. Gratzel, N. G. Park, *Sci Rep-Uk* **2012**, *2*; b) J. Burschka, N. Pellet, S. J. Moon, R. Humphry-Baker, P. Gao, M. K. Nazeeruddin, M. Gratzel, *Nature* **2013**, *499*, 316-+.
- [106] M. M. Lee, J. Teuscher, T. Miyasaka, T. N. Murakami, H. J. Snaith, *Science* **2012**, *338*, 643-647.

- [107] a) S.-J. Moon, *PhD thesis-EPFL* **2011**; b) N. Pootrakulchote, *PhD thesis-EPFL* **2012**; c) J. BURSCHKA, *PhD thesis-EPFL* **2013**.
- [108] a) M. Z. Liu, M. B. Johnston, H. J. Snaith, *Nature* **2013**, *501*, 395-+; b) O. Malinkiewicz, A. Yella, Y. H. Lee, G. M. Espallargas, M. Graetzel, M. K. Nazeeruddin, H. J. Bolink, *Nat Photonics* **2014**, *8*, 128-132.
- [109] K. S. Novoselov, V. I. Fal'ko, L. Colombo, P. R. Gellert, M. G. Schwab, K. Kim, *Nature* **2012**, *490*, 192-200.
- [110] a) K. S. Novoselov, A. K. Geim, S. V. Morozov, D. Jiang, Y. Zhang, S. V. Dubonos, I. V. Grigorieva, A. A. Firsov, *Science* **2004**, *306*, 666-669; b) A. S. Mayorov, D. C. Elias, M. Mucha-Kruczynski, R. V. Gorbachev, T. Tudorovskiy, A. Zhukov, S. V. Morozov, M. I. Katsnelson, V. I. Fal'ko, A. K. Geim, K. S. Novoselov, *Science* **2011**, *333*, 860-863.
- [111] A. A. Balandin, *Nat Mater* **2011**, *10*, 569-581.
- [112] C. Lee, X. D. Wei, J. W. Kysar, J. Hone, *Science* **2008**, *321*, 385-388.
- [113] R. R. Nair, P. Blake, A. N. Grigorenko, K. S. Novoselov, T. J. Booth, T. Stauber, N. M. R. Peres, A. K. Geim, *Science* **2008**, *320*, 1308-1308.
- [114] L. Liao, Y. C. Lin, M. Q. Bao, R. Cheng, J. W. Bai, Y. A. Liu, Y. Q. Qu, K. L. Wang, Y. Huang, X. F. Duan, *Nature* **2010**, *467*, 305-308.
- [115] F. Schwierz, *Nat Nanotechnol* **2010**, *5*, 487-496.
- [116] a) K. Nakada, M. Fujita, G. Dresselhaus, M. S. Dresselhaus, *Phys Rev B* **1996**, *54*, 17954-17961; b) A. Narita, X. Y. Wang, X. L. Feng, K. Mullen, *Chem Soc Rev* **2015**, *44*, 6616-6643.
- [117] a) Y. W. Son, M. L. Cohen, S. G. Louie, *Nature* **2006**, *444*, 347-349; b) J. Z. Liu, P. Ravat, M. Wagner, M. Baumgarten, X. L. Feng, K. Muller, *Angew Chem Int Edit* **2015**, *54*, 12442-12446.
- [118] a) X. Y. Yang, X. Dou, A. Rouhanipour, L. J. Zhi, H. J. Rader, K. Mullen, *J Am Chem Soc* **2008**, *130*, 4216-+; b) A. Narita, X. L. Feng, Y. Hernandez, S. A. Jensen, M. Bonn, H. F. Yang, I. A. Verzhbitskiy, C. Casiraghi, M. R. Hansen, A. H. R. Koch, G. Fytas, O. Ivasenko, B. Li, K. S. Mali, T. Balandina, S. Mahesh, S. De Feyter, K. Mullen, *Nat Chem* **2014**, *6*, 126-132.
- [119] Y. C. Chen, D. G. de Oteyza, Z. Pedramrazi, C. Chen, F. R. Fischer, M. F. Crommie, *Acs Nano* **2013**, *7*, 6123-6128.
- [120] P. Ruffieux, S. Wang, B. Yang, C. Sanchez, J. Iju, L. T. Dienel, P. Shinde, C. A. Pignedoli, D. Passerone, T. Dumslaff, X. Feng, K. Muellen, R. Fasel, *Nature* **2016**, *accepted*.
- [121] A. Stabel, P. Herwig, K. Mullen, J. P. Rabe, *Angewandte Chemie-International Edition in English* **1995**, *34*, 1609-1611.
- [122] V. S. Iyer, K. Yoshimura, V. Enkelmann, R. Epsch, J. P. Rabe, K. Mullen, *Angew Chem Int Edit* **1998**, *37*, 2696-2699.
- [123] V. S. Iyer, M. Wehmeier, J. D. Brand, M. A. Keegstra, K. Mullen, *Angewandte Chemie-International Edition in English* **1997**, *36*, 1604-1607.
- [124] A. Ronlan, V. D. Parker, *Journal of the Chemical Society D-Chemical Communications* **1970**, 1567-&.
- [125] L. Q. Qin, Y. A. Zhang, X. Y. Wu, L. Nian, Z. Q. Xie, L. L. Liu, Y. G. Ma, *Small* **2015**, *11*, 3028-3034.
- [126] H. John, R. Bauer, P. Espindola, P. Sonar, J. Heinze, K. Mullen, *Angew Chem Int Edit* **2005**, *44*, 2447-2451.
- [127] a) H. Ogawa, R. Okuda, Y. Shirota, *Appl Phys a-Mater* **1998**, *67*, 599-602; b) J. Q. Ding, B. H. Zhang, J. H. Lu, Z. Y. Xie, L. X. Wang, X. B. Jing, F. S. Wang, *Adv Mater* **2009**, *21*, 4983-+.
- [128] a) K. L. Tong, S. K. So, H. F. Ng, L. M. Leung, M. Y. Yeung, C. F. Lo, *Synthetic Met* **2004**, *147*, 199-203; b) Z. Q. Gao, C. S. Lee, I. Bello, S. T. Lee, R. M. Chen, T. Y. Luh, J. Shi, C. W. Tang, *Appl Phys Lett* **1999**, *74*, 865-867.
- [129] S. Janietz, A. Wedel, *Adv Mater* **1997**, *9*, 403-&.
- [130] a) C. H. Chen, W. S. Huang, M. Y. Lai, W. C. Tsao, J. T. Lin, Y. H. Wu, T. H. Ke, L. Y. Chen, C. C. Wu, *Adv Funct Mater* **2009**, *19*, 2661-2670; b) A. P. Kulkarni, X. X. Kong, S. A. Jenekhe, *Adv Funct Mater* **2006**, *16*, 1057-1066.
- [131] P. I. Shih, Y. H. Tseng, F. I. Wu, A. K. Dixit, C. F. Shu, *Adv Funct Mater* **2006**, *16*, 1582-1589.
- [132] C. H. Chen, J. T. Lin, M. C. P. Yeh, *Org Lett* **2006**, *8*, 2233-2236.

Chapter 2 Pyrene-Based Polyphenylene Dendrimers for Blue OLEDs

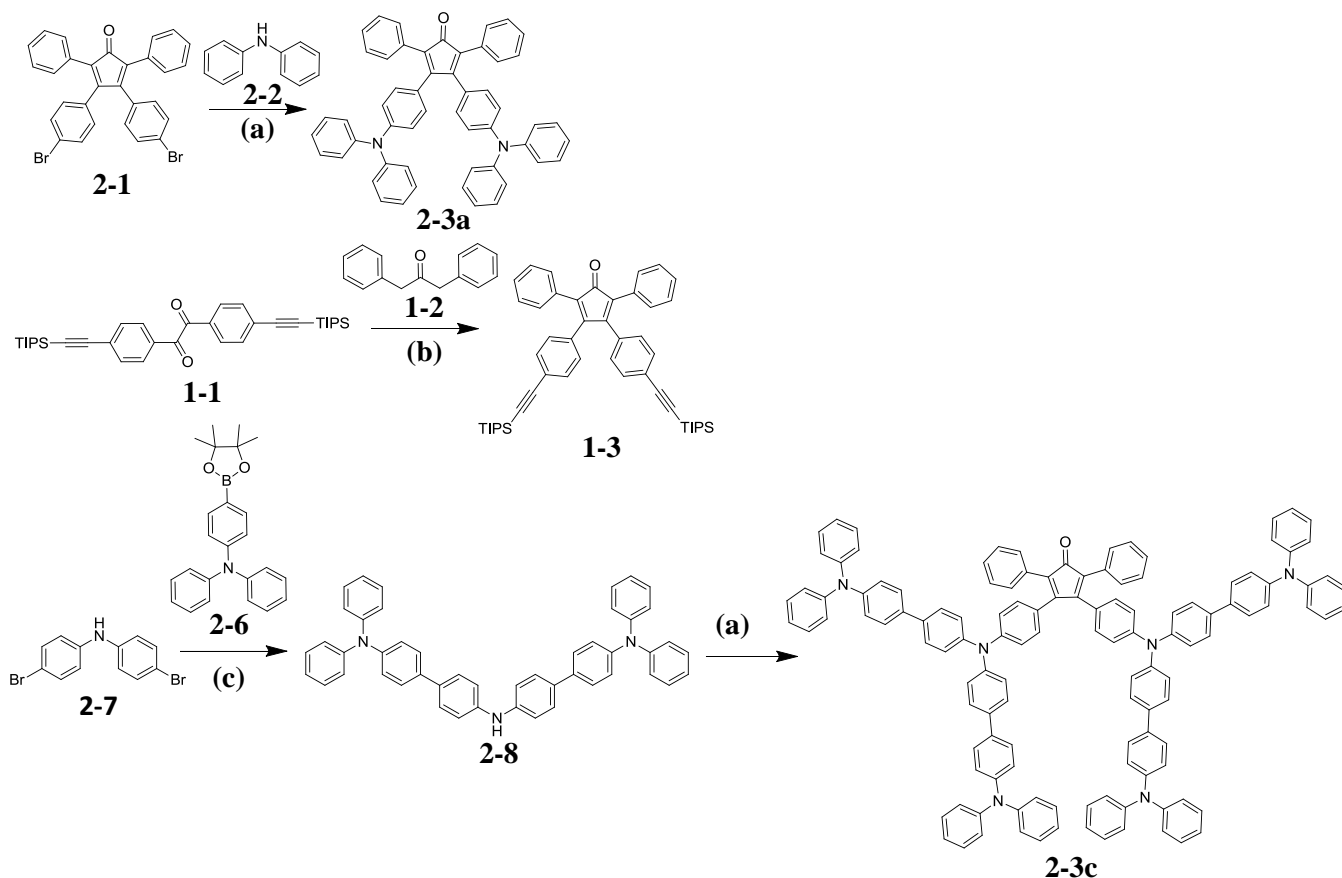
In this chapter, the synthesis, structural characterizations, photophysical and electrochemistry properties and **OLED** performances of several kind of pyrene-based polyphenylene dendrimers (**PYPPDs**) with different peripheral chromophores (**PCs**) are described and discussed. The first part is about the peripheral-triphenylamine (**TPA**) **PYPPDs**; the second part concerns the synthesis of **PYPPDs** with other **PCs**, e.g. 9-phenylcarbazole and the third part involves bipolar **PYPPDs** with both donor and acceptor moieties in the periphery. The selection of **PCs** is based on their good hole or electron transporting performances, fluorescence quantum yields and their good emission overlaps with the absorption of the core. The functions of the **PCs** include reducing the hole/electron injection barrier from the electrodes, recombining both holes and electrons to form excitons and transporting the excitons quickly by Förster resonant energy transfer (FRET) to the core which emits light eventually.

2.1 Peripheral-TPA **PYPPDs**

2.1.1 Synthesis of Peripheral-TPA **PYPPDs**

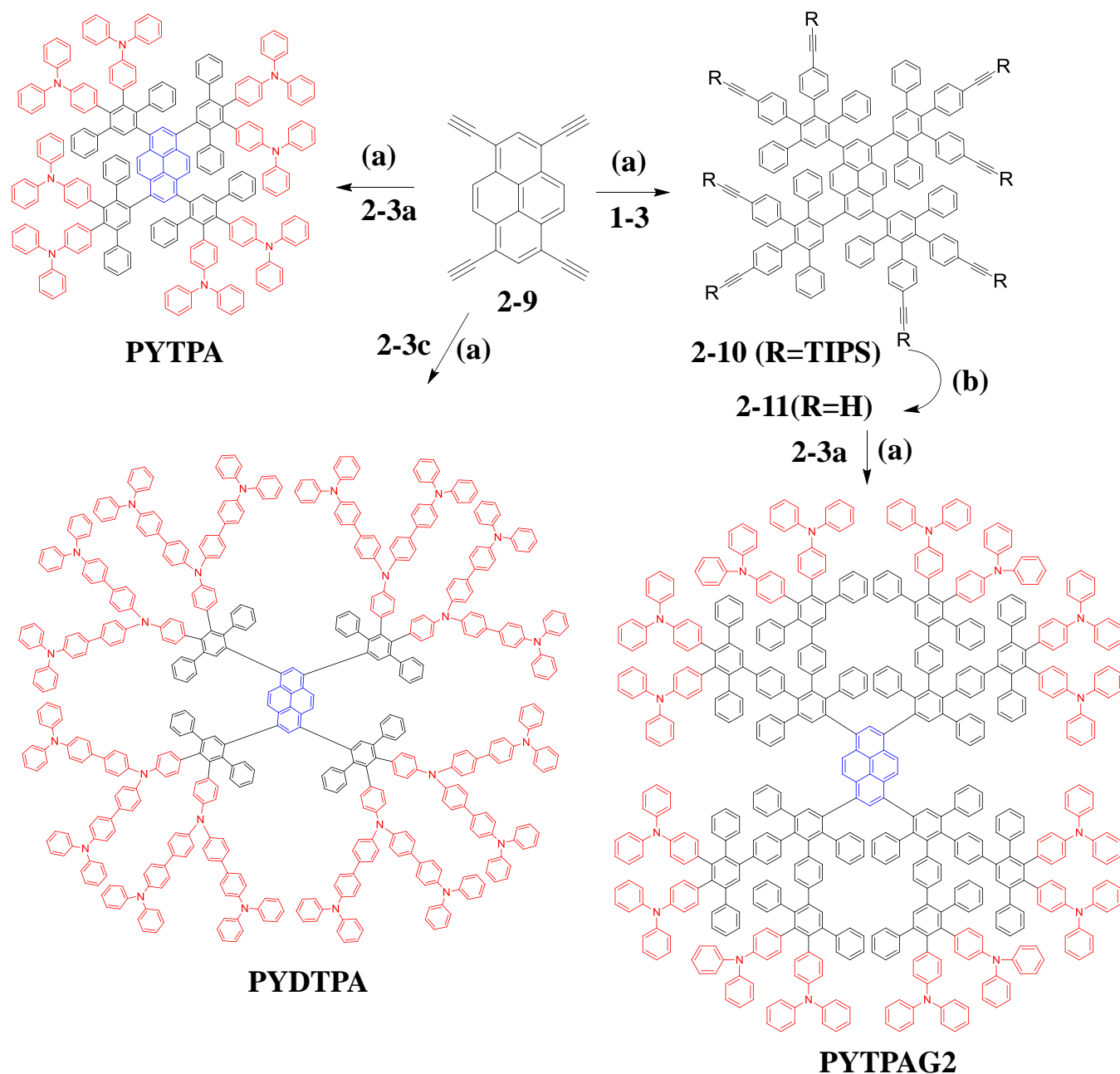
TPA functionalized **PYPPDs**, i.e. the first-generation one (**PYTPA**), the second-generation one (**PYTPAG2**) and the first-generation one with extended **TPAs** (**PYDTPA**) were synthesized (Scheme 2.2). They were used to compare with the performance of the published **PYGTPA** in **OLEDs**.^[1]

To synthesize the dendrimers, the functional **CPs** were prepared first. As displayed in Scheme 2.1, The **TPA**-functionalized **CP** (**2-3a**) was easily produced by a Buchwald-Hartwig coupling between dibromo-**CP** (**2-1**) and diphenylamine (**2-2**) in high yield (70%). To **PYTPAG2**, the triisopropylsilylethynyl(TIPSE)-functionalized **CP** (**1-3**) was first prepared between 4,4'-di(TIPSE)benzil (**1-1**) and 1,3-diphenylacetone (**1-2**) by a Knoevenagel condensation in moderate yield (50%). In addition, the extended-**TPA**-functionalized **CP** (**2-3c**) was afforded readily in two steps: first, a Suzuki coupling between compound **2-6** and **2-7** gave birth to 4,4'-di(4-triphenylamino)diphenylamine (**2-8**) which then underwent a Buchwald-Hartwig reaction with compound **2-1** to procure compound **2-3c** in 20% yield.



Scheme 2.1: Synthetic routes for new CPs. (a) $\text{Pd}_2(\text{dba})_3$, $t\text{-BuONa}$, $(t\text{-Bu})_3\text{P}$, toluene, 12 h, 70 °C, 70% for compound **2-3a** and 60 °C, 20.5% for compound **2-3c**; (b) KOH , ethanol, 80 °C, 10 min, 50%; (c) $\text{Pd}(\text{PPh}_3)_4$, Na_2CO_3 , toluene, water, 110 °C, 24 h, 60%.

With the CPs available, the dendrimers were synthesized easily (Scheme 2.2). At the beginning, 1,3,6,8-tetraethynylpyrene (**2-9**) was produced according to the published procedures.^[2] Then, a [4+2] Diels-Alder reaction between CP (**2-3a**) and compound **2-9** in *o*-xylene at 140 °C and argon protection proceeded for 24 hours to provide **PYTPA** in 70% yield after purifications by silica gel flash column and gel permeation chromatography (GPC) methods. To make **PYTPAG2**, the TIPSE-functionalized **PYPPD** (**2-10**) was first afforded with a similar reaction condition as **PYTPA** in 82% yield. Then the ethynyl groups were activated using tetrabutylammonium fluoride (TBAF) and 90% yield of product (**2-11**) was received after purifications. Then, compound **2-11** reacted with CP (**2-3a**) to produce **PYTPAG2**. This step needed longer time to finish than **PYTPA** because the reactive sites in compound **2-11** were twice as many as compound **2-9**. It was found that 48 hours' stirring at 160 °C was able to complete the reaction. Finally, after purifications by silica gel flash column and GPC methods, a light-yellow-colored product was received in 50% yield. **PYDTPA** was synthesized between compound **2-9** and compound **2-3c** in 43% yield with a similar reaction condition as **PYTPA**. All three dendrimers had good solubilities in organic solvents like DCM, THF and toluene (≥ 8 g/l), making them easy to be characterized.



Scheme 2.2: Synthetic routes for **PYTPA**, **PYTPAG2** and **PYDTPA**. (a) o-xylene, 140 °C, 24 h, 70% for **PYTPA**, 82% for compound **2-10**, 43% for **PYDTPA**, 160 °C, 48 h, 50% for **PYTPAG2**; (b) TBAF, THF, rt, 90% for compound **2-11**.

2.1.2 Characterization of dendrimers

All the dendrimers were characterized by ^1H NMR and ^{13}C NMR spectroscopy, MALDI-TOF mass spectrometry, high resolution mass spectrometry (HRMS), UV-Vis absorption and photoluminescence spectroscopy and cyclic voltammetry (CV). As depicted in Figure 2.1, each MALDI-TOF mass spectra clearly showed a single peak of the molecular ion, consistent with predicted molecular mass of the target molecule. In addition, the HRMS spectra of **PYTPA** exhibited an isotope pattern which matched well with the calculated one. Thus, the desired dendrimers were synthesized and they displayed monodisperse properties.

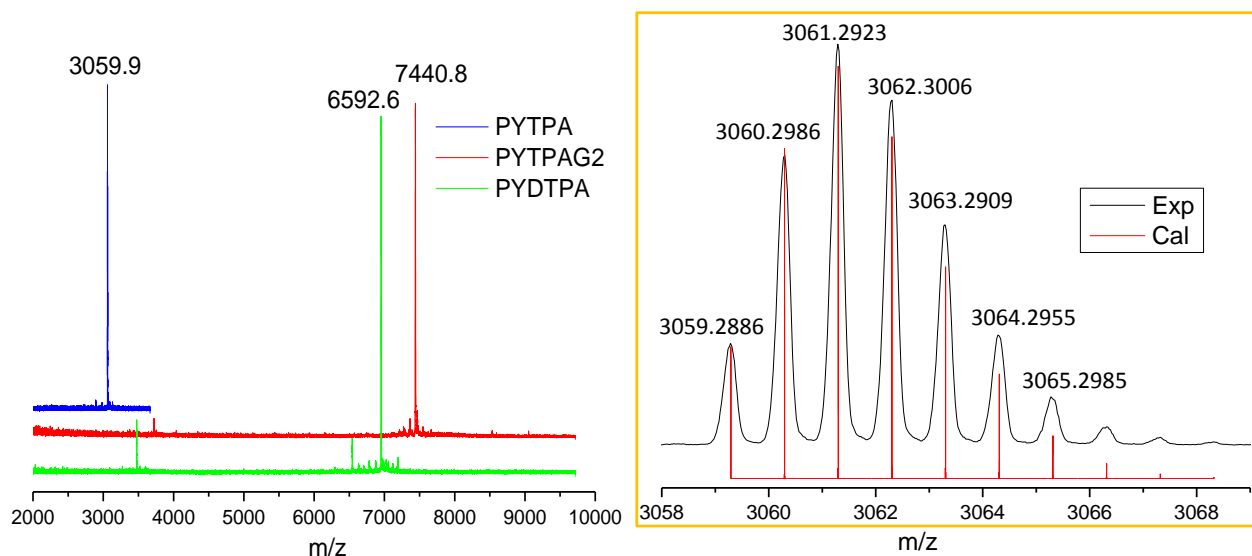


Figure 2.1: MALDI-TOF mass spectra of new **PYPPDs** (left) and HRMS spectra of **PYTPA** (right).

As depicted in Figure 2.2, ^1H NMR spectra could distinguish some specific protons, like the six protons on pyrene and the four protons on the four phenyl groups directly bonded to the core. For **PYTPA**, the multiplet peaks at around 7.91 ppm corresponded to the six protons of pyrene (Ha and Hb) and the multiplet peak centered around 7.54 ppm represented the four isolated protons (Hc) of the four phenyl rings directly bonded to pyrene. In addition, the strong band between 7.31-7.12 ppm for **PYTPA** was attributed to protons of polyphenylenes. Moreover, the majority of the protons on **TPAs** had signals between 6.97 and 6.60 ppm. The relative intensities of these bands correlated well with the number of respective protons.

For **PYTPAG2**, similarly, the six protons of pyrene resonated at around 7.73 ppm. The second lowest field multiplet peak was identified as 12 protons by integrations and represented the proton signals (Hc and Hd) from the phenyl groups of the branching points of the dendrimer. The rest of the aromatic signals included two strong bands from the protons of polyphenylenes and **TPAs**. In addition, the integrations of these signals were in good agreement with the number of specific protons as well. Consequently, ^1H NMR spectroscopy can analyze and provide supports on the structures of this kind of dendrimers.

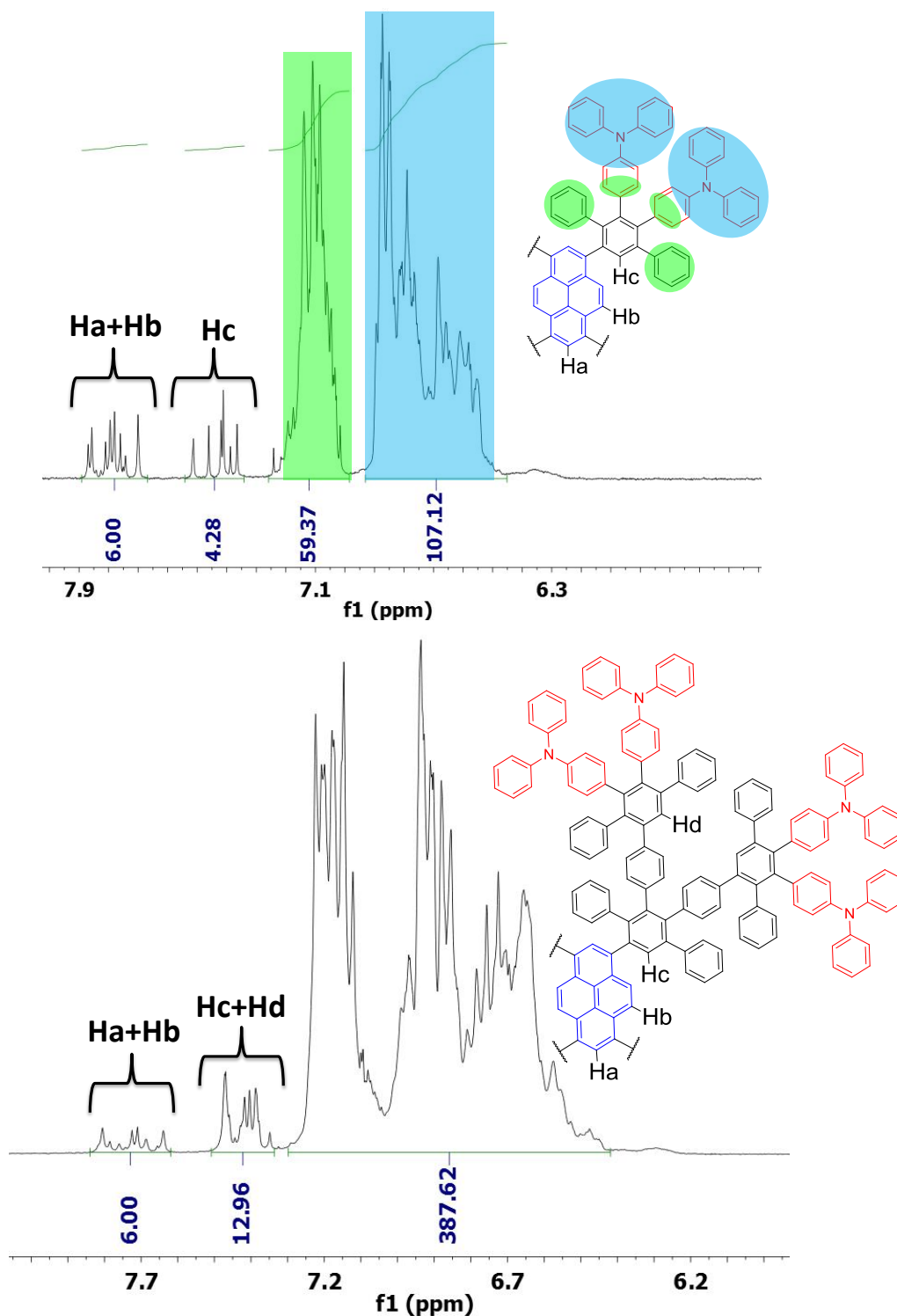


Figure 2.2: ^1H NMR spectra of **PYTPA** (top) and **PYTPAG2** (bottom) in the aromatic regions.

The strong splitting of the peaks for proton Ha, Hb and Hc in **PYTPA** (Figure 2.2) are due to the five possible configurations of the dendrimer. To support this conclusion, a model compound, i.e. 1,3,6,8-tetra[(1,4-diphenyl)phenyl]pyrene (**PYTTP**) was used to conduct structural optimizations for its 5 possible isomers (Figure 2.3). First, the 4 protons which were on the four pyrene-bonded phenyl groups and ortho to pyrene were named as α protons. The 5 possible configurations were based on the spatial arrangements of the α protons, i.e. all four α protons in one side (all-up), three α protons in one side and

one in the other side of pyrene (3-up-1-down), and two α protons in each side of pyrene plane which included 3 possibilities, namely, two α protons of the 1,3-position dendrons at one side and the other two in the other side (2-head-up-2-head-down), two α protons of 1,8-position dendrons at one side and the other two in the other side (2-side-up-2-side-down) and two α protons of 1,6-position dendrons at one side and the other two in the other side (2-cross-up-2-cross-down) (Figure 2.3). To find out which configuration was more favorable, structural optimizations based on DFT (6-31G) calculations of the 3-up-1-down isomer and 2-side-up-2-side-down one were carried out and their energies were calculated to be -3387.667235 Hartree and -3387.667573 Hartree respectively. The energy difference between these two isomers was so small ($\sim 3.4 \times 10^{-4}$ Hartree) that these two isomers probably coexisted in the dendrimer material. Because of the time limit, no more DFT calculations were conducted. But, it could be tentatively concluded that several different isomers coexisted in **PYTTP**, which explained the multiplet signals for proton Ha, Hb and Hc in this dendrimer. It was further confirmed by high temperature ^1H NMR (400 K, $\text{C}_2\text{D}_2\text{Cl}_2$) spectra, in which the multiplet peaks for those protons still existed, ruling out the possible peak splitting induced by free rotations of the dendrons in the molecule in solutions.

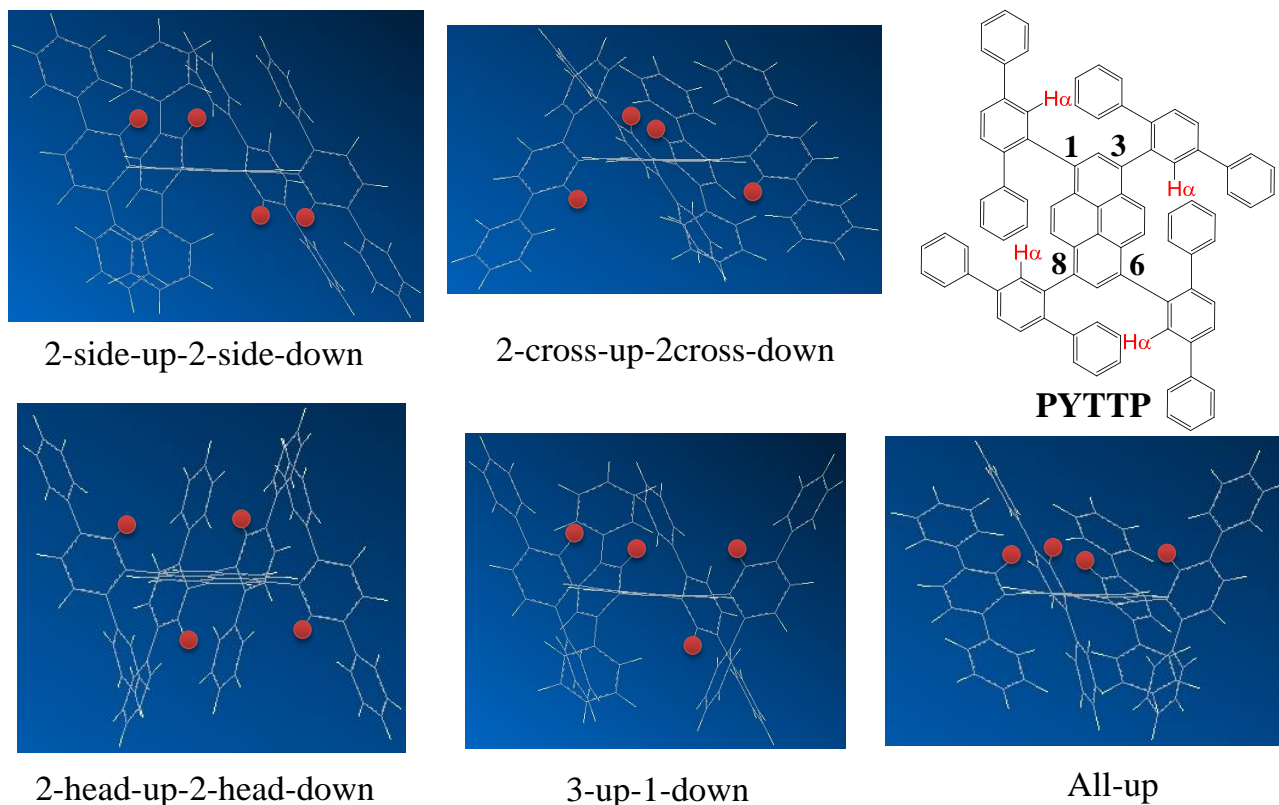


Figure 2.3: Molecular structure of **PYTTP** and its five possible spatial isomers looking parallel with the pyrene plane (red balls denote the α -protons).

2.1.3 Photophysical properties

The absorption properties of these dendrimers were first explored in solutions. As depicted in Figure 2.4, the absorption of **PYTPA** and **PYTPAG2** were very similar except for their extinction coefficients. They both had two absorption bands. One was strong and broad with the peak absorption at around 310 nm and the other one was weak and broad ranging between 370 and 421 nm. The former was due to the absorption of **TPAs**, together with the contributions from polyphenylenes.^[2-3] The second one resulted from the π - π^* transitions of the core.^[2] Comparing the extinction coefficients, **PYTPAG2** had almost twice as much absorbance as **PYTPA** in the first band ($2.6 \times 10^5 \text{ l mol}^{-1} \text{ cm}^{-1}$ vs $1.4 \times 10^5 \text{ l mol}^{-1} \text{ cm}^{-1}$) since the number of **TPA** groups per mole was doubled in **PYTPAG2** compared with **PYTPA**. However, for the second band, both spectra exhibited very similar extinction coefficient ($4.2 \times 10^4 \text{ l mol}^{-1} \text{ cm}^{-1}$ vs $5.0 \times 10^4 \text{ l mol}^{-1} \text{ cm}^{-1}$) because the number of cores per mole of dendrimers was the same. For **PYDTPA**, the absorption also included two bands, a small one at around 310 nm and a strong one at around 369 nm. The first peak was due to the **TPA**-centered absorption and the second one was due to the π - π^* transitions of the extended **TPA** moieties.^[4] Going to thin films, all three dendrimers exhibited similar absorption as in solutions with a little bathochromic shift in **TPA** absorptions, probably due to the close intermolecular interactions among the surface groups in thin films (Table 2.1).

As depicted in Figure 2.4, the emission spectra of the three dendrimers in solutions appeared the same after normalizations with a peak emission at around 431 nm and a little shoulder at around 450 nm when excited at 310 nm. The same results were obtained when excited at the core (392 nm), indicating that the emission were merely from the core and surface-to-core energy transfers occurred.

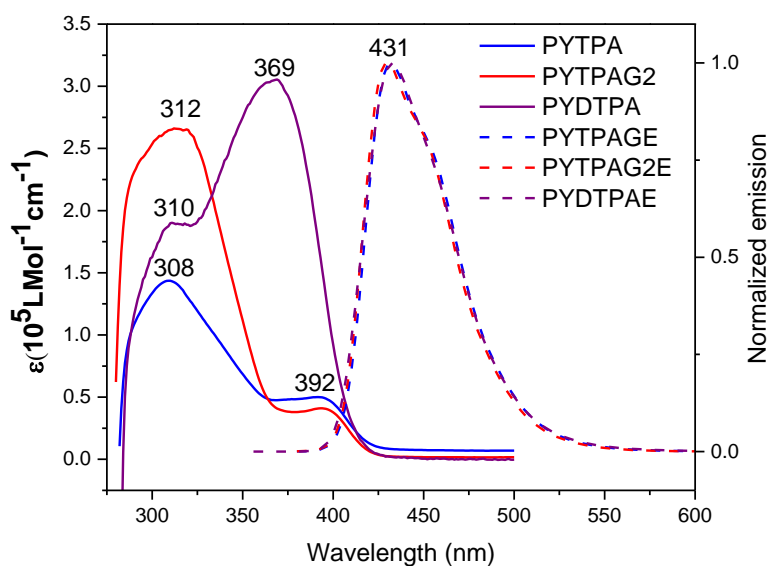


Figure 2.4: UV-vis absorption (solid lines) and photoluminescence spectra (dashed lines, excited at 310 nm) spectra of **PYTPA**, **PYTPAG2** and **PYDTPA** ($1 \times 10^{-5} \text{ M}$, toluene).

Table 2.1: Photophysical and electrochemical properties of **PYPPDs**

	$\lambda_{ab}(\text{nm})$		$\lambda_{em}(\text{nm})$		PLQY ^{a)}		HOMO	LUMO	E_g
	Sol	Film	Sol	Film	Excitation		(eV) ^{b)}	(eV) ^{b)}	(eV) ^{c)}
					Surface	Core			
PYTPA	308, 392	311, 391	431	450	0.65	0.71	-5.36	-2.40	2.94
PYTPAG2	312, 392	315, 393	431	438	0.32	0.63	-5.31	-2.34	2.94
PYDTPA	310, 369	314, 370	433	452	0.65	0.73	-5.07	--	3.01

^{a)} Measured in THF solution with quinine sulfate in 0.5 M H₂SO₄ solution as the standard; ^{b)} calculated from CV by comparing the first redox onset of **PYPPDs** and the oxidation onset of ferrocene; ^{c)} calculated from the absorption edge of the longest wavelength band.

Going to thin films, as displayed in Table 2.1, the emission of **PYTPA** and **PYDTPA** suffered notable bathochromic shifts (~ 20 nm) compared with solutions, probably due to incomplete protection of the core by the dendrons. For **PYTPAG2**, the bathochromic shift was minor (~7 nm), probably due to better protections of the core by the much bigger dendrons of **PYTPAG2** than those of first-generation dendrimers. In addition, the photoluminescence quantum yield (PLQY) was measured in solutions with quinine sulfate in 0.5 M H₂SO₄ solution as the standard (Table 2.1). When excited at the surface chromophores, they exhibited strong PLQYs especially for first-generation dendrimers, **PYTPA** (0.65) and **PYDTPA** (0.65). These values were very close to the results after excitation at the core (~ 0.70) for **PYTPA** and **PYDTPA**. Based on the same emission wavelengths and very close PLQYs either excited at the surface or the core, it was extrapolated that there were efficient surface-to-core energy transfers for the first-generation dendrimers. This is partially due to the very close distance between the surface chromophores and the core. For **PYTPAG2**, due to the much longer surface-core distance, the PLQY excited at the surface dropped significantly (~0.32) but it remained strong (0.63) when excited at the core.

2.1.4 Electrochemistry

The redox properties of the dendrimers were characterized by CV using one-compartment, 3-electrode setup. As depicted in Figure 2.5, for **PYTPA**, both the oxidation and reduction waves were identified. There was a broad and strong oxidation couple ($E_{1/2}$: ~ 0.92 V), due to the oxidation of **TPAs**. A small oxidation wave centered at around 1.3 V was reversible and stemmed from the oxidation of the core.^[5] In the reduction part, there appeared only a small reversible wave with the half wave potential at around -2.0 V. This was traced back to the reduction of the core.^[5-6] The HOMO of **TPA** and LUMO of the core could be calculated by comparing with the oxidation of the reference ferrocene. The HOMO was calculated to be -5.36 eV, which was almost identical to that of bare **TPA**,^[3] indicating little conjugated interactions between the surface chromophores and the core by the highly twisted biphenyls in between. The LUMO of **PYTPA** was provided by the core and calculated at -2.40 eV. The electrochemistry of

PYTPAG2 was similar as that of **PYTPA** with a strong oxidation from the surface chromophores. However, the oxidation of the core was not observable probably due to the much lower ratio of the core among all the chromophores in **PYTPAG2** comparing with **PYTPA**. The reduction process was much less notable and was from the core. For **PYDTPA**, three reversible oxidation couples appeared and the first oxidation couple was more negative than **PYTPA**. They were attributed to the extended-**TPA** moieties which elevated the HOMO level (-5.07 eV).^[4]

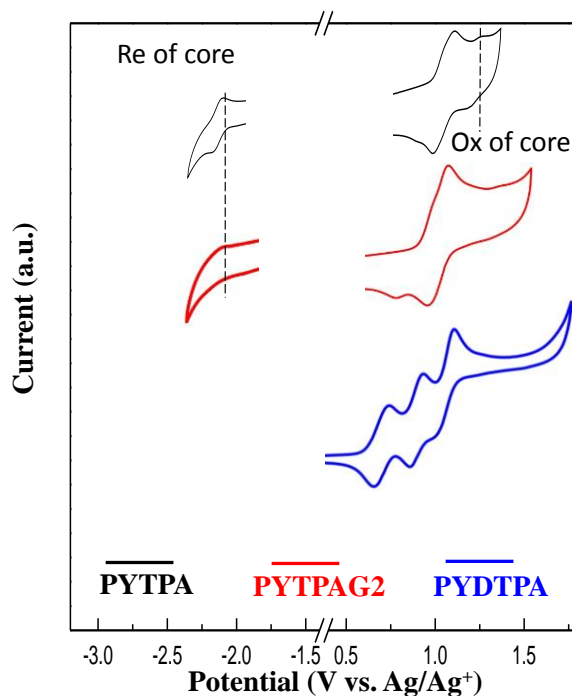


Figure 2.5: CV curves of the redox of **PYTPA**, **PYTPAG2** and **PYDTPA**.

2.1.5 Device performances

The device fabrications and performances of these dendrimers were studied by our collaborators, Manuel Auer, Dr. Roman Trattnig and Prof. Emil List-Kratochvil at NanoTecCenter Weiz, Austria. All three were tested in **OLEDs** with a structure of ITO/PEDOT:PSS/TFB/**PYPPDs**/Ca/Al (Figure 2.6), in which poly(3,4-ethylenedioxythiophene):polystyrenesulfonate (PEDOT:PSS) as a conductive buffer layer was used to reduce the energy barrier for hole injection,^[7] and TFB as a triphenylamine and fluorene based copolymer worked as the hole transport material.^[8] All organic layers were spin-coated layer-by-layer on ITO and finally Ca and Al were deposited sequentially. The detailed preparation procedures were included in chapter 8.

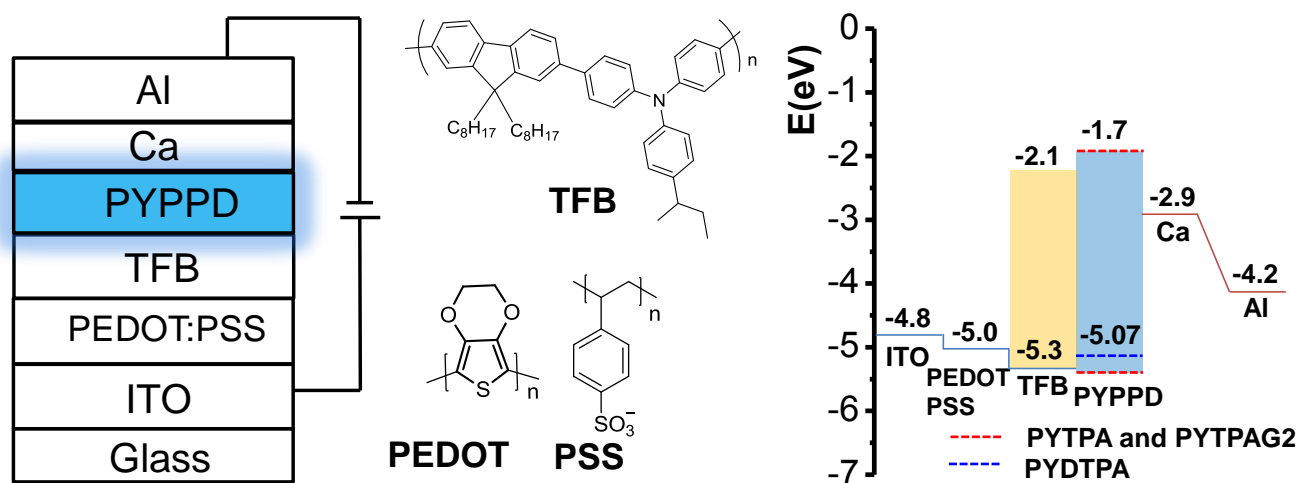


Figure 2.6: Electroluminescent (EL) device configurations (left), molecular structure of PEDOT:PSS and TFB and energy levels of EL devices (middle) and CIE coordinate (right).

As displayed in Table 2.2, the current efficiencies of all devices were quite low (≤ 0.01 cd/A). The luminance was 154 cd/m² which was from **PYTPA**. All three devices had pure blue emission as indicated from the CIE coordinates. For **PYTPAG2**-based device, the emission was deep blue (CIE_{xy}: 0.16, 0.08), probably due to a better protection of the core by its much bigger dendrons compared with the first-generation dendrimers. This is consistent with the smaller bathochromic shift of emission in thin films than the other two dendrimers. The device performance of **PYDTPA** was the poorest among the three. The reason for the generally poor device performance for all devices was probably the poor electron transport from the cathode to the emitting layer as there was a high energy barrier (~ 1.2 eV) for electrons to inject into **TPAs** of the dendrimers from the calcium cathode as shown in Figure 2.6. The LUMO level of **TPA** was estimated to be -1.7 eV obtained from its optical band gap and its HOMO level.^[3]

Table 2.2: Device performance of **PYPPDs** in two-layer devices.

	$V_{on}(V)$	$\eta(\text{cd/A})$	$L_{max}(\text{cd/m}^2)$	CIE (x, y)
PYTPA	4.3	0.007	154	0.17, 0.16
PYTPAG2	4.9	0.01	95	0.16, 0.08
PYDTPA	5.2	0.0003	9.1	0.17, 0.13

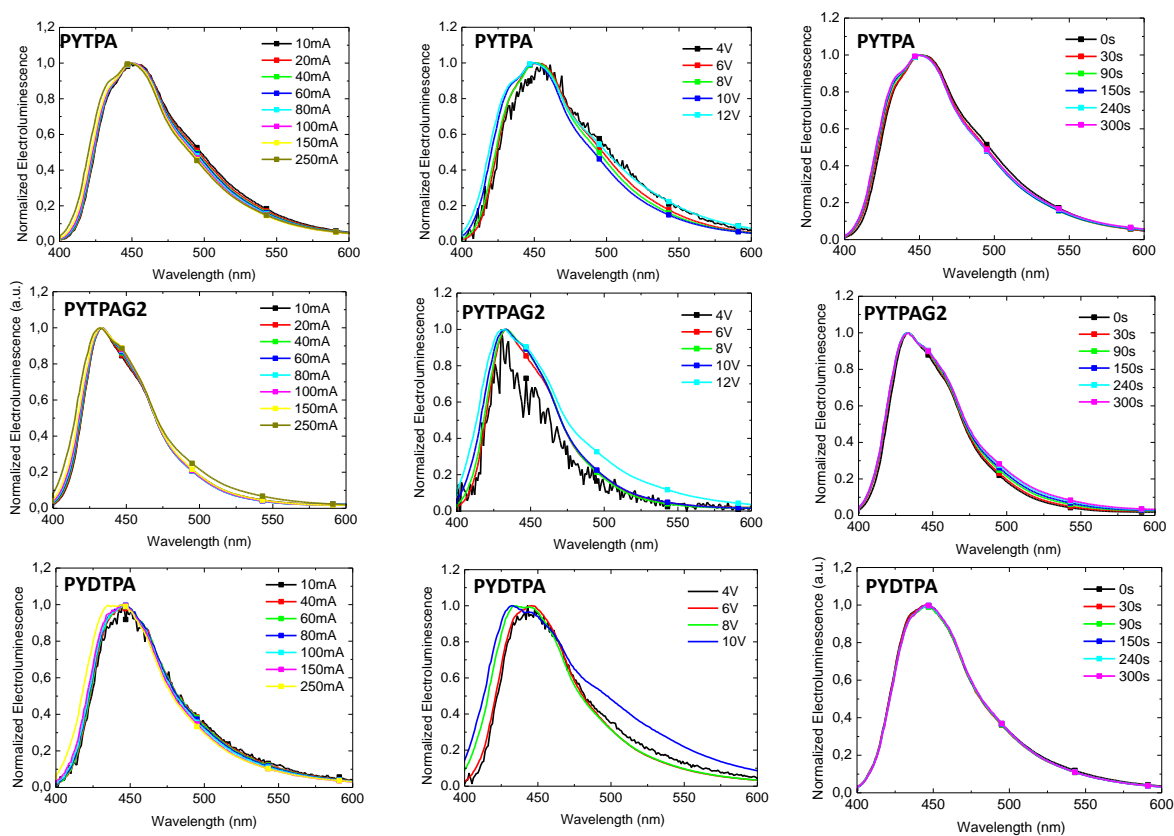


Figure 2.7: Current (left), voltage (middle) and time (right) (current controlled at 50 mA for **PYTPA** and **PYTPAG2** and 70 mA for **PYDTPA**) dependent EL spectra of **PYPPD**-based OLEDs.

The stabilities of these devices were investigated under different current, voltage and time scales (Figure 2.7). It suggested that all the three dendrimers were quite stable in devices under current between 10 mA and 250 mA. Also, good stabilities remained within 5 minutes. In voltage-dependent experiments, the emission were very stable at relatively low voltages. But at 10 V, all dendrimers experienced slightly broadening in their emission.

Afterwards, device optimizations by introducing an electron transporting layer were investigated (Figure 2.8). This time only **PYTPA** and **PYTPAG2** were tested due to their relatively high performances in the initial trials. In the three-layer device, a PEG-functionalized polyfluorene copolymer (PEGPF) was used as the electron transporting material.^[7] The FMOs of PEGPF were not conducted with the CV method but came from the knowledge on polyfluorenes. The HOMO and LUMO level of PEGPF were postulated to be around -5.45 and -2.40 eV respectively.^[9] This polymer in 1 mg/ml methanol solution was spin-coated on top of the **PYPPD** layer. After that, 1 nm Cs_2CO_3 and 100 nm Al were deposited on top of PEGPF layer sequentially.

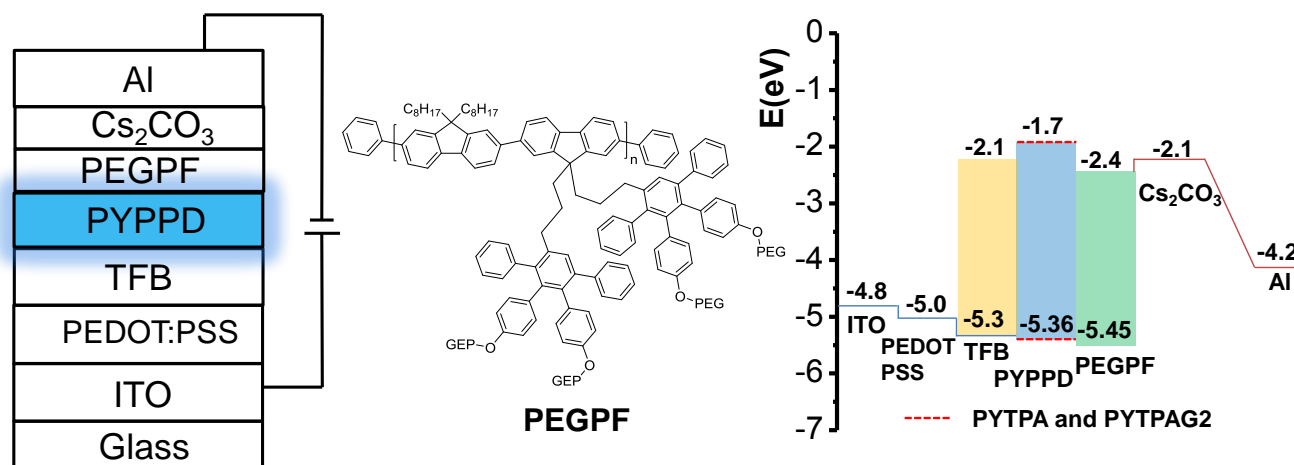


Figure 2.8: Three-layer EL device configurations (left), structure of PEGPF (middle) and energy levels of EL device (right).

Table 2.3: Device performances of **PYTPA** and **PYTPAG2** in three-layer devices.

	$V_{on}(V)$	$\eta(\text{cd/A})$	$L_{max}(\text{cd/m}^2)$	CIE (x, y)
PYTPA	3.7	0.42	2251	0.16, 0.19 ^{a)}
	4.5	0.41	1450	0.16, 0.19 ^{b)}
PYTPAG2	5.8	0.02	186	0.17, 0.11 ^{b)}

^{a)}Device structure: ITO/PEDOT:PSS/TFB/**PYPPD**_s/PEGPF/Cs₂CO₃(1.5nm)/Al,

^{b)}Device structure: ITO/PEDOT:PSS/TFB/**PYPPD**_s/PEGPF/Cs₂CO₃(1.5Å)/Al

The device performance of **PYTPA** was considerably improved compared with the two-layer device (Table 2.3 and Figure 2.9). Firstly, the current efficiency was increased to 0.42 cd/A which was 60 times that of the two-layer device. Also, the luminance reached a value as high as 2251 cd/m² and the emission was in the pure blue area with CIE coordinate of (0.16, 0.19). In addition, the onset voltage was reduced to 3.7 V. The generally improved performance of this device probably resulted from the reduced energy barrier for electron injection from the cathode and transport into the emitting layer with the aid of Cs₂CO₃ and PEGPF (Figure 2.8). On the other hand, the device performance of **PYTPAG2** increased not much in comparison to the initial try.

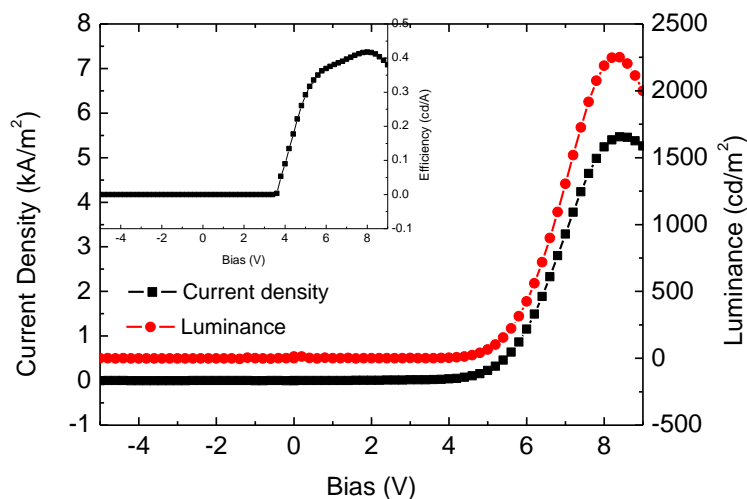


Figure 2.9: Voltage, current, luminance and efficiency characteristics of **PYTPA** in a three-layer device.

Due to the good performance of **PYTPA** in a three-layer device and good hole transporting property of **TPAs**, a two-layer device with PEGPF but without TFB was built (Figure 2.10). As shown in Table 2.4, the current efficiency decreased a little compared with the three-layer device. However, the efficiency of 0.36 cd/A surpassed the efficiency of the core-shell-surface functionalized dendrimer (**PYGTPA**) (0.26 cd/A) in a two-layer device.^[1] At the same time, the luminance of **PYTPA** (1480 cd/m²) was comparable to **PYGTPA** (1400 cd/m²). As a result, it is concluded that **PYTPA** is superior to **PYGTPA** because a better device performance is obtained from the former in similar devices and **PYTPA** is much easier to be synthesized than **PYGTPA**.

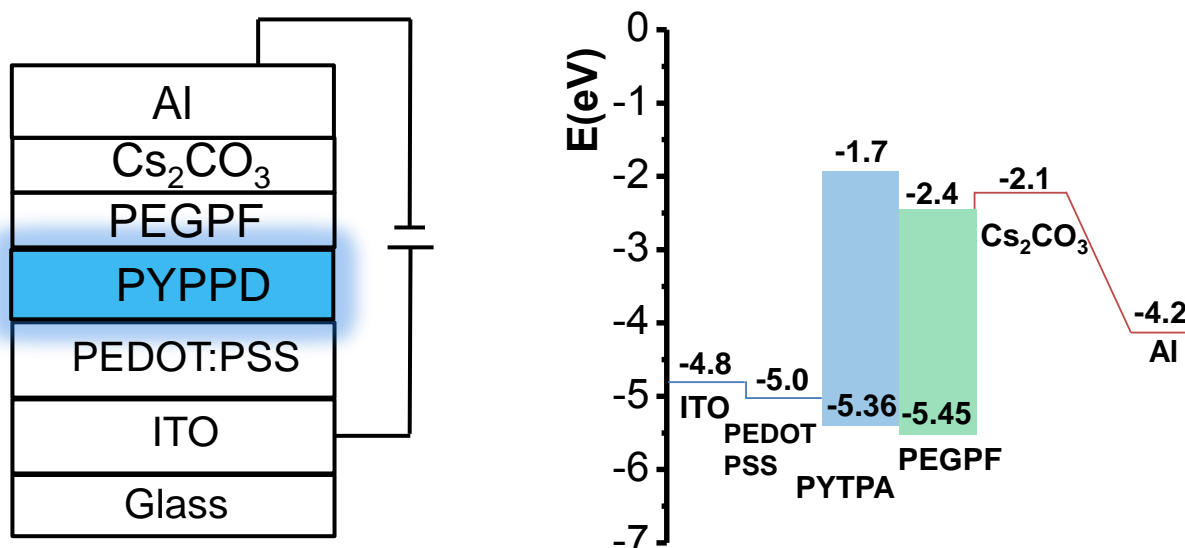


Figure 2.10: Two-layer EL device configurations (left) and energy levels of EL device (right).

Table 2.4: Device performance of **PYTPA** in two-layer device.*

	$V_{on}(V)$	$\eta(cd/A)$	$L_{max}(cd/m^2)$	CIE (x, y)
PYTPA	4.1	0.36	1480	0.16, 0.14

*Device structure: ITO/PEDOT:PSS/**PYPPDs**/PFPEG/Cs₂CO₃(1.5 Å)/Al

In sum, **PYTPA**, **PYTPAG2** and **PYDTPA** were synthesized in moderate to high yields. From their photophysical properties, the emission stemmed solely from the core with very high PLQYs for all dendrimers. In addition, efficient surface-to-core energy transfers were found, especially for the first-generation ones. The device performances of these three dendrimers suggested that the easiest synthesized **PYTPA** was better than the others. Also, **PYTPA** overwhelmed **PYGTPA** in general and represented the best **PPD** as a pure blue emitter in **OLEDs** so far. Thus, it seems not necessary to synthesize second-generation **PYPPDs** for **OLEDs** and the first-generation ones look more promising due to two points:

- (1) The synthesis of a first-generation dendrimer is much easier than that of a higher-generation one.
- (2) The first-generation dendrimers possess efficient surface-to-core energy transfer due to the short distance between the surface and the core.

2.2 Synthesis of first-generation **PYPPDs** with other peripheral chromophores

PYTPA has proven to work well in **OLEDs**, which is largely attributed to the reduced hole-injection barrier by introduction of **TPAs** on the surface and efficient surface-to-core energy transfer. Besides **TPA**, there are many other chromophores which could work as hole or electron transport moieties.^[10] Thus, it is worthwhile to functionalize the surface of a **PYPPD** with other chromophores and to explore their device performances. To design new **PYPPDs** for potentially efficient emitters in devices, two principles should be followed: first, the **PCs** should have efficient hole or electron transport properties, meaning that they should have proper HOMO or LUMO levels to reduce the energy barrier with the electrode; second, efficient surface-to-core energy transfer is required, meaning that the PLQYs of the **PCs** should be good and there should be enough overlaps between the emission of the **PCs** and the absorption of the core.

First of all, carbazole (**CAB**)^[11] and N, N-diphenyl-1-naphthylamine (**NPA**)^[12] were selected because they are widely used in hole transport materials similar as **TPA**. In addition, placing electron transporting groups at the surface of a **PYPPD** should be interesting. In this instance, 2-(4-biphenyl)-5-(4-t-butylphenyl)-1,3,4-oxadiazole (**PBD**) as one of the most popular electron transporting material in **OLEDs** was chosen because its LUMO level of -2.4 eV could effectively reduce the energy barriers between the emitter and the cathode for electrons injection and its very deep HOMO level (<-6.0 eV) could block the holes from transporting into the cathode.^[13] In addition, phenanthrene (**PAN**) was also

employed to functionalize the surface due to its much higher PLQY (~ 0.125)^[14] than triphenylene (~ 0.065)^[14] which was used as energy transfer moiety in **PYPPDs** before.^[1] Moreover, **PAN** worked well in some blue light emitting materials, partly due to its good electron transport ability.^[15] The overlaps between the emission of the **PCs** and the absorption of the core were carefully evaluated from the published results^[12a, 16] and all the **PCs** selected were expected to be good energy-transfer moieties for the core.

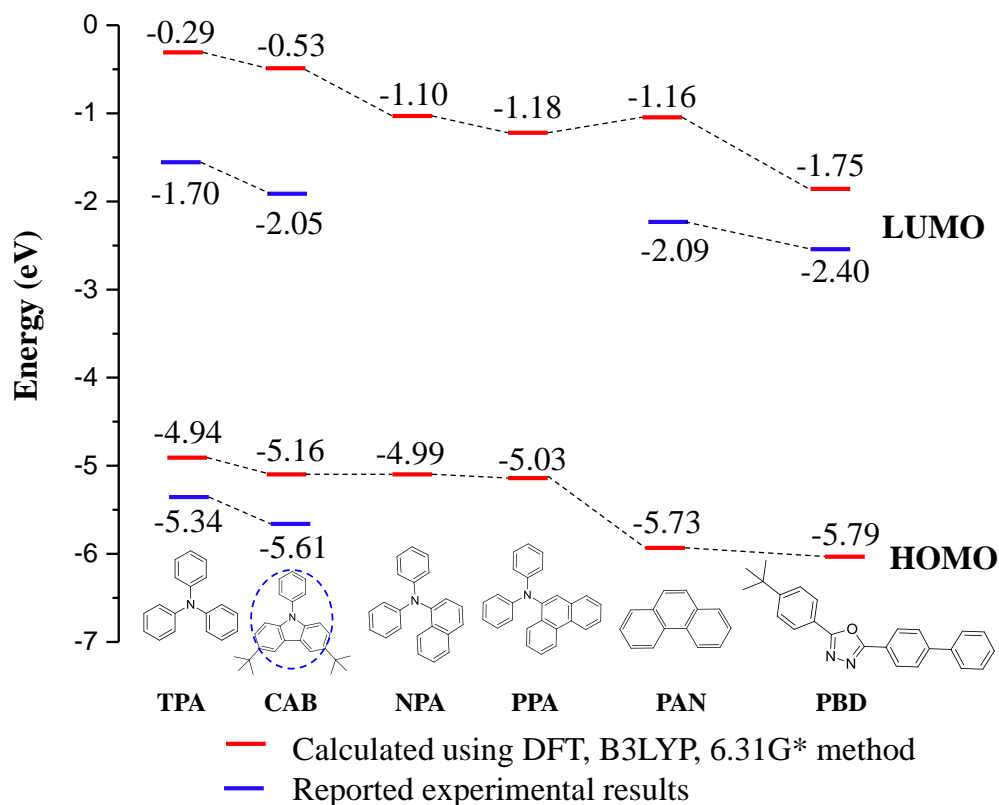


Figure 2.11: Calculated and experimental results of the FMOs of selected chromophores (note: the experimental result of 9-phenylcarbazole belongs to the structure inside of the blue circle).

Before the synthesis, FMOs of the selected chromophores were calculated with Gaussian software and compared with the reported experimental results if available.^[3, 13a, 15-16] As depicted in Figure 2.11, the calculated HOMO and LUMO levels were in good consistency with the experimental ones. For example, comparing the LUMOs of **TPA**, **CAB**, **PAN** and **PBD**, they were in the order of **TPA>CAB>PAN>PBD** from the experimental results and the same order was obtained for the calculated ones. In addition, both the calculated HOMOs of **TPA** and **CAB** were roughly 0.5 eV higher than those of experimental results. As a result, it should be a useful tool to estimate the FMOs of chromophores for potential applications. For example, **NPA** had a similar HOMO level as **TPA** from calculations, and its LUMO level was in between those of **CAB** and **PAN**. Thus, the LUMO of **NPA** was extrapolated to lie in between -2.05 and -2.09 eV, with which it could reduce the electron injection barrier as well. In addition, N, N-diphenyl-9-phenanthrenamine (**PPA**) was calculated and it was found

to be suitable for charge transport as well due to its similar HOMO as **NPA** and its lower LUMO level than **NPA**. Thus, **PPA** should be able to reduce the electron injection barrier further. Consequently, **CAB**, **NPA** and **PPA** all showed potential abilities to reduce both hole and electron injection barriers in devices. Therefore, **PYPPDs** with these **PCs** promise better device performances by balancing both hole and electrons in the emitting layer.

As a result, new first-generation **PYPPDs** with the peripheral chromophores mentioned above were proposed (Figure 2.12). Their synthesis, structural characterizations, photophysical and electrochemistry properties and device performances will be described and discussed in the following part.

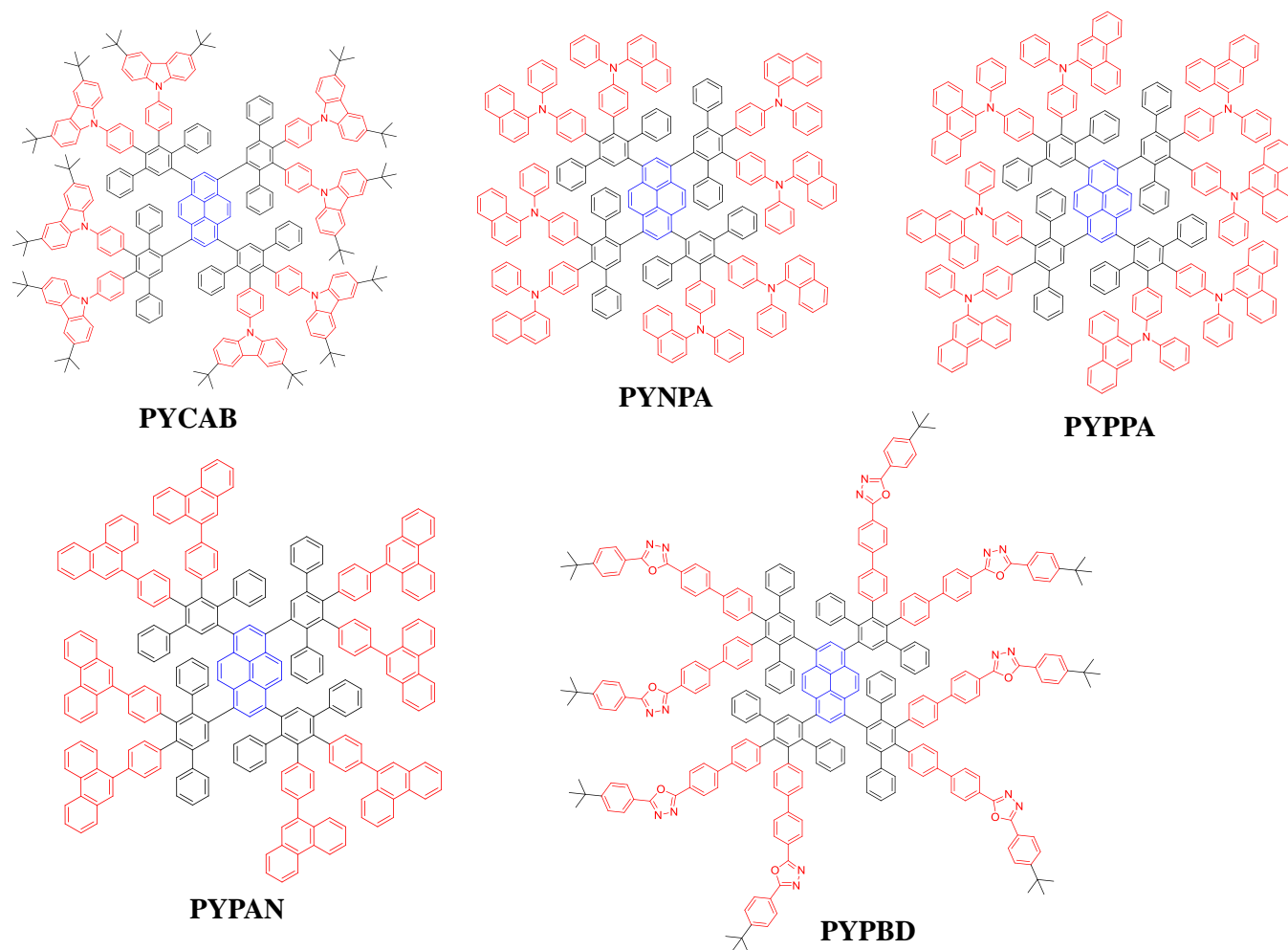
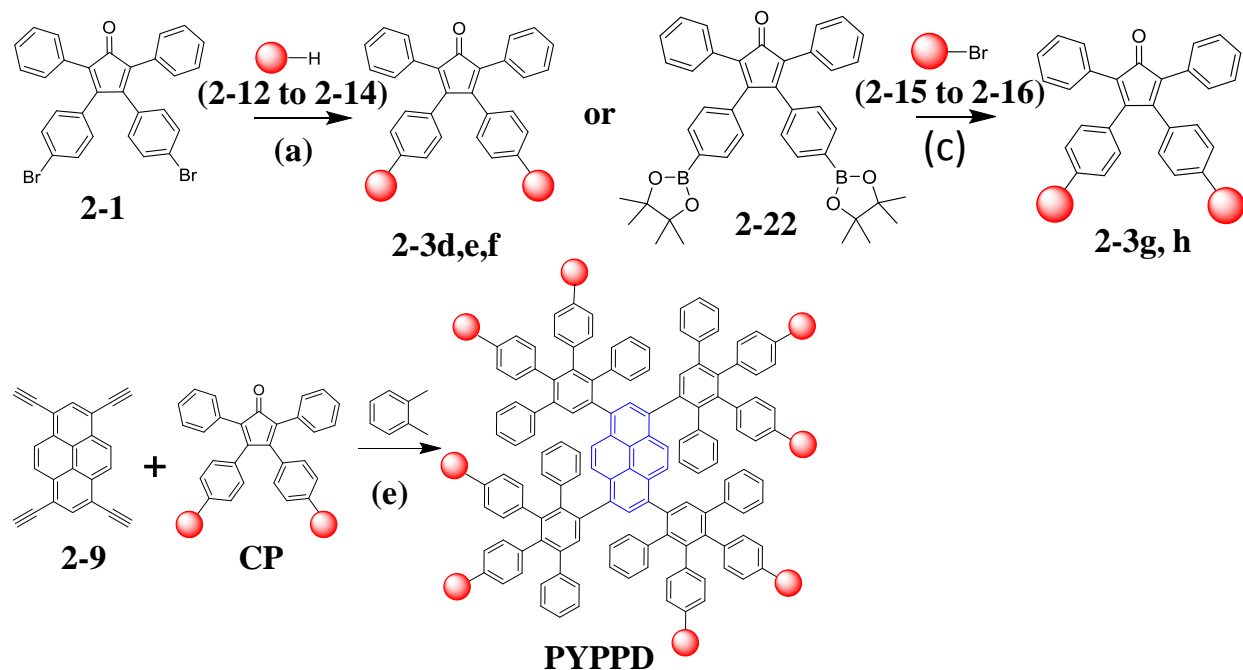


Figure 2.12: Molecular structures of **PYPPDs** with novel **PCs**.

2.2.1 Synthesis of new dendrimers

To synthesize new dendrimers, the **CPs** were produced first. As displayed in Scheme 2.3, the preparation of **CAB**, **NPA** and **PPA** functionalized **CPs** (compound **2-3d**, **2-3e** and **2-3f**) were by the Buchwald-Hartwig reaction between dibromo-**CP** (**2-1**) and the aromatic amines (compound **2-13** and **2-14**) or 3,6-ditertbutylcarbazole (**2-12**). This reaction worked well with high yields for compound **2-3e**: (73%) and **2-3f** (67%) after heated at 70 °C for 24 hours. To introduce carbazoles on the **CP**, it required

a higher temperature, e.g. 110 °C and after reacting for 24 hours, compound **2-3d** was obtained in high yield (68%) as well after purifications.



	=					
SM		2-12	2-13	2-14	2-15	2-16
CP		2-3d	2-3e	2-3f	2-3g	2-3h
PYPPDs		PYCAB	PYNPA	PYPPA	PYPAN	PYPBD

Scheme 2.3: Synthetic routes for new CPs and dendrimers. (a) Pd₂(dba)₃, t-BuONa, (t-Bu)₃P, toluene, 24 h, 110 °C, 68% for **2-3d**, 70 °C, 73% for **2-3e** and 70 °C, 67% for **2-3f**; (c) Pd(PPh₃)₄, K₂CO₃, tetrabutylammonium bromide, toluene, H₂O, 48 h, 80 °C, 60% for **2-3g**, 110 °C 87% for **2-3h**; (e) 145 °C, 72 h, 77% for **PYCAB**, 150 °C, 24 h, 29% for **PYNPA**, 140 °C, 24 h, 77% for **PYPPA**, 145 °C, 48 h, 57% for **PYPAN**, 150 °C, 24 h, 26% for **PYPBD**.

The **PBD** and **PAN** functionalized CPs (**2-3g** and **2-3h**) were made by Suzuki coupling between the boronic ester-functionalized CP (**2-22**) and the chromophore-bromides (**2-15** and **2-16**). This reaction worked effectively and high yields of products were obtained after heating to 80 °C (compound **2-3g**, 60%) or 110 °C (compound **2-3h**, 87%) for 48 hours. The colors of the CPs after drying were yellow-brown, purple or dark-purple in solids, probably due to the push-pull effects between the chromophores and the cyclopentadienone. With the CPs available, the synthesis of dendrimers was through one-step Diels-Alder reaction (Scheme 2.3). After heating under reflux condition between 24 and 72 hours depending on the CPs, the reaction could finish, as monitored by MALDI-TOF mass spectrometry. The

products were received as light-yellow or yellow-colored solids after purifications by silica-gel flash and preparative GPC columns and vacuum drying. The yields of these targets were in between 26% and 77%.

The structures of these dendrimers were fully characterized by ^1H and ^{13}C NMR spectroscopy and MALDI-TOF mass and HRMS spectrometry. As depicted in Figure 2.13, the MALDI-TOF mass spectra showed a single peak of the molecular ion for each dendrimer. In addition, the HRMS spectra of **PYCAB** displayed clear isotope patterns, which were consistent with the calculated result. Therefore, the desired dendrimers were synthesized.

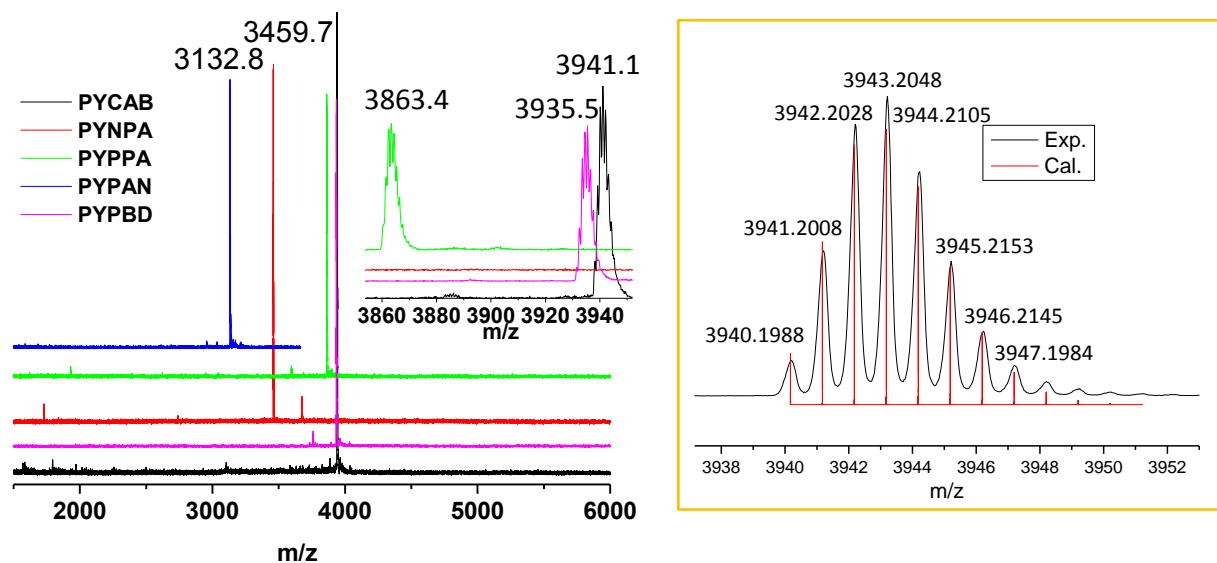


Figure 2.13: MALDI-TOF mass spectra (left) of new dendrimers (inset: the zoom-in spectra of **PYPPA**, **PYPAN** and **PYPBD**) and HRMS spectra of **PYCAB** (right).

2.2.2 Photophysical properties

As depicted in Figure 2.14, the absorption spectra of these **PYPPDs** generally consisted of two parts except **PYNPA** and **PYPPA**. A pronounced band (ϵ : 140000~280000 $\text{lmol}^{-1}\text{cm}^{-1}$) with distinctive absorbance in the UV region originated from **PCs** and polyphenylenes.^[2] The significantly less noticeable band bordering in the visible spectral range was the result of π - π^* transition of the core (λ_{max} ~392 nm, ϵ ~50000 $\text{lmol}^{-1}\text{cm}^{-1}$).^[2, 17] In **PYNPA**, however, the absorptions of **NPA** (λ_{max} ~370 nm) and pyrene overlapped and caused a slight intensification of the weaker band. **PYPPA** was similar as **PYNPA**. Photoluminescence spectra of the investigated compounds revealed that the emission originated exclusively from the core independent of the excitation wavelength (at the surface or at the core) with a peak emission at around 430 nm and a little shoulder at around 450 nm in solution (Figure 2.14 and Table 2.5).

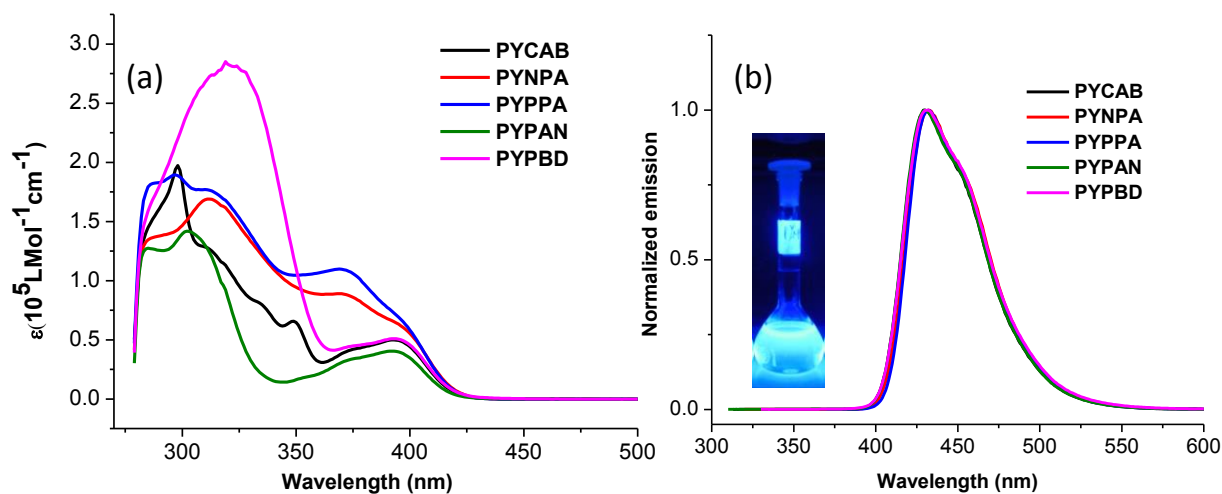


Figure 2.14: UV-vis absorption (a) and Photoluminescence spectra (b, excited at the surface of dendrimer) spectra of **PYPPDs** (10^{-5} M, toluene) (inset picture: the emission of **PYNPA** in toluene, excited at 365 nm).

Table 2.5: Photophysical and electrochemical properties of **PYPPDs**.

	$\lambda_{ab}(nm)$		$\lambda_{em}(nm)$		PLQY ^{a)}		HOMO (eV) ^{b)}	LUMO (eV) ^{b)}	E_g (eV) ^{c)}
	Sol	Film	Sol	Film	Excitation				
					Surface	Core			
PYCAB	298, 392	299, 393	430	434	0.59	0.75	-5.59	-2.44	2.96
PYNPA	312, 370	314, 370	432	445	0.59	0.54	-5.27	-2.35	2.94
PYPPA	297, 370	300, 369	432	453	0.46	0.66	-5.25	-2.35	2.96
PYPAN	302, 392	308, 396	430	446	0.73	0.80	-5.51	-2.38	2.96
PYPBD	320, 392	320, 393	431	453	0.66	0.78	-5.50	-2.52	2.97

^{a)} Measured in THF solution with quinine sulfate in 0.5 M H_2SO_4 solution as the standard; ^{b)} calculated from CV by comparing the first redox onset of **PYPPDs** and the oxidation onset of ferrocene; ^{c)} calculated from the absorption edge of the longest wavelength band.

In thin films, all compounds except **PYCAB** experienced bathochromic shifts of the emission, likely due to inadequate protection of the core (Table 2.5),^[7] while the **CAB** surface groups seemingly provided a sufficient shielding to pyrene. PLQYs of **PYPPDs** were generally quite high (~ 0.7) when excited at 392 nm except for **PYNPA**, in which case a considerable amount of light was absorbed by **NPA** groups. Hence excitation at the core or the surface led to remarkably similar PLQY values (Table 2.5). The absence of any emission from the surface chromophores and high PLQYs even when the surface groups were excited coupled with the fact that the recorded emission stemmed exclusively from pyrene justified the assumption that an efficient FRET took place in all compounds. For **PYPPA**, however, the PLQY from surface excitation was clearly smaller than that from the core. This was possibly due to less surface-to-core energy transfer occurring in this dendrimer than the others because the emission of **PPA** (λ_{em} : ~ 430 nm in DCM) had less overlaps with the absorption of the core.^[18] As a result, when excited at

the surface, the major emission might be from surface-self emission and when it was excited at the core, the emission was mainly attributed to the core.^[18a] The energy gaps deduced from the absorption edges of the longest wavelength bands were all around -2.96 eV within measurement errors (Table 2.5).

2.2.3 Electrochemistry

The redox properties of these dendrimers were evaluated by CV using the same setup as those mentioned before. As depicted in Figure 2.15, the CV curves of these **PYPPDs** displayed clear oxidation/reduction of the core and **PCs**. Generally, both the oxidation and reduction of the core were observed in all compounds and were reversible. In addition, distinctive redox properties of the **PCs** were found among different dendrimers. For example, in **PYCAB** and **PYNPA**, both the oxidation and reduction of **CAB** and **NPA** were present and for **PYPAN** and **PYPBD**, only the reductions of their **PCs** were observed because their ionization potentials were too high to be detected within the potential window of dichloromethane. Additionally, in **PYCAB**, the oxidation wave of **CAB** and the core merged to one, indicating similar HOMO levels between **CAB** and pyrene. The HOMO or LUMO levels of these chromophores were obtained by comparison with ferrocene as the reference (Table 2.5 and Figure 2.16). These energy levels were crucial for charge transport in devices.^[1] In **PYCAB** for example, the HOMO and LUMO level of **CAB** were calculated to be -5.59 eV and -1.97 eV, which were almost identical to those of bare **CAB**,^[16a] indicating little conjugated interactions between the surface chromophores and the core by the highly twisted biphenyls in between.

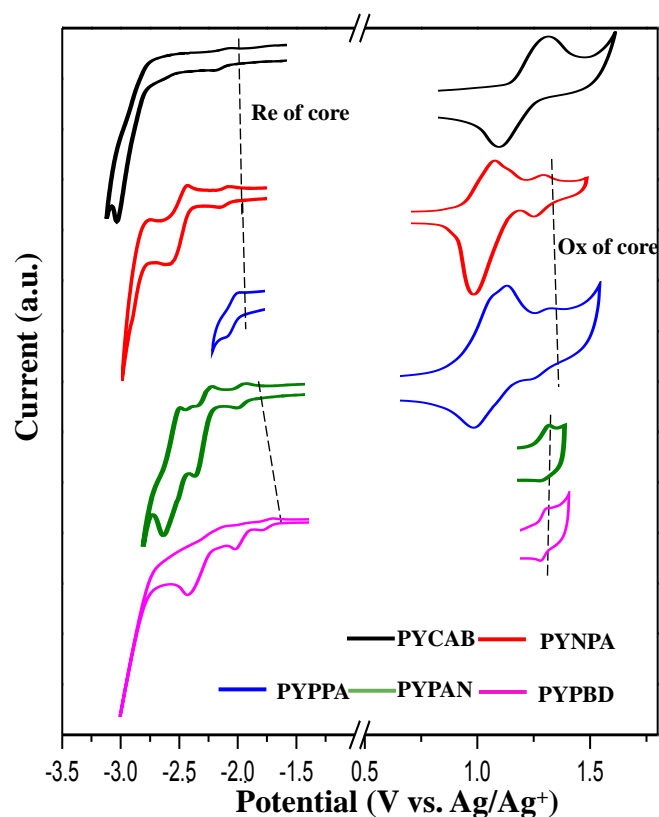


Figure 2.15: CV curves of the redox of **PYPPDs**.

By comparing the energy gaps between the work function of an ITO buffer layer, PEDOT:PSS^[7] and the HOMO levels of the **PCs** (Figure 2.16), **NPA** and **PPA** were found to be the best suitable hole injector (energy gap ~ 0.17 eV) with the hole injection ability in the order of **NPA** \approx **PPA** $>$ **CAB** $>$ **PAN** and **PBD**. Also, **NPA** and **CAB** exhibited potential electron injection properties as the energy gaps between the work function of one cathode material, Cs₂CO₃^[19] and LUMO levels of them were roughly 0.1 eV (Figure 2.16). Unfortunately, the reduction wave of **PPA** was not detected, which was unexpected in that the LUMO level of **PPA** should be a little lower than that of **NPA** from calculations (Figure 2.16). The LUMOs of **PYPPDs** were all around -2.40 eV and were from the core, except **PYPBD**, in which the core was possibly influenced by the electron-withdrawing effects of the **PBDs** and the LUMO was reduced a little bit (Table 2.5).

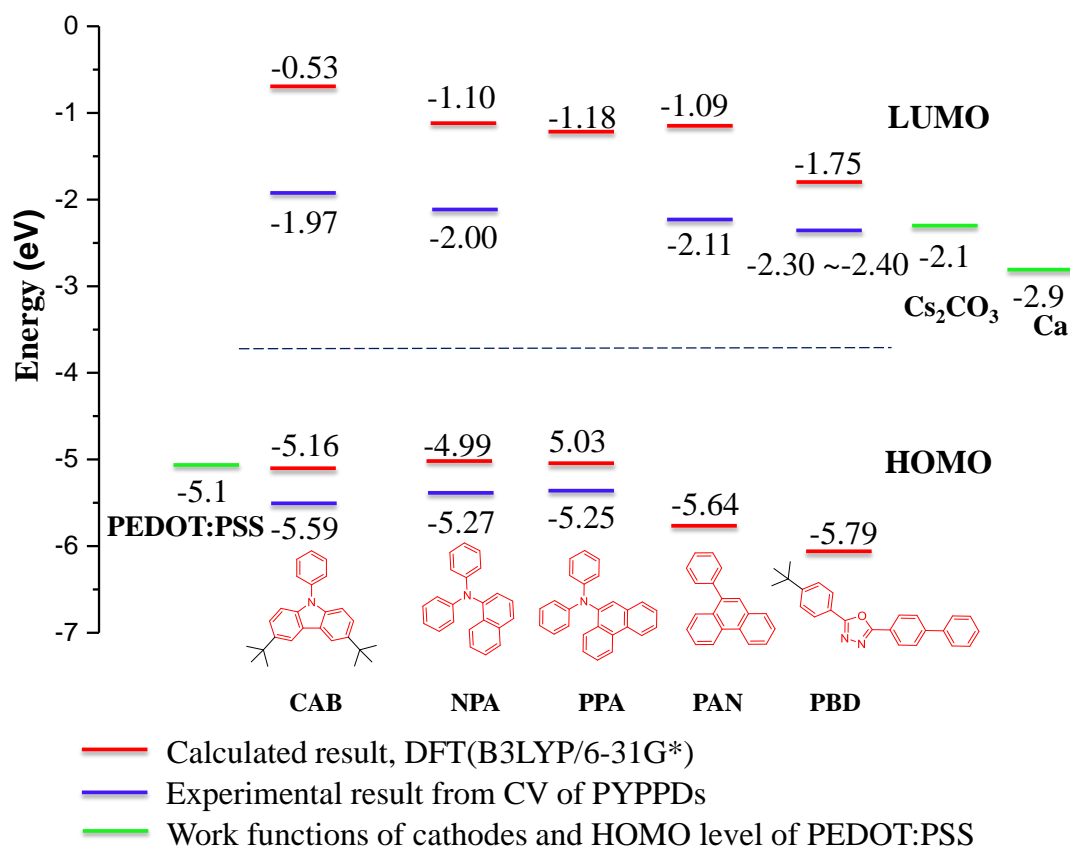


Figure 2.16: HOMO and LUMO levels of **PCs** estimated from CV of **PYPPDs** and DFT calculations of **PCs** (B3LYP/6-31G*), the work function of PEDOT:PSS, Cs₂CO₃ and Ca.^[7, 19-20]

Moreover, there existed an overlap between the reduction wave of the core and **PBD** due to an enhancement of the reduction peak of the core (Figure 2.15). The LUMO level of **PBD** was estimated to be between -2.30 and -2.40 eV as a result.^[13a] On the other hand, the reduction wave of the core and those of **PCs** in **PYPAN** looked well separated, thus the LUMO of **PAN** was calculated as -2.11 eV. This value was very close to the reported LUMO value of phenanthrene (-2.09 eV).^[15] The HOMOs, however differed depending on the surface chromophores. The HOMO of the core was around -5.50 eV

as estimated from the oxidations of **PYPBD** and **PYPAN** and the oxidations of **PAN** and **PBD** were beyond the detection limit. This was consistent with the calculated HOMO levels which were much lower than for other **PCs** (Figure 2.16).

From the photophysical results, it appears that these compounds have efficient surface-to-core energy transfer and pure core, deep blue emission with high PLQYs. In addition, electrochemical analysis suggests that the surface chromophores, e.g. **NPA** and **CAB**, facilitate both hole and electron injection. These properties strongly support our core-surface-functionalized-**PPDs** design principles for high-performance, solution-processed, deep-blue organic light-emitting materials.

2.2.4 Device performances

Following the success of **PYTPA** in **OLEDs**, **PYCAB** and **PYNPA** were first tested in single-layer and three-layer devices. The single-layer devices had an ITO/PEDOT:PSS/**PYPPD**/Ca/Al structure, where **PYPPDs** in THF, chloroform or toluene solutions were spin coated on top of PEDOT:PSS layer because all of these solvents dissolved the dendrimers well. As displayed in Table 2.6, for single-layer devices, **PYNPA** showed a better performance than **PYTPA** and **PYCAB** with a current efficiency of 0.24 cd/A and a luminance of 715 cd/m² because **NPA** groups reduced both hole and electron injection barriers from the electrodes due to its proper HOMO and LUMO levels (Figure 2.16). **PYCAB** was second to **PYNPA**. One possible reason might be the energy barrier between the HOMO of PEDOT:PSS and the HOMO of **PC** in **PYCAB** was larger than that for **PYNPA** (Figure 2.16). The current efficiency of **PYTPA** was far behind that of **PYNPA** and **PYCAB**. This was probably attributed to the too high energy barrier for electron injection in a device of **PYTPA**.

Table 2.6: Device performances of **PYPPDs**.^{a)}

	$V_{on}(V)$	$\eta(cd/A)$	$L_{max}(cd/m^2)$	CIE (x, y)
PYCAB	6.6	0.06	395	0.16, 0.16
	5.7	0.52	1526	0.17, 0.20
PYNPA	5.2	0.24	715	0.16, 0.20
	4	0.45	3726	0.16, 0.21
PYTPA	5	0.006	112	0.16, 0.15
	4.5	0.41	1450	0.16, 0.19

^{a)} Single-layer (black) and three-layer (blue) device data

PYCAB and **PYNPA** similar as **PYTPA** were further optimized in three-layer devices with the structure of ITO/PEDOT:PSS/TFB/**PYPPD**/PEGPF/Cs₂CO₃(1.5Å)/Al, where TFB and PEGPF worked as hole and electron transporting layers respectively.^[7] All the organic layers were spin coated on a TFB surface. The device data indicated that current efficiencies and luminance were significantly enhanced for both of them. In addition, the onset voltages were both reduced comparing with single-layer devices. They suggested that both hole and electron injection and transport were much improved and better charge

confinement in the emitting layer was achieved with the help of TFB and PEGPF layers in devices (Table 2.6). Overall, **PYCAP** showed the highest current efficiency of 0.52 cd/A which was 2 times higher than that of the reported core-shell-surface functionalized **PYGTPA**,^[1] probably due to the more balanced hole and electron injection ability of **CAB** surface chromophores than **TPA**. **PYNPA** had the highest luminance of 3726 cd/m², lowest onset voltage of 4 V, a current efficiency of 0.45 cd/A and stable, pure blue emission with CIE_{xy}= (0.16, 0.21) (Table 2.6 and Figure 2.17). It was regarded as the best example among the three, which was again ascribed to both the hole and electron transport ability of **NPA** groups.

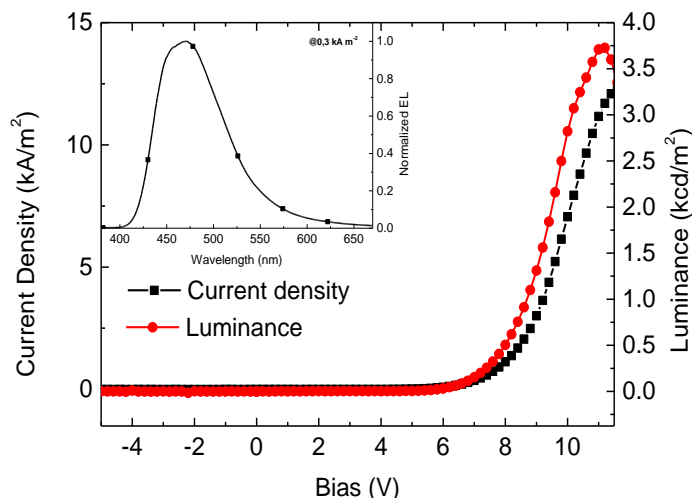


Figure 2.17: Voltage-current-luminance characteristics of **PYNPA** in a three-layer device.

PYPPA, **PYPAN** and **PYPBD** were tested in single-layer (ITO/PEDOT:PSS/**PYPPD**/Ca/Al), two-layer (ITO/PEDOT:PSS/TFB/**PYPPD**/Ca/Al) and three-layer (ITO/PEDOT:PSS/TFB/**PYPPD**/PEGPF/Ca/Al) devices. The energy levels of these devices are shown in Figure 2.18.

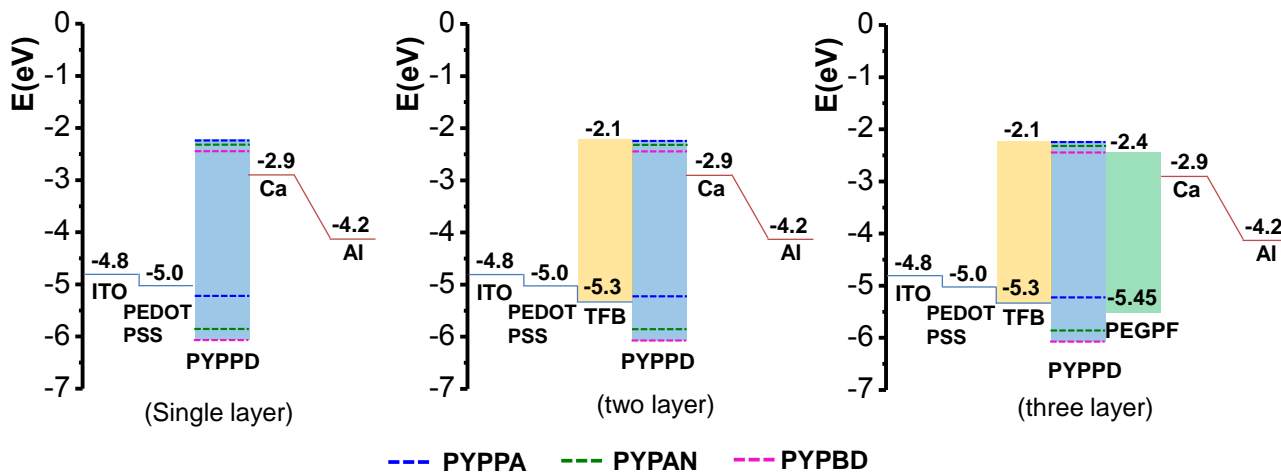


Figure 2.18: Energy levels of EL devices for **PYPPA**, **PYPAN** and **PYPBD**.

As displayed in Table 2.7, all single-layer devices generally showed poor performances and the best one was from **PYPBD** with a maximum current efficiency of 0.04 cd/A, highest luminance of 277 cd/m² and a pure blue emission with CIE_{xy}(0.18, 0.18), possibly due to the relatively small electron injection barrier for **PYPBD** comparing with the other dendrimers. The generally low efficiencies in single-layer devices were due to the unbalanced hole and electron injection from the electrodes.

Table 2.7: Device performances of **PYPPA**, **PYPAN** and **PYPBD**.^{a)}

	V _{on} (V)	η(cd/A)	L _{max} (cd/m ²)	CIE (x, y)
PYPPA	9	0.0015	29	0.16, 0.08
	4	0.014	101	0.16, 0.09
	4	0.24	2736	0.16, 0.09
PYPAN	7	0.021	166	0.16, 0.12
	7	0.06	927	0.16, 0.12
	5.4	0.25	3410	0.16, 0.12
PYPBD	9.7	0.04	277	0.18, 0.18
	7	0.17	854	0.18, 0.18
	7	0.24	1288	0.18, 0.18

^{a)}Single-layer (black), two-layer (blue) and three-layer (blue and bold) device data

In two-layer devices, TFB was introduced between PEDOT:PSS and the emitting layer, working as the hole transporting layer to reduce the hole injection barrier from the anode to the emitting layer. The device data indicated that the current efficiency and luminance were both enhanced several times compared with single-layer device for all three dendrimers. At the same time, the color purities of emission were kept the same for all of them (Table 2.7, Figure 2.19), demonstrating that the emission solely stemmed from the dendrimers. In two-layer devices, the best performance was also from **PYPBD** with an efficiency of 0.17 cd/A and a luminance of 854 cd/m², probably due to the more balanced hole and electron accumulations in the emitting layer with a good electron injection from the electrode and enhanced hole transport assisted by TFB layer. The other two dendrimers were behind **PYPBD** in efficiencies, possibly due to the relatively large electron injection barriers for both **PYPPA** and **PYPAN** (Figure 2.18). As a result, when trying to get more balanced holes and electrons in device, it might be advisable to try to reduce the electron-injection barrier while keeping a little hole-injection barrier.

To reduce the electron-injection barrier and collect more holes and electrons in the emitting layer, PEGPF was introduced between emitting layer and cathode. Three-layer devices displayed better performances than two-layer devices in general (Table 2.7). All three materials reached current efficiencies of approximate 0.24 cd/A and luminance higher than 1000 cd/m². The reason for the better device performances was probably the reduced electron-injection barrier between the cathode and **PYPPDs**. Especially for **PYPPA** and **PYPAN**, the energy gaps between the **PCs** and the cathode were markedly reduced in contrast to **PYPBD**, as a result, their efficiencies and luminance were increased

much more than **PYPBD** from two-layer to three-layer devices. In addition, the emission colors of these dendrimers remained the same as single-layer devices (Table 2.7, Figure 2.19), suggesting that the emission were solely from the dendrimers in two- and three-layer devices. The best performances in three-layer devices belonged to **PYPPA** and **PYPAN**. **PYPAN** had a luminance of 3400 cd/m² and exhibited a pure blue emission with CIE_{xy} (0.16, 0.12). **PYPPA**, on the other hand, had slightly lower luminance (~ 2700 cd/m²) than **PYPAN** but its emission was deep blue with CIE_{xy} of (0.16, 0.09). This number was very close to the blue standard CIE coordinates of (0.14, 0.08) of National Television System Committee (NTSC) for display applications.^[15, 21] This was also the second polyphenylene dendrimer known so far (the first one was **PYTPAG2** mentioned above) that obtained deep blue emission with CIE_{xy}(y < 0.10) in **OLEDs**. The emission of **PYPPA** should be attributed to the moderate surface-to-core energy transfer between **PPA** and the core and partial **PPA**-self radiative decays which resulted in the blue shift in emission. This was supported by the deep blue emission of **PPA** in thin film (λ_{max} : ~ 421 nm)^[18a] but the emission of **PYPPA** in thin film was bathochromically shifted (λ_{max} : ~450 nm) and its peak emission in devices were 437 nm (single-layer), 438 nm (two-layer) and 445 nm (three-layer) respectively.

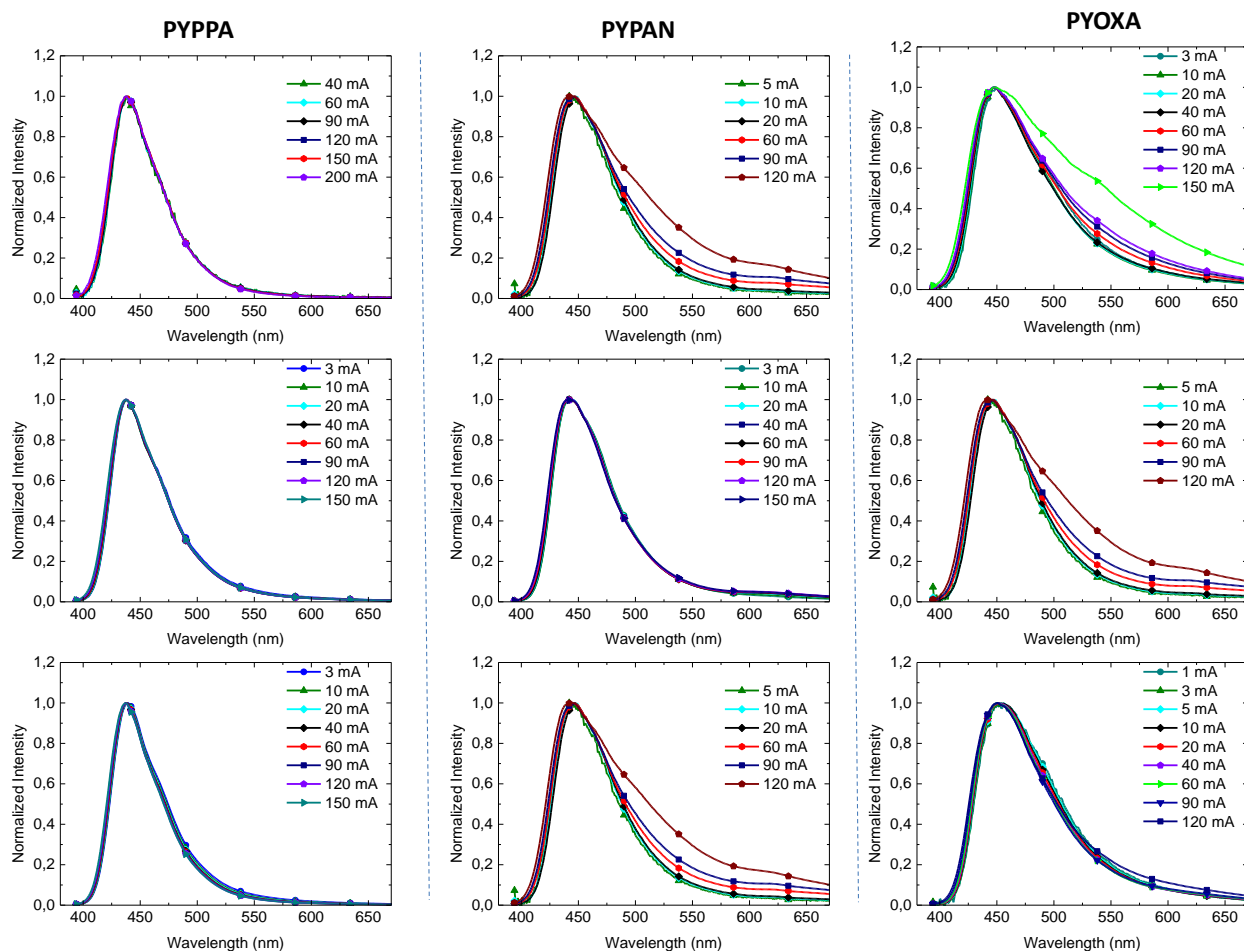


Figure 2.19: Current dependence of EL spectra of **PYPPA** (Left), **PYPAN** (middle) and **PYPBD** (right) in single-layer (top), two-layer (mid) and three-layer (down) devices.

In summary, several new **PYPPDs** with novel peripheral chromophores were synthesized and fully characterized. The device performances of these **PYPPDs** with **PCs** of distinctive hole and electron transport abilities were carefully compared and several points were generalized here:

- (1) Both **PYCAB** and **PYNPA** with the same device structure as **PYTPA** demonstrated better device performances than **PYTPA**. It is probably a result of both the hole and electron transport ability of the **PCs** in the first two dendrimers rather than hole-only transport ability of **TPA** in **PYTPA**. In addition, **PYCAB** and **PYNPA** represent the best device results among **PYPPDs** so far. As a result, for new dendrimer designs in the future, bipolar surface with stronger charge transporting abilities (both holes and electrons) might be a better choice.
- (2) From the **OLED** performances of **PYPPA**, **PYPAN** and **PYPBD**, it is concluded that trying to minimize the electron injection barrier and at the same time keeping a moderate hole injection barrier is a way to better balance the amount of holes and electrons in the emitting layer. Moreover, deep blue emission in **PYPPA** was obtained ($CIE_y < 0.10$). This might be due to the partial self-emission from the surface groups.

2.3 Synthesis of **PYPPDs** with two kinds of peripheral chromophores

As discussed above, the selection of surface chromophores of a **PYPPD** is essential in determining its device performances. Those dendrimers with **PCs** of both hole and electron transporting abilities usually could boost the device performances. Consequently, it is worth improving both the hole and electron transporting abilities of the surfaces of dendrimers further. A good way is to introduce both efficient hole and electron transport groups on the surface of a **PYPPD**.

In this section, the synthetic work toward bipolar-surface **PYPPDs** and their **OLED** performances will be described. Here we select **CAB** and **PBD** as the surface chromophores of the first dendrimer (**PYCABPBD**), **TPA** and **PBD** as **PCs** of the second dendrimer (**PYTPAPBD**) and **TPA** and **PAN** as the **PCs** of the third one (**PYTPAPAN**) (Figure 2.20).

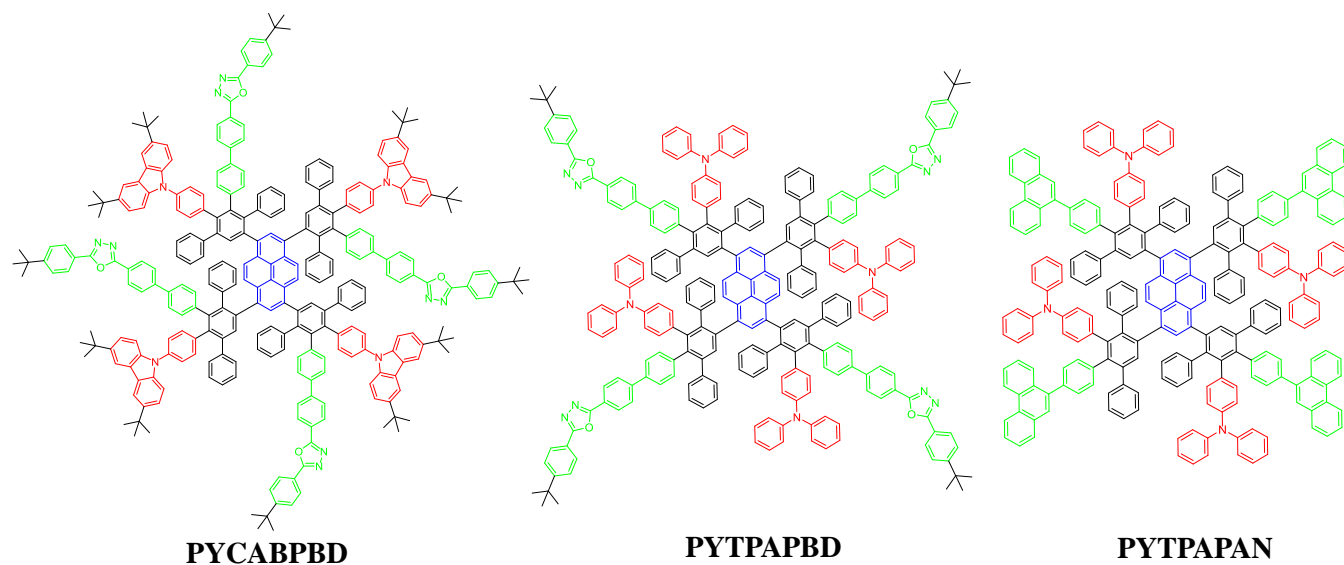
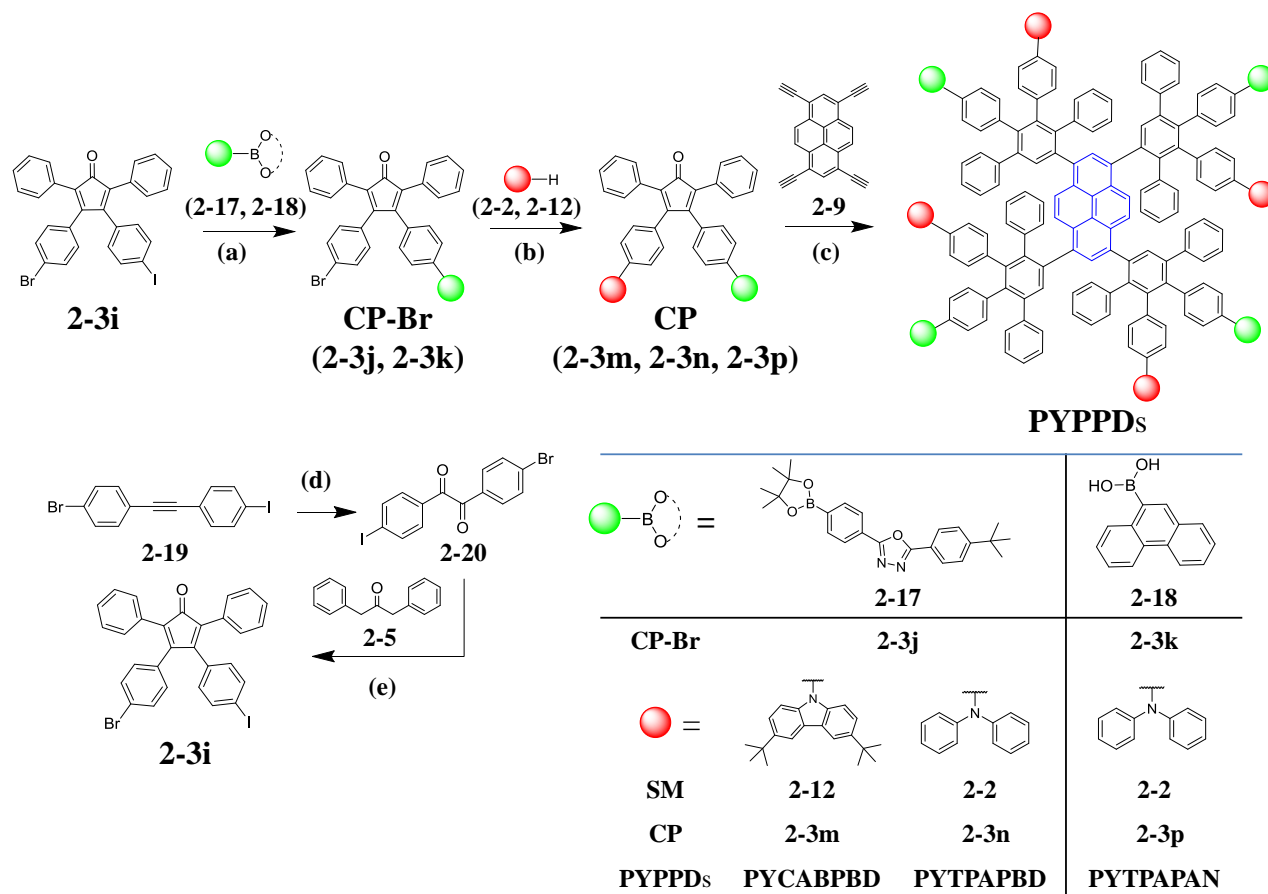


Figure 2.20: Molecular structures of bipolar-surface **PYPPDs**.

2.3.1 Synthesis of peripherally-bipolar **PYPPDs**

Herein, as displayed in Scheme 2.4, a new and efficient synthetic method to afford peripherally-bipolar **PYPPDs** will be introduced by using bromo-iodo-functionalized **CP** (**2-3i**). Compound **2-3i** was synthesized starting from the reported 1-(4-bromophenyl)-2-(4-iodophenyl)ethyne (**2-19**) which was made by a one-pot double elimination process in high yield (67%).^[22] Then it was oxidized by I₂ and DMSO to give 1-(4-iodophenyl)-2-(4-bromophenyl) diketone (**2-20**) in high yield (89%). After that, compound **2-20** was reacted with 1,3-diphenylacetone (**2-5**) to form compound **2-3i** through Knoevenagel condensation in high yield (76%). Then, the two-chromophore functionalized **CPs** (**2-3m**, **2-3n** and **2-3p**) were prepared in two steps. First, a Suzuki coupling between compound **2-3i** and **PBD**-boronic ester (**2-17**) or 9-phenanthrenylboronic acid (**2-18**) at 80 °C for 48 hours generated bromo-chromophore functionalized **CP-Br** (**2-3j** and **2-3k**) in high yields (100% and 79% respectively). The high selectivity of Suzuki coupling was a key for the next step.

Next, Buchwald-Hartwig reactions between **CP-Br** and 3,6-di(*t*-butyl)-9-*H*-carbazole (**2-12**) or diphenylamine (**2-2**) were performed to give birth to the final **CPs** (**2-3m**, **2-3n** and **2-3p**) in moderate to high yields (78%, 39% and 74% respectively). The dendrimers were procured in a one-step Diels-Alder reaction between 1,3,6,8-tetra-ethynyl-pyrene (**2-8**) and the **CPs** in moderate to high yields (45%-73%) similar as the previously mentioned first-generation **PYPPDs**. It was found that the reaction at temperature as low as 120 °C could start and reach high yields of product, i.e. **PYTPAPAN**, which was at least 20 degrees lower than the synthetic conditions of the previously described dendrimers.



Scheme 2.4: Synthetic routes for new **CPs** and dendrimers. (a) $\text{Pd}(\text{PPh}_3)_4$, K_2CO_3 , tetrabutylammonium bromide, toluene, H_2O , 48 h, $80\text{ }^\circ\text{C}$, 100% for **2-3j**, 79% for **2-3k**; (b) $\text{Pd}_2(\text{dba})_3$, $t\text{-BuONa}$, $(t\text{-Bu})_3\text{P}$, toluene, 24 h, $110\text{ }^\circ\text{C}$, 78% for **2-3m**, $75\text{ }^\circ\text{C}$, 39% for **2-3n** and $75\text{ }^\circ\text{C}$, 74% for **2-3p**; (c) *o*-xylene, $130\text{ }^\circ\text{C}$, 24 h, 50% for **PYCABPBD**, 45% for **PYTPAPBD**, $120\text{ }^\circ\text{C}$, 24 h, 73% for **PYTPAPAN**; (d) I_2 , DMSO, $155\text{ }^\circ\text{C}$, 24 h, 89%; (e) KOH , EtOH, $80\text{ }^\circ\text{C}$, 1 h, 76%.

2.3.2 Structural characterizations of the new CPs and dendrimers

When growing single crystals of the **CPs**, compound **2-3m** and **2-3p** could successfully form long-needle single crystals using two-phase slow dispersion method between chloroform and *n*-pentane. These needles were good enough for X-ray single crystal diffraction measurements which were conducted by Dr. Dieter Schollmeyer in University of Mainz. As depicted in Figure 2.21, the crystal structure of compound **2-3m** showed that the torsion angles of C2-C3-C12-C13 and C5-C4-C39-C44 were as high as 53° and 48° respectively, probably due to the strong repulsion between hydrogen atoms from adjacent phenyls on the **CP**. The highly twisted structure indicated little conjugations between the chromophores and the cyclopentadienone group. This was consistent with the separated redox properties between the core and **PCs** of the dendrimers discussed before. In addition, the torsion angles of C43-C42-C45-C50, C49-C48-C51-O55 and O55-C54-C56-C61 were 30° , 11° and 14° respectively. They were in general slightly bigger than the reported bare **PBD** single crystal results, namely 26° , 8° and 4° .^[23] This suggested that the conjugation of **PBD** moiety in the **CP** was less than that of the separated

state, which was consistent with the slightly higher LUMO level of the **PBD** in the **PYPBD** than that of bare **PBD**.^[13a]

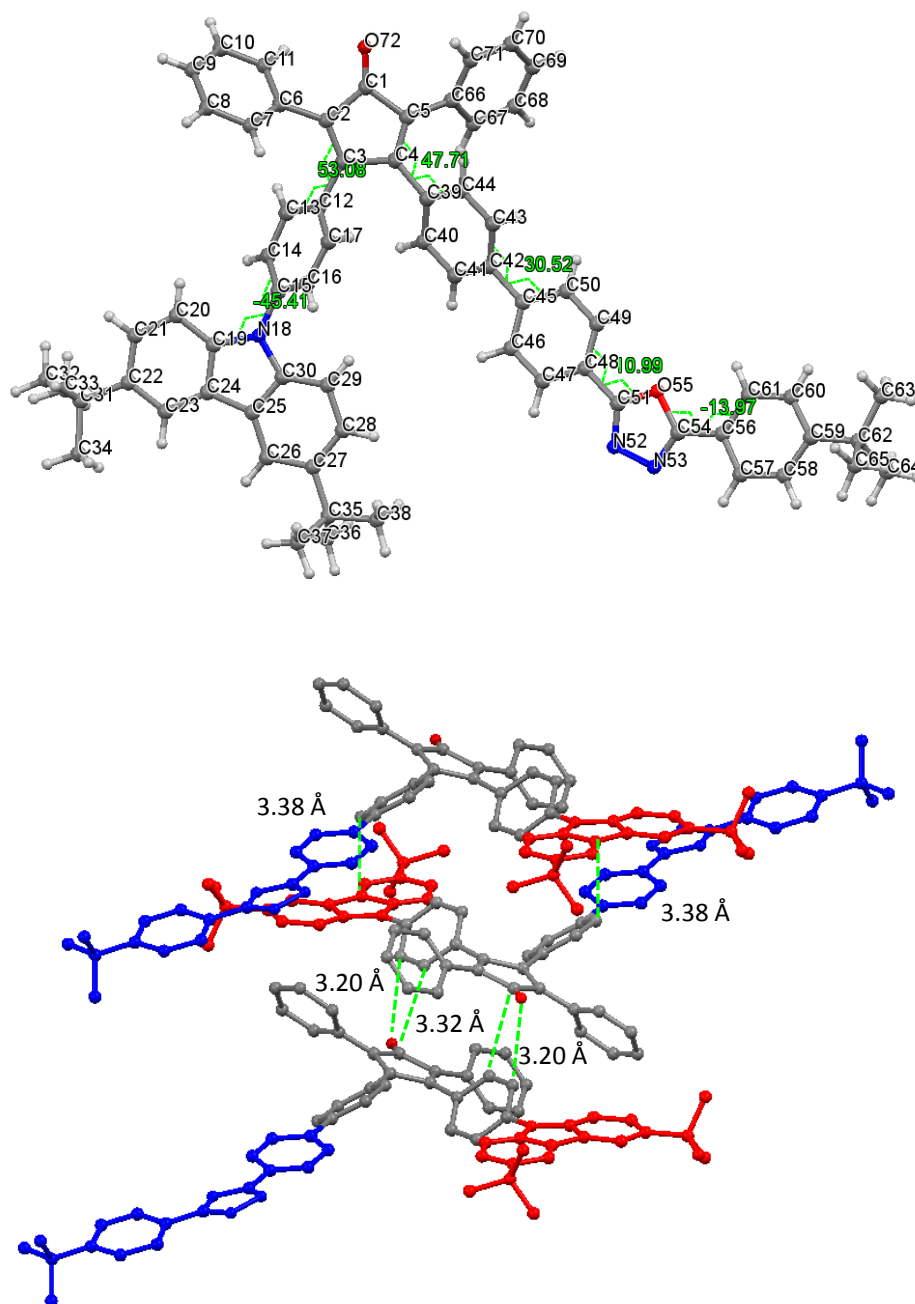


Figure 2.21: Single crystal structure of compound **2-3m** (top) and its crystal packing (bottom, hydrogen atoms hidden).

In addition, there were some close contacts between the adjacent molecules. For example, the distance between a carbazole-carbon and a β -phenyl-carbon of **PBD** was 3.38 Å, probably due to the attractions between the partially electron-positive character of the former and partially electron-negative property of the later. In addition, strong interactions between the carbonyl group of one molecule and two carbon atoms on the 9-phenyl groups of 9-phenyl-carbazole were found. The distance between the oxygen atom and one carbon atom was as close as 3.20 Å and the carbonyl carbon atom had a short distance of 3.32 Å

with one carbon atom of another molecule. The short contacts probably resulted from the polar interactions, which together contribute to the specific tail-to-tail and face-to-face packing structure.

As depicted in Figure 2.22, in the crystal structure of compound **2-3p**, there also existed strong distortions between the cyclopentadienone moiety and the phenyl groups directly bonded to the chromophores with torsions of 44° and 43° respectively due to the repulsion effects between the hydrogen atoms of adjacent phenyl groups of the **CP**. In addition, the crystal packing exhibited parallel and barely-one-dimensional tail-to-tail interactions between **TPA** of one molecule and **PAN** of another. This was probably due to the donor-acceptor effect between those two groups. Moreover, no close contacts were detected in the crystal packing.

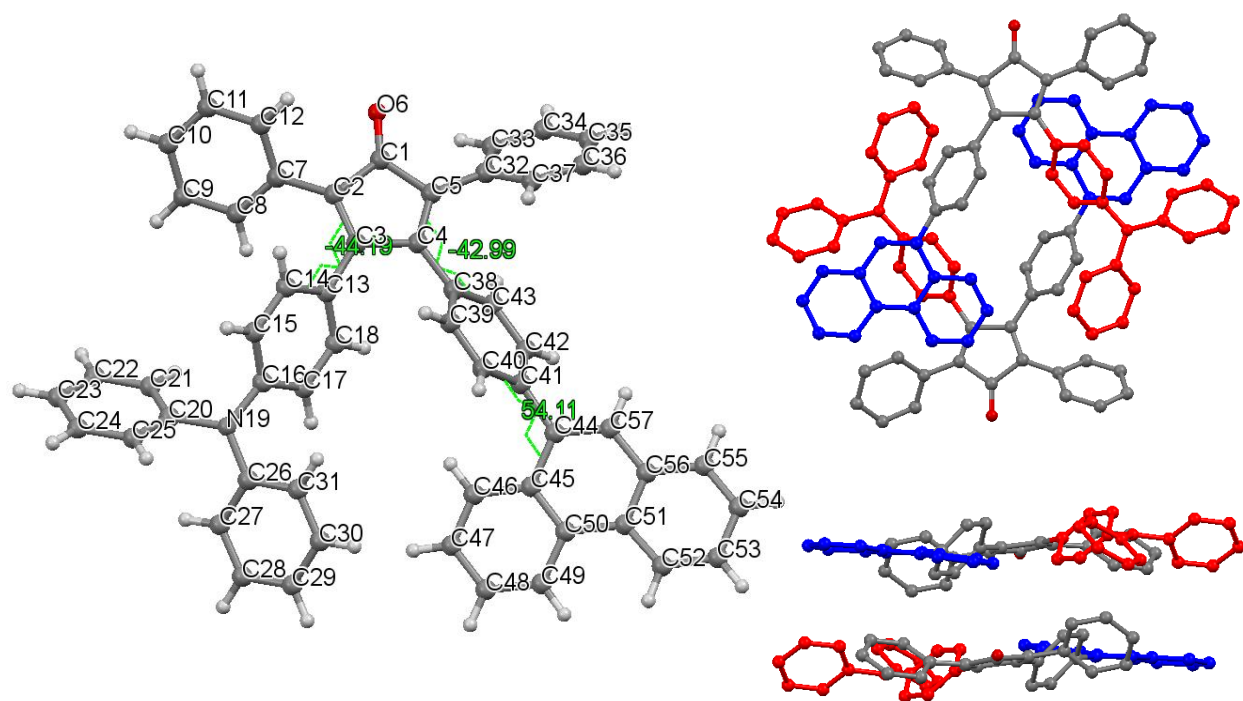


Figure 2.22: Single crystal structure of compound **2-3p** (left) and its crystal packing (right, hydrogen atoms hidden, perpendicular (top) and parallel (bottom) to the cyclopentadienone plane).

The dendrimers were readily soluble in organic solvents, e.g. DCM, THF and toluene (≥ 8 g/l), similar as other **PYPPDs**. They were purified by silica gel flash column and GPC chromatography methods. Their purities, structures, photophysical and electrochemical properties were characterized by ^1H NMR and ^{13}C NMR spectroscopy, MALDI-TOF Mass and HRMS spectrometry, UV-vis absorption, photoluminescence spectroscopy and cyclic voltammetry. Even though there were many different aromatic protons in the dendrimer structures. The ^1H NMR spectra could distinguish some special ones. As depicted in Figure 2.23, in **PYCABPBD**, proton signals of H_a and H_b which were closest to 1,3,4-oxidazole groups appeared at the lowest fields due to the strong electron-withdrawing effect of 1,3,4-oxidazole. The signals of protons on pyrene (H_d and H_e) and 4- and 5-positon protons (H_c) on carbazole moieties overlapped with that of proton H_b in between 8.09 and 8.05 ppm. The rest of aromatic signals

ranging between 7.82 and 6.61 ppm represented all the other aromatic protons in the molecule. In addition, two singlet peaks at 1.39 and 1.36 ppm in **PYCABPBD** originated from the protons of tert-butyl groups on **PBD** and **CAB** respectively. Moreover, the relative intensities of each peak correlated well with the number of corresponding protons in the molecule.

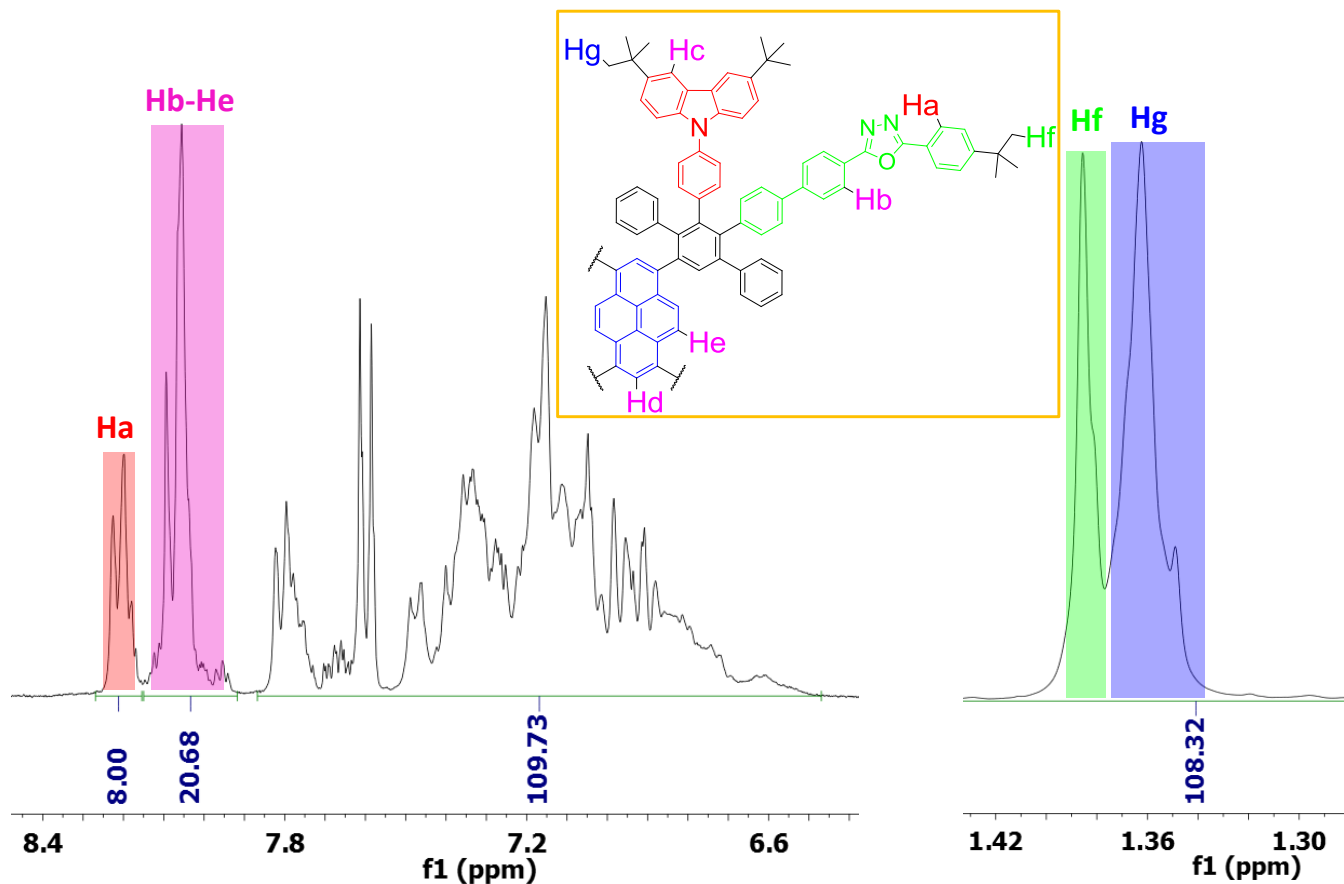


Figure 2.23: ^1H NMR spectra of **PYCABPBD** (solvent: CD_2Cl_2).

As depicted in Figure 2.24, the MALDI-TOF mass spectra showed solely the peaks of the molecular ions of the dendrimers. In addition, the HRMS spectra of **PYCAPBD** exhibited clear isotope patterns of its molecular ion, which was consistent with the calculated result. Therefore, the desired dendrimers were synthesized.

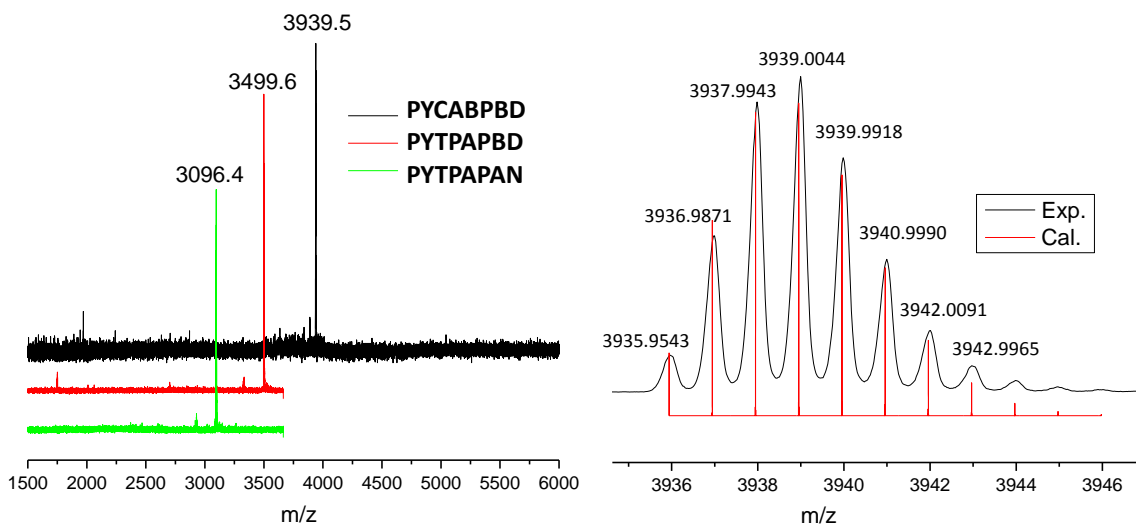


Figure 2.24: MALDI-TOF spectra of **PYCABPBD**, **PYTPAPBD** and **PYTPAPAN** (left) and HRMS spectra of **PYCABPBD** (right).

2.3.3 Photophysical properties

As depicted in Figure 2.25, the absorption of these dendrimers generally displayed two absorption bands. One at UV region, with characteristic shape and intense absorbance was attributed to the energy transitions of **PCs** and polyphenylenes.^[2] For example, there were two peaks in this area for **PYCABPBD**, a sharp one at 299 nm which was characteristic for **CABs** absorption as mentioned before, and another broad one centered at 319 nm which was in good agreement with the absorption of **PBDs** similar as that of **PYPBD**. The other much smaller band centered at 392 nm was due to the π - π^* transitions of the core.^[2, 17] The values of the extinction coefficients for the intense bands were the results of contributions of the two kinds of surface chromophores in the dendrimers. But for the small band, they were almost the same ($\sim 5.6 \times 10^4 \text{ Lmol}^{-1} \text{ cm}^{-1}$) because all three dendrimers had the same core. Going to thin films, the absorptions were very similar as those in solutions (Table 2.8).

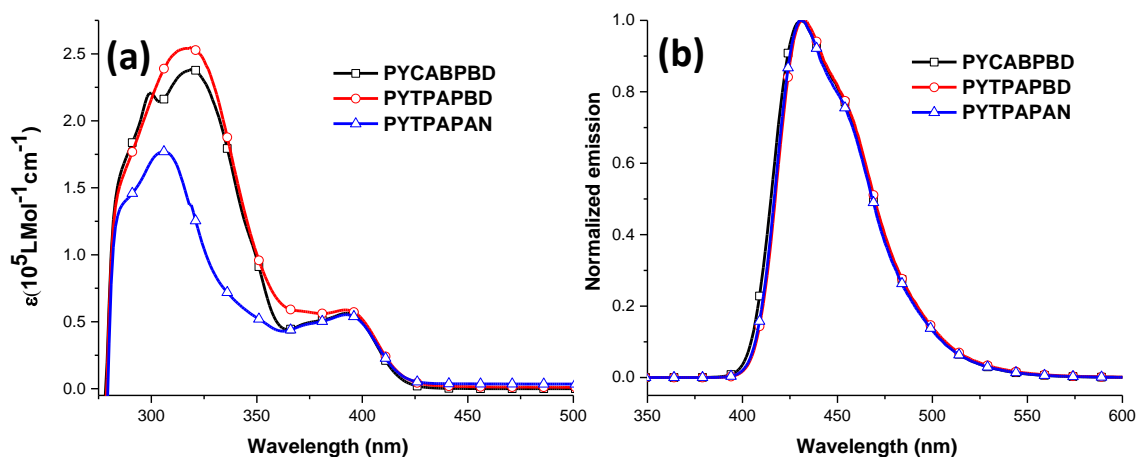


Figure 2.25: UV-vis absorption (a) and Photoluminescence spectra (b, excited at 319 nm for **PYCABPBD** and **PYTPAPBD**, 306 nm for **PYTPAPAN**) spectra of **PYPPDs** (10^{-5} M , toluene).

Table 2.8: Photophysical and electrochemical properties of bipolar **PYPPDs**.

	$\lambda_{ab}(\text{nm})$		$\lambda_{em}(\text{nm})$		PLQY ^{a)}		HOMO (eV) ^{b)}	LUMO (eV) ^{b)}	E_g (eV) ^{c)}
	Sol	Film	Sol	Film	Excitation				
					Surface	Core			
PYCABPBD	299,319, 392	300,316,391	431	446	0.80	0.93	-5.52	-2.45	2.95
PYTPAPBD	319, 392	313, 393	432	440	0.59	0.85	-5.34	-2.44	2.95
PYTPAPAN	306, 392	261,306,397	431	449, 469	--	--	-5.36	-2.41	2.95

^{a)} Measured in THF solution with quinine sulfate in 0.5 M H₂SO₄ solution as the standard; ^{b)} calculated from CV by comparing the first redox onset of **PYPPDs** and the oxidation onset of ferrocene; ^{c)} calculated from the absorption edge of the longest wavelength band.

Regarding the emission of these dendrimers in solutions, as depicted in Figure 2.25, they were almost the same with a peak emission centered at 432 nm and a little shoulder at around 455 nm. This was characteristic emission of the core. In addition, when excited at the surface chromophores, only the emissions from the core were observed, suggesting a surface-to-core energy transfer. The PLQYs were measured using quinine sulfate as the reference and very high quantum yields were obtained. For example, the PLQY of **PYCABPBD** reached 0.93 when excited at the core and it was still very high (0.80) when excited at the surface. The high PLQYs of these dendrimers either excited at the core or the surface together with the emission merely from the core demonstrated that there exists efficient surface-to-core energy transfer in these dendrimers. The thin-film emission spectra revealed some bathochromic shift compared with the solutions for all three dendrimers (Table 2.8), probably due to insufficient protection of the core by the dendrons in first-generation dendrimers.

2.3.4 Electrochemistry

CV was used to explore the oxidation and reduction properties of these dendrimers. As depicted in Figure 2.26, the CV curves of these dendrimers showed both the redox of the **PCs** and the core. Similar as other **PYPPDs**, the oxidation wave of the core was observed with the peak potential at around 1.1 V (vs. Ag/Ag⁺) as shown for **PYTPAPBD** and **PYTPAPAN**. For **PYCABPBD**, the oxidation of the core coincided with the oxidation wave of carbazoles due to their very close oxidation potentials, similar as **PYCAB** mentioned before. The reduction of the core occurred at around -1.8 V (vs. Ag/Ag⁺), which was seen for all three dendrimers. This potential was used to calculate the LUMO level of these dendrimers by comparing with the oxidation potential of ferrocene. The LUMO levels were all at around -2.4 eV (Table 2.8), considering the measurement errors. In addition, the reduction curves of the surface chromophores, i.e. **CAB**, **PBD**, and **PAN** were identified as well. For example, in the reduction curve of **PYTPAPBD**, besides the reduction of the core, there was a strong reduction wave at lower potential. This was the reduction of **PBD**. For **PYTPAPAN**, the reduction curve exhibited multiple reduction

processes due to the phenanthrene moieties. In addition, the oxidation waves of **TPAs** and **CABs** representing the major oxidation processes of **PYTPAPBD** and **PYCABPBD** were used to calculate the HOMOs of the dendrimers (Table 2.8). The HOMO of **PYCABPBD** was consistent with that of **PYCAB** and also the HOMOs of **PYTPAPBD** and **PYTPAPAN** was almost the same as that of **PYTPA**. Consequently, the redox of the surface chromophores and the core all resembled those of their counterparts of **PYPPDs** with solely one kind of **PCs**, indicating that the bipolar-surface **PYPPDs** should have the abilities to transport both holes and electrons in devices.

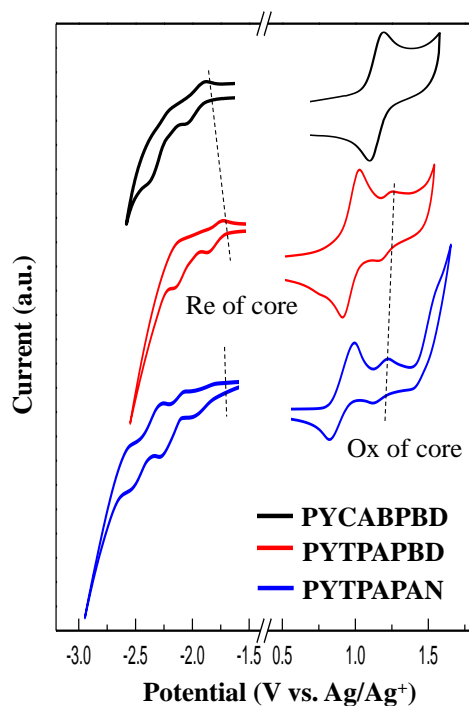


Figure 2.26: CV curves of the redox of bipolar **PYPPDs**.

From the photophysical and electrochemical properties of these dendrimers, all dendrimers showed very high PLQYs with efficient surface-to-core energy transfers and the surface chromophores displayed almost identical redox properties as their counterparts in **PYTPA** and **PYCAB**. As a result, these dendrimers hold promise for **OLED** applications.

2.3.5 Device performances

PYCABPBD were tested in single-, two- and three-layer devices. As was shown in Table 2.9, the current efficiency and luminance in single-layer device were quite low and it had a pure blue emission.

Table 2.9: Device performance of bipolar **PYPPDs**.

	$V_{on}(V)$	$\eta(\text{cd/A})$	$L_{max}(\text{cd/m}^2)$	CIE (x, y)
PYCABPBD	4	0.048	388	0.159, 0.104 ^{a)}
	5.5	0.13	1866	0.164, 0.121 ^{b)}
	4.4	0.21	2701	0.163, 0.121 ^{c)}
PYTPAPBD	4.8	0.02	203	0.198, 0.185 ^{b)}
PYTPAPAN	3.9	0.03	303	0.154, 0.096 ^{b)}

Device structure: ^{a)}ITO/PEDOT:PSS/**PYPPD**/Ca/Al; ^{b)}ITO/PEDOT:PSS/TFB/**PYPPD**/Ca/Al;

^{c)}ITO/PEDOT:PSS/TFB/**PYPPD**/PEGPF/Ca/Al

After introducing a TFB layer, a much better performance was achieved with the highest current efficiency of 0.13 cd/A and luminance of 1866 cd/m^2 due to a better charge confinement in the emitting layer with the help of TFB. In a three-layer device with a PEGPF layer added, the device performance was further enhanced. The current efficiency reached 0.21 cd/A and the luminance was as high as 2700 cd/m^2 due to the enhanced charge injection and better charge confinement within the emitting layer with the help of both hole and electron transporting layers. In addition, the CIE coordinate in a three-layer device was identical to the two-layer device. In general, the emission in two- and three-layer devices both came from the core of the dendrimer. This could be postulated from their emission spectra that all three devices showed peak emission at 444 nm, nearly the same as the emission wavelength of **PYCABPBD** thin film (446 nm).

Accordingly, the performance of **PYCABPBD** in three-layer device is comparable with **PYPAN** in the same device structure (see the last section) and no significant improvement was achieved by this bipolar periphery design. One reason might be that the hole-electron recombination in **PYCABPBD** was not effective, which was elucidated by its very high current density comparing with some more efficient emitters, e.g. **PYNPA** (Figure 2.27).

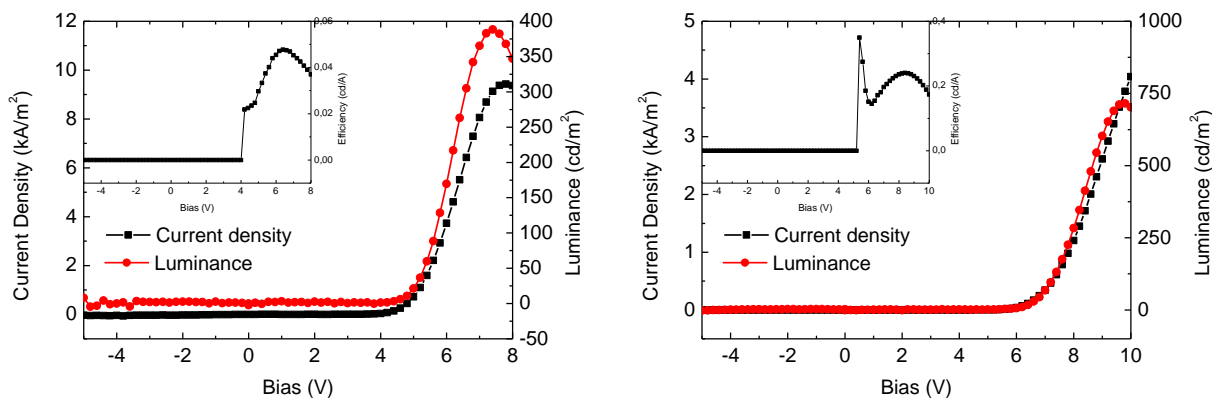


Figure 2.27: Voltage-current-luminance characteristics of **PYCABPBD** (left) and **PYNPA** (right) in single-layer device.

For example, the device of **PYCABPBD** had a current density of around 9 KA/m^2 at 8 V but for **PYNPA**, it was only around 1 KA/m^2 at the same potential, indicating that the charge transport in **PYCABPBD**-based device was much stronger than for the **PYNPA**-based device due to the enhanced both hole and electron injection ability in the former. While comparing their current efficiencies, it was postulated that holes and electrons were transported through the device but did not recombine effectively. One possible reason is that holes transport through **CABs** and electrons transport through **PBDs** and the possibility of charge recombination are lower than those of **PYNPA** in which **NPA** by itself transports both holes and electrons.

PYTPAPBD and **PYTPAPAN** were only tested in a two-layer device. The results suggested that their current efficiencies and luminance were both lower than those of **PYCABPBD** and as a result, they were not further optimized in devices.

2.4 Summary

In this chapter, **PYPPDs** with different **PCs** were readily synthesized by Suzuki and Buchwald-Hartwig couplings and [4+2] Diels–Alder reaction. Bipolar **PYPPDs** with two kinds of **PCs** were prepared with the help of a new iodo-bromo-functionalized **CP**.

All the **PYPPDs** had good solubilities in organic solvents, e.g. DCM, THF and toluene which made them characterized by ^1H and ^{13}C NMR spectroscopy, MALDI-TOF mass spectrometry, UV-vis absorption, photoluminescence spectroscopy and cyclic voltammetry. Their photophysical properties indicated that efficient surface-to-core energy transfers occurred with pure core emission. This effect was more pronounced in the first-generation dendrimers. In addition, the CV results revealed that there were little conjugation effects between the core and **PCs** due to the highly-twisted biphenyls in between so that both surface chromophores and the core could play their roles in devices.

The device performances demonstrated that judicious tuning the **PCs** was important to improve the device performances in that careful selection of **PCs** could reduce the charge injection barriers and ensure efficient surface-to-core energy transfer. Among all **PYPPDs**, **PYCAB** could reach a current efficiency of 0.52 cd/A which is the highest value obtained so far. This is due to the fact that **CABs** of **PYCAB** worked as both hole and electron transporting moieties in the selected device.

In addition, **PYPPA** in a three-layer device could reach a deep blue emission with $\text{CIE}_y (< 0.1)$ and current efficiency of 0.24 cd/A , probably due to the emission from both **PPAs** and the core.

For bipolar **PYPPDs**, no considerable device improvements were achieved compared with the other **PYPPDs**, probably due to the less effective hole-electron recombination in these bipolar dendrimers in that holes transported among donor moieties and electrons transported through the acceptor moieties and

there were less chances for them to meet with each other than **PYPPDs** with one kind of **PCs**, e.g. **NPA** which transported both holes and electrons.

Literature

- [1] T. S. Qin, W. Wiedemair, S. Nau, R. Trattnig, S. Sax, S. Winkler, A. Vollmer, N. Koch, M. Baumgarten, E. J. W. List, K. Mullen, *J Am Chem Soc* **2011**, *133*, 1301-1303.
- [2] S. Bernhardt, M. Kastler, V. Enkelmann, M. Baumgarten, K. Mullen, *Chem-Eur J* **2006**, *12*, 6117-6128.
- [3] Z. Fang, V. Chellappan, R. D. Webster, L. Ke, T. F. Zhang, B. Liu, Y. H. Lai, *J Mater Chem* **2012**, *22*, 15397-15404.
- [4] M. R. Zhu, J. H. Zou, X. He, C. L. Yang, H. B. Wu, C. Zhong, J. G. Qin, Y. Cao, *Chem Mater* **2012**, *24*, 174-180.
- [5] W. L. Jia, T. McCormick, Q. D. Liu, H. Fukutani, M. Motala, R. Y. Wang, Y. Tao, S. N. Wang, *J Mater Chem* **2004**, *14*, 3344-3350.
- [6] Y. J. Xing, X. J. Xu, P. Zhang, W. J. Tian, G. Yu, P. Lu, Y. Q. Liu, D. B. Zhu, *Chem Phys Lett* **2005**, *408*, 169-173.
- [7] R. Trattnig, L. Pevzner, M. Jager, R. Schlesinger, M. V. Nardi, G. Ligorio, C. Christodoulou, N. Koch, M. Baumgarten, K. Mullen, E. J. W. List, *Adv Funct Mater* **2013**, *23*, 4897-4905.
- [8] S. A. Choulis, V. E. Choong, A. Patwardhan, M. K. Mathai, F. So, *Adv Funct Mater* **2006**, *16*, 1075-1080.
- [9] a) C. Y. Chi, G. Wegner, *Macromol Rapid Comm* **2005**, *26*, 1532-1537; b) D. Neher, *Macromol Rapid Comm* **2001**, *22*, 1366-1385.
- [10] a) Y. Shirota, H. Kageyama, *Chem Rev* **2007**, *107*, 953-1010; b) G. Hughes, M. R. Bryce, *J Mater Chem* **2005**, *15*, 94-107.
- [11] a) H. Ogawa, R. Okuda, Y. Shirota, *Appl Phys a-Mater* **1998**, *67*, 599-602; b) A. P. Kulkarni, X. X. Kong, S. A. Jenekhe, *Adv Funct Mater* **2006**, *16*, 1057-1066.
- [12] a) K. L. Tong, S. K. So, H. F. Ng, L. M. Leung, M. Y. Yeung, C. F. Lo, *Synthetic Met* **2004**, *147*, 199-203; b) Z. Q. Gao, C. S. Lee, I. Bello, S. T. Lee, R. M. Chen, T. Y. Luh, J. Shi, C. W. Tang, *Appl Phys Lett* **1999**, *74*, 865-867.
- [13] a) S. Janietz, A. Wedel, *Adv Mater* **1997**, *9*, 403-&; b) Y. Cao, I. D. Parker, G. Yu, C. Zhang, A. J. Heeger, *Nature* **1999**, *397*, 414-417; c) C. Adachi, T. Tsutsui, S. Saito, *Appl Phys Lett* **1989**, *55*, 1489-1491; dS. Hoshino, K. Ebata, K. Furukawa, *J Appl Phys* **2000**, *87*, 1968-1973.
- [14] W. R. Dawson, M. W. Windsor, *J Phys Chem-Us* **1968**, *72*, 3251-&.
- [15] S. Tang, W. J. Li, F. Z. Shen, D. D. Liu, B. Yang, Y. G. Ma, *J Mater Chem* **2012**, *22*, 4401-4408.
- [16] a) J. Q. Ding, B. H. Zhang, J. H. Lu, Z. Y. Xie, L. X. Wang, X. B. Jing, F. S. Wang, *Adv Mater* **2009**, *21*, 4983-+; b) M. Berggren, A. Dodabalapur, R. E. Slusher, Z. Bao, *Nature* **1997**, *389*, 466-469; c) S. R. Pujari, P. N. Bhosale, P. M. R. Rao, S. R. Patil, *Mater Res Bull* **2002**, *37*, 439-448.
- [17] a) T. Oyamada, S. Akiyama, M. Yahiro, M. Saigou, M. Shiro, H. Sasabe, C. Adachi, *Chem Phys Lett* **2006**, *421*, 295-299; b) T. Oyamada, H. Uchiuzou, S. Akiyama, Y. Oku, N. Shimoji, K. Matsushige, H. Sasabe, C. Adachi, *J Appl Phys* **2005**, *98*.
- [18] a) M. X. Yu, M. J. Wang, X. H. Chen, B. B. Hong, X. Y. Zhang, C. H. Cheng, *J Chem Res-S* **2005**, 558-560; b) M. Osawa, M. Hoshino, T. Wada, Y. Araki, O. Ito, *Chem Phys Lett* **2006**, *427*, 338-342.
- [19] J. S. Huang, Z. Xu, Y. Yang, *Adv Funct Mater* **2007**, *17*, 1966-1973.
- [20] X. H. Yang, D. Neher, D. Hertel, T. K. Daubler, *Adv Mater* **2004**, *16*, 161-+.
- [21] a) C. H. Chien, C. K. Chen, F. M. Hsu, C. F. Shu, P. T. Chou, C. H. Lai, *Adv Funct Mater* **2009**, *19*, 560-566; b) K. Wang, F. C. Zhao, C. G. Wang, S. Y. Chen, D. Chen, H. Y. Zhang, Y. Liu, D. G. Ma, Y. Wang, *Adv Funct Mater* **2013**, *23*, 2672-2680.
- [22] a) A. Orita, K. Miyamoto, M. Nakashima, F. Ye, J. Otera, *Adv Synth Catal* **2004**, *346*, 767-776; b) A. Orita, H. Taniguchi, J. Otera, *Chem-Asian J* **2006**, *1*, 430-437.
- [23] F. Emmerling, I. Orgzall, B. Dietzel, B. Schulz, J. Larrucea, *J Mol Struct* **2012**, *1030*, 209-215.

Chapter 3 Iridium-Complex-Based Polyphenylene Dendrimers as Phosphorescent Emitters

In this chapter, several new Ir-complex-based small molecules and polyphenylene dendrimers will be described and discussed. The first part involves the synthesis of **(dfppy)₃Ir**-based monomers and dendrimers. As depicted in Figure 3.1, carbazoles were incorporated into the surface of the dendrimer to reduce the charge injection barrier and function as energy transfer moieties to the core. The second part is about the synthesis of 1,3-diphenyl-benzoimidazole-carbene-chelated iridium complex (**(dpbic)₃Ir**)-based monomers and dendrimers. **(dpbic)₃Ir** by itself is a violet blue emitter. With the attachments of polyphenylene dendrons outside, the new dendrimer might emit pure blue due to the conjugation effects between the core and the dendrons. Therefore, the other target molecule is **fac(dpbic)₃Ir-CAB-G1** (Figure 3.1). Their structural characterizations and photophysical properties will be discussed in detail.

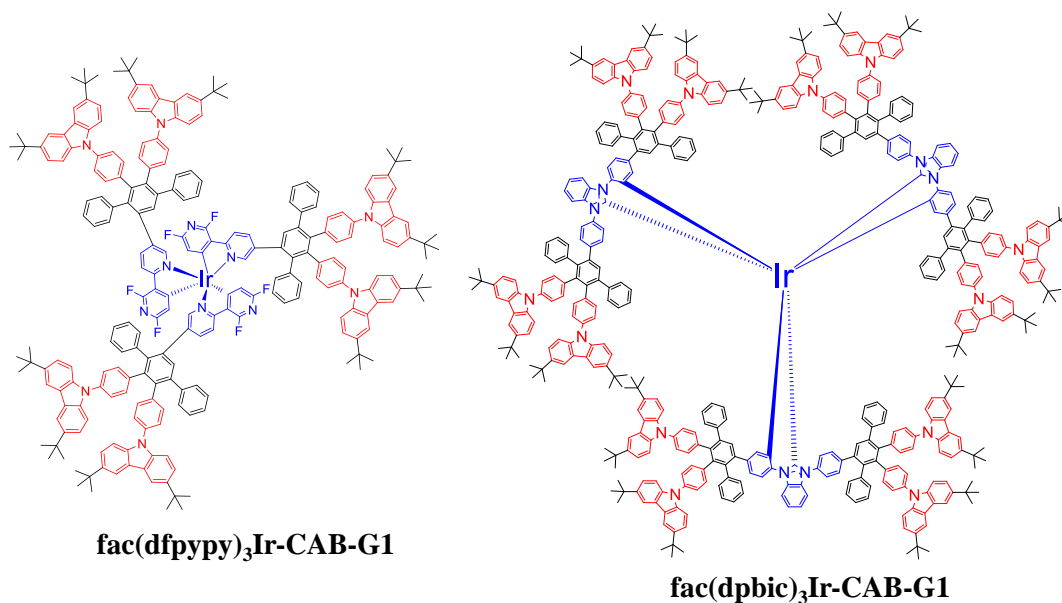


Figure 3.1: Target polyphenylene dendrimers as potential blue phosphorescent emitters.

3.1 Synthesis of **(dfppy)₃Ir**-based materials

The synthesis of a homoleptic Ir-complex generally can be divided into two pathways (Figure 3.2).^[1] The most easy way is a one-step reaction between the ligands (C[^]N) and Ir[(acac)₃] (acac=acetylacetonate) by refluxing them in ethylene glycol or glycerol.^[2] Another way involves two-step reactions. First, the ligands (C[^]N) are reacted with iridium trichloride in 2-ethoxyethanol under reflux to form the chloride-bridged Ir-complex dimer.^[2d, 3] This dimer can be separated by filtration or a silica-gel flash column. Then, it reacts with one equivalent of the ligand in a basic solution upon heating to form the homoleptic Ir-complex.^[2d, 4] The resulting Ir-complex adopts an octahedral geometry and usually consists of a

mixture of two configurations, i.e. the facial and meridional one.^[2d, 5] The two isomers can be separated by column chromatography method upon careful selection of the eluting solvent. The facial one has a symmetry of C₃, while the meridional one possesses C₁ symmetry (Figure 3.2). In addition, there are apparent differences between facial and meridional isomers in their photophysical properties. Frequently, the meridional one shows a bathochromic shift in emission and lower PLQY as compared with the facial one.^[2d, 5a] But it was also reported that both isomers could have comparable PLQYs and the emission of meridional one was hypsochromically shifted in comparison with the facial one.^[5b] The reason for their difference in photophysical properties is largely dependent on the structure-change-induced excited state energy changes which determine the emission and PLQY.^[5] Moreover, the meridional one can be easily transformed into the facial isomer by UV-light irradiation because the latter one is thought as the more thermally stable state and the former is the kinetically favorable product.^[2d, 6]

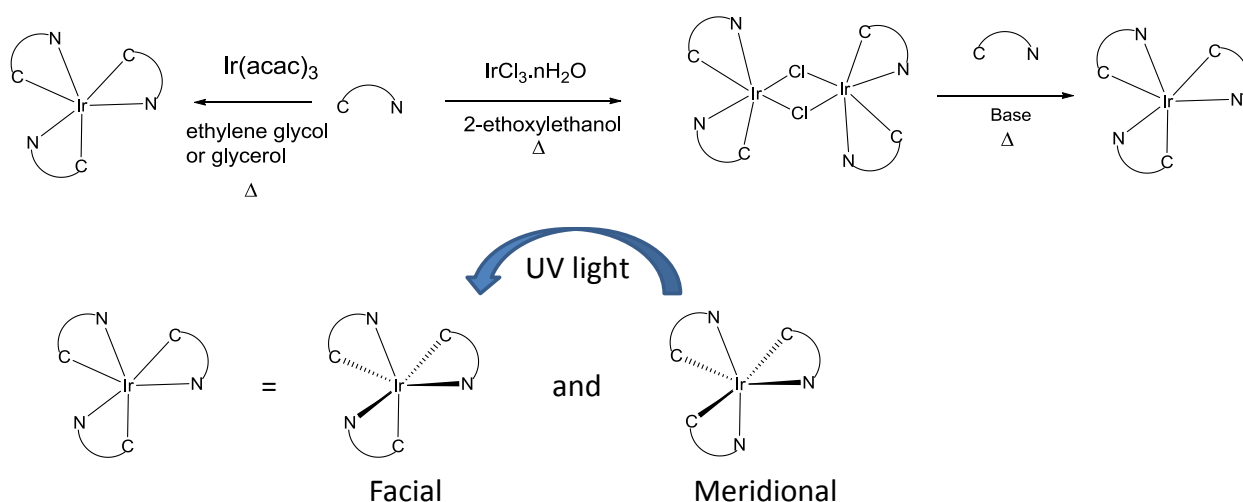
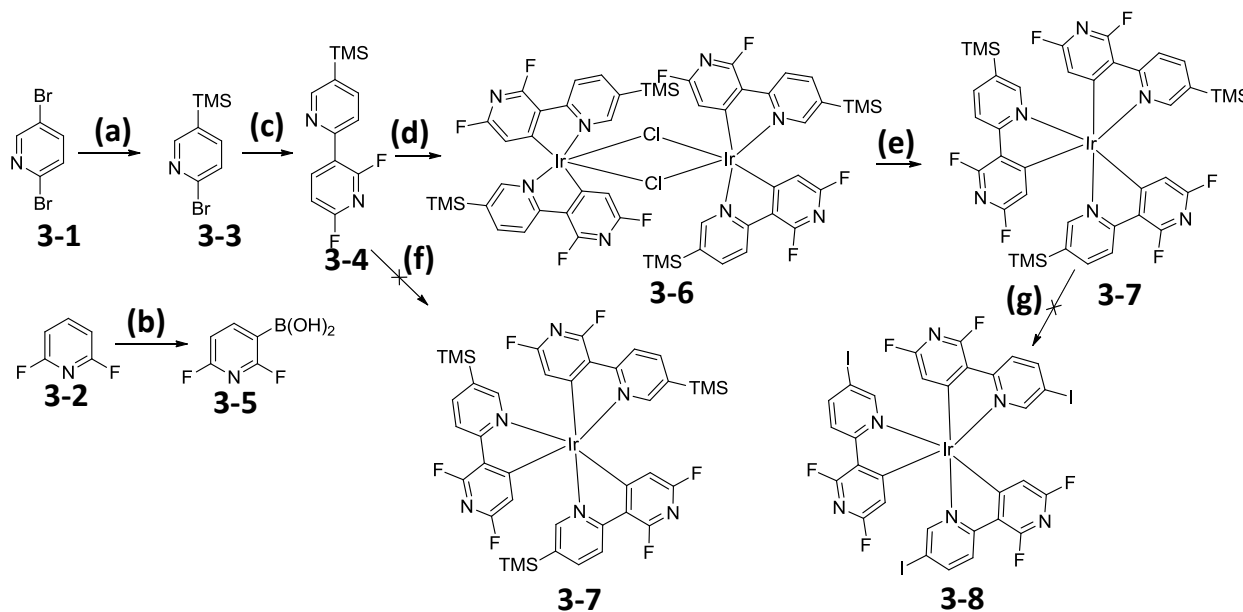


Figure 3.2: Synthetic pathways for Ir(C^N)₃.

3.1.1 Synthesis of Ir-complex monomers

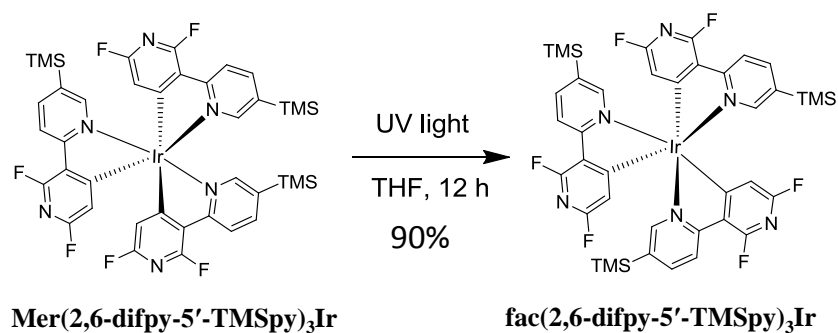
As an initial attempt, a trimethylsilyl (TMS)-functionalized Ir-complex was proposed because similar molecules have appeared in a patent^[7] and the TMS groups could be transferred into iodine atom later on by a single-step reaction.^[8] Thus a new synthetic route was designed (Scheme 3.1). In this instance, 2-bromo-5-trimethylsilylpyridine (**3-3**) was first synthesized from 2,5-dibromo-pyridine (**3-1**) by n-BuLi and trimethylsilylchloride (TMSCl) in high yield (82%). Then it was reacted with 2,6-difluoropyridinyl-3-boronic acid (**3-5**) which was prepared from commercially available 2,6-difluoropyridine(**3-2**) to form the bipyridine ligand (**3-4**) by a Suzuki coupling in moderate yield (50%). After that, the one-step pathway to make the Ir-complex was tried but it did not work. As a result, the two-step method was carried out by refluxing the ligands (**3-4**) and IrCl₃ in 2-ethoxyethanol overnight and finally the dimer (**3-6**) was separated successfully as a yellow-colored solid in 48% yield after filtration and drying under vacuum. For the second step, a special base system was selected from the literature.^[4] It was a mixture

of silver trifluoromethanesulfonate (AgSO_3CF_3) and potassium carbonate. After heating the system at $170\text{ }^\circ\text{C}$ for 24 hours, a yellow-colored solid (**3-7**) in 53% yield was received after purification by silica gel flash column and drying. It was then tried to replace the TMS group by an iodine atom but the reaction did not work.



Scheme 3.1: Synthetic routes for TMS-functionalized (**dfppy**)₃Ir. (a) (1) *n*-BuLi, Et₂O, $-78\text{ }^\circ\text{C}$, 1 h, (2) TMSCl, r.t, 12 h, 82%; (b) (1) isopropylamine, THF, *n*-BuLi, $0\text{ }^\circ\text{C}$, 30 min for making fresh LDA, (2) LDA, THF, $-78\text{ }^\circ\text{C}$, 1 h, (3) triisopropylborate, rt, 12h, 1M HCl (aq), 100%; (c) compound **3-5**, Pd(PPh₃)₄, K₂CO₃, THF, water, $85\text{ }^\circ\text{C}$, 24 h, 50%; (d) IrCl₃·*n*H₂O, 2-ethoxyethanol, $140\text{ }^\circ\text{C}$, 24 h, 48%; (e) compound **3-4**, AgSO₃CF₃, K₂CO₃, mesitylene, $170\text{ }^\circ\text{C}$, 24 h, 53%; (f) Ir(acac)₃, ethylene glycol, $200\text{ }^\circ\text{C}$; (g) ICl, CCl₄, $80\text{ }^\circ\text{C}$, 12 h.

The separated TMS-functionalized Ir-complex (**2,6-difpy-5'-TMSpy**)₃Ir was proven to be meridional. It was confirmed with the ¹H and ¹⁹F NMR spectra (Figure 3.3) and single crystal structure (Figure 3.4). The facial isomer was easily synthesized from the meridional one by photochemistry and after purification by a silica-gel flash column and a bright-yellow-colored solid was received in 90% yield (Scheme 3.2). The facial isomer was also identified from ¹H and ¹⁹F NMR spectra (Figure 3.3) and single crystal structure (Figure 3.4).



Scheme 3.2: Photochemistry-promoted transformation of **mer(2,6-difpy-5'-TMSpy)₃Ir** into facial one.

As depicted in Figure 3.3, from the NMRs, it is easy to distinguish these two isomers. Clearly, there are many more peaks in the ^1H and ^{19}F NMR spectra of the meridional isomer than of the facial one. Due to the C_1 symmetry configuration of the former, all the protons in that molecule are not magnetically equivalent. As a result, there appear many peaks with the relative intensity of one. The same situation applies to fluorine atoms. As there are totally six fluorine atoms in one molecule, there appear totally six peaks in ^{19}F NMR spectra of **mer(2,6-difpy-5'-TMSpy)₃Ir**. For **fac(2,6-difpy-5'-TMSpy)₃Ir**, however, due to its C_3 symmetry, each ligand is magnetically equivalent. Thus, the ^1H and ^{19}F NMR spectra are simpler and the total number of resonances is equivalent to the total number of non-equivalent proton or fluorine atoms of a single ligand. As a result, there exist only 4 aromatic proton signals which correspond to the specific protons based on the splitting and coupling interactions and one single peak at around 0.05 ppm from TMS. In addition, there are only two peaks detected in the ^{19}F NMR spectra of the facial one.

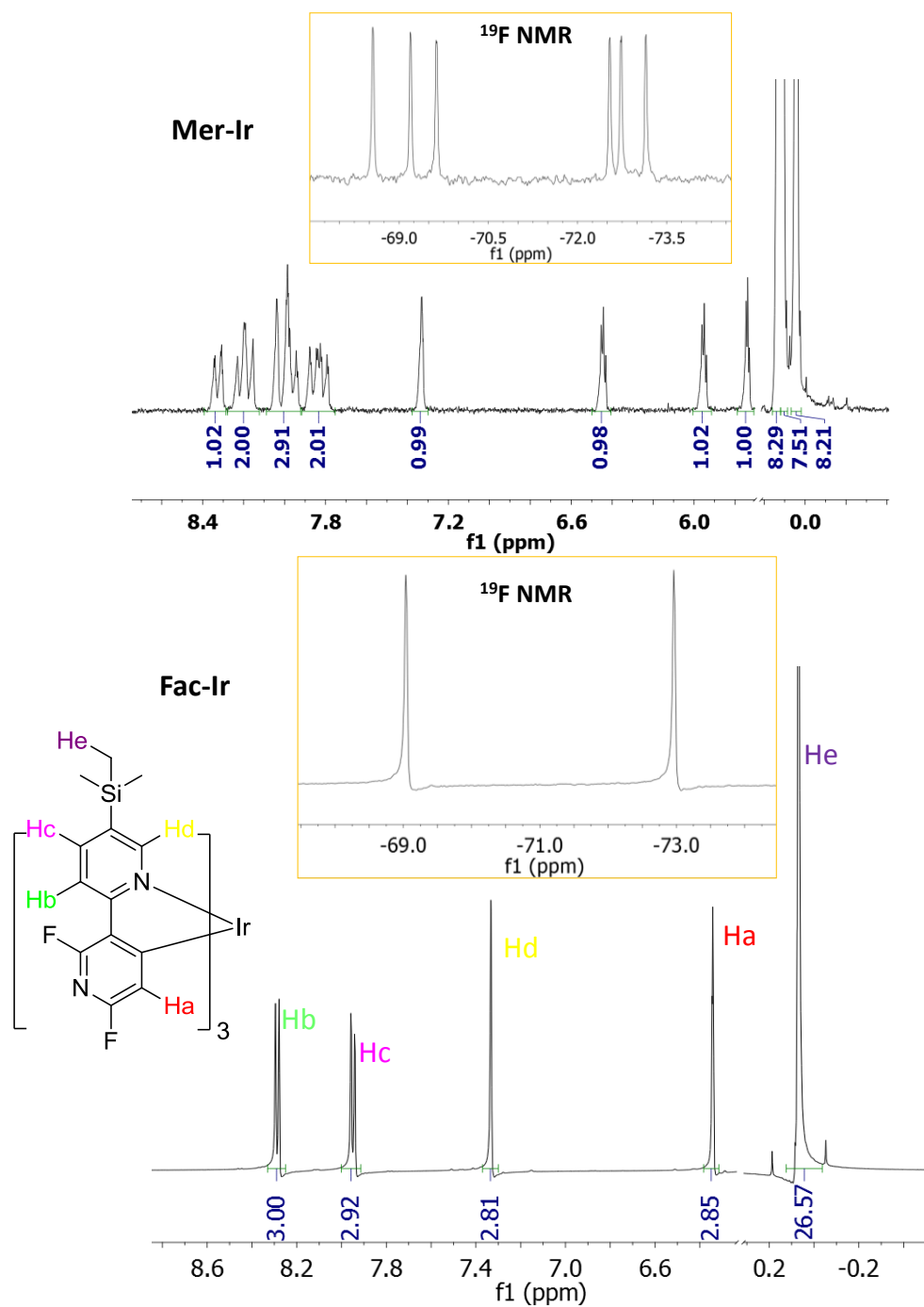


Figure 3.3: ^1H NMR and ^{19}F NMR (inset) spectra of **mer(2,6-difpy-5'-TMSpy) $_3$ Ir** (top) and **fac(2,6-difpy-5'-TMSpy) $_3$ Ir** (bottom) (solvent: CD_2Cl_2).

The single crystals of these two isomers were successfully grown by two-phase slow dispersion and evaporation between DCM and methanol. They both appeared as long needles. Their single crystal structures were extracted using a single-crystal X-ray diffraction method by Dr. Dieter Schollmeyer in University of Mainz. As depicted in Figure 3.4, the two structures were different in that the N_1 and Si_1 atoms were downward in the facial one but they were upward in the meridonal one viewing at the same direction. Referring to the bond lengths of Ir-N and Ir-C bonds (Table 3.1), the facial configuration had nearly identical bond lengths for three Ir-N bonds (~ 2.12 Å, bond length difference ≤ 0.008 Å) and also

three Ir-C bonds ($\sim 2.00\text{\AA}$, bond difference $\leq 0.005\text{\AA}$). This is consistent with the C3 symmetry of the isomer. For the meridional one, however, the bond length of Ir-N2 was notably larger than the other two Ir-N bonds (bond length difference: $\sim 0.1\text{\AA}$). For the Ir-C bonds of the meridional isomer, all three bonds exhibited a notable difference in bond lengths in contrast to the facial one. The discrepancy in the bond lengths of meridional isomer further confirms the C1 symmetry of this configuration. In addition, the markedly longer bond lengths of Ir-N2 and Ir-C2 in the meridional one suggest that this geometry is not the thermally stable one and these bonds might break and reorganize to form the thermally stable isomer under external energy. This is consistent with the successful meridional-to-facial transformation by photochemistry.

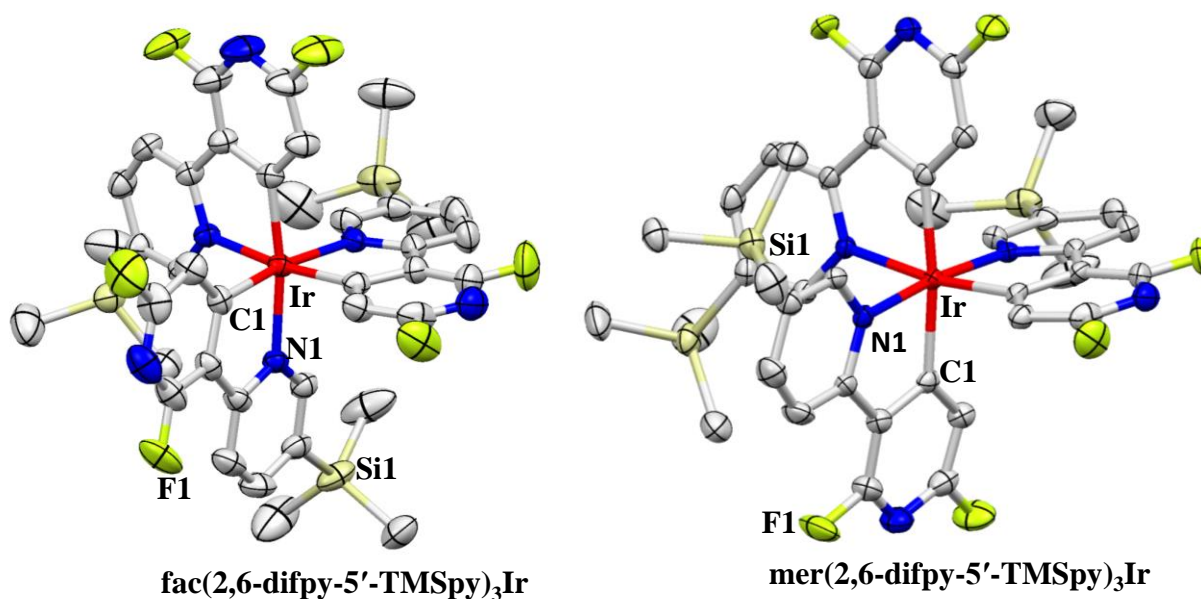


Figure 3.4: Structure views of **fac-** and **mer(2,6-difpy-5'-TMSpy)₃Ir** with ellipsoids at 50% probability (proton atoms were hidden for clarity).

Table 3.1: Selected bond lengths (\AA) of **fac-** and **mer(2,6-difpy-5'-TMSpy)₃Ir**.

	Fac-Ir	Mer-Ir
Ir-N1	2.128	2.070
Ir-N2	2.126	2.161
Ir-N3	2.120	2.060
Ir-C1	2.000	2.076
Ir-C2	2.005	2.089
Ir-C3	2.000	2.006

3.1.2 Photophysical properties of Ir-complex monomers

The UV-vis absorption and photoluminescence performances of these two isomers were investigated (Figure 3.5). From the absorption spectra, both the isomers exhibited strong absorption in the ultraviolet region between 250-350 nm which were due to the ligand-based $\pi-\pi^*$ transitions. The relatively weak bands between 350-400 nm were attributed to the metal-to-ligand charge transfer (MLCT).^[2a, 2d]

Compared with the meridional isomer, the facial one exhibited finer structures in the absorption spectra. In the photoluminescence spectra, the emission of the facial isomer was hypsochromically shifted by around 5 nm compared with the meridional one. In addition, the emission intensity of the facial isomer was much stronger than that of the meridional one (around 2 times), measured under the same condition. This further confirmed that the facial configuration of the Ir-complex was probably better for blue **OLED** applications based on the color purity and emission intensity. Moreover, both emissions displayed fine structures with two major peaks in the blue color region and a little shoulder in the green color area (> 500 nm). For the facial isomer, the two peaks were at 445 nm and 472 nm respectively. They were around 7 nm bathochromically-shifted compared with the reported **Ir(dfppy)₃**,^[2a] probably due to the TMS groups' electron donating effects which slightly reduced the energy gap of the Ir-complex.

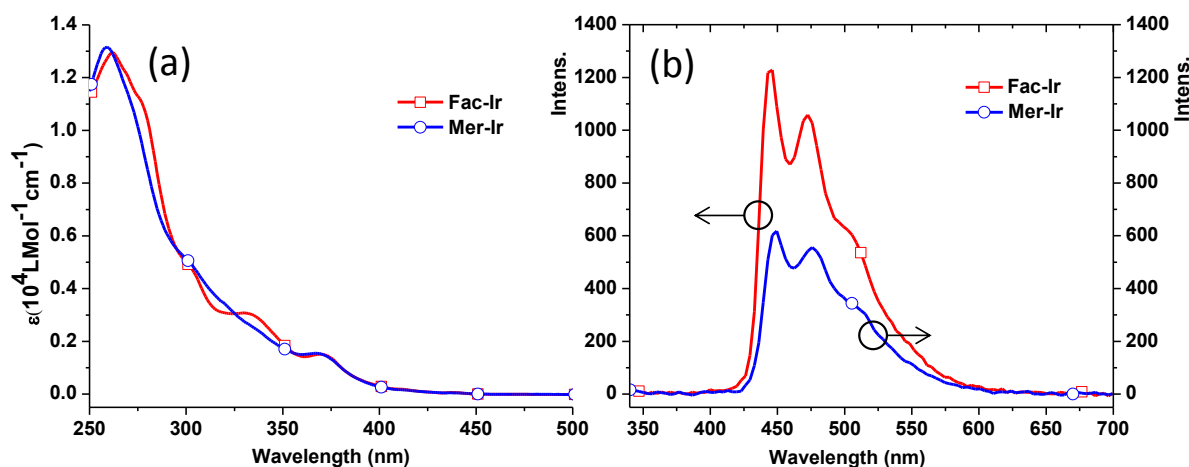


Figure 3.5: UV-vis absorption (a) and photoluminescence spectra (b) of facial and meridional **(2,6-difpy-5'-TMSpy)₃Ir** in 10^{-4} M DCM solution (excited at 330 nm).

3.1.3 Electrochemistry of Ir-complex monomers

The oxidation curves of the facial and meridional **(2,6-difpy-5'-TMSpy)₃Ir** were scanned by cyclic voltammetry with the standard one-component and three-electrodes setup. As depicted in Figure 3.6, both the facial and meridional species started to be oxidized at nearly identical potentials (oxidation onset: 1.23 V and 1.21 V respectively, versus ferrocene). As a result, the HOMO levels of them were deduced to be -6.01 and -6.03 eV respectively, supposing that the HOMO of ferrocene in the vacuum level is at -4.8 eV. In addition, their CV exhibited two oxidation processes and both were not reversible, indicating that their radical cations were not stable.

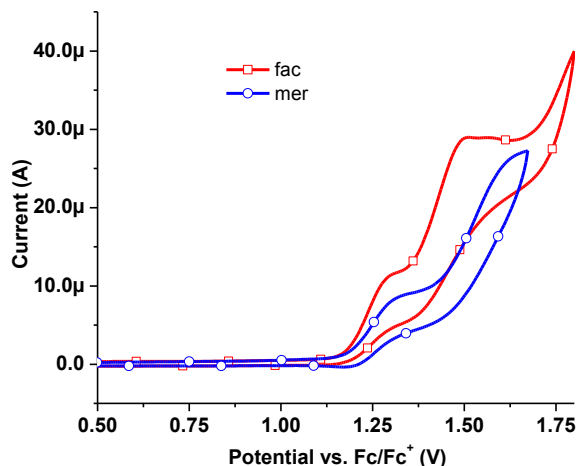
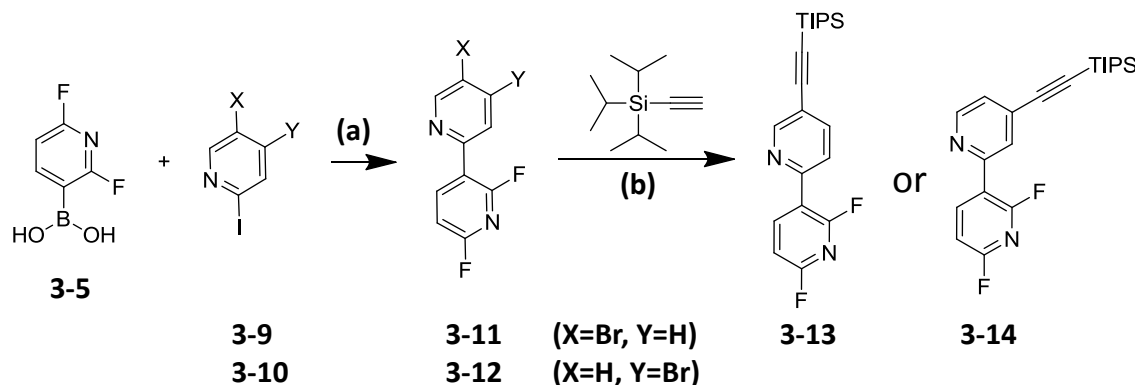


Figure 3.6: CV curves of the oxidation of **fac**- and **mer**(2,6-difpy-5'-TMSpy)₃Ir.

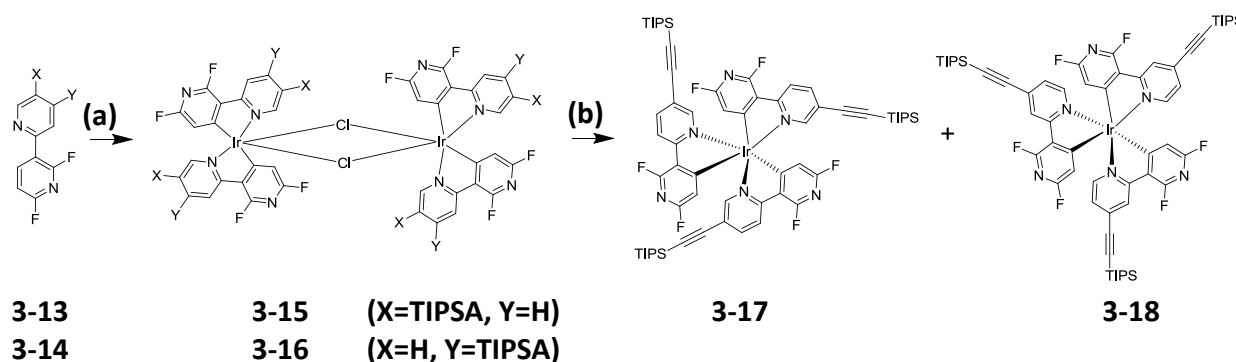
3.1.4 Synthesis of (dfppy)₃Ir -based polyphenylene dendrimers

With the successful synthesis of (2,6-difpy-5'-TMSpy)₃Ir (**3-7**), the preparation of (dfppy)₃Ir-based polyphenylene dendrimers also became possible. First of all, the ligand had to be produced. Due to the final Diels-Alder reaction, a triple bond must be introduced in the ligand. Finally, the TIPSE-functionalized ligands (**3-13**, **3-14**) were designed and made successfully (Scheme 3.3). The first step was to generate the bromo-functionalized bipyridine between 2,6-difluoro-pyridine-5-boronic acid (**3-5**) and 2-iodo-4-bromopyridine (**3-10**) or 2-iodo-5-bromopyridine (**3-9**) by a Suzuki coupling in which the iodo position was reacted due to the much higher reactivity of iodine than bromine atom. The bromo-functionalized bipyridines (**3-11** and **3-12**) in this step were obtained in moderate yields (39% and 34%). Then compounds **3-11** and **3-12** reacted with (triisopropylsilyl)acetylene by a Sonogashira coupling to give birth to compound **3-13** and **3-14**, both of which were received in high yields after purifications (85% and 96%). The ligands were identified by ¹H and ¹³C NMR spectra and FD-mass results.



Scheme 3.3: Synthetic routes for TIPSE-functionalized difluorobipyridine ligands. (a) Pd(PPh₃)₄, K₂CO₃, THF, water, 80 °C, 24 h, 39% for **3-11**, 34% for **3-12**; (b) Pd(PPh₃)₂Cl₂, PPh₃, CuI, triethylamine, (triisopropylsilyl)acetylene, 80 °C, 24 h, 85% for **3-13** and 96% for **3-14**.

With the ligands ready, the next step was to synthesize the Ir-complexes and the dendrimers. As displayed in Scheme 3.4, first, the ligands reacted with $\text{IrCl}_3 \cdot n\text{H}_2\text{O}$ in 2-ethoxyethanol under reflux to give the chloride-bridged Ir-complex dimers (**3-15** and **3-16**) in moderate yields (57% and 24%). These dimers were processed via precipitation by adding water and then filtration to get yellow-brown-colored solids. They were not purified further and directly used for the next step. After that, TIPSE-functionalized Ir-complexes (**3-17** and **3-18**) were obtained by a reaction between the dimer and ligand under basic and high temperature conditions. This step only provided relatively low yields of products (25% and 20%). In addition, both Ir-complexes were found to be meridional isomers from their ^1H and ^{19}F NMR results (chapter 8).



Scheme 3.4: Synthetic routes for TIPSE-functionalized Ir-complex monomers. (a) $\text{IrCl}_3 \cdot n\text{H}_2\text{O}$, 2-ethoxyethanol, 140 °C, 24 h, 57% for **3-15**, 24% for **3-16**; (b) K_2CO_3 , AgSO_3CF_3 , 1,3,5-trimethylbenzene, 170 °C, 24 h, 25% for **3-17**, 20% for **3-18**.

The ^1H NMR spectra of the ligands and their Ir-complex exhibited some complicated proton couplings (Figure 3.7). The correlations between the signals in the spectra and the protons in the molecules were extracted with the help of the ^1H - ^1H COSY spectra and the splitting of each peaks. For example, the spectra of compound **3-11** displayed five well-resolved signals, representing 5 protons in that molecule. However, the protons (marked red and blue) showed complicated multiplets instead of simple doublets based on the first-order splitting rule.^[9] This was due to the ^1H - ^{19}F couplings.^[10] As there was a three-bond distance between proton Ha (marked red) and one fluorine atom, the proton-fluorine coupling effect was strong and the splitting of it was doublet-doublet with relatively large coupling constants. For proton Hb (marked blue), as its distance with the fluorine atom was relatively large, as a result, its splitting was a doublet-doublet with a small coupling constant for the second doublet. To match each proton with each signal was difficult from just splitting.

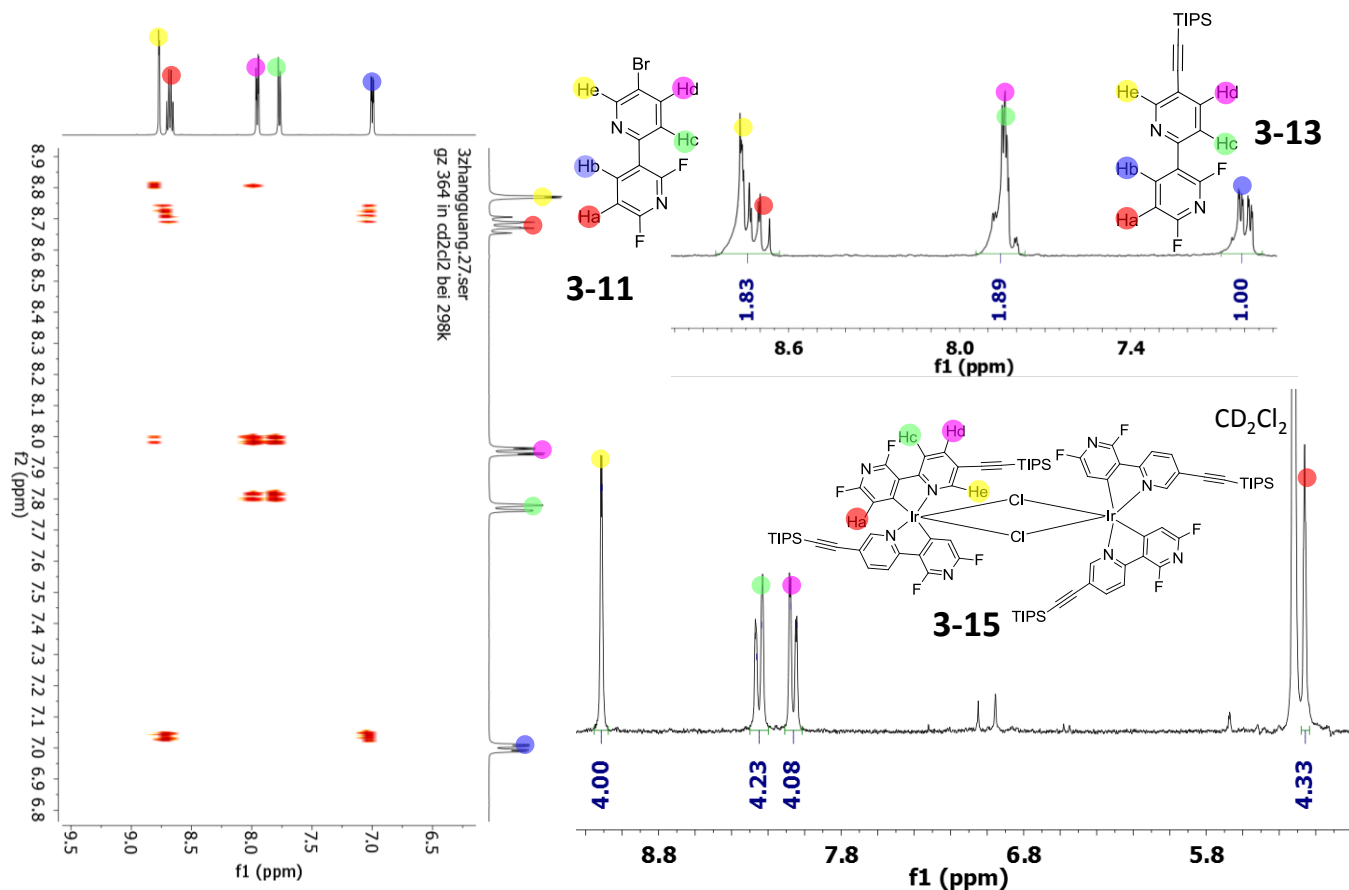
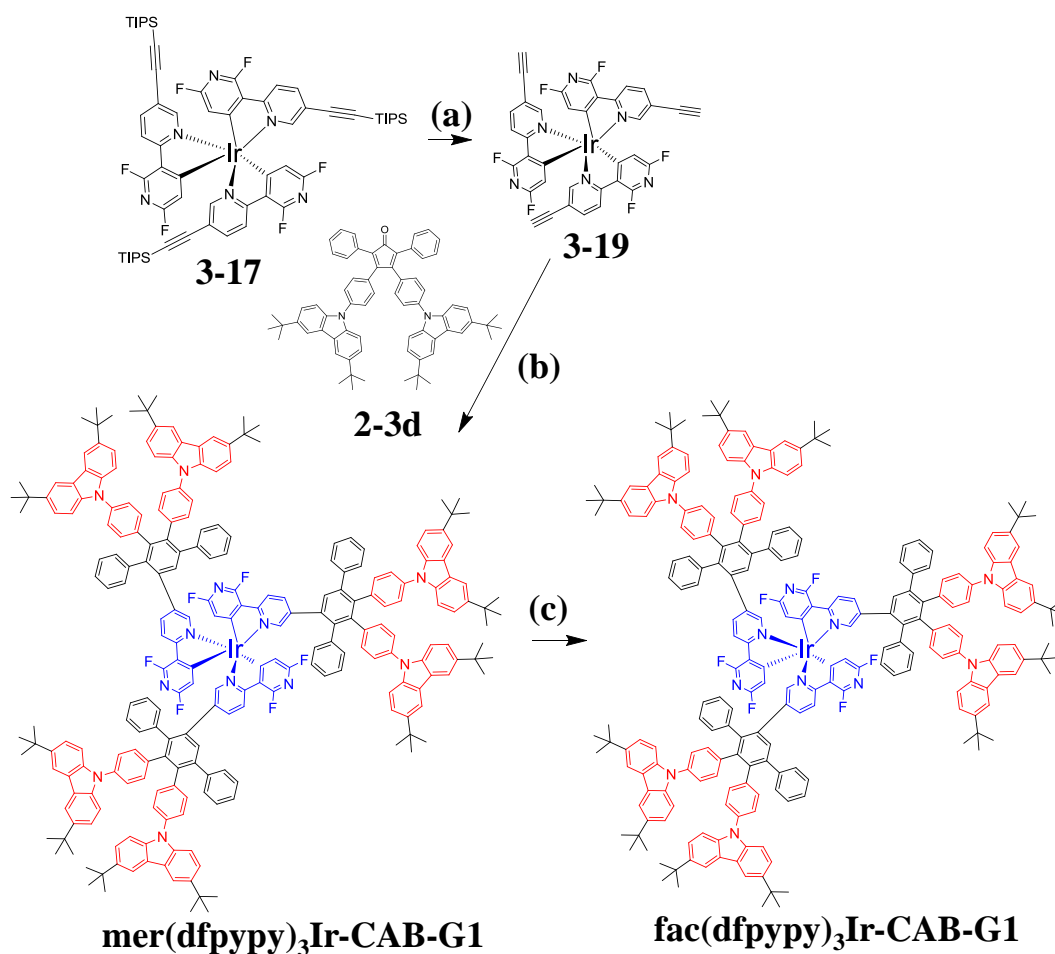


Figure 3.7: ^1H - ^1H COSY spectra of compound **3-11** (left) and ^1H NMR spectra of **3-13** (top right) and **3-15** (bottom right) (solvent: CD_2Cl_2).

The ^1H - ^1H COSY spectra was very helpful. As could be seen in the COSY spectra, the blue signal had a strong coupling with the red one and the pink signal had a strong coupling with the green one as well. However, the yellow peak had a weak coupling with the pink one. Its weak coupling with the pink one, together with its doublet splitting with a small coupling constant correlated well with proton He (marked yellow) which had a weak interaction with proton Hd (marked pink) due to their relatively large distance. After the identification of proton Hd, proton Hc (marked green) was figured out as well with a doublet peak. With the understanding of the ^1H NMR spectra of compound **3-11**, the ^1H NMR spectra of compound **3-12** was easily understood. Going to the ^1H NMR spectra of the Ir-complex dimer (**3-15**), the protons (marked yellow, green and pink) were identified easily based on their splitting and referring to the ligands. However, due to the C-Ir coordination, proton H_b was missing in the dimer and the chemical environment of proton H_a was changed markedly compared with those in the ligands. Its chemical shift appeared upfield at 5.26 ppm, consistent with other published results.^[11]

Compound **3-17** in meridional configuration could not transform into its facial isomer by photochemistry, probably due to decomposition of the material under long time irradiation of strong UV light. This was confirmed by FD-mass result, in which no desired product peak was detected after the reaction. Thin-layer chromatography also suggested that no desired product spot was found. As a result,

the meridional dendrimer was synthesized first (Scheme 3.6). First, the TIPS groups of compound **3-17** were removed by TBAF in THF solution.^[12] With the ethynyl-functionalized Ir-complex (**3-19**) available, the dendrimer could be easily obtained by a Diels-Alder reaction between compound **3-19** and carbazole-CP (**2-3d**) in moderate yield (55%). The resulting product was a solely meridional isomer as confirmed by its ¹H NMR and ¹⁹F NMR spectra (chapter 8). As the facial isomer probably displayed a better emission property, it was successfully prepared by photochemistry from the meridional one. Finally, a yellow-colored solid was received after purification in 83% yield. The facial dendrimer was characterized by ¹H and ¹⁹F NMR spectroscopy, MALDI-TOF and HRMS spectrometry, UV-vis absorption and photoluminescence spectroscopy methods, due to its good solubilities in organic solvents, e.g. DCM, THF and toluene.



Scheme 3.6: Synthetic routes for **fac(dfppy)₃Ir-CAB-G1**. (a) TBAF, THF, r.t, 46%; (b) o-xylene, 150 °C, 48 h, 55%; (c) UV light, THF, 12 h, r.t, 83%.

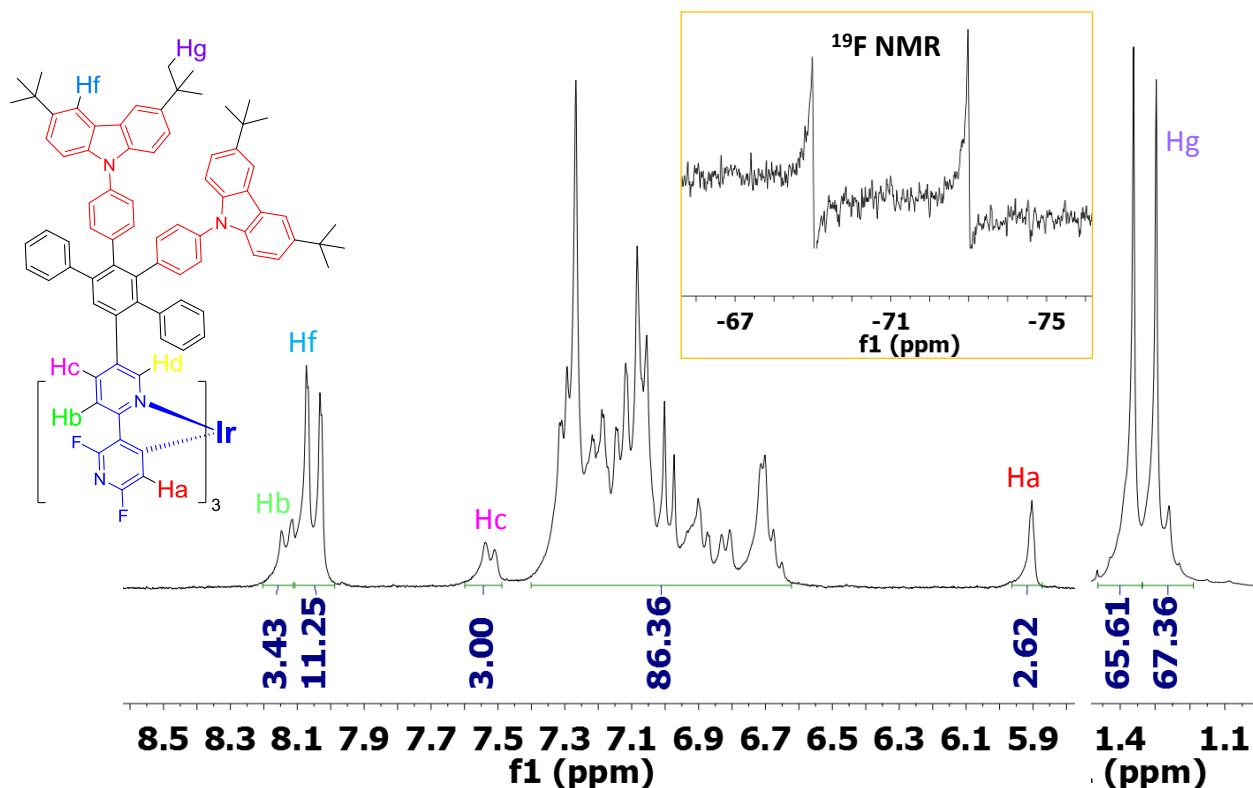


Figure 3.8: ^1H NMR and ^{19}F NMR (inset) spectra of **fac(dfppy) $_3$ Ir-CAB-G1** (solvent: CD_2Cl_2).

The ^1H NMR spectra of the facial dendrimer (Figure 3.8) could identify some special protons in the molecule. For example, the proton Ha ortho to fluorine atom had a singlet peak at around 5.90 ppm. Proton Hb and Hc resonated at 8.13 and 7.52 ppm respectively. In addition, 4,5-position protons (Hf) of carbazole group had signals at around 8.05 ppm and the tertbutyl group proton signals were at around 1.33 ppm. The relative intensities of each peaks correlated well with the number of respective protons in the molecule. Moreover, there were only two peaks observed in the ^{19}F NMR of the facial isomer, corresponding to the two fluorine atoms in one ligand of the molecule, supporting its C_3 symmetry.

As depicted in Figure 3.9, the MALDI-TOF mass spectra of **fac(dfppy) $_3$ Ir-CAB-G1** exhibited a single peak of the molecular ion which was in good agreement with the molecular mass of the dendrimer. The HRMS spectra showed clear isotope patterns of the molecular ion, which was consistent with the calculated result. Consequently, the desired product was synthesized.

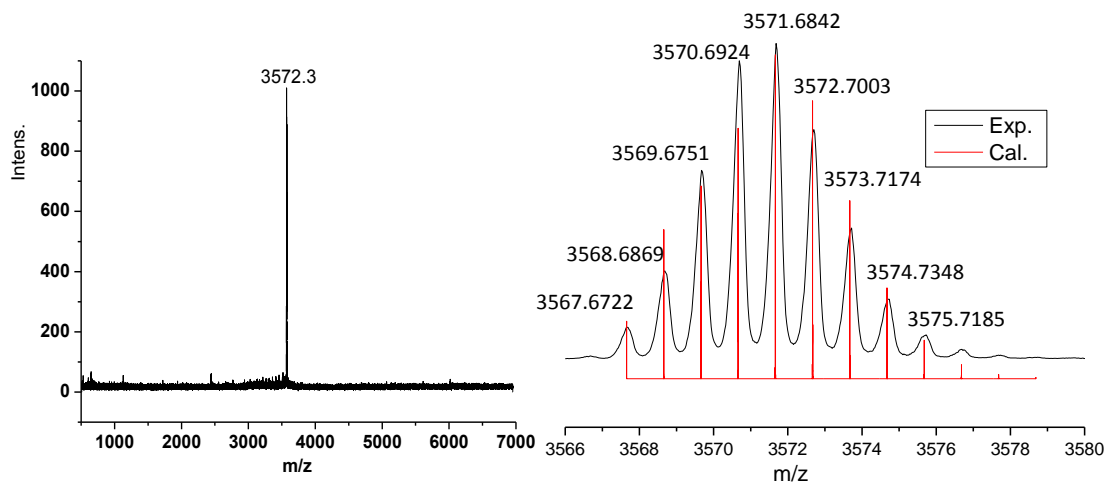


Figure 3.9: MALDI-TOF mass (left) and HRMS (right) spectra of **fac(dfppy)₃Ir-CAB-G1**.

3.1.5 Photophysical properties

The absorption and emission spectra of the TIPSE-functionalized Ir-complexes (**3-17** and **3-18**) were measured in DCM solutions. As depicted in Figure 3.10, both molecules displayed three absorption bands. The first two were between 270 and 350 nm due to the ligand self-absorptions. The less notable band between 370 nm and 420 nm was attributed to the MLCTs. In addition, the absorption of compound **3-18** were generally hypsochromically shifted compared with compound **3-17** (270 nm vs 290 nm, 328 nm vs 349 nm and 380 nm vs 385 nm). In the emission spectra, there also existed a slight hypsochromic shift of compound **3-18** compared with compound **3-17**. The emission of both compounds shifted to the green region. In contrast to **(2,6-difpy-5'-TMSpy)₃Ir**, the conjugation length was clearly extended for compound **3-17** and **3-18**. This was probably the reason for the strong bathochromic shifts in emission. The emission of compound **3-18** was centered at 508 nm with a shoulder at around 485 nm. The emission of compound **3-17** showed fine structures with two peaks at 489 and 525 nm respectively and a shoulder at around 567 nm.

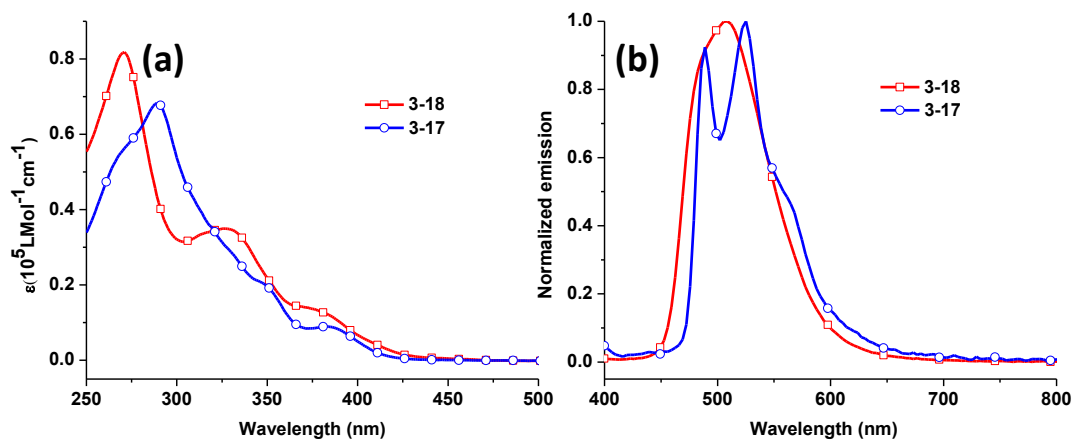


Figure 3.10: UV-vis absorption (a) and emission spectra (b) of compound **3-17** and **3-18** (10^{-5} M in DCM, ex: 385 nm).

The photophysical properties of Ir-complexes are highly related to the FMOs of its ligands and the HOMO and LUMO distributions on the ligands.^[13] By judicious selection of the ligands, diverse-color emitters were obtained.^[14] As a result, red, green and blue light-emitting Ir-complexes have been designed and synthesized successfully.^[15] The calculations on the molecular orbitals of the Ir-complexes are under progress. However, the FMOs of compound **3-13** and **3-14** were calculated using DFT (B3LYP, 6-31G) method by Gaussian software. As depicted in Figure 3.11, the HOMO and LUMO orbitals are highly overlapped across the whole molecular structure for both molecules, except that the TIPS groups seemingly only contribute to the HOMO. As reported, the HOMO of (**dfppy**)₃Ir extends all over the molecule and its LUMO is only located on its ligands.^[2a] Considering the elongated conjugations and the resulting reduced HOMO-LUMO energy gaps induced by the TIPSE groups in the ligands (**3-13** and **3-14**), together with the strong contributions of the ligands to HOMO and LUMO orbitals in (**dfppy**)₃Ir, it is postulated that the energies of the emissive excited states of compound **3-17** and **3-18** are probably reduced, which renders the strong bathochromic shifts of **3-17** and **3-18** in emission compared with (**dfppy**)₃Ir.

The HOMO-LUMO energy gap of compound **3-14** is higher than that of compound **3-13**, probably due to the shorter effective conjugations in the former. This is consistent with some published results that bended structures (the conjugation planes are V-shaped) usually have shorter effective conjugations than their straight counterparts, e.g. phenanthrene vs. anthracene and p-terphenyl vs. m-terphenyl.^[16] In addition, the hypsochromic shifts of compound **3-18** in both its absorption and emission in comparison with compound **3-17** are probably due to the shorter effective conjugations in the former.

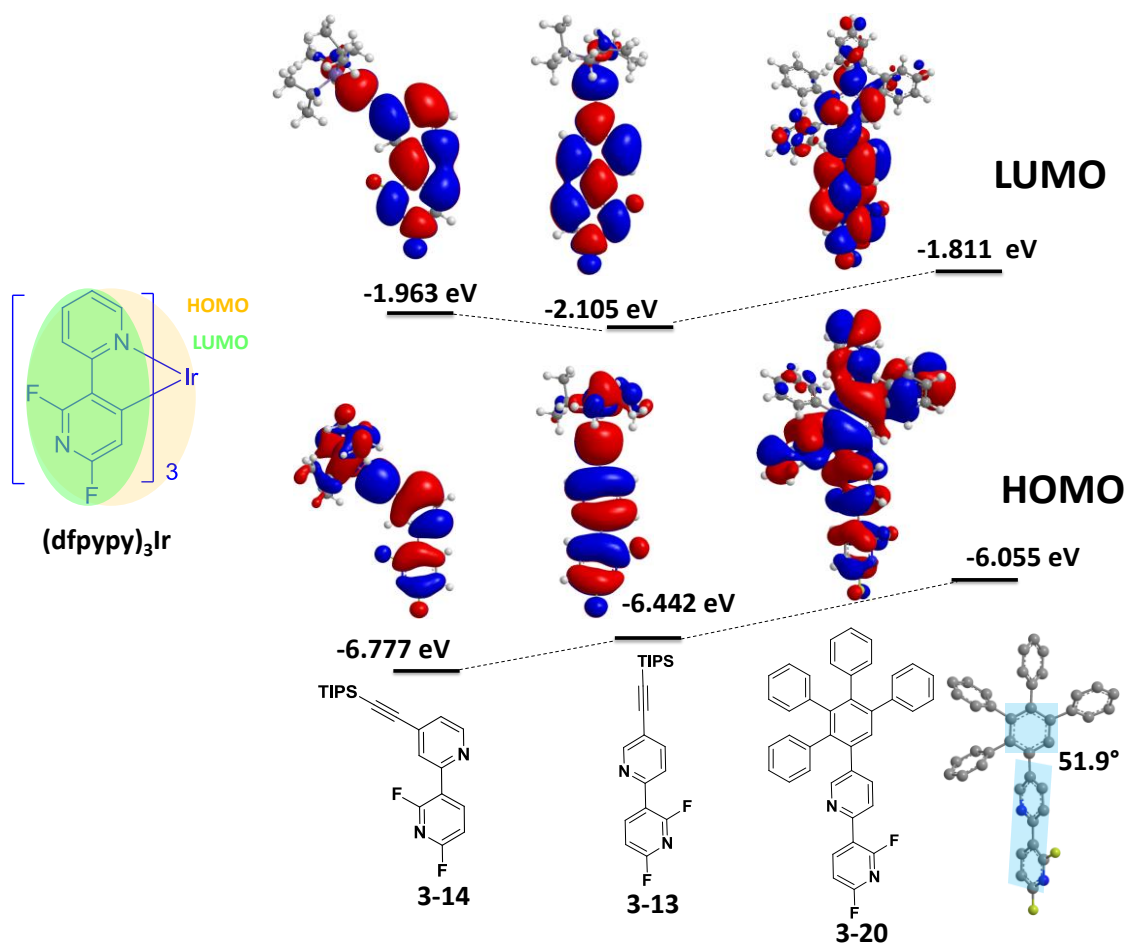


Figure 3.11: Molecular orbital distributions and energy levels of FMOs of the ligands (calculated using DFT, B3LYP, 6.31G method).

The absorption and emission of the facial and meridional dendrimers were characterized as well (Figure 3.12). From the absorption spectra, it appeared that both spectra were very similar in the absorption bands and intensities (considering the measurement errors). There was a strong band at around 297 nm for both spectra. This was the characteristic absorption of **CABs**, also observed in **PYCAB** (chapter 2).^[17] The little peaks centered at 333 and 348 nm were probably due to π - π^* transitions of the ligands similar as the Ir-complex monomers mentioned above. The weak absorbance above 370 nm was due to the MLCTs. Going to emission spectra, both dendrimers showed similar emission. The facial one had slightly stronger emission than the meridional one and their peak emissions were at around 515 nm and 512 nm respectively, both with shoulders at around 485 nm. These emissions also shifted to the green region.

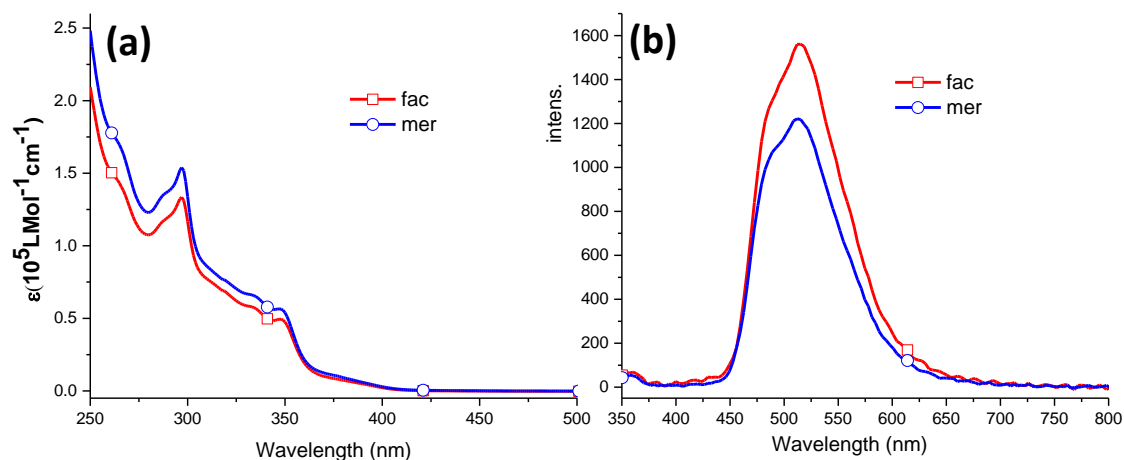


Figure 3.12: Absorption (a) and emission spectra (b) of **fac-** and **mer(dfppy)₃Ir-CAB-G1** (10^{-5} M in DCM, ex: 348 nm).

The strong bathochromic shifts (~ 70 nm) in the emission of the dendrimers compared with **(dfppy)₃Ir** was probably due to the extended conjugations in the ligands of the Ir-complex in the dendrimers. As shown in Figure 3.11, the structure optimization of pentaphenylene-functionalized bipyridine (**3-20**) was done by the DFT method. It appeared that the dihedral angle between the plane of bipyridine and the plane of the central phenyl ring of the pentaphenylene segment was as high as 52° , indicating that the two planes were highly twisted and little conjugation effects between them were expected. But from electron-density distributions of the HOMO and LUMO of compound **3-20**, it turned out that the pentaphenylene group had very strong donation to the HOMO orbital and much less contribution to the LUMO orbital. As a result, the HOMO energies of the ligands of the Ir-complex in the dendrimer were probably increased significantly but the LUMO energies were not changed much. This big change of the energy levels of FMOs probably had caused the energies of the emissive excited state of the dendrimers to decrease and the emission of the dendrimers to shift bathochromically. The notable bathochromic shift of a Ir-complex-based phenylene dendrimer compared with its blue-emitting core was reported by Samuel, et al. (Figure 3.13). Compared with the monomer (**3-21**), 1,3-diphenylbenzene-dendronized dendrimer (**3-22**) was red shifted by around 20 nm in emission.^[18]

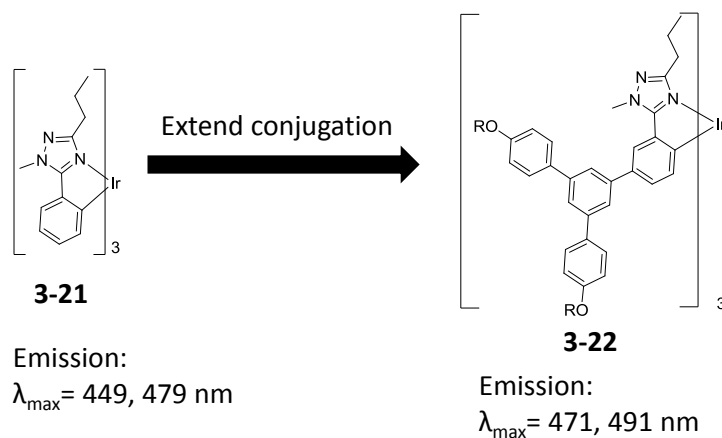


Figure 3.13: conjugation effects of triplet emitters on their emission wavelengths.

In sum, many **(dfppy)₃Ir**-based small molecules and dendrimers were successfully synthesized. Even though the TMS-functionalized **(dfppy)₃Irs** remained the blue emission, the emission of the **(dfppy)₃Ir-based PPDs** shifted to green color with around 70 nm bathochromic shift compared with the bare core. The reason is probably the extended conjugations in the ligands of the Ir-complex in the dendrimer with the considerable contributions of the dendrons to molecular orbitals of the Ir-complex. This probably reduced the energy of the emissive excited state and prompted severe bathochromic shifts in the emission.

3.2 (dpbic)₃Ir-based polyphenylene dendrimers

Currently, the major strategy to control the blue emission of Ir-complex-based dendrimers is to break the conjugations totally between the core and the dendrons. Therefore, alkyl chains were introduced between them.^[4, 18-19] This on the other hand increased the flexibility of the molecules. It is desirable to make rigid dendrimers which have defined positions of the core and peripheral groups and make each part play their roles separately. Blue emitters are highly sensitive towards extended conjugations on the ligands as mentioned above. Therefore, preparing rigid and blue light emitting Ir-complex-based dendrimers is a challenging task. Currently, there are some reported Ir-complexes with violet blue emission (λ_{\max} : ~400 nm) at room temperature and good PLQYs (Figure 3.14).^[14, 20] These candidates are N-heterocyclic carbene (NHC)-based Ir complexes in which the iridium atom coordinates with two carbon atoms (C[^]C) rather than C[^]Ns, one from the carbene carbon atom and the other from one phenyl group of the ligand. Due to their violet blue emission, it might be a good idea to functionalize these monomers with polyphenylene dendrons and push their emission into pure blue.

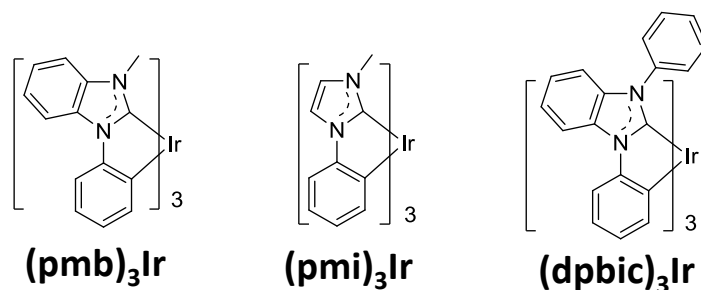
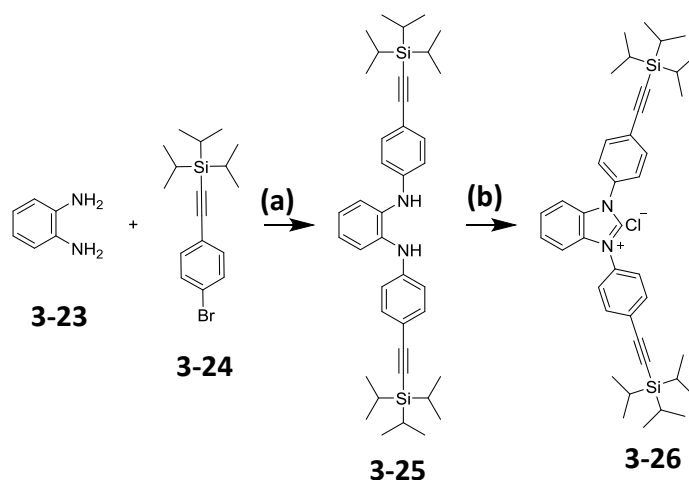


Figure 3.14: Carbene-based Ir-complexes emitting at violet region.

In this work, **(dpbic)₃Ir** was selected as the core for new **PPD** synthesis as the para-positions of 1,3-diphenyls on the ligands can be functionalized with triple bonds and therefore, six-armed dendrimers could be procured (Scheme 3.8), which shall provide a better protection to the core.

3.2.1 Synthesis of dendrimers

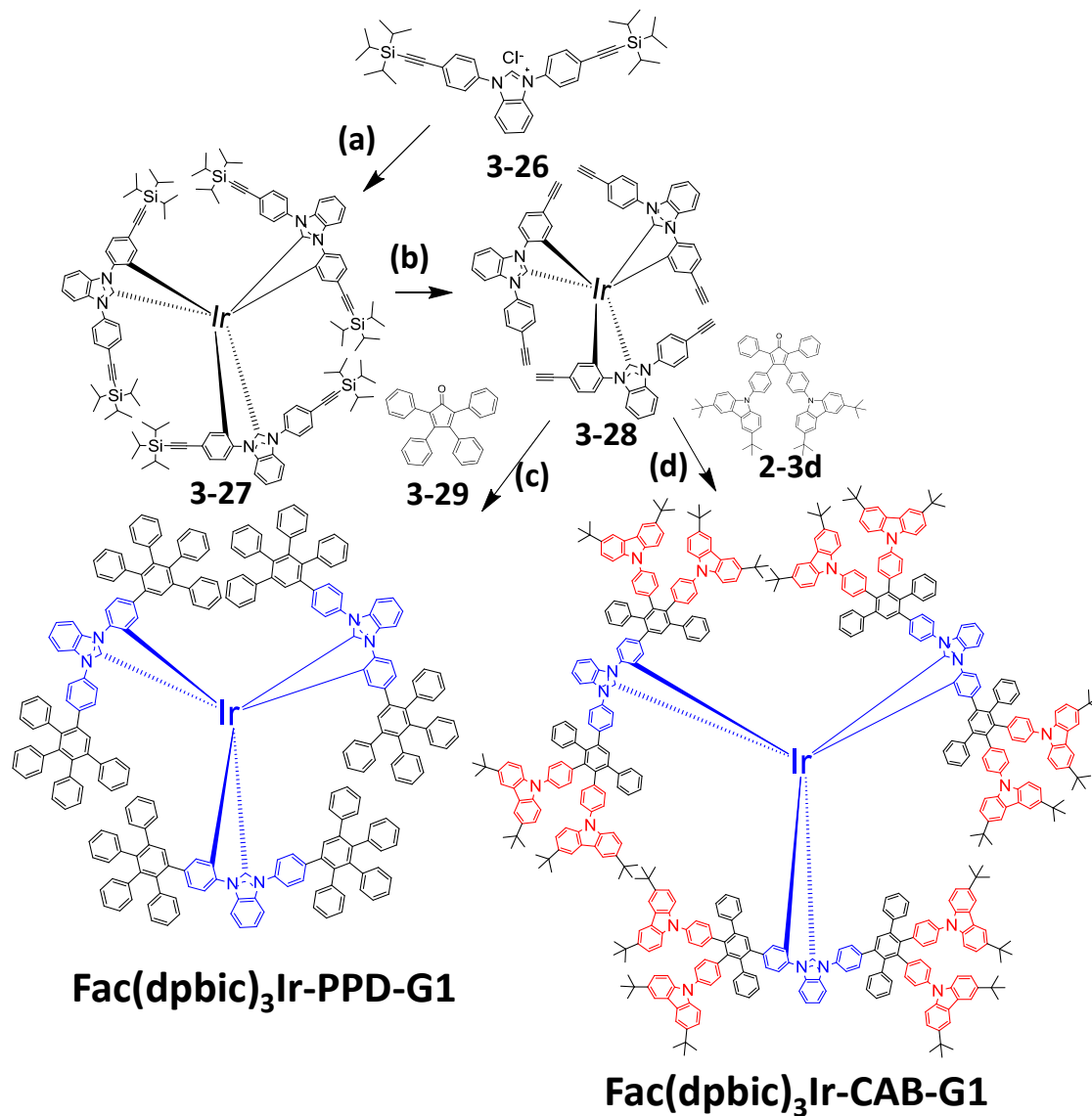
To synthesize the dendrimers, the ligands were prepared first. As shown in Scheme 3.7, the TIPSE-functionalized 1,3-diphenylbenzimidazolium chloride (**3-26**) was obtained in two steps. The first step was a two-fold Buchwald-Hartwig coupling between 1,2-diaminobenzene (**3-23**) and 1-bromo-4-TIPSE-benzene (**3-24**) and compound **3-25** was received in high yield (89%).^[21] Next, compound **3-25** was reacted with triethyl orthoformate and conc. HCl solution to give the benzimidazolium chloride (**3-26**) in high yield (86%).^[22]



Scheme 3.7: Synthetic routes for compound **3-26**. (a) NaOtBu, Pd₂(dba)₃, 2,2'-bi(diphenylphosphino)-1,1'-dinaphthalene, toluene, 90 °C, 13 h, 89%; (b) triethyl orthoformate, conc. HCl, 80 °C, 14 h, 86%.

The next step was to make the Ir-complex-based monomers and dendrimers (Scheme 3.8). The TIPSE-functionalized NHC-chelated Ir-complex (**3-27**) was obtained by a reaction between IrCl₃ and compound **3-26** under a basic condition (Na₂CO₃/Ag₂CO₃, 1/1).^[23] After that, the triple bonds were activated by TBAF to form compound **3-28** in moderate yield (45%). Then compound **3-28** reacted with

the CPs (**3-29** and **2-3d**) to afford the dendrimers by Diels-Alder reactions in moderate to high yields (36% to 72%).



Scheme 3.8: Synthetic routes for NHC-Ir-complex-based polyphenylene dendrimers. (a) IrCl₃·nH₂O, Na₂CO₃, Ag₂CO₃, 2-ethoxyethanol, 145 °C, 20 h, 22%; (b) TBAF, THF, 0 °C, 1 h, 45%; (c) o-xylene, 140 °C, 24 h, 36%; (d) o-xylene, 150 °C, 48 h, 72%.

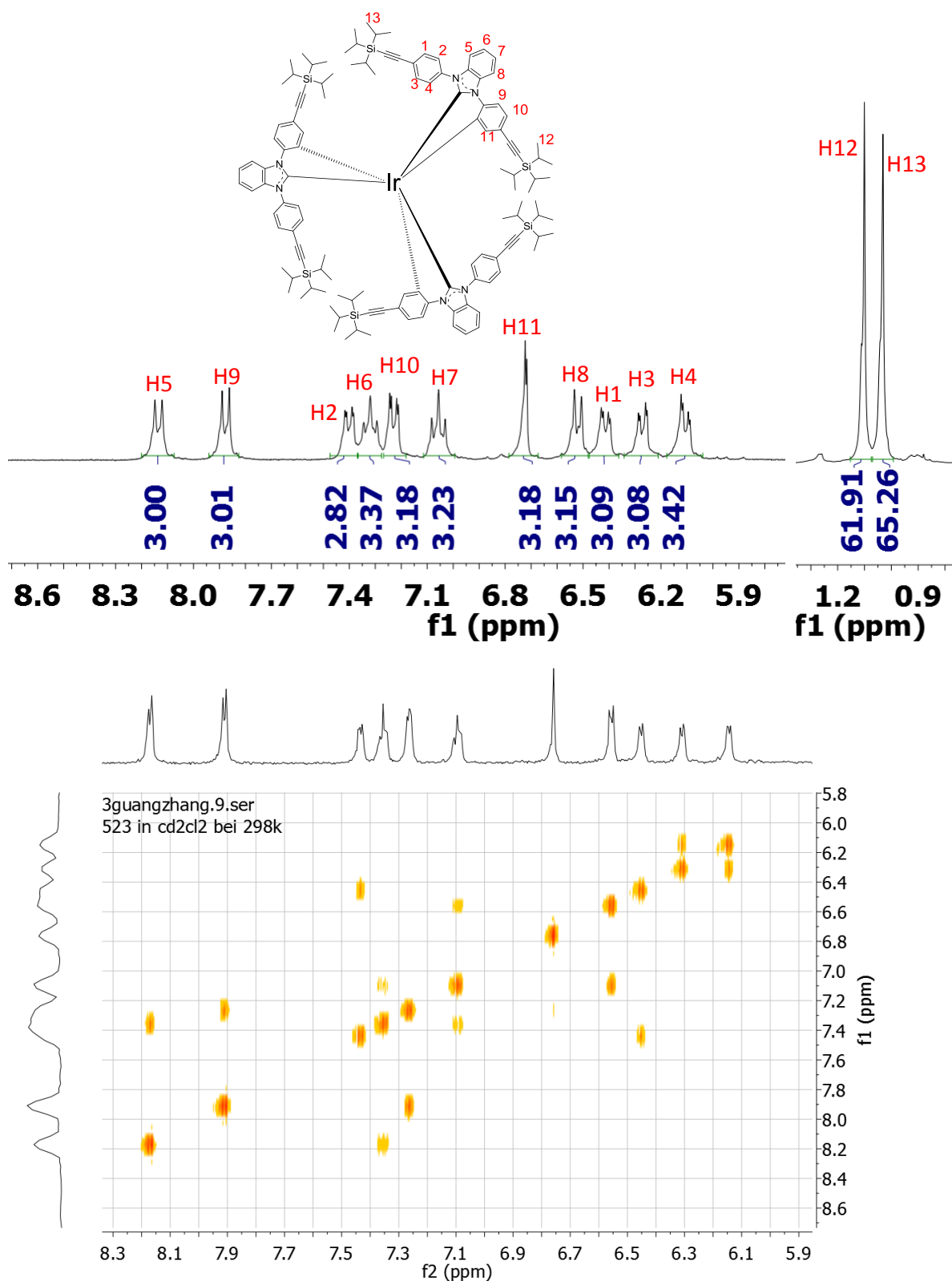


Figure 3.15: ^1H NMR (top) and ^1H - ^1H COSY (bottom) spectra of compound **3-27** (solvent: CD_2Cl_2).

This Ir-complex (**3-27**) was confirmed by ^1H , ^{13}C NMR, and FD-Mass spectra after purification by a silica-gel flash column. From the ^1H NMR spectra, compound **3-27** was demonstrated to be a facial isomer (Figure 3.15) because there were totally eleven proton signals in the aromatic region with equal relative intensities and there were also totally eleven aromatic protons in one ligand as well. Therefore, the proton signals of one ligand represented all the proton signals of the molecule, indicating a C3

symmetry of this molecule. The correlation between each proton and its chemical shift was confirmed with the help of ^1H - ^1H COSY spectra and the splitting patterns of each signal.

The dendrimers were characterized by ^1H and ^{13}C NMRs spectroscopy and MALD-TOF mass and HRMS spectrometry. As depicted in Figure 3.16, MALDI-TOF mass spectra of each dendrimer exhibited a single peak of the molecular ion. In addition, the HRMS spectra of **fac(dpbic)₃Ir-PPD-G2** showed clear isotope patterns of the molecular ion, which was consistent with the calculated result. Therefore, it confirms the successful synthesis of the desired products. The NMR data of the dendrimers are available in chapter 8.

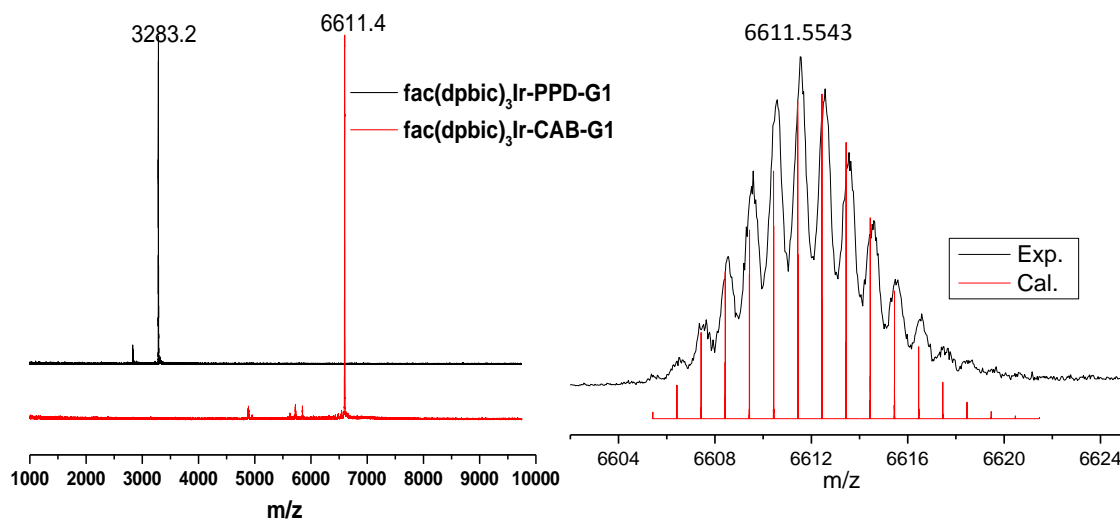


Figure 3.16: MALDI-TOF mass spectra of **fac(dpbic)₃Ir-PPD-G1** and **fac(dpbic)₃Ir-CAB-G1** (left) and HRMS spectra of **fac(dpbic)₃Ir-PPD-G2** (right).

3.2.2 Photophysical properties

The synthesized Ir-complexes, including the monomer (**3-27**) and dendrimers were characterized by UV-vis absorption and photoluminescence spectra. As depicted in Figure 3.17, from the absorption of compound **3-27**, a major band (~ 262 nm) with several shoulders (~ 286 , 313 and 360 nm) in the UV region was due to the energy transitions of the ligands. This was consistent with the absorption of compound **3-26**. The small band above 350 nm for compound **3-27** was attributed to the MLCT.

Compound **3-27** exhibited strong and pure blue emission in solutions at room temperature with argon protection because oxygen easily quenched the triplet states.^[24] In a 0.5 mg/ml (2.4×10^{-4} M) THF solution, a strong blue emission was obtained with the peak emission at 440 nm and 469 nm respectively and a shoulder at around 500 nm. Compared with the emission of **(dpbic)₃Ir** (λ_{max} : ~ 400 nm),^[20] compound **3-27** was bathochromically shifted by around 40 nm. This was due to the extended conjugations in the ligands by the triple bonds similar as compound **3-17** and **3-18** mentioned before. In addition, the emission was measured at 77 K as well. First, a quartz tube containing the solution of

compound **3-27** in 2-methyltetrahydrofuran (2-MeTHF) was immersed inside liquid nitrogen until the solution was solidified. Then the tube was quickly put into the measurement cell to collect the data. The emissions (λ_{max} : 440 nm and 469 nm) were very strong and nearly identical as those measured at room temperature (Figure 3.17, b). This illustrated that the emission at room temperature was phosphorescent (triplet energy was calculated to be 2.82 eV, taking the peak emission wavelength of the highest energy). Moreover, the thin film of the TIPSE-functionalized 1,3-benzoimidazonium chloride (**3-26**) showed a strong and featureless deep blue emission (λ_{max} : 426 nm).

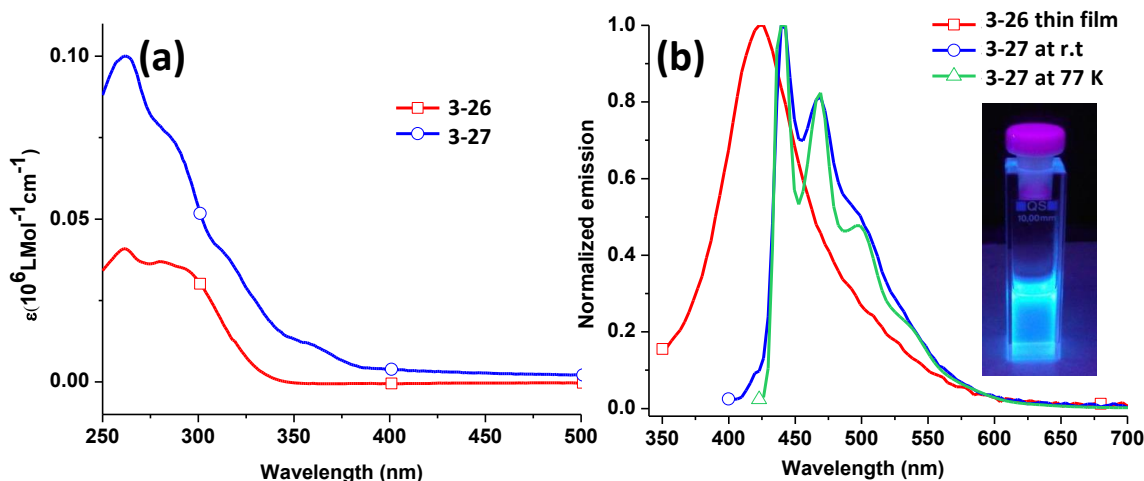


Figure 3.17: UV-vis absorption (a) and emission spectra (b) of compound **3-26** and **3-27** (10^{-6} M in DCM for absorption, emission: thin film for compound **3-26**, ex: 300 nm, 0.5mg/ml THF (at rt, argon protection) or 2-MeTHF (77 K) for compound **3-27**, ex: 375 nm, inset image: emission of compound **3-27** at rt, ex: 365 nm).

Going to dendrimers, as depicted in Figure 3.18, there existed two shoulders (~ 280 and 320 nm) and a weak absorbance between 350 and 400 nm in the absorption of **fac(dpbc)₃Ir-PPD-G1**. The shoulders were due to the ligand- and polyphenylene-based energy transitions.^[25] The absorption above 350 nm was probably attributed to the MLCTs. For **fac(dpbc)₃Ir-CAB-G1**, similarly, the absorption below 350 nm represented the energy transitions of the ligands, polyphenylene dendrons and surface chromophores. For example, the absorption peak at around 298 nm and 349 nm was characteristic of carbazoles.^[17] The dendrimers in solution were non-emissive (could not be observed by naked eyes and not detected by the photoluminescence spectrometer) at room temperature even with argon protection. This could be explained by the existence of nonradiative excited states (NR) in the dendrimer, which had small energy barriers with the emissive excited state, the T1 state. As a result, T1 state could be easily excited to the NR at room temperature and the emission could be extremely weak at room temperature.^[14, 26] Or it can be argued that the decay of the emissive excited state is consumed by the vibrations or rotations of the polyphenylene dendrons as there are still some degrees of rotational flexibility in solution. This is

supported by the observed slight emission in thin films of these dendrimers. But, this kind of material was usually strongly emissive at very low temperatures, e.g. 77 K.^[26] Therefore, photoluminescence measurements were also conducted at 77 K. As expected, the emissions were very strong at 77 K (Figure 3.18, b). **fac(dpbc)₃Ir-PPD-G1** had two emission peaks at 462 and 488 nm respectively. This was sky blue and the triplet energy was calculated to be 2.68 eV. It was even bathochromically shifted by around 20 nm compared with compound **3-27**. For **fac(dpbc)₃Ir-CAB-G1**, the emission (λ_{max} : 462 nm and 489 nm, a shoulder: ~522 nm) was slightly bathochromically shifted compared with **fac(dpbc)₃Ir-PPD-G1**.

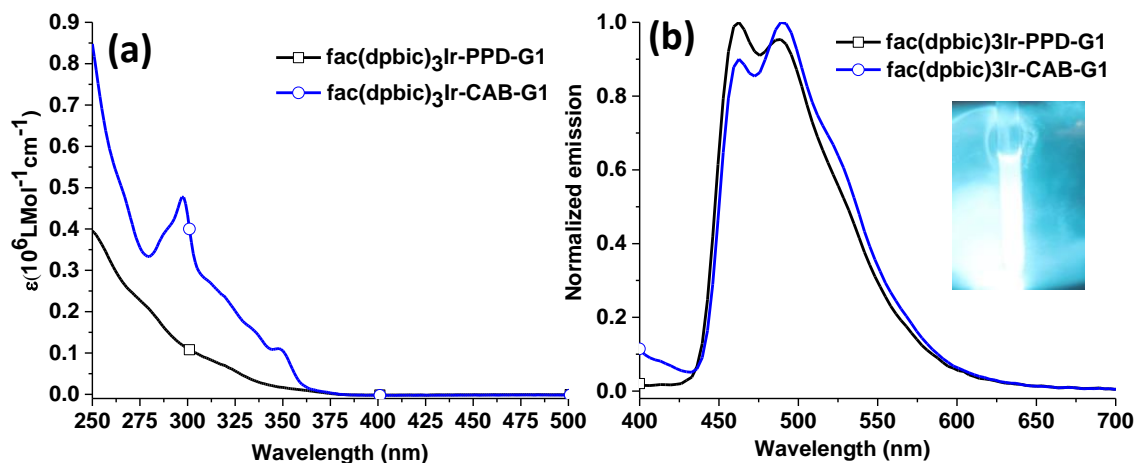


Figure 3.18: UV-vis absorption (a) and emission spectra (b) of **fac(dpbc)₃Ir-PPD-G1** and **fac(dpbc)₃Ir-CAB-G1** (10^{-6} M in DCM for absorption, 1mg/ml 2-MeTHF (77 K) for emission, ex: 360 nm, inset picture: the emission of **fac(dpbc)₃Ir-PPD-G1** at 77 K, ex: 365 nm).

The bathochromic shifts (~60 nm) in emission of the dendrimers compared with the bare core are probably due to the elongated conjugations of the ligands of the Ir-complex in the dendrimer. A model compound, i.e. pentaphenylene-functionalized 1-phenylbenzimidazole (**3-30**) was structurally optimized using the DFT method (Figure 3.19). The dihedral angle between the 1-phenyl plane and the central phenyl plane was as high as 53°. This highly twisted structure could not block the contributions of the pentaphenylene group to the FMOs of the molecule however. The pentaphenylene group contributed to both the HOMO and LUMO orbital of this structure considerably. This explained the significant bathochromic shift in the dendrimer emission compared with the bare core because the energies of the emissive excited states of the Ir-complex in the dendrimer probably had decreased with the changes of the molecular orbitals of the ligands.

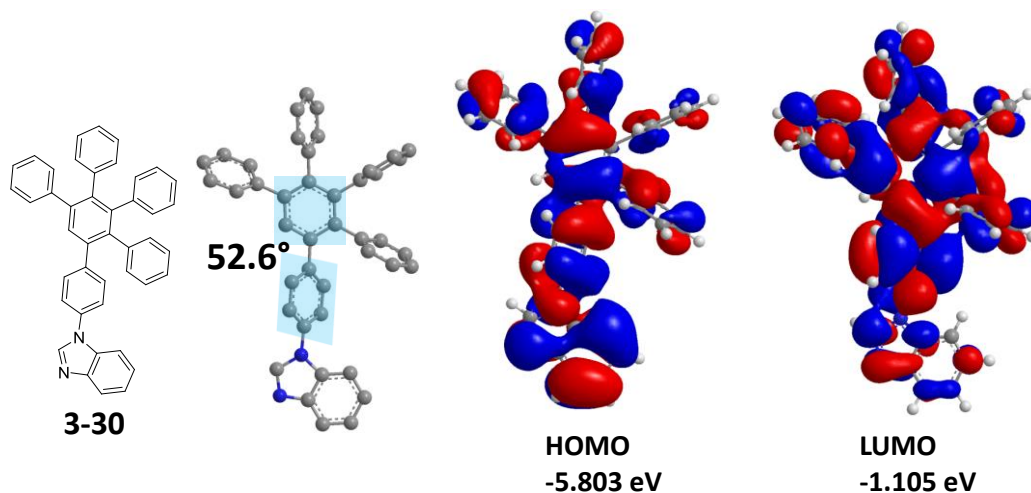


Figure 3.19: Optimized molecular structure and molecular orbital distributions of FMOs of compound **3-30** (DFT, B3LYP, 6.31G method).

In conclusion, the TIPSE-functionalized $(\text{dpbic})_3\text{Ir}$ and $(\text{dpbic})_3\text{Ir}$ -based polyphenylene dendrimers were successfully synthesized in three and five steps respectively. The TIPSE-functionalized $(\text{dpbic})_3\text{Ir}$ monomer showed a pure blue emission at room temperature in solution. The reason for the bathochromic shift of its emission (~ 40 nm) compared with $(\text{dpbic})_3\text{Ir}$ is the extended conjugation in the ligands. The dendrimers were not emissive at room temperature in solution. However, they were strong sky blue emitters at 77 K. The reason for their non-emission at room temperature was the possible existence of nonradiative excited states in these dendrimers, which had small energy barriers with the emissive excited states or the consumption of the triplet energies by vibrations or rotations of the polyphenylene dendrons in solutions.

3.3 Summary

$(\text{dfppy})_3\text{Ir}$ -based small molecules and dendrimers were successfully synthesized and characterized. The facial and meridional TMS-functionalized $(\text{dfppy})_3\text{Ir}$ were obtained as pure blue emitters. The facial one was a stronger emitter than the meridional one but it exhibited a slight bathochromic shift (~ 7 nm) compared with $(\text{dfppy})_3\text{Ir}$, probably due to the electron-donating effect of TMS groups to the molecules. The TIPSE-functionalized $(\text{dfppy})_3\text{Ir}$ s showed significant bathochromic shifts (~ 70 nm) in emission compared with $(\text{dfppy})_3\text{Ir}$ and both were green emitters due to the extended conjugations by the TIPSE groups which contributed to the molecular orbitals and changed the emissive excited states considerably. The $(\text{dfppy})_3\text{Ir}$ -based dendrimers, i.e. **fac-** and **mer** $(\text{dfppy})_3\text{Ir-CAB-G1}$ also displayed green emission with strong bathochromic shifts (~ 77 nm) compared with the bare core. This is also attributed to the notable change of the molecular orbitals of the core of the dendrimers by the contributions of polyphenylene dendrons even though there are very big dihedral angles between the bipyridine moiety and the phenyl ring directed bonded to the bipyridine.

The **(dpbic)₃Ir**-based small molecules and dendrimers were prepared in three and five steps respectively. The TIPSE-functionalized **(dpbic)₃Ir (3-27)** was a pure blue emitter at room temperature in solution. Comparing with **(dpbic)₃Ir**, its emission was bathochromically shifted by approximate 40 nm due to the extended conjugation of the ligands by TIPSE groups. The dendrimers, i.e. **fac(dpbic)₃Ir-PPD-G1** and **fac(dpbic)₃Ir-CAB-G1** both were non-emissive at room temperature in solution and exhibited very weak emissions in thin films, probably due to the existence of nonradiative excited states which had small energy barriers with the emissive excited states or the consumption of the emissive triplets by the vibrations or rotations of the dendrons in solutions. Both dendrimers were strong sky blue emitters at 77 K in 2-MeTHF, however. Their emissions were bathochromically shifted by around 60 nm compared with **(dpbic)₃Ir** due to the contributions of the polyphenylene dendrons to the molecular orbitals of the ligands of the Ir-complex in the dendrimer.

Consequently, direct bonding polyphenylenes to a blue-color-emissive Ir-complex normally will cause a significant bathochromic shift of emission due to the extended conjugation effects. In addition, non-emission or weak emission at room temperature may occur in the dendrimers due to the changes of the energies of the molecular orbitals of the Ir-complex by polyphenylenes, which may result in nonradiative transitions from the new emissive excited state to the nonradiative excited state because of their small energy gap. Accordingly, it is unpredictable and very difficult to make rigid dendrimer-based and efficient blue phosphorescent emitters at the moment.

Literature

- [1] W. Y. Wong, C. L. Ho, *J Mater Chem* **2009**, *19*, 4457-4482.
- [2] a) S. J. Lee, K. M. Park, K. Yang, Y. Kang, *Inorg Chem* **2009**, *48*, 1030-1037; b) M. R. Zhu, Y. H. Li, S. J. Hu, C. G. Li, C. L. Yang, H. B. Wu, J. G. Qin, Y. Cao, *Chem Commun* **2012**, *48*, 2695-2697; c) M. R. Zhu, J. H. Zou, X. He, C. L. Yang, H. B. Wu, C. Zhong, J. G. Qin, Y. Cao, *Chem Mater* **2012**, *24*, 174-180; d) A. B. Tamayo, B. D. Alleyne, P. I. Djurovich, S. Lamansky, I. Tsyba, N. N. Ho, R. Bau, M. E. Thompson, *J Am Chem Soc* **2003**, *125*, 7377-7387.
- [3] a) M. Nonoyama, *B Chem Soc Jpn* **1974**, *47*, 767-768; b) Y. Kang, Y. L. Chang, J. S. Lu, S. B. Ko, Y. L. Rao, M. Varlan, Z. H. Lu, S. N. Wang, *J Mater Chem C* **2013**, *1*, 441-450.
- [4] D. B. Xia, B. Wang, B. Chen, S. M. Wang, B. H. Zhang, J. Q. Ding, L. X. Wang, X. B. Jing, F. S. Wang, *Angew Chem Int Edit* **2014**, *53*, 1048-1052.
- [5] a) R. Ragni, E. A. Plummer, K. Brunner, J. W. Hofstraat, F. Babudri, G. M. Farinola, F. Naso, L. De Cola, *J Mater Chem* **2006**, *16*, 1161-1170; b) C. H. Yang, K. H. Fang, C. H. Chen, I. W. Sun, *Chem Commun* **2004**, 2232-2233.
- [6] a) A. R. McDonald, M. Lutz, L. S. von Chrzanowski, G. P. M. van Klink, A. L. Spek, G. van Koten, *Inorg Chem* **2008**, *47*, 6681-6691; b) T. Karatsu, T. Nakamura, S. Yagai, A. Kitamura, K. Yamaguchi, Y. Matsushima, T. Iwata, Y. Hori, T. Hagiwara, *Chem Lett* **2003**, *32*, 886-887.
- [7] M. ZHOU, P. Wang, J. Zhang, L. liang, in *CN 103571454 A*, China, **2014**.
- [8] M. Schlosser, T. Rausis, *Eur J Org Chem* **2004**, 1018-1024.
- [9] *Proton Nuclear Magnetic Resonance (1H-NMR) Spectroscopy*, http://www.chem.ucla.edu/harding/notes/notes_14C_nmr03.pdf.
- [10] <http://chem.ch.huji.ac.il/nmr/whatisnmr/hetcoup.htm>.
- [11] a) S. B. Meier, W. Sarfert, J. M. Junquera-Hernandez, M. Delgado, D. Tordera, E. Orti, H. J. Bolink, F. Kessler, R. Scopelliti, M. Gratzel, M. K. Nazeeruddin, E. Baranoff, *J Mater Chem C* **2013**, *1*, 58-68; b) F.

- Kessler, Y. Watanabe, H. Sasabe, H. Katagiri, M. K. Nazeeruddin, M. Gratzel, J. Kido, *J Mater Chem C* **2013**, *1*, 1070-1075.
- [12] a) T. S. Qin, J. Q. Ding, L. X. Wang, M. Baumgarten, G. Zhou, K. Mullen, *J Am Chem Soc* **2009**, *131*, 14329-14336; b) T. S. Qin, J. Q. Ding, M. Baumgarten, L. X. Wang, K. Mullen, *Macromol Rapid Comm* **2012**, *33*, 1036-1041.
- [13] L. F. Gildea, J. A. G. Williams, **2013**, 77-113.
- [14] T. Sajoto, P. I. Djurovich, A. Tamayo, M. Yousufuddin, R. Bau, M. E. Thompson, R. J. Holmes, S. R. Forrest, *Inorg Chem* **2005**, *44*, 7992-8003.
- [15] a) L. X. Xiao, Z. J. Chen, B. Qu, J. X. Luo, S. Kong, Q. H. Gong, J. J. Kido, *Adv Mater* **2011**, *23*, 926-952; b) R. Meerheim, R. Nitsche, K. Leo, *Appl Phys Lett* **2008**, *93*; c) H. Sasabe, T. Chiba, S. J. Su, Y. J. Pu, K. I. Nakayama, J. Kido, *Chem Commun* **2008**, 5821-5823; d) S. J. Su, T. Chiba, T. Takeda, J. Kido, *Adv Mater* **2008**, *20*, 2125-+; e) S. O. Jeon, S. E. Jang, H. S. Son, J. Y. Lee, *Adv Mater* **2011**, *23*, 1436-1441.
- [16] a) S. Tang, W. J. Li, F. Z. Shen, D. D. Liu, B. Yang, Y. G. Ma, *J Mater Chem* **2012**, *22*, 4401-4408; b) S. J. Su, D. Tanaka, Y. J. Li, H. Sasabe, T. Takeda, J. Kido, *Org Lett* **2008**, *10*, 941-944.
- [17] J. Q. Ding, B. H. Zhang, J. H. Lu, Z. Y. Xie, L. X. Wang, X. B. Jing, F. S. Wang, *Adv Mater* **2009**, *21*, 4983-+.
- [18] S. C. Lo, R. N. Bera, R. E. Harding, P. L. Burn, I. D. W. Samuel, *Adv Funct Mater* **2008**, *18*, 3080-3090.
- [19] a) S. C. Lo, R. E. Harding, C. P. Shipley, S. G. Stevenson, P. L. Burn, I. D. W. Samuel, *J Am Chem Soc* **2009**, *131*, 16681-16688; b) S. C. Lo, G. J. Richards, J. P. J. Markham, E. B. Namdas, S. Sharma, P. L. Burn, I. D. W. Samuel, *Adv Funct Mater* **2005**, *15*, 1451-1458; c) S. C. Lo, R. E. Harding, E. Brightman, P. L. Burn, I. D. W. Samuel, *J Mater Chem* **2009**, *19*, 3213-3227.
- [20] C. Schildknecht, G. Ginev, A. Kammoun, T. Riedl, W. Kowalsky, H. H. Johannes, C. Lennartz, K. Kahle, M. Egen, T. Geßner, M. Bold, S. Nord, P. Erk, *proceedings of SPIE* **2005**, 5937.
- [21] a) H. Wang, Y. Y. Xia, S. Lv, J. L. Xu, Z. H. Sun, *Tetrahedron Lett* **2013**, *54*, 2124-2127; b) A. R. Chianese, A. Mo, D. Datta, *Organometallics* **2009**, *28*, 465-472.
- [22] a) F. M. Rivas, U. Riaz, A. Giessert, J. A. Smulik, S. T. Diver, *Org Lett* **2001**, *3*, 2673-2676; b) D. M. Khrarnov, C. W. Bielawski, *J Org Chem* **2007**, *72*, 9407-9417.
- [23] K. Tsuchiya, S. Yagai, A. Kitamura, T. Karatsu, K. Endo, J. Mizukami, S. Akiyama, M. Yabe, *Eur J Inorg Chem* **2010**, 926-933.
- [24] a) C. Grewer, H. D. Brauer, *J Phys Chem-US* **1994**, *98*, 4230-4235; b) L. K. Patterson, G. Porter, M. R. Topp, *Chem Phys Lett* **1970**, *7*, 612-614.
- [25] S. Bernhardt, M. Kastler, V. Enkelmann, M. Baumgarten, K. Mullen, *Chem-Eur J* **2006**, *12*, 6117-6128.
- [26] T. Sajoto, P. I. Djurovich, A. B. Tamayo, J. Oxgaard, W. A. Goddard, M. E. Thompson, *J Am Chem Soc* **2009**, *131*, 9813-9822.

Chapter 4 Polyphenylene Dendrimers in Chemical Sensors

In this chapter, **PYTPA** and **PYTPAG2** will be introduced as chemical sensors in detecting explosives, metal ions and some aromatic vapors (Figure 4.1). There are two reasons for selecting them: first, the “N” atoms of **TPAs** contain lone pairs of electrons and provide good binding site for metal ions;^[1] secondly, both dendrimers with high PLQYs from their cores which could interact with the explosives, e.g. TNT and fluorescence quenching could occur by photo-induced electron transfer from the core to the explosive.^[2]

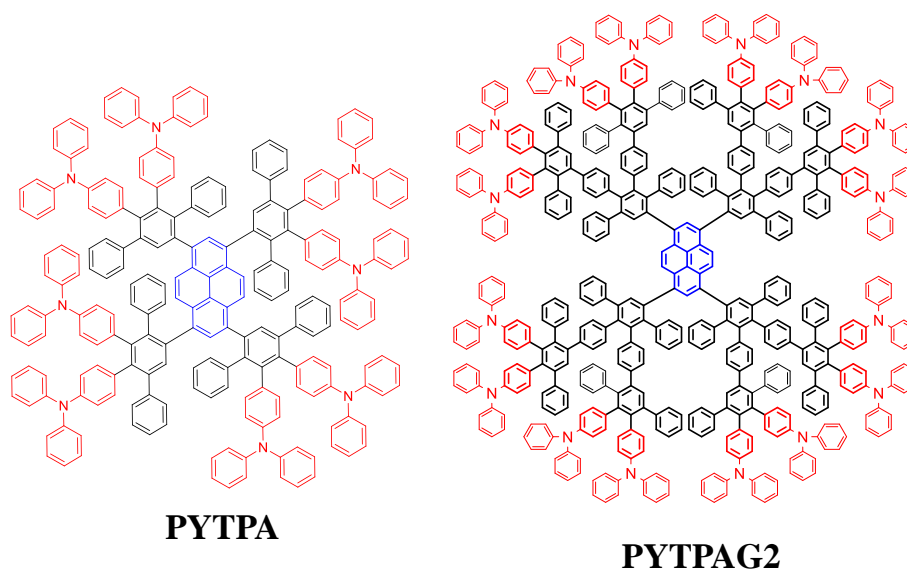


Figure 4.1: Molecular structures of **PYTPA** and **PYTPAG2**.

4.1 Sensitivities of **PYTPA** and **PYTPAG2** to explosives and metal ions

4.1.1 Fluorescence quenching of dendrimer solutions to TNT

All the chemical sensor experiments were conducted by the group members of Prof. Ming Zhang from State Key Laboratory of Supramolecular Structure and Materials, Jilin University, China. First **PYTPA** and **PYTPAG2** were attempted to test TNT in thin films. The thin films were spin-coated on quartz substrates. TNT powder was placed in a quartz cuvette sealed with a cap for 60 minutes to make a saturated TNT vapor. Then a thin film was put inside the quartz cuvette which was then sealed with cap. As depicted in Figure 4.2, the fluorescence spectra were recorded at different times under the excitation wavelength of 360 nm. The fluorescence quenched in both films were weak (~ 25% for **PYTPA** after 300 seconds and ~zero for **PYTPAG2** up to 120 seconds). The reason for the low sensitivities of the films towards TNT is probably the very limited amount of explosive vapors which diffused inside the films and interacted with pyrene moieties due to the possibly densely-packed films by self-assembling.

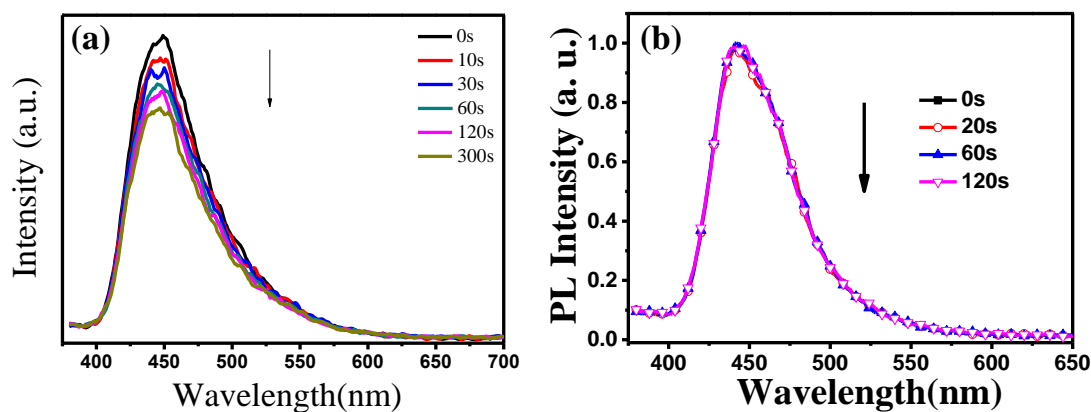


Figure 4.2: Time-dependent fluorescence spectra of **PYTPA** (a) and **PYTPAG2** (b) films upon exposure to TNT.

This postulation was supported by the **PYTPA**'s enhanced sensitivity to TNT in solutions. The concentrations of TNT solutions were set at 10^{-7} , 10^{-6} and 10^{-5} M respectively. As depicted in Figure 4.3, the quenching increased from 48% to 81% with the enhancement of TNT concentrations. This was probably attributed to better interactions between TNT molecules and pyrene moieties of **PYTPAs** in solutions, in which the intermolecular distances among dendrimer molecules were much bigger than those in thin films and much more empty space was provided for TNT vapors to interact with the cores of the dendrimers. Even though the fluorescence quenching of **PYTPA** solutions by TNT is effective, a thin-film-based fluorescence sensor is necessary for practical detection of TNT vapors. As a result, research in this field was stopped at this point.

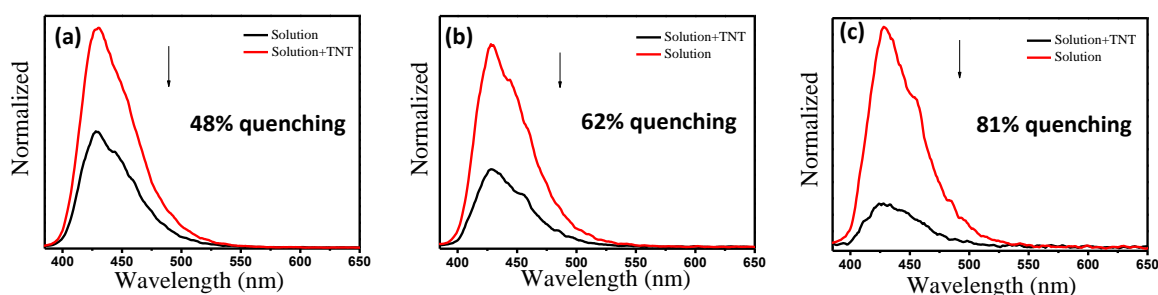


Figure 4.3: Fluorescence quenching of **PYTPA** solution to TNT (conc. of TNT: 10^{-7} M (a), 10^{-6} M (b) and 10^{-5} M (c)).

4.1.2 Fluorescence quenching of dendrimer solutions to metal ions

As the dendrimer films showed poor sensitivities to TNT vapors, it was attempted to detect metal ions. Solutions of the dendrimers were prepared (**PYTPA**: 10^{-6} M in THF and **PYTPAG2**: 10^{-6} M in THF/water (8/2, v/v). Metal salts included $\text{MgCl}_2 \cdot 6\text{H}_2\text{O}$, $\text{MnCl}_2 \cdot 4\text{H}_2\text{O}$, $\text{AlCl}_3 \cdot 6\text{H}_2\text{O}$, $\text{CoCl}_2 \cdot 6\text{H}_2\text{O}$, $\text{CuCl}_2 \cdot 2\text{H}_2\text{O}$, $\text{FeCl}_3 \cdot 6\text{H}_2\text{O}$, $\text{NiCl}_2 \cdot 6\text{H}_2\text{O}$, $\text{CrCl}_3 \cdot 6\text{H}_2\text{O}$, $\text{ZnCl}_2 \cdot 6\text{H}_2\text{O}$, NaCl, HgCl_2 and $\text{Pb}(\text{NO}_3)_2$, purchased from Sinopharm Chemical Reagent Co., Ltd. Each salts were prepared as 0.1 M methanol

solutions for **PYTPA** and as 0.1 M water solutions for **PYTPAG2**. After that, a salt solution was added into a quartz cuvette containing a dendrimer solution and after a while, the fluorescence spectra were measured and the emission intensity was compared with that of the pure dendrimer solution. All the salts were tested according to the procedure mentioned above. The magnitude of fluorescence quenching was denoted as $1 - I/I_0$, where I and I_0 meant the fluorescence intensity after and before adding metal salt solution.

As depicted in Figure 4.4, both dendrimer solutions were highly sensitive to Fe^{3+} with strong fluorescence quenching. Cu^{2+} partially quenched the emission of **PYTPA** (~30%). Al^{3+} and Zn^{2+} had minor effects to **PYTPA** (~5%). Other metal ions, i.e. Mg^{2+} , Mn^{2+} , Co^{2+} and Ni^{2+} did not response to **PYTPA** at all. For **PYTPAG2**, surprisingly, except Fe^{3+} , other metal ions displayed no quenching effects at all. The high selectivity of **PYTPAG2** to Fe^{3+} makes it a promising chemical sensor for Fe^{3+} .

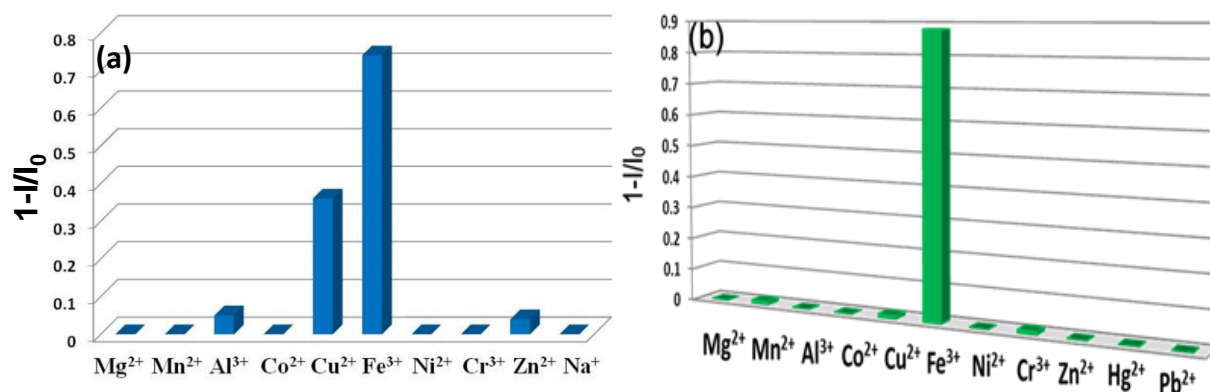


Figure 4.4: Fluorescence quenching of **PYTPA** (a) and **PYTPAG2** (b) solutions by metal ions.

The reason for the strong fluorescence quenching by Fe^{3+} can be explained by the interactions between the peripheral **TPAs** of the dendrimers with ferric ions. As **TPA** is a strong donor with a nitrogen atom containing a lone pair of electrons, Fe^{3+} could accept the lone pair of electrons to form weakly coordinated “**TPA-Fe**” complexes.^[3] This is supported by the increase of the absorption intensity of the dendrimer solution after the addition of Fe^{3+} . As depicted in Figure 4.5, with the concentration of the Fe^{3+} increasing, the absorption intensity was increased considerably and the starting peak wavelength centered at around 308 nm (**TPA**-self absorption, see chapter 2) was gradually red-shifted to around 330 nm when the concentration of ferric ion reached 50 μM or higher. This proved the interactions between Fe^{3+} and **TPAs**. The absorption band of the core between 370 and 422 nm was not increased markedly in comparison. In addition, the absorption onset (~422nm) corresponding to the energy gap of the core kept the same during the addition of ferric ions. Consequently, it was deduced that ferric ions interacted with **TPAs** rather than the core. As to the fluorescence quenching, after excitation at 370 nm, the strong absorption by the surface **TPA-Fe** complexes reduced the amount of photons absorbed by the core significantly. Moreover, the surface-to-core energy transfer did not work any more probably due to the

non-emissive property of the TPA-Fe complexes. What's more, the fluorescence life time was not changed before and after the addition of ferric ions, suggesting that photo-induced electron transfer probably did not occur.^[4]

The reason for the high selectivity of the dendrimers towards Fe^{3+} could be rationalized by its very high reduction potential (corresponding to strong electron affinity) and its small size (making it easier to get close to the "N" atoms and accept electrons).^[5] As displayed in Table 4.1, Fe^{3+} has higher reduction potentials than most other metal ions in the experiments. Even though Hg^{2+} ions exhibit a higher reduction potential than Fe^{3+} , its much bigger diameter (2.0 Å) than Fe^{3+} (1.1 Å) limits the interactions with electron rich "N" atoms of TPAs significantly, due to the steric hindrance from the two N-phenyl groups of TPA (distance between them: ~ 2.4 Å, obtained from single crystal structure of triphenylamine,^[6] measured between the two carbon atoms directly bonded to the "N" atom). The moderate quenching effect of Cu^{2+} toward PYTPA is consistent with its lower reduction potential and bigger size than Fe^{3+} . Due to the much lower reduction potentials of most other metal ions than Fe^{3+} , together with their bigger sizes than Fe^{3+} , the quenching effects of most metal ions were trivial. The reason for the higher selectivity of PYTPAG2 than PYTPA is that the surface-to-core energy transfer in the former is much more difficult to be blocked than the latter in that the former has twice as many TPAs as the latter so that the surface of PYTPAG2 is even harder to be fully doped by other metal ions except Fe^{3+} .

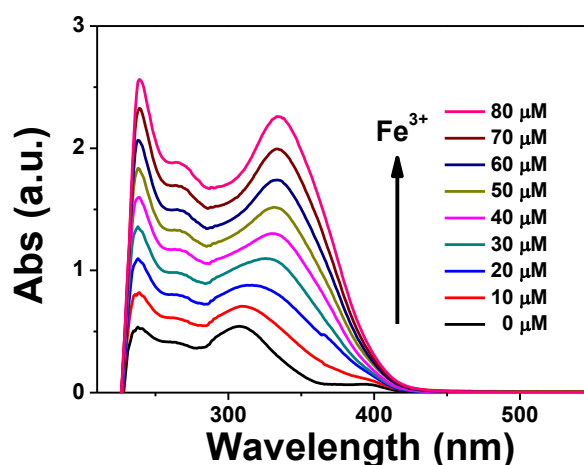


Figure 4.5: UV-vis absorption spectra of PYTPAG2 solution with different concentrations of Fe^{3+} .

Table 4.1: Standard reduction potentials (RP°) and diameters of metal ions. ^{[7] [8]}

	Fe^{3+}	Hg^{2+}	Cu^{2+}	Mg^{2+}	Al^{3+}	Ni^{2+}	Co^{2+}	Zn^{2+}	Pb^{2+}	Mn^{2+}	Cr^{3+}
RP°/V	0.77	0.85	0.34	-2.36	-1.66	-0.25	-0.28	-0.76	-0.13	-1.18	-0.74
Diameter/Å	1.1	2.0	1.5	1.4	1.1	1.4	1.5	1.6	2.3	1.3	1.5

The detailed photoluminescence spectra of **PYTPAG2** solution upon the addition of Fe^{3+} were shown in Figure 4.6 (a). After gradual addition of Fe^{3+} , the fluorescence of **PYTPAG2** was quenched very fast with a quick response in 1–2 seconds, suggesting that **PYTPAG2** had a rapid response to Fe^{3+} . From the fluorescence titration curve (Figure 4.6 (a) inset) of **PYTPAG2** upon addition of Fe^{3+} , the fluorescence static quenching coefficient (K_{sv}) was calculated from the slope of the titration curve at low concentrations according to the modified Stern-Volmer equation:

$$\lg(I_0-I)/I = \lg K_{sv} + n \lg(Q) \quad \text{Equation 1}$$

Where I_0 and I represented the fluorescence intensity in the absence and presence of Fe^{3+} , Q was the concentration of Fe^{3+} , and n meant the ratio between metal ions and the sensing materials. The K_{sv} and n of **PYTPAG2** upon addition of Fe^{3+} were calculated to be 4.64×10^8 and 1.92, respectively. From the linear response of fluorescence quenching and the concentration of Fe^{3+} as shown in Figure 4.6 (a) inset, the fluorescence detection limit of **PYTPAG2** solution to Fe^{3+} was calculated to be 6.5×10^{-7} M, which was much lower than the drinking water maximum contaminant level (MCL) ($\sim 5.357 \times 10^{-6}$ M) of the U.S Environmental Protection Agency (EPA).^[9]

It is known that the detection of Fe^{3+} is easily interfered by pH.^[10] As depicted in Figure 4.6 (b), however, **PYTPAG2** presented comparatively stable fluorescence quenching towards pH between 1 and 11. In addition, Mn^{2+} , Cu^{2+} and Cr^{3+} are known as the major interfering ions for the detection of Fe^{3+} .^[11] As depicted in Figure 4.6 (c), the fluorescence intensity of the **PYTPAG2** did not change noticeably after the addition of Mn^{2+} , Cu^{2+} and Cr^{3+} but decreased by 88% after the addition of Fe^{3+} . Furthermore, different counter anions' influences on the sensing performance of **PYTPAG2** solution were studied with $\text{Fe}_2(\text{SO}_4)_3$ and $\text{Fe}(\text{NO}_3)_3$. It turned out that the fluorescence quenching was barely influenced by the counter anions.

In order to confirm the practicability of **PYTPAG2** for real world applications, natural water including tap, snow, drinking and lake (South Lake at Chang Chun City) water were collected and directly utilized for experiments and **PYTPAG2** in deionized water was used as the reference. As depicted in Figure 4.6 (d), all the natural water had little effect on the fluorescence of the dendrimer solution. However, after adding Fe^{3+} into the solutions, the fluorescence intensities of the solutions were significantly decreased with similar quenching magnitude as that of **PYTPAG2** in deionized water (above 90%).

These results demonstrated that **PYTPAG2** solutions have high sensitivity and selectivity toward Fe^{3+} detection under all kinds of environments, e.g. different pH, different metal ions and counter anions and natural water system.

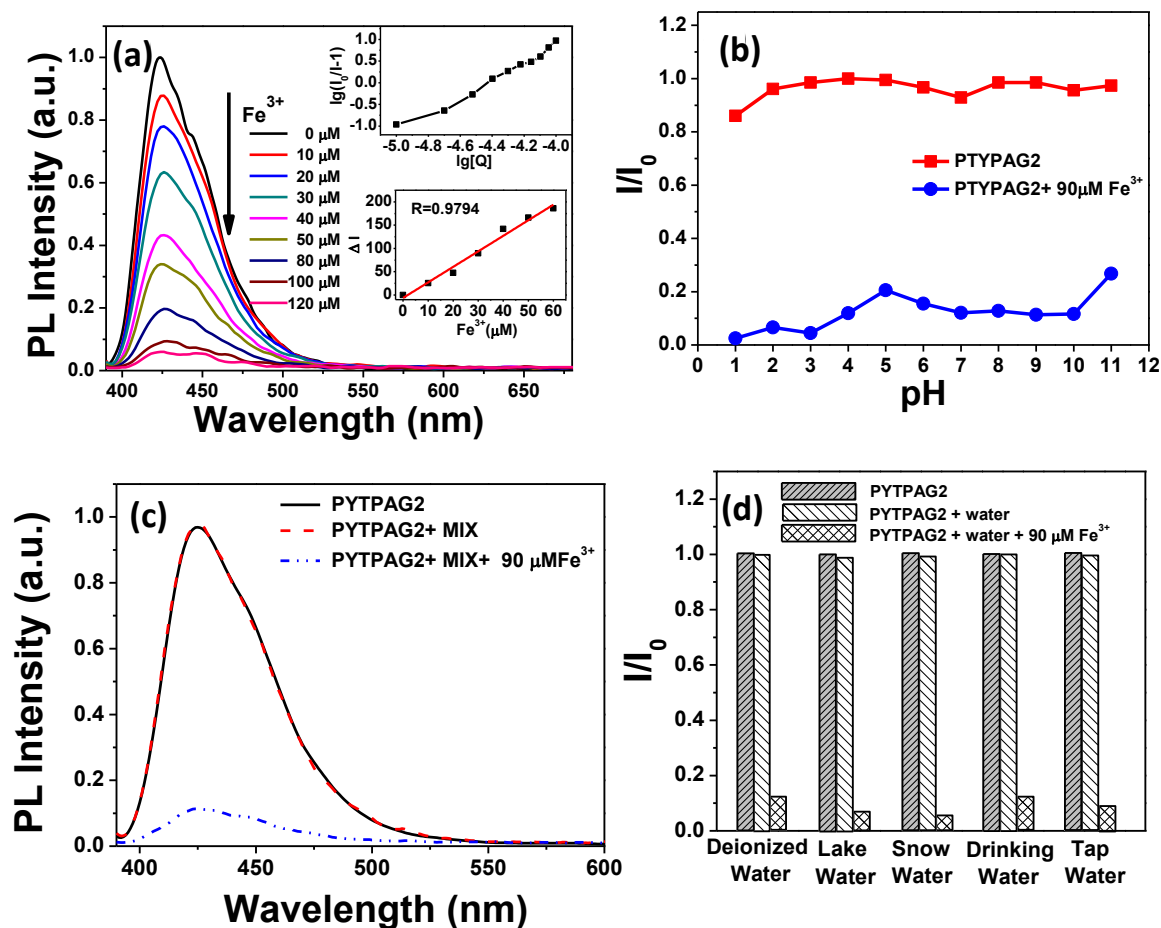


Figure 4.6: (a) photoluminescence spectra of **PYTPAG2** solutions with different concentration of Fe^{3+} (Inset: the titration curve (up) and linear relationship between fluorescence quenching and concentration of Fe^{3+} (down)); (b) relationship between fluorescence quenching of **PYTPAG2** solutions upon the addition of 90 μM Fe^{3+} and different pH; (c) interfering effects of mixed metal ions (Mn^{2+} , Cu^{2+} and Cr^{3+} , each 200 μM) on the fluorescence quenching of **PYTPAG2** solutions by Fe^{3+} (90 μM); (d) the interfering effects of real world water on the fluorescence quenching of **PYTPAG2** solutions by Fe^{3+} (90 μM).

4.1.3 Fluorescence quenching of PYTPAG2 thin films to metal ions

In terms of practicality, thin films are of more interest compared with solutions. Thereby, spin-coated films of **PYTPAG2** were employed to detect Fe^{3+} . As depicted in Figure 4.7, The fluorescence quenching of the film reached around 50% by the addition of 40 μM Fe^{3+} , similar as that obtained in solutions (Figure 4.6(a)), suggesting almost identical quenching effect of thin films and solutions of **PYTPAG2** toward Fe^{3+} . As the dendrimer surface was filled with **TPAs**, Fe^{3+} could easily interact with **TPAs** on the film surface. This was different from the trivial fluorescence quenching of **PYTPAG2** thin films by TNT, in which the interactions between TNT molecules and the cores of the dendrimers were significantly restricted due to the protection of the core by the bulky dendrons and the densely packed films.

According to the modified Stern-Volmer equation, the K_{sv} and “n” of **PYTPAG2** upon addition of Fe^{3+} were calculated to be 2.3×10^9 and 2.12 respectively (Figure 4.7). Based on a linear response between fluorescence quenching and the concentration of Fe^{3+} , the fluorescence detection limit of **PYTPAG2** thin film to Fe^{3+} was calculated to be 5.0×10^{-7} M which was similar as the value obtained in **PYTPAG2** solutions. As shown in Table 4.2, the quick response (1-2 seconds in this work vs. >10 minutes for others), high selectivity (only sensitive to Fe^{3+} vs. many interfered by other ions) and low detection limit (5×10^{-7} M in thin films) of **PYTPAG2** towards Fe^{3+} make this material among the best fluorescence sensors for Fe^{3+} detection.

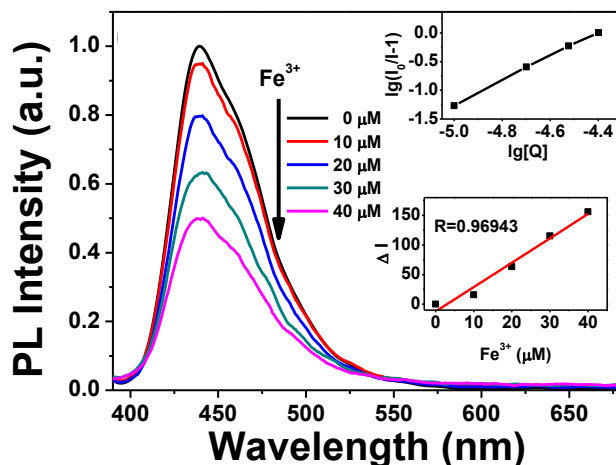


Figure 4.7: Photoluminescence spectra of **PYTPAG2** films under different concentrations of Fe^{3+} (inset: the titration curve (up) and linear response between ΔI and conc. (Fe^{3+}) (down)).

Table 4.2: Comparison of the performances of some reported Fe^{3+} sensors.

Sensor	Reaction time	Detection limit		Selectivity (interfering ions)
		Solution (K_{sv})	Film (K_{sv})	
This work	1-2 s	6.5×10^{-7} M (4.6×10^8)	5×10^{-7} M (2.3×10^9)	High
M2 ^[1]	10 min		6×10^{-5} M	Medium (Mn^{2+} , N^{2+})
HPS-PC ^[2]	12 min		5×10^{-9} M	Poor (Hg^{2+})
UMCM-1-NH2 ^[3]			(2.5×10^5)	High
Fluoranthene-NH2 ^[4]		2.5×10^{-7} M		High
Film-P1 ^[5]	30 min		1.5×10^{-7} M (1.3×10^6)	Medium (Cu^{2+} , Co^{2+})
M1 ^[6]		5×10^{-6} M (1.4×10^7)		Medium (Cu^{2+})
MIL-53(Al) ^[7]	30 min		9×10^{-7} M	High
BODIPY1 ^[8]		1.3×10^{-7} M		High
S-GQD ^[9]	10 min	4.2×10^{-9} M		High

To examine the detection capability of the films in real world environment, natural water samples were tested as well. As depicted in Figure 4.8 (a), natural water (e.g. lake water, snow water) did not notably

change the fluorescence intensity of the film. However, significant fluorescence quenching for all samples ($\sim 50\%$ quenching) were observed after the addition of Fe^{3+} ($40 \mu\text{M}$). In addition, as depicted in Figure 4.8 (b), mixed metal ions (Mn^{2+} , Cu^{2+} and Cr^{3+} , each $100 \mu\text{M}$) did not quench the fluorescence of the film but considerable fluorescence quenching occurred after adding Fe^{3+} ($40 \mu\text{M}$). Moreover, this film also showed high reusability. The used films were recycled successfully by sequentially washing with ethylene diaminetetraacetic acid (EDTA) and water for 3 times and then annealing in vacuum at 45°C for 3 hours. As depicted in Figure 4.8 (c), after recycling for 3 times, the fluorescence quenching of the film by Fe^{3+} still reached around 40% .

Therefore, thin films of **PYTPAG2** exhibited high sensitivity and selectivity toward Fe^{3+} . The high performances were remained under real world environments, e.g. nature water and interfering metal ions, similar as **PYTPAG2** solutions. In addition, it demonstrated high reusability of the films.

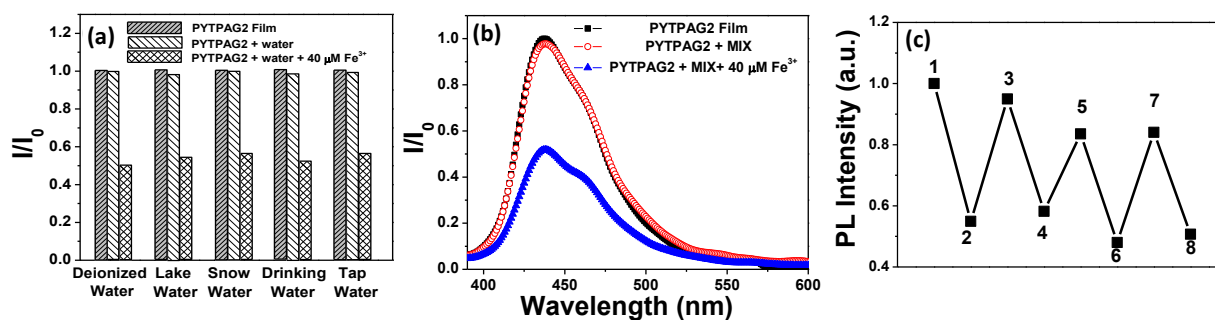


Figure 4.8: Fluorescent response of **PYTPAG2** films to Fe^{3+} in nature water (a); fluorescent response of **PYTPAG2** films to mixed metal ions (Mn^{2+} , Cu^{2+} and Cr^{3+} , each $100 \mu\text{M}$) with and without Fe^{3+} (b); fluorescence recovery cycles of **PYTPAG2** films (c).

In summary, thin films of **PYTPA** and **PYTPAG2** both manifested very poor sensitivity towards TNT vapors, probably due to the densely packed films and lack of a pathway for TNT molecules to penetrate inside the films and to interact with the pyrene moieties of the dendrimers. However, both **PYTPA** and **PYTPAG2** solutions displayed high sensitivities towards Fe^{3+} due to its stronger electron affinity and smaller size than most other metal ions, which enabled Fe^{3+} ions accept the shielded lone pair of electrons of “N” atoms in triphenylamines much easier. Especially, **PYTPAG2** exhibited better selectivity to Fe^{3+} than **PYTPA** due to the double-numbered **TPAs** in the former. The performance of **PYTPAG2** thin films was similar as its solutions and was remained under natural environments, e.g. interfering metal ions and natural water. Moreover, **PYTPAG2** films showed good reusability. Consequently, **PYTPAG2** promises to be a good fluorescence sensor for Fe^{3+} .

In the next section, a new strategy to further improve the sensor performance of **PYTPAG2** will be described.

4.2 Electropolymerized (EP) thin films of PYTPAG2 for chemical sensors

Electrochemistry is a way to grow organic thin films on the working electrode from organic materials containing electroactive moieties, e.g. thiophene, pyrrole, triphenylamine and carbazole by intermolecular oxidative couplings.^[18] It was utilized to produce three-dimensional networks by polymerizing a dendrimer with oligothiophenes in the periphery.^[19] In addition, cross-linked films on ITO were made by this method and worked as hole injection or emitting layer in OLEDs, due to the insolubility of the cross-linked films in most organic solvents, which is beneficial for orthogonally coating of other layers.^[18d] Moreover, thin films obtained by intermolecular couplings of molecules bearing carbazoles were employed in detecting metal ions due to the microporous structures of the cross-linked films which provided sufficient surface areas to interact with the analytes.^[12]

Therefore, it will be a good idea to polymerize **PYTPAG2** by electrochemistry and form a cross-linked film to increase its sensitivity to TNT and Fe^{3+} because the obtained film is microporous with more surface areas than spin-coated films. As depicted in Figure 4.9, the electropolymerized (**EP**), cross-linked films were prepared by intermolecular couplings of **TPAs** among **PYTPAG2** molecules and subsequent formation of tetraphenylbenzidines (**TPBs**) as the bridges of the 3-dimensional architecture.

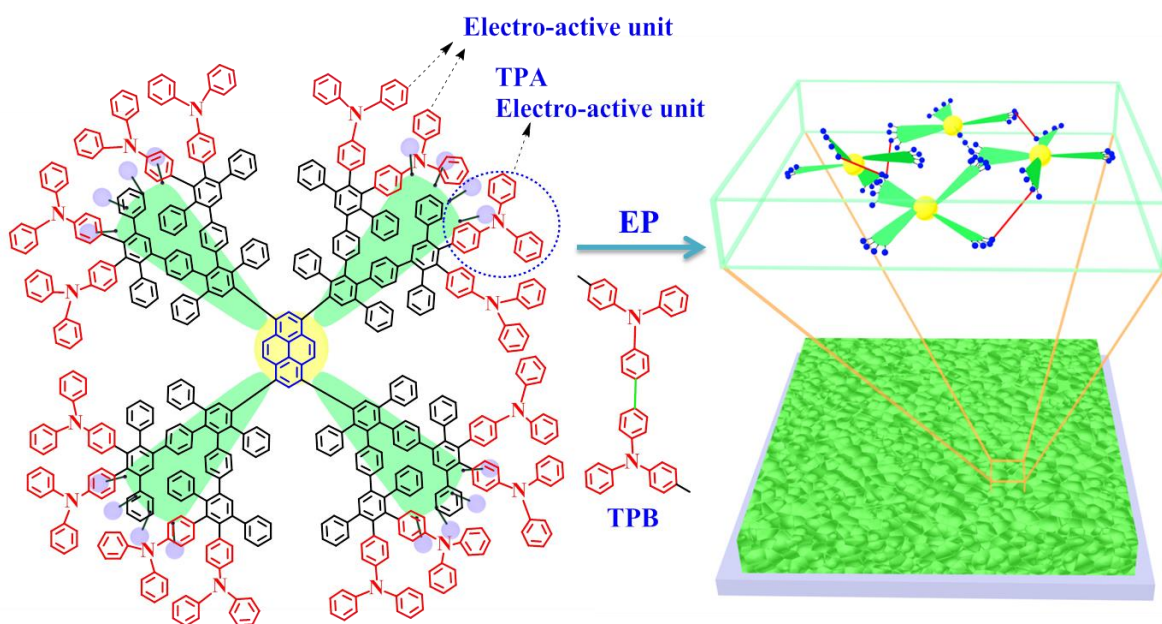


Figure 4.9: The process of formation of **PYTPAG2**-based **EP** films by electrochemistry.

4.2.1 Fabrication of EP films

The **EP** film fabrications and sensor experiments were carried out by the research group of Prof. Ming Zhang from State Key Laboratory of Supramolecular Structure and Materials, Jilin University, China. Cyclic voltammetry was utilized to prepare **EP** films using a standard one-compartment, three-electrode electrochemical cell. A titanium metal worked as the counter electrode ($\sim 2 \times 4 \text{ cm}^2$). An ITO ($\sim 1.3 \times 2.5 \text{ cm}^2$) served as the working electrode and a silver wire was the reference electrode. The film growth was

conducted in 0.1 M tetrabutylammonium perchlorate (TBAP) solution in DCM. The concentration of **PYTPAG2** was 1×10^{-5} M. Thin films were formed directly on ITO surface.

From the CV curves (Figure 4.10), one oxidation peak centered at around 0.80 V was observed in the first scan. It was attributed to the oxidization of **TPAs**.^[20] In the reverse scan, two reduction waves were observed, one at around 0.7 and the other at 0.50 V. The first one corresponded to the reduction of **TPA**⁺ into its neutral form and the second one was due to the reduction of **TPB**⁺ which was formed during the first forward scan. The oxidation wave of **TPB** started from the second cycle with a more negative potential (~ 0.55 V) than that of **TPAs** due to the increased conjugations of **TPB**.^[21] Moreover, the current intensity increased with the number of scans, indicating the growing of a dendrimer-based, cross-linked film on ITO surface. The lowest scanning potential was set at -0.2 V to decrease the amount of electrolyte doped in the **EP** films and reduce the risk of fluorescence quenching of the films by the electrolyte.^[18d]

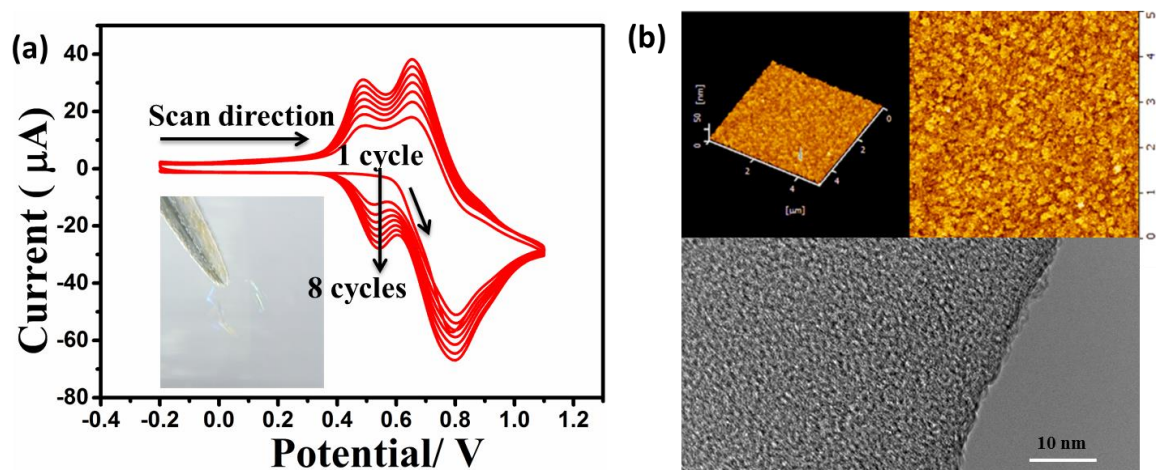


Figure 4.10: CV curves of **PYTPAG2** for 8 cycles (scan rate: 100 mV/s, the inset: image of a free-standing film obtained by immersing the **EP** film on ITO into a diluted HCl solution for 60 s) (a); AFM and TEM images of an **EP** film (RMS: 3.08 nm) (b).

The film thickness could be controlled by the number of sweeps and films after 8 CV cycles (thickness: ~ 16 nm) were selected as the fluorescent probes. The films were transparent after washing with pure DCM for several times. Then, they were dried in vacuum at 40°C for three hours and were ready for sensor experiments. In addition, as depicted in Figure 4.10 (a, inset), the films could be peeled off easily by immersing them into diluted HCl solutions for 60 seconds. Due to the cross-linked architectures of the films, they were stable and insoluble in many organic solvents, such as DCM, toluene and THF.

The porosity of the **EP** film was studied by atomic force microscopy (AFM) and transmission electron microscopy (TEM). As depicted in Figure 4.10 (b), the film possessed a porous structure (pore size: ~ 1 nm). In addition, the **EP** film exhibited strong blue emission (Figure 4.11). Based on its strong

fluorescence and cross-linked porous structure, **PYTPAG2**-based **EP** film suggests a promising candidate in detecting explosives, metal ions and arene vapors.^[2a] [14, 22]

4.2.2 EP films as chemical sensors

4.2.2.1 Fluorescence quenching of EP films by explosives

First, **EP** films were studied as fluorescence quenching (turn-off) probes for TNT, DNT, cyclotrimethylenetrinitramine (RDX), methyl-2,4,6-trinitrophenylnitramine (Tetryl), 1,3,5,7-tetranitro-1,3,5,7-tetraazacyclooctane (HMX), pentaerythritol tetranitrate (PETN), 2,4,6-trinitrophenol (TNP), 2,4-dinitrophenol (DNP) and 4-nitrophenol (NP) vapors. The procedure for the tests is as follows:

The explosive powder was put into the bottom of the cell and a suitable filter paper was covered on it to prevent direct contact of the EP film with the analyte. Then the quartz cell was sealed. After 60 minutes, a saturated explosive vapor was reached at ambient condition and an **EP** film was placed inside the cell. Then, the fluorescence spectra were recorded at varying time (0 s, 10 s, 20 s, 60 s and 120 s) with the excitation wavelength of 360 nm.

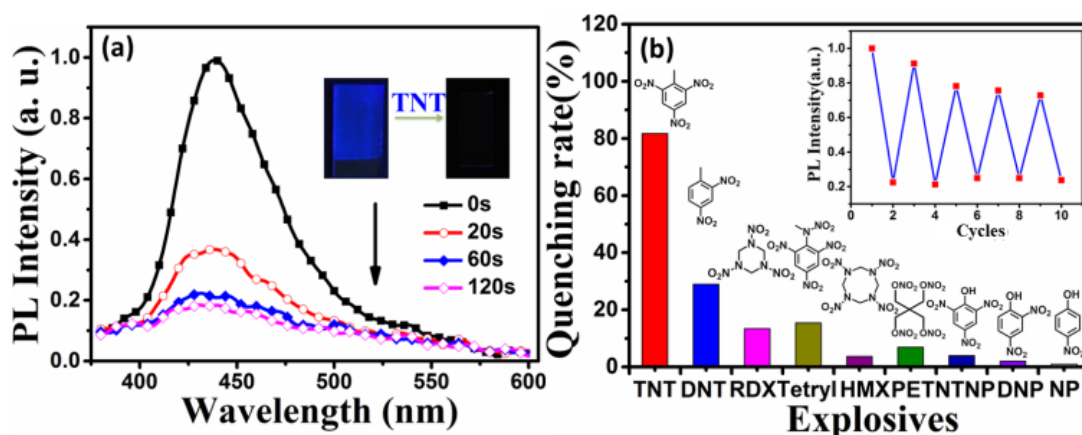


Figure 4.11: (a) Time-dependent photoluminescence spectra of an **EP** film upon exposure to TNT (inset: the emission of an **EP** film before and after exposed to TNT for 120 s); (b) Fluorescence quenching rates of EP films exposed to different nitro-rich molecules after 120 s (inset: the fluorescent recovery cycles of an EP film exposed to TNT).

As depicted in Figure 4.11, the **EP** film had high sensitivity and selectivity to TNT. For comparison, the emission of a pure **EP** film was first obtained with the peak wavelength of 438 nm which was exactly the same as that of the bare spin-coated **PYTPAG2** film (see chapter two), indicating the emission of the **EP** film was from the core.^[20b] After being exposed to TNT vapor, the emission of the **EP** film was quenched by 63 % in 20 s and by 82 % in 120 s, suggesting a quick response to TNT. On the other hand, other nitro-rich compounds could barely influence the emission of this **EP** film, except DNT which quenched the fluorescence by around 30% after 120 s. As displayed in Table 4.3,^[23] the **EP** film is

among the best fluorescence sensors reported so far to detect TNT due to the **EP** film's quick response to TNT than many other fluorescence sensors. For example, the **EP** film was quenched by 79% in 60 seconds but many other sensors can not reach this value within the same time.

Table 4.3: Reported fluorescence quenching data for explosives.

Sensor (explosives)	Fluorescence Quenching Rate (exposure time)		Reference
EP films(TNT)	79 % (60 s)	82 % (120 s)	This work [10]
P2 (TNB)	63 % (60 s)	89% (600 s)	[11]
PTBPE/PLA (TNB)	52% (120 s)	75 % (1800 s)	[12]
PCZ (TNT)	73 % (60 s)	-	[13]
P1-porous film (TNT)	64 % (60 s)	82% (300 s)	[14]
S1(PA)	21 % (120 s)	80% (600 s)	[15]
TCAC-EP films (TNT)	39 % (60 s)	66% (600 s)	[16]
FTPA-HBCPN (TNT)	16 % (60 s)	60% (600 s)	[17]
F5 thin film (PA)	40 % (60 s)	91% (210 s)	[18]
P1 (DNT)	48% (10 s)	97 % (300 s)	[19]
Fluorophore 3 (DNT)	-	~69 % (600 s)	[20]
Py-PES films (TNT)	50 % (15 s)	95% (60 s)	[21]
F1 film (TNT)	32 % (10 s)	87.4 % (300 s)	

The reason for the high sensitivity and selectivity of the **EP** film to TNT is related to its strong electron affinity of TNT because it has three nitro groups^[2a] and its relatively high vapor pressure. Pyrene moieties have been reported to work as fluorescence sensors for explosives.^[2c] The strong electro-accepting ability of TNT (LUMO= -3.74 eV) could accept electrons easily from pyrene (LUMO: ~ -2.40 eV) under excitation and as a result, quenches the emission of pyrene.^[24] For DNT, even though it has much higher vapor pressure than TNT (Table 4.4),^[24] its electron affinity is reduced due to its fewer nitro groups than TNT, as a result, the sensitivity of the **EP** film to DNT is much weaker than TNT. The reason for minimal quenching effects to the **EP** films from other nitro-rich compounds can be attributed to their generally much smaller vapor pressures than TNT.

Table 4.4: Vapor pressures of different explosives at 25 °C.^[25]

Explosive	Vapor pressure (atm)
2,4-DNT	4.11E ⁻⁷
TNT	9.15E ⁻⁹
TNP	9.71E ⁻¹⁰
PETN	1.07E ⁻¹¹
Tetryl	7.41E ⁻¹²
RDX	4.85E ⁻¹²
HMX	2.37E ⁻¹⁷

The quick response of the **EP** film in comparison with nearly no response of the spin-coated **PYTPAG2** film to TNT (see Figure 4.2) demonstrated that the cross-linked and microporous **EP** films provided much more space for the TNT vapors to penetrate inside the film and interact with pyrene moieties

adequately and the trivial fluorescence quenching of spin-coated films by TNT was due to its densely packed architecture.

Consequently, it is demonstrated that **PYTPAG2**-based, cross-linked films fabricated by electrochemistry could detect TNT with high sensitivity and selectivity. The cross-linked and microporous structure is essential, which provides pathways for TNT to penetrate inside of the film and interact adequately with pyrenes.

4.2.2.2 Fluorescence quenching of EP films by metal ions

As **PYTPAG2** has demonstrated high sensitivity and selectivity towards Fe^{3+} both in solutions and thin films, it is worthwhile to explore the **EP** film's responses to metal ions. To detect the ions, the **EP** film was immersed in an aqueous solution of a metal salt with a defined concentration for 5 seconds and a fluorescence spectra of the resulted **EP** film was measured. As depicted in Figure 4.12, the **EP** film was only quenched by Fe^{3+} and other ions showed minor effects towards this film. Fe^{2+} was also tried but its quenching was less than 5% as compared with the 89% quenching for Fe^{3+} . Thus it could be used to discriminate ferric and ferrous ion.^[26] The reason for the high sensitivity and selectivity of the **EP** film to Fe^{3+} rather than other metal ions is the general higher electron affinity together with the smaller size of Fe^{3+} than most other metal ions (refer to Table 4.1) to enable Fe^{3+} interact with the shielded "N" atoms of triphenylamines much easier. Moreover, as depicted in Figure 4.12 (inset), according to the fluorescent titration curve obtained by the addition of Fe^{3+} aqueous solutions, the quenching coefficient (K_{sv}) and the detection limit were calculated to be $3.6 \times 10^4 \text{ M}^{-1}$ and $8.5 \times 10^{-8} \text{ M}$ respectively.

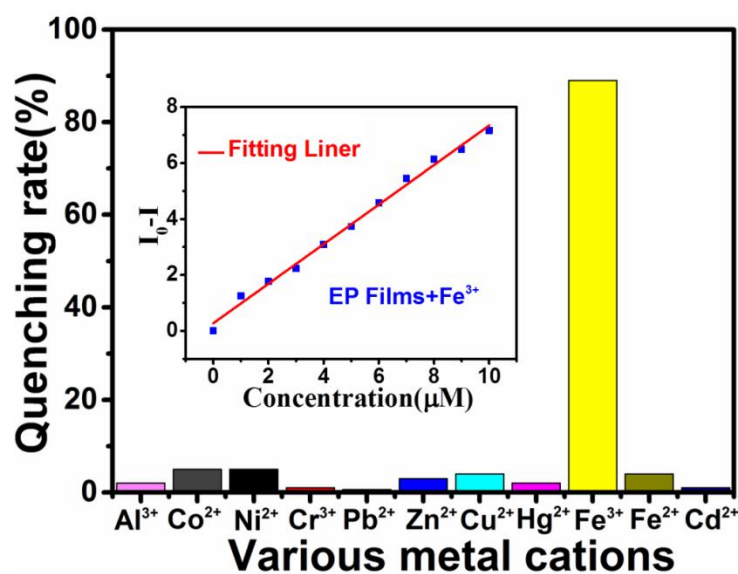


Figure 4.12: The quenching rates of **EP** films towards different aqueous solutions of metal ions ($1 \times 10^{-4} \text{ M}$) (inset: the titration curve of an **EP** film in Fe^{3+} aqueous solution).

The lower detection limit (8.5×10^{-8} M) of the **EP** film than that of spin-coated thin film (5.0×10^{-7} M) demonstrates that the former with porous structure and bigger surface areas than the latter enables Fe^{3+} not only interact with TPAs at the surface of the film but also interact with TPAs hidden inside of the film for stronger responses between the sensor and the analyte.

To detect the **EP** film's performance in real world environment, the influences of mixed metal ions, counter ions and pH to the film's response to Fe^{3+} were studied. As depicted in Figure 4.13 (a), a mixture of Al^{3+} , Co^{2+} , Ni^{2+} , Cr^{3+} , Pb^{2+} , Zn^{2+} , Cu^{2+} , Hg^{2+} , Fe^{2+} and Cd^{2+} ions was used to test the selectivity of **EP** film to ferric ion. It indicated that the fluorescence of the **EP** film was decreased only by 15 % after the addition of the ion mixture (1×10^{-4} M). However, upon addition of Fe^{3+} (1×10^{-4} M), the fluorescence intensity decreased by 89%. These results suggested that the **EP** film kept a high selectivity to Fe^{3+} with minor interference by other metal ions. In addition, counter anions' effects by $\text{Fe}_2(\text{SO}_4)_3$ and $\text{Fe}(\text{NO}_3)_3$ turned out that the fluorescence quenching was barely influenced by these anions. Moreover, pH dependence of fluorescence quenching showed that the quenching of **EP** films by Fe^{3+} was not interfered by pH ranging between 3 and 11 (Figure 4.13, b).

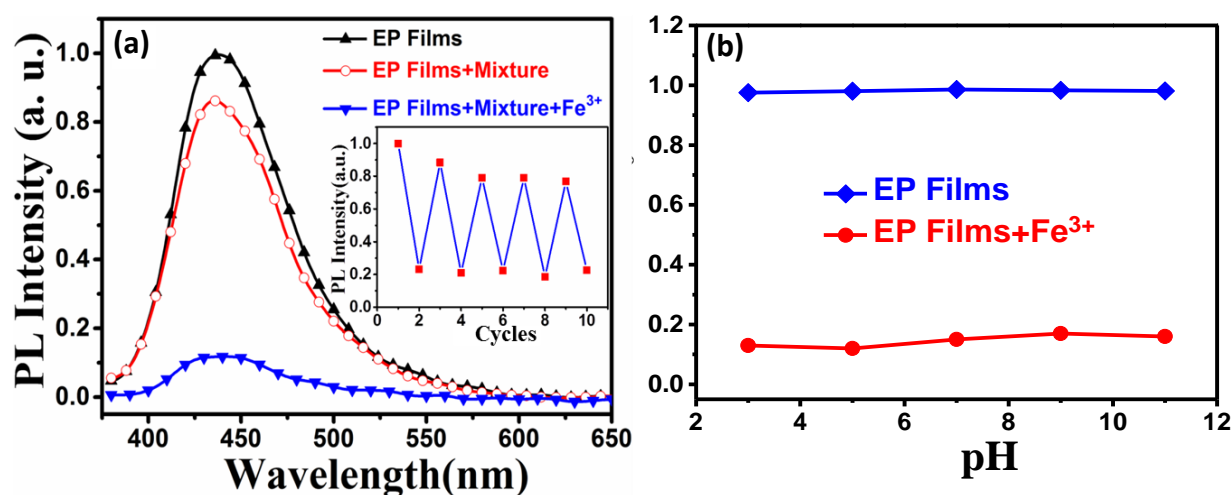


Figure 4.13: The influences of metal ions (a) and pH (b) on the fluorescence quenching of the **EP** film toward ferric ion (inset: the recycles of the **EP** film after Fe^{3+} detections).

In addition, this film showed good reusability. After sequentially washing the used **EP** film with ethylene diaminetetraacetic acid (EDTA) and water for three times, followed by drying in vacuum at 45°C for 3 hours, they were ready for use again. As depicted in Figure 4.13 (a, inset), even after 4 times' recycles, the fluorescence of the film still reached 78% of the new film, probably due to the small amount of Fe^{3+} trapped inside the film. The fluorescence quenching was around 58% in the 5th time detection.

Consequently, due to the quick response, high sensitivity and selectivity towards ferric ion and based on the little interference by other metal ions, counter anions and different pH and the good reusability, it is concluded that the **EP** film is a good chemical sensor for detecting Fe^{3+} in real-world environment. In addition, even though both the **EP** film and spin-coated film of **PYTPAG2** have demonstrated high sensitivity and selectivity toward ferric ion, the detection limit of the former is around one order of magnitude smaller than the latter (8.5×10^{-8} M vs. 5.0×10^{-7} M), revealing that the cross-linked and microporous structure is better than the spin-coated one for chemical sensor applications.

4.2.2.3 Fluorescence enhancements of EP films by arene vapors

The **EP** films can also work as fluorescence-enhancing (turn-on) probes to arene vapors, e.g. benzene, toluene and chlorobenzene. This effect has been observed in microporous metal-organic framework,^[22a] microporous conjugated polymer,^[22b] and linear conjugated polymers.^[27]

As depicted in Figure 4.14, the films displayed significant fluorescence enhancements when exposed to benzene, toluene and chlorobenzene vapors. Upon exposure to benzene vapor, the fluorescence intensity of the **EP** film increased 2 times in 20 seconds and nearly 4 times in 120 seconds. However, the fluorescence enhancements were around 1.7 times for toluene and 1.3 times for chlorobenzene respectively after 120 seconds. The higher sensitivity towards benzene is probably due to the higher vapor pressure of benzene (95.2 mmHg) than toluene (28.4 mmHg) and chlorobenzene (11.8 mmHg),^[22b] together with its smaller size to penetrate inside the film easier.

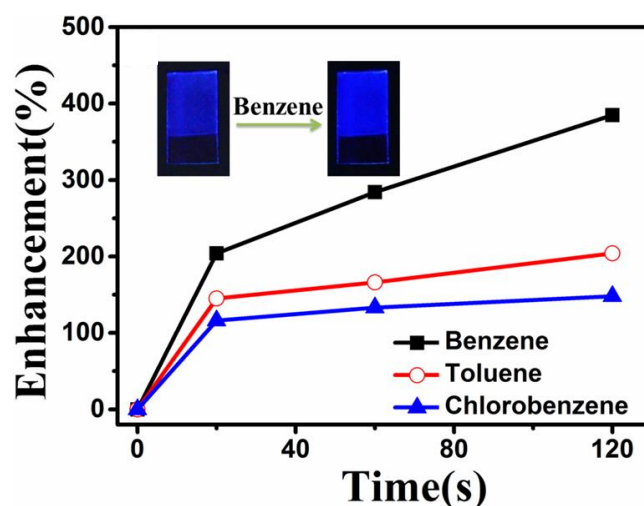


Figure 4.14: Time-dependent fluorescence enhancements of **EP** films upon exposure to benzene, toluene and chlorobenzene (inset: the emission of an **EP** film before and after exposing to benzene vapors for 120 s).

Currently, there are generally two explanations for fluorescence enhancements of the films by arene vapors. The first one is the electron donating of the arene vapors to the fluorescent films. As depicted in Figure 4.15, generally, small arene molecules, e.g. benzene, have very broad HOMO and LUMO energy

gaps. Benzene has a LUMO around -1.38 eV ^[22b], while the fluorescent moiety, pyrene in this system with a LUMO of around -2.4 eV (see chapter 2). As a result, it is proposed that an electron transfer occurs from arene vapor to the fluorescence sensor and radiative decay of the fluorescence sensor is follows.^[22]

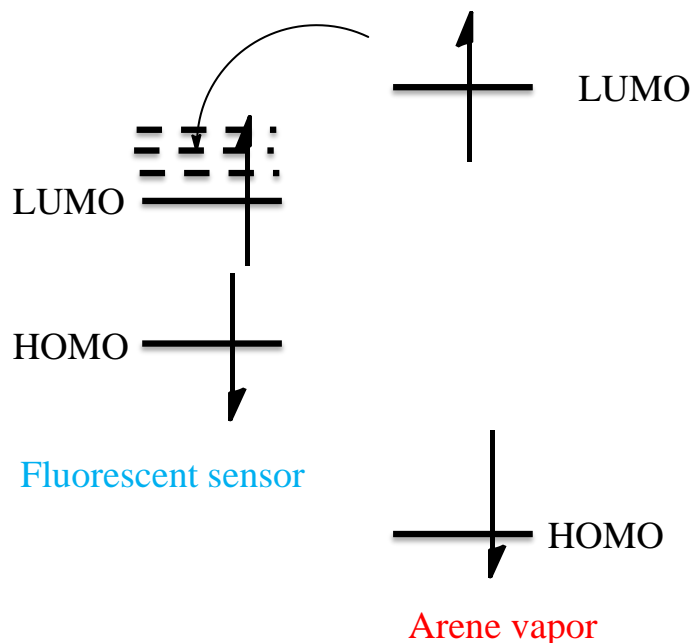


Figure 4.15: Electron donating from arene vapor to fluorescence sensor.

Another explanation is the swelling effect of the fluorescent materials after accommodating the arene molecules. The swelling of the film results in the enlarged intermolecular distances among the fluorescent molecules and reduces the aggregation-induced fluorescence quenching. This explanation has been applied to some polymer sensors with enlarged interchain distances under arene vapors as supported by theoretical simulations.^[27] The fluorescence enhancement of the **EP** film by arene vapors is more likely to be rationalized by an arene-to-pyrene electron transfer mechanism. The swelling mechanism could be excluded with several considerations: first, the cross-linked structure is quite rigid and the swelling of the network is highly difficult; second, pyrene moieties are well protected by the bulky dendrons and aggregation induced fluorescence quenching should be minimal.

The **EP** films also exhibited high reusability. The used films were recycled by drying under vacuum at $45\text{ }^{\circ}\text{C}$ for 3 hours. As depicted in Figure 4.16 a (inset), the fluorescence enhancement of the film generally kept around 200% among 5 cycles. The cleaned film showed slight fluorescence enhancement after each time of using, probably due to small amount of benzene vapor trapped inside the film. Higher temperature of drying should help to remove all benzene molecules in the film.

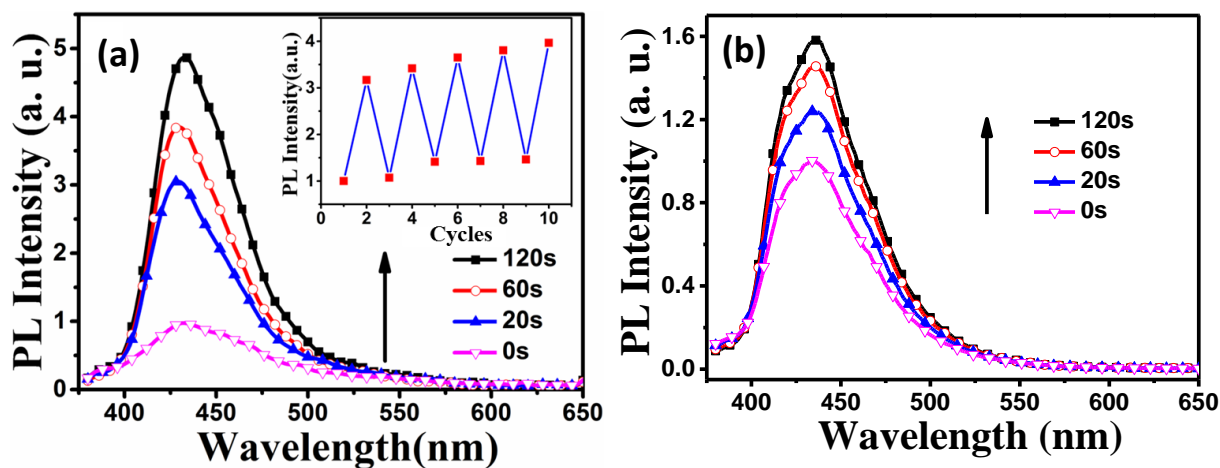


Figure 4.16: Time-dependent photoluminescence spectra of an **EP** film (a) and a spin-coated film (b) of **PYTPAG2** upon exposure to benzene vapor (inset: the recycling of an **EP** film exposing to benzene vapor for 20 s for each cycle).

For comparison, the spin-coated film of **PYTPAG2** was tested for fluorescence enhancement to benzene vapors. As depicted in Figure 4.16 b, the fluorescence intensity increased around 20% in 20 s and 60% in 120 s. This relatively small fluorescence enhancement compared with the substantial fluorescence enhancement of the **EP** film (200% enhancement in 20 s) again revealed that there were much less arene molecules going inside the spin-coated film which was self-assembled and densely packed. Once more, it demonstrated that the cross-linked and microporous **EP** film represented a better choice for chemical sensor applications.

4.3 Summary

PYTPA and **PYTPAG2** have been tested for chemical sensor applications. Both dendrimers demonstrated high sensitivities with significant fluorescence quenching towards Fe^{3+} . The reason is the very strong electron affinity of Fe^{3+} together with its smaller size than many other metal ions, which enable Fe^{3+} ions accept the free electrons of shielded “N” atoms of triphenylamines easily and block the surface-to-core energy transfer. In addition, **PYTPAG2** showed higher selectivity than **PYTPA** in detecting metal ions because the much more peripheral **TPA** in the former made the metal ions more difficult to block the surface-to-core energy transfer. The detection limits of **PYTPAG2** in solutions and thin films were both in 10^{-7} M range.

Both thin films of **PYTPA** and **PYTPAG2** exhibited very poor sensitivity towards TNT due to the lack of a pathway for the TNT vapors to penetrate inside the film and interact with pyrenes by the densely packed architecture. However, **EP** films obtained from electropolymerizing **PYTPAG2** demonstrated high sensitivity to TNT with fluorescence quenching by around 79% within 60 seconds, representing one of the best fluorescence sensors for TNT by now (see Table 4.3). The reason for the improved performance compared with spin-coated films is the cross-linked and microporous architecture of the

EP films which rendered the TNT molecules to interact with pyrene moieties hidden inside the films adequately. The reason for the high sensitivity of EP films to TNT rather than other nitro-rich molecules is attributed to TNT's strong electron affinity and its relatively higher vapor pressure than most others. In addition, the **EP** film was a good fluorescence sensor for Fe^{3+} with improved detection limit (8.5×10^{-8} M) compared with spin-coated films (5.0×10^{-7} M). Moreover, arene vapors, i.e. benzene, toluene and chlorobenzene enhanced the fluorescence of the **EP** films substantially. Especially, benzene vapor prompted 200% fluorescence enhancement in 20 seconds. The reason for the fluorescence enhancement is possibly related to the electron transfers from arene vapor to the LUMO of pyrene. In general, **EP** films in comparison with spin-coated films displayed better performances as chemical sensors and paved the way for better fluorescence sensor designs.

Literature

- [1] a) G. Aragay, J. Pons, J. Garcia-Anton, X. Solans, M. Font-Bardia, J. Ros, *J Organomet Chem* **2008**, 693, 3396-3404; b) W. F. Li, H. C. Ma, C. Lu, Y. Ma, C. X. Qi, Z. W. Zhang, Z. M. Yang, H. Y. Cao, Z. Q. Lei, *Rsc Adv* **2015**, 5, 6869-6878; c) J. L. Bricks, A. Kovalchuk, C. Trieflinger, M. Nofz, M. Buschel, A. I. Tolmachev, J. Daub, K. Rurack, *J Am Chem Soc* **2005**, 127, 13522-13529.
- [2] a) J. S. Yang, T. M. Swager, *J Am Chem Soc* **1998**, 120, 11864-11873; b) S. W. Thomas, G. D. Joly, T. M. Swager, *Chem Rev* **2007**, 107, 1339-1386; c) J. V. Goodpaster, V. L. McGuffin, *Anal Chem* **2001**, 73, 2004-2011.
- [3] a) Z. X. Li, L. F. Zhang, X. Y. Li, Y. K. Guo, Z. H. Ni, J. H. Chen, L. H. Wei, M. M. Yu, *Dyes Pigments* **2012**, 94, 60-65; b) Z. H. Xiang, C. Q. Fang, S. H. Leng, D. P. Cao, *J Mater Chem A* **2014**, 2, 7662-7665.
- [4] L. J. Fan, Y. Zhang, C. B. Murphy, S. E. Angell, M. F. L. Parker, B. R. Flynn, W. E. Jones, *Coordin Chem Rev* **2009**, 253, 410-422.
- [5] Y. Q. Zhang, X. D. Li, L. J. Gao, J. H. Qiu, L. P. Heng, B. Z. Tang, L. Jiang, *Chemphyschem* **2014**, 15, 507-513.
- [6] A. N. Sobolev, V. K. Belsky, I. P. Romm, N. Y. Chernikova, E. N. Guryanova, *Acta Crystallogr C* **1985**, 41, 967-971.
- [7] *Standard reduction potentials*, <http://www.csudh.edu/oliver/chemdata/data-e.htm>.
- [8] R. D. Shannon, *Acta Crystallogr A* **1976**, 32, 751-767.
- [9] <http://www.epa.gov/safewater/consumer/pdf/mcl.pdf>.
- [10] N. R. C. Campbell, B. B. Hasinoff, *Brit J Clin Pharmacol* **1991**, 31, 251-255.
- [11] H. Weizman, O. Ardon, B. Mester, J. Libman, O. Dwir, Y. Hadar, Y. Chen, A. Shanzer, *J Am Chem Soc* **1996**, 118, 12368-12375.
- [12] P. Li, C. Y. Ji, H. W. Ma, M. Zhang, Y. F. Cheng, *Chem-Eur J* **2014**, 20, 5741-5745.
- [13] X. F. Wu, B. W. Xu, H. Tong, L. X. Wang, *Macromolecules* **2010**, 43, 8917-8923.
- [14] P. Li, Y. Zhao, L. Yao, H. R. Nie, M. Zhang, *Sensor Actuat B-Chem* **2014**, 191, 332-336.
- [15] C. X. Yang, H. B. Ren, X. P. Yan, *Anal Chem* **2013**, 85, 7441-7446.
- [16] B. L. Sui, S. M. Tang, T. H. Liu, B. S. Kim, K. D. Belfield, *Acs Appl Mater Inter* **2014**, 6, 18408-18412.
- [17] S. H. Li, Y. C. Li, J. Cao, J. Zhu, L. Z. Fan, X. H. Li, *Anal Chem* **2014**, 86, 10201-10207.
- [18] a) E. Ruckenstein, J. S. Park, *Synthetic Met* **1991**, 44, 293-306; b) A. F. Diaz, J. I. Castillo, J. A. Logan, W. Y. Lee, *J Electroanal Chem* **1981**, 129, 115-132; c) E. T. Seo, R. F. Nelson, J. M. Fritsch, L. S. Marcoux, D. W. Leedy, R. N. Adams, *J Am Chem Soc* **1966**, 88, 3498-3503; d) C. Gu, W. Y. Dong, L. Yao, Y. Lv, Z. B. Zhang, D. Lu, Y. G. Ma, *Adv Mater* **2012**, 24, 2413-2417.
- [19] a) B. C. Sih, A. Teichert, M. O. Wolf, *Chem Mater* **2004**, 16, 2712-2718; b) H. John, R. Bauer, P. Espindola, P. Sonar, J. Heinze, K. Mullen, *Angew Chem Int Edit* **2005**, 44, 2447-2451.
- [20] a) R. F. Nelson, R. N. Adams, *J Am Chem Soc* **1968**, 90, 3925-3930; b) G. Zhang, M. Baumgarten, M. Auer, R. Trattnig, E. J. W. List-Kratochvil, K. Mullen, *Macromol Rapid Comm* **2014**, 35, 1931-1936.

- [21] J. Natera, L. Otero, L. Sereno, F. Fungo, N. S. Wang, Y. M. Tsai, T. Y. Hwu, K. T. Wong, *Macromolecules* **2007**, *40*, 4456-4463.
- [22] a) S. Pramanik, C. Zheng, X. Zhang, T. J. Emge, J. Li, *J Am Chem Soc* **2011**, *133*, 4153-4155; b) X. M. Liu, Y. H. Xu, D. L. Jiang, *J Am Chem Soc* **2012**, *134*, 8738-8741.
- [23] a) W. Y. Dong, Y. Y. Pan, M. Fritsch, U. Scherf, *J Polym Sci Pol Chem* **2015**, *53*, 1753-1761; b) K. Yuan, P. Y. Guo-Wang, T. Hu, L. Shi, R. Zeng, M. Forster, T. Pichler, Y. W. Chen, U. Scherf, *Chem Mater* **2015**, *27*, 7403-7411; c) H. R. Nie, Y. Zhao, M. Zhang, Y. G. Ma, M. Baumgarten, K. Mullen, *Chem Commun* **2011**, *47*, 1234-1236; d) B. W. Xu, Y. X. Xu, X. C. Wang, H. B. Li, X. F. Wu, H. Tong, L. X. Wang, *Polym Chem-Uk* **2013**, *4*, 5056-5059; e) N. Venkatramaiah, S. Kumar, S. Patil, *Chem Commun* **2012**, *48*, 5007-5009; f) H. W. Ma, L. Yao, P. Li, O. Ablikim, Y. F. Cheng, M. Zhang, *Chem-Eur J* **2014**, *20*, 11655-11658; g) X. F. Wu, H. B. Li, Y. X. Xu, B. W. Xu, H. Tong, L. X. Wang, *Nanoscale* **2014**, *6*, 2375-2380; h) S. Kumar, N. Venkatramaiah, S. Patil, *J Phys Chem C* **2013**, *117*, 7236-7245; i) K. R. Ghosh, S. K. Saha, Z. Y. Wang, *Polym Chem-Uk* **2014**, *5*, 5638-5643; j) S. Shanmugaraju, H. Jadhav, R. Karthik, P. S. Mukherjee, *Rsc Adv* **2013**, *3*, 4940-4950; k) G. B. Demirel, B. Daglar, M. Bayindir, *Chem Commun* **2013**, *49*, 6140-6142; l) P. Beyazkilic, A. Yildirim, M. Bayindir, *Acs Appl Mater Inter* **2014**, *6*, 4997-5004.
- [24] C. P. Chang, C. Y. Chao, J. H. Huang, A. K. Li, C. S. Hsu, M. S. Lin, B. R. Hsieh, A. C. Su, *Synthetic Met* **2004**, *144*, 297-301.
- [25] R. G. Ewing, M. J. Waltman, D. A. Atkinson, J. W. Grate, P. J. Hotchkiss, *Trac-Trend Anal Chem* **2013**, *42*, 35-48.
- [26] M. E. A. Fegley, T. Sandgren, J. L. Duffy-Matzner, A. T. Chen, W. E. Jones, *J Polym Sci Pol Chem* **2015**, *53*, 951-954.
- [27] G. He, N. Yan, H. Y. Kong, S. W. Yin, L. P. Ding, S. X. Qu, Y. Fang, *Macromolecules* **2011**, *44*, 703-710.

Chapter 5 PYPPDs as Hole Transporting Materials in Perovskite Solar Cells

In this chapter, **PYTPA**, **PYNPA** and **PYPPA** which have been discussed in chapter 2 are applied as hole transporting materials (**HTMs**) in Perovskite solar cells (**PSCs**). The initial device results will be presented and discussed.

5.1 Introduction

Perovskite solar cells (**PSCs**) have received magnificent attentions among the photovoltaic community within the last three years and evolved as a promising candidate for large area applications by replacing silicon-based solar cells because of the cheap materials, cost-effective device fabrications by solution-processing and very high PCEs (~20.1%, 2015)^[1] with prospects of further enhancements.^[2]

Currently, there are many strategies to engineer **PSCs** for better performances, e.g. device structure optimizations,^[3] methods for high-quality film formations,^[1, 3a, 3c, 3e, 4] composition control of Perovskite materials^[5] and attempts with novel **HTMs**.^[6] The most widely used **HTM** in **PSCs** is 2,2',7,7'-tetrakis-(N,N-di-4-methoxyphenylamino)-9,9'-spirobifluorene (**spiro-OMeTAD**) (Figure 5.1). Its initial report as **HTM** in solar cells was in 1998 by Grätzel and his coworkers who applied it as the **HTM** in solid-state **DSSC** and an overall PCE of 0.74% was obtained.^[7] With the emergence of Perovskite as a new light absorber in solar cells, device performances using **spiro-OMeTAD** as the **HTM** have obtained significant improvements with PCEs from 9% in 2012^[3a] to 19.3% in 2014.^[8] The reason for its high performance should relate to its proper HOMO level (-5.22 eV) which matches the valence band energy (VBE) of Perovskite, e.g. CH₃NH₃PbI₃ (**MAPbI₃**) (VBE: ~ -5.44 eV)^[9] and its spatial geometry which might facilitate charge transport. Even though many other small molecules with three-dimensional architectures have been utilized as **HTMs** in **PSCs** so far, their device performances could not compete with the reported best results employing **spiro-OMeTAD**.^[6] Only very few examples could get close to the performance of **spiro-OMeTAD** by now, for example, Gratia and his coworkers reported a triphenylamine-carbazole-based small molecule (**V886**, Figure 5.1) which reached a PCE of 16.9%.^[10]

Another important **HTM** is poly(triarylamine) (**PTAA**) (Figure 5.1), which contributes to several record performance **PSCs**,^[1, 5d, 11] the one with a PCE of 20.1%. The advantage of **PTAA** over other polymer materials in **PSCs** was explored by Soek and his coworkers who found that the device with **PTAA** exhibited the highest PCE (9.0%) among those with other **HTMs**, i.e. **P3HT** (6.7%), poly(2,6-(4,4-bis-(2-ethylhexyl)-4H-cyclopenta[2,1-b;3,4-b']dithiophene)-alt-4,7(2,1,3-benzothiadiazole) (**PCPDTBT**) (5.3%) and poly(N-9"-heptadecanyl-2,7-carbazole-alt-5,5-(4',7'-di-2-thienyl-2',1',3'-benzothiadiazole)

(PCDTBT) (4.2%). The authors tentatively attributed the higher performance of **PTAA** to the existence of specific chemical interactions between **PTAA** and **MAPbI₃** (e.g. between N and Pb atoms) and further studies were needed to confirm this.^[11] In addition, the higher hole mobility of **PTAA** ($\sim 1 \times 10^{-2}$ to 1×10^{-3} cm²/Vs) than the other polymers ($\sim 1 \times 10^{-4}$ cm²/Vs) should be another factor which contributes to the better performance.^[11]

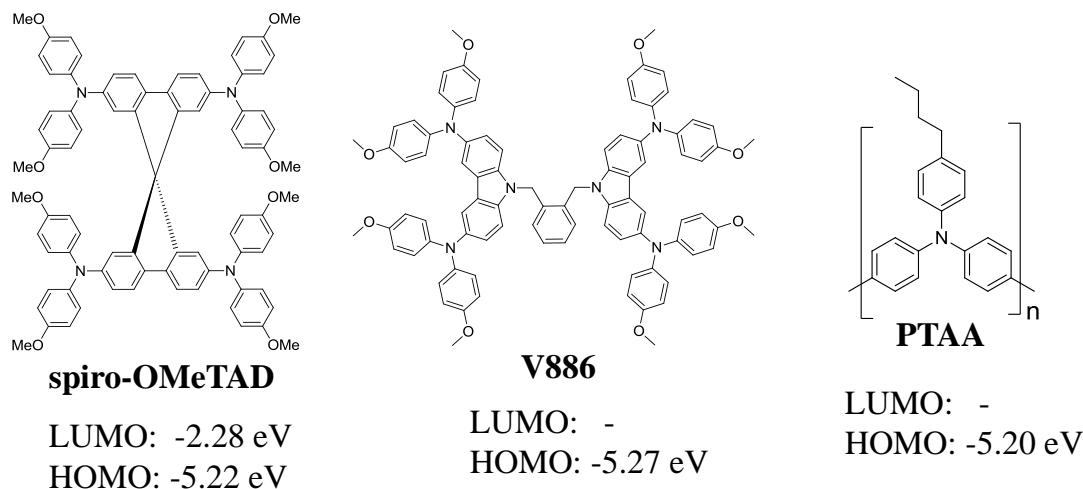


Figure 5.1: Molecular structures of **spiro-OMETAD**, **V886** and **PTAA** and their FMO levels (estimated from CV method for spiro-OMETAD^[9] and V886,^[10] from photo electron spectroscopy for **PTAA**^[12]).

PYTPA, **PYNPA** and **PYPPA** (Figure 5.2) were selected as **HTMs** in **PSCs** based on several considerations: first, they have demonstrated efficient hole transporting abilities in **OLEDs** (see chapter 2); second, their HOMO levels stem solely from their surface chromophores (between -5.36 and -5.25 eV) and have small energy barriers with the VBE of **MAPbI₃** for hole extractions; third, the very high LUMO levels of **TPA**, **NPA** and **PPA** compared with the conduction band energy of **MAPbI₃** (~ -3.93 eV) produce giant barriers to block electron transport from Perovskite to **HTMs**; fourth, the good solubilities of these dendrimers in organic solvents, e.g. THF and chlorobenzene make them suitable for solution-processed **PSC** fabrications.

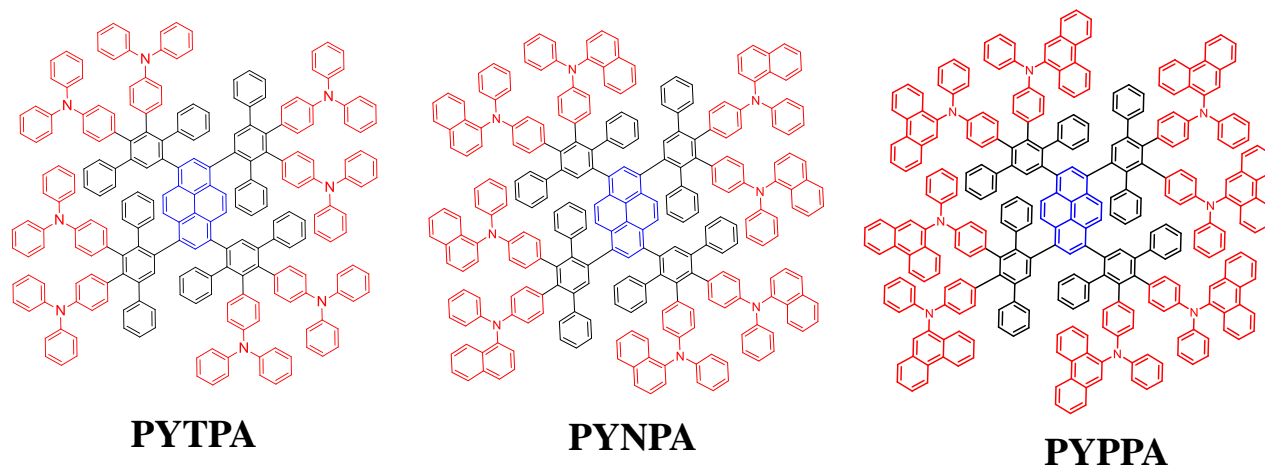


Figure 5.2: Molecular structures of **PYTPA**, **PYNPA** and **PYPPA**.

5.2 Device fabrications and performances

The device fabrications and characterizations were carried out by the research groups of Prof. Nanfeng Zheng and Prof. Yuanzhi Tan from Xiamen University, China. For device fabrications, mesoscopic device structures (Figure 5.3 and Figure 5.4) were employed. In the device, mesoporous TiO_2 worked as the electron transport material to collect the electrons generated in the interface between it and Perovskite layer and **PYPPDs** were the **HTMs** to neutralize the oxidized Perovskite quickly with electron transfers from the gold electrode to **PYPPDs** and subsequently to the Perovskite layer (Figure 5.3). The simplified device procedures for device fabrications are as follows:

First, a fluorine-doped tin oxide (FTO) glass substrate was patterned by etching with zinc powder and 2 M hydrochloric acid and washed thoroughly before use. Then a compact thin TiO_2 layer was introduced by spin coating using 0.15 M titanium tetraisopropanolate in 1-butanol solution with subsequent annealing process. Then, a mesoporous TiO_2 layer was added with approximate 200 nm thickness by spin coating TiO_2 pastes in ethanol, followed by heating at 550 °C for 30 minutes. After that, a Perovskite layer was deposited in two steps: first, a hot solution of PbI_2 in DMF was spin coated on the mesoporous surface of TiO_2 with subsequent drying at 120 °C for 5 minutes; second, a solution of $\text{CH}_3\text{NH}_3\text{I}$ in 2-propanol was spin coated on top and a layer of **MAPbI3** was formed instantly. After that, **PYPPD** in chlorobenzene (15 mg/ml) was spin-coated on top of the Perovskite layer. Finally, a gold electrode was deposited on top of the **PYPPD** layer.

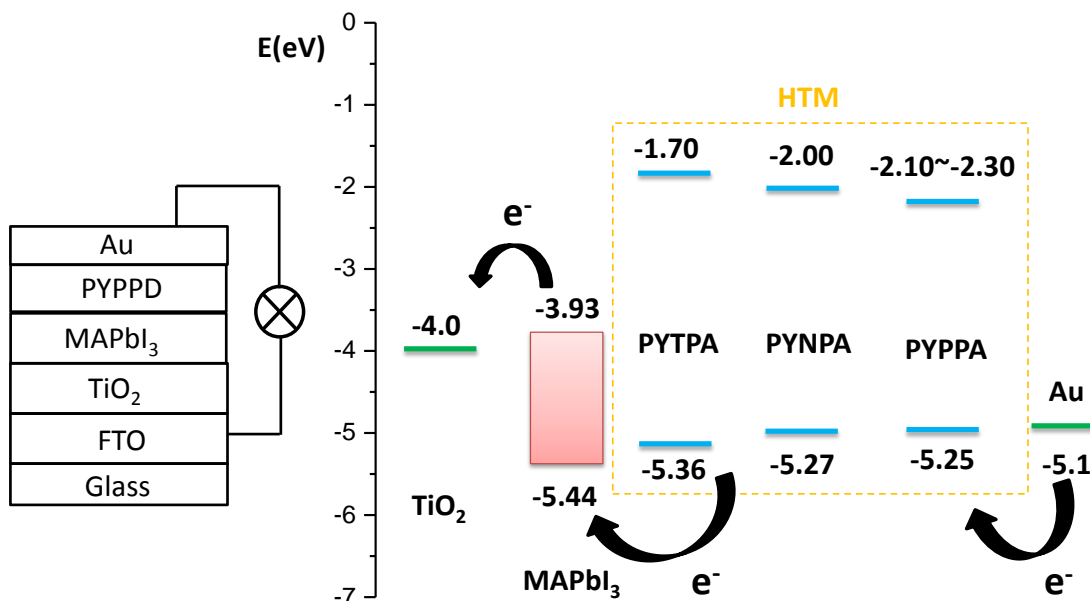


Figure 5.3: Device configuration (left) and the energy levels of each layer in a PSC (right).

Figure 5.4 depicted a cross-sectional scanning electron microscopy (SEM) image of a representative device with **PYTPA** as the **HTM**. Each layer was clearly distinguished. The Perovskite layer was identified as crystalline structures with large grain sizes.

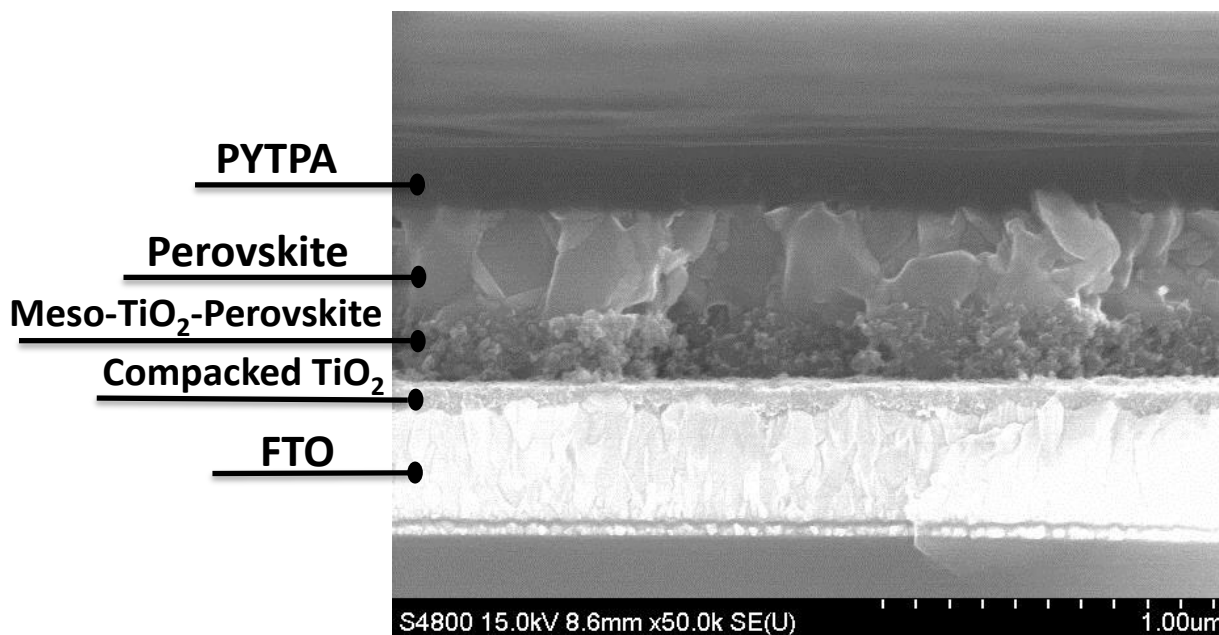


Figure 5.4: A cross-sectional SEM image of a PSC device with **PYTPA** as the **HTM**.

The J-V characteristics of the devices were measured under the illumination of AM 1.5, 100 mW/ cm². As shown in Figure 5.5 and Table 5.1, it demonstrated that all the dendrimers worked as effective hole transporting materials in PSCs and the PCEs were over 13% in general.

As displayed in Table 5.1, the device with **PYTPA** had a J_{sc} , V_{oc} and FF of 21.3 mA/cm^2 , 1.0 V and 70.7% respectively, which combined to reach a PCE of 15.7% . This was the highest efficiency obtained among three devices without doping lithium salts. It is probably attributed to the lowest HOMO level (-5.36 eV) of **PYTPA** among the three dendrimers, which renders a highest V_{oc} and reduces the energy barrier for hole transport as supported by the highest J_{sc} obtained in **PYTPA**-based device (an indication of better charge transportation). To the best of our knowledge, the highest efficiency of a dopant-free device was reported to be at around 13% ^[13] and all the three devices have surpassed it. For comparison, a device containing **spiro-OMeTAD** with the same configuration as the other devices was fabricated and measured under the same conditions as the others. It reached a PCE of 13% without doping, which was generally lower than the dendrimer-based devices.

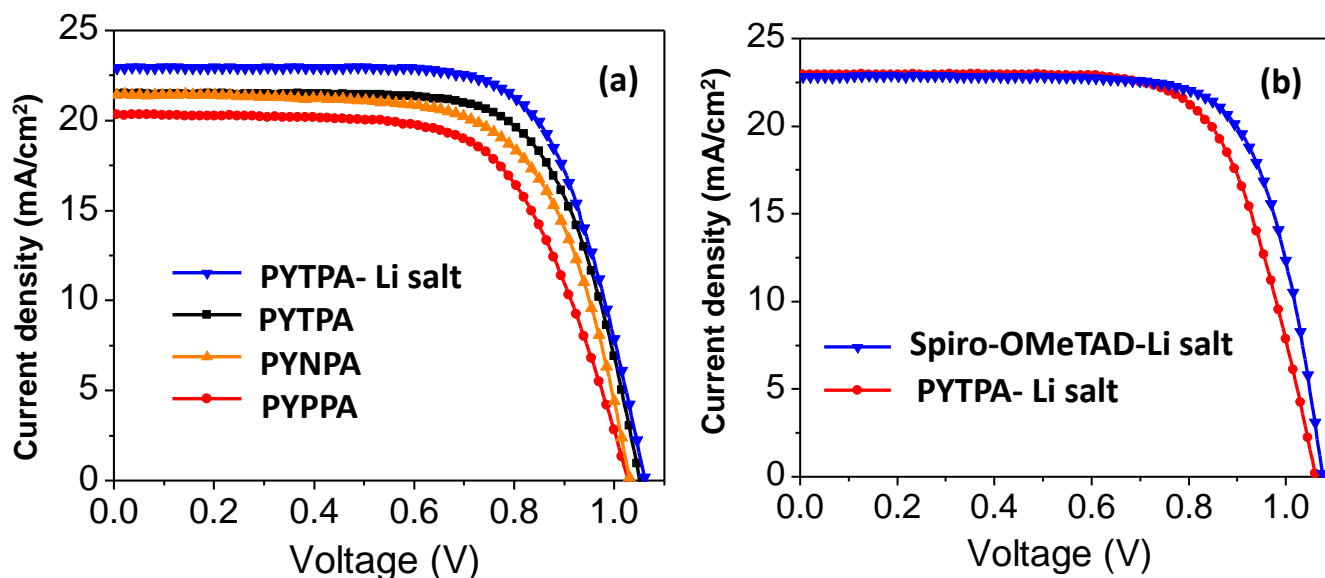


Figure 5.5: J-V curves of PSCs with different **PYPPDs** (a) and **spiro-OMeTAD-Li salt** (b).

Table 5.1: PSC performances using different **HTMs**.

HTM	$J_{sc}/\text{mA}\cdot\text{cm}^{-2}$	V_{oc}/V	FF/%	$\eta/\%$	$R_s/\Omega\cdot\text{cm}^{-2}$
PYTPA	21.3	1.05	70.7	15.7	6.8
PYNPA	21.2	1.03	67.4	15.0	6.5
PYPPA	20.6	1.01	63.7	13.3	1.0
PYTPA-Li salt	23.0	1.06	70.0	17.1	6.4
Spiro-OMeTAD-Li salt	23.0	1.08	75.8	18.8	5.1

The device with **PYNPA** exhibited a moderate PCE of 15.0% among the three, which was a high efficiency as well. The high efficiency was probably owing to its good charge transport property which was demonstrated in chapter 2. The **PYPPA**-based device displayed the lowest PCE (13.3%) among the three, possibly due to the enlarged energy barrier between Perovskite and the HOMO level of **PYPPA**

for hole transport and the reduced energy barrier between the LUMO of **PPA** and the conduction band energy of Perovskite for blocking electrons, compared with **PYTPA** and **PYNPA**.

Normally the dopant-free **HTMs** result in increased device stabilities because doping with lithium salts will render the hole transport layer hydrophilic and hygroscopic and destroy the Perovskite layer. On the other hand, high efficiency is still the most important factor for **PSCs**. The currently reported highly efficient **PSCs** have unambiguously employed bis(trifluoromethanesulfonylimide)lithium (**LiTFSI**) and 4-tert-butylpyridine (**t-BP**) as the dopants. Both of them were added into the **HTM** solutions before spin coating.^[6] In general, the effects of **LiTFSI** and **t-BP** include: improving the conductivity of **HTM** and restricting the interface charge carrier recombinations.^[7, 14]

As shown in Figure 5.5 and Table 5.1, when **PYTPA** was doped with **LiTFSI** and **t-BP**, the device efficiency was enhanced to 17%, due to an enhanced J_{sc} , an indication of enhanced photocurrent after doping. However this performance was still lower than the device with doped **spiro-OMeTAD** which reached a PCE of 18.8%. As shown in Table 5.1, the J_{sc} and V_{oc} between these two doped devices were almost the same. However, the fill factor of **PYTPA-Li salt**-based device was notably lower than that of **spiro-OMETAD-Li salt**-based one, which determined the different device efficiencies. The lower FF of the former than the latter was possibly attributed to the lower conductivity of the former as supported by the larger resistance of the former device than the latter one ($6.44 \Omega \cdot \text{cm}^{-2}$ for **PYTPA-Li** and $5.09 \Omega \cdot \text{cm}^{-2}$ for **spiro-OMeTAD-Li**).

Even though these dendrimers demonstrated nice performances in **PSCs**, newly synthesized **PYTPA** however, could not repeat these performances and a PCE of only around 1% was obtained for the non-doped devices. This huge performance deviation (15.7% vs 1%) between the first batch samples (**PYTPA**, **PYNPA** and **PYPPA** synthesized 2 years ago) and the second batch sample (**PYTPA**, newly synthesized) is very surprising and the reason for that should be studied in depth. Referring to the high performance **HTMs** in **PSCs**, e.g. **spiro-OMeTAD** which was reported to be oxidized into radical cations by cobalt complexes to enhance the conductivity in devices,^[15] it was proposed that the old samples might have been oxidized into their radical cations by O_2 after long time of storage in air.

To confirm the existence of radical cations in the old samples (first batch), the UV-vis absorption spectra of **PYTPA** and **PYNPA** (first batch) were measured. As depicted in Figure 5.6, it looks that there is indeed an extra peak centered around 620 nm for **PYTPA** and **PYNPA**, consistent with the reported absorption wavelength of triphenylamine radical cation (~ 650 nm).^[16] However, this peak is so weak that it must be zoomed in to be observed, indicating the oxidation ratio is very low (the ratio: $\sim 10^{-3}$, based on their absorbance). For comparison, the UV-vis absorption spectra of pure toluene and the newly synthesized **PYTPA** (second batch) do not display this band, suggesting the small peak centered around 620 nm is due to the oxidation of the dendrimers after long time of store in air.

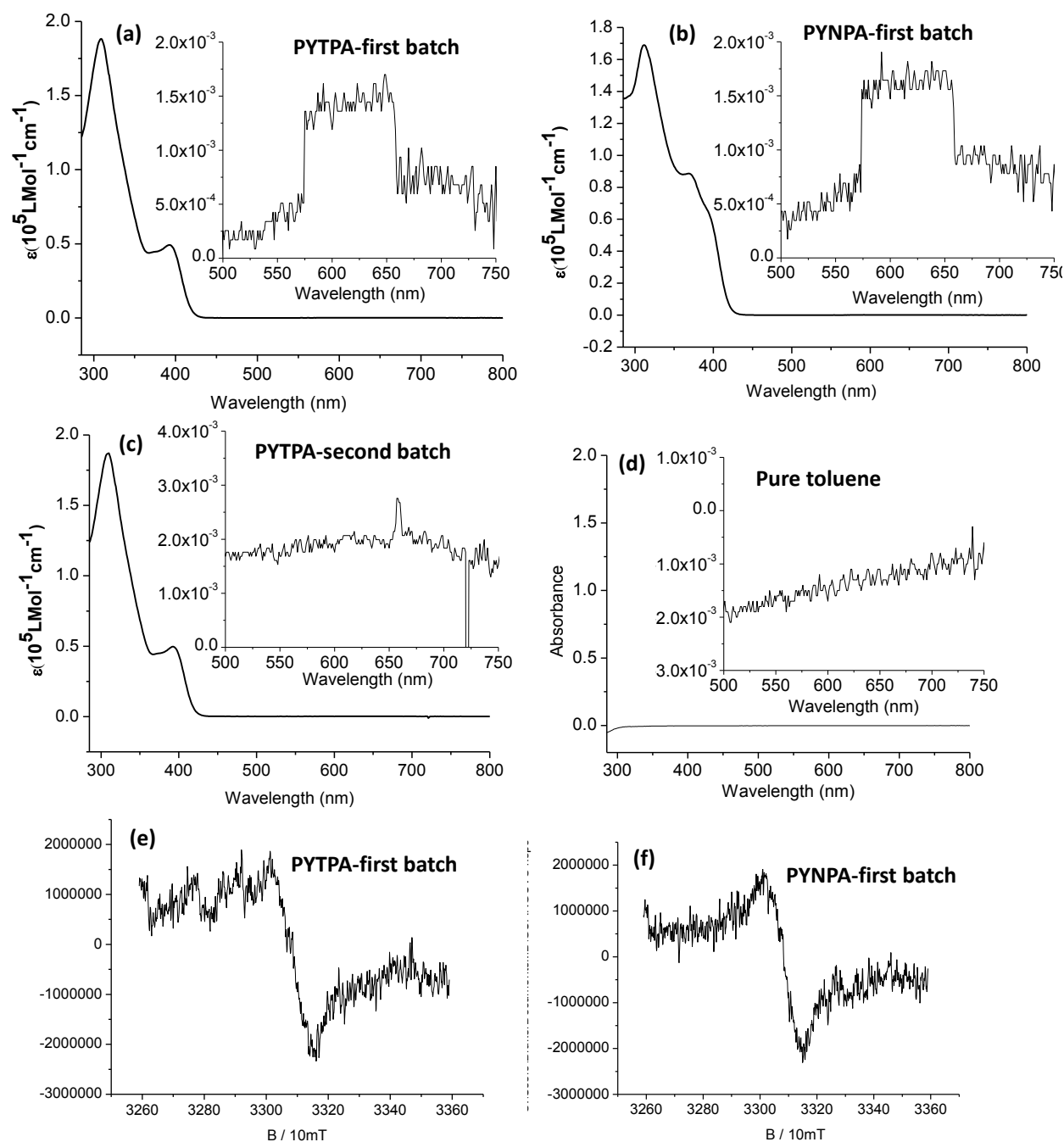


Figure 5.6: UV-vis absorption spectra of first-batch **PYTPA** (a), first-batch **PYNPA** (b), second-batch **PYTPA** (c) and pure toluene (d) and EPR spectra of first-batch **PYTPA** (e) and first-batch **PYNPA** (f) (10^{-5} M, toluene).

To further demonstrate the existence of radical cation in the first batch dendrimers, electron paramagnetic resonance (EPR) spectra were measured by Prof. Martin Baumgarten for first-batch **PYTPA** and **PYNPA** using the same solutions as those for UV-vis absorption measurements. As depicted in Figure 5.6, a weak peak was observed in both samples indicating that radicals existed in the dendrimers but the content of radicals should be very low.

PYTPA was taken as an example to evaluate the potential of the oxidations of these dendrimers by oxygen. As depicted in Figure 5.7, the redox potential of **PYTPA** ($\text{PYTPA} \leftrightarrow \text{PYTPA}^{\cdot+}$) was determined to be around 0.54 V versus ferrocene (see chapter 2). Assuming the redox potential of ferrocene was around 0.70 V versus the normal hydrogen electrode (NHE),^[17] the redox potential of **PYTPA** should be around 1.24 V versus NHE. The redox potential of O_2 ($\text{O}_2 \leftrightarrow \text{H}_2\text{O}$) was around 0.57 V (pH=7) versus the standard calomel reference electrode (SCE) and the potential of SCE was around 0.24 V versus NHE.^[18] As a result, the redox potential of O_2 should be around 0.81 versus NHE. As shown in Figure 5.7, if the two reductive half reactions are combined, the potential difference is around -0.43 V. This suggests that the Gibbs free energy for this reaction is positive and the oxidation of **PYTPA** by O_2 should not occur spontaneously. In addition, it has been predicated by de Leeuw et al. in 1997 that a non-doped p-type material with a redox potential above 0.5 V versus SCE, corresponding to 0.74 V vs NHE should be air-stable.^[18] Consequently, **PYTPA** should be quite stable at ambient condition and the oxidation of **PYTPA** by O_2 should be trivial based on the analysis.

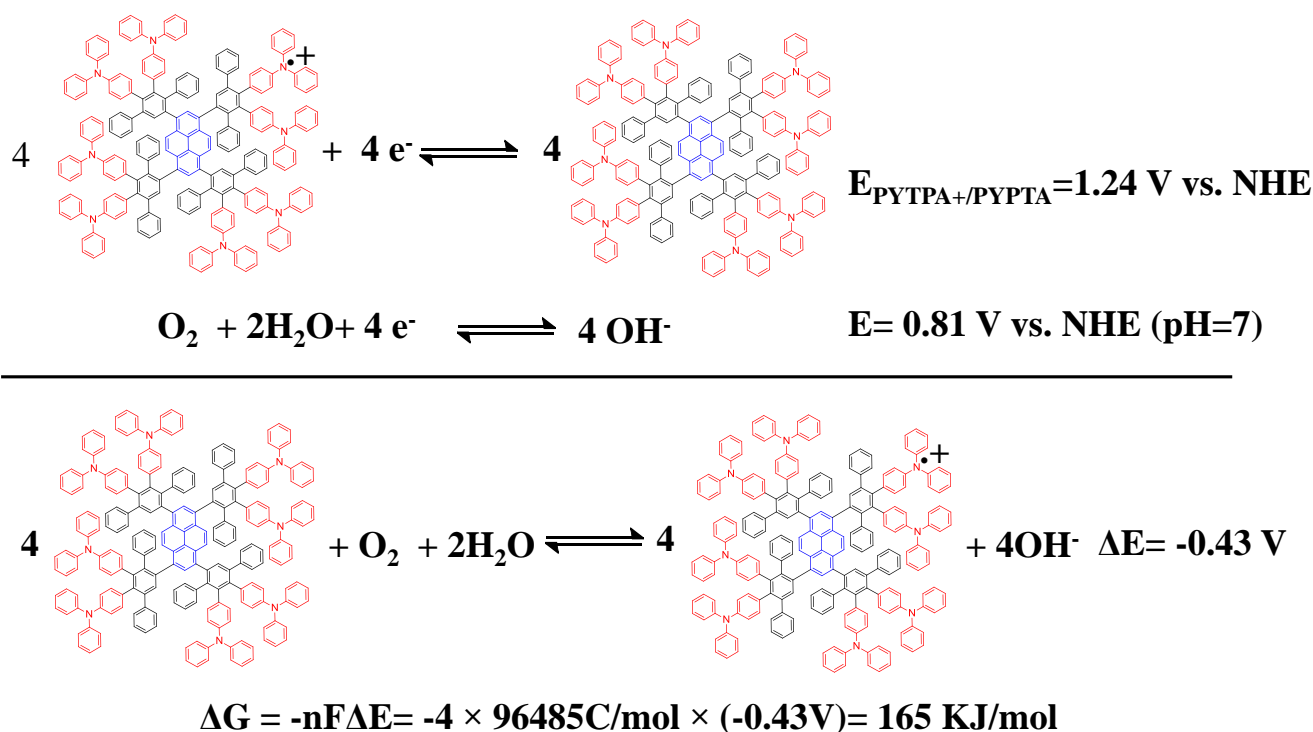


Figure 5.6: Evaluation on the possibility of the oxidation of **PYTPA** by O_2 .

As a result, it can be concluded that the oxidations of the first batch samples indeed have occurred but the oxidation ratio is very small based on the strength of the absorption and EPR signals of the formed radical cations, the positive Gibbs free energy of the oxidation of **PYTPA** by O_2 and the absence of observable differentiation in the ^1H NMR and MALDI-TOF mass spectra between the first batch and second batch materials. In addition, besides radicals, intermolecular couplings could occur easily upon

radical formations and as a result, dendrimer-based, cross-linked networks could coexist in the old samples, even though no direct proof of their existence has been obtained.

Consequently, the enhanced performances of the first batch materials compared with the second batch one is probably due to the existence of radicals or the cross-linked structure or both in the former. However, the fact that the trivial doping of a dendrimer hugely boosts the **PSC** performances is very surprising. Currently, the newly synthesized **PYTPAs** have been attempted to be oxidized by I_2 and devices could reach PCEs around 11% by now. More research is going on in Prof. Yuanzhi Tan and Prof. Nanfeng Zheng's side to oxidize or dope **PYTPAs** in a controlled manner and characterize them in devices.

5.3 Summary

The first batch materials of **PYTPA**, **PYNPA** and **PYPPA** all have demonstrated high hole transporting performances in **PSCs**. Especially, **PYTPA** without doping Li salt prompted the PCE to 15.7% and after doping with Li salt, the device efficiency was further enhanced to 17%. These results, no matter with or without doping with Li salt, reveal that these materials are among the best reported **HTMs** in **PSCs** by now.

The newly synthesized **PYTPA**, however, could not reproduce the device performances of the first batch samples due to the slight oxidations of the old samples by O_2 and the existence of radical cations as proved by UV-vis absorption and EPR spectroscopies and possible existence of cross-linked structures. Trivial doping of the dendrimers can render huge boosts of **PSC** performances. More studies are going on by controlled oxidations of the newly synthesized dendrimers to try to reach the performances of the old samples.

Literature

- [1] W. S. Yang, J. H. Noh, N. J. Jeon, Y. C. Kim, S. Ryu, J. Seo, S. I. Seok, *Science* **2015**, *348*, 1234-1237.
- [2] a) M. A. Green, A. Ho-Baillie, H. J. Snaith, *Nat Photonics* **2014**, *8*, 506-514; b) M. Gratzel, *Nat Mater* **2014**, *13*, 838-842.
- [3] a) H. S. Kim, C. R. Lee, J. H. Im, K. B. Lee, T. Moehl, A. Marchioro, S. J. Moon, R. Humphry-Baker, J. H. Yum, J. E. Moser, M. Gratzel, N. G. Park, *Sci Rep-Uk* **2012**, *2*; b) M. M. Lee, J. Teuscher, T. Miyasaka, T. N. Murakami, H. J. Snaith, *Science* **2012**, *338*, 643-647; c) M. Z. Liu, M. B. Johnston, H. J. Snaith, *Nature* **2013**, *501*, 395-+; d) O. Malinkiewicz, A. Yella, Y. H. Lee, G. M. Espallargas, M. Graetzel, M. K. Nazeeruddin, H. J. Bolink, *Nat Photonics* **2014**, *8*, 128-132; e) N. J. Jeon, J. H. Noh, Y. C. Kim, W. S. Yang, S. Ryu, S. Il Seol, *Nat Mater* **2014**, *13*, 897-903.
- [4] J. Burschka, N. Pellet, S. J. Moon, R. Humphry-Baker, P. Gao, M. K. Nazeeruddin, M. Gratzel, *Nature* **2013**, *499*, 316-+.
- [5] a) J. H. Noh, S. H. Im, J. H. Heo, T. N. Mandal, S. I. Seok, *Nano Lett* **2013**, *13*, 1764-1769; b) J. W. Lee, D. J. Seol, A. N. Cho, N. G. Park, *Adv Mater* **2014**, *26*, 4991-4998; c) N. Pellet, P. Gao, G. Gregori, T. Y. Yang, M. K. Nazeeruddin, J. Maier, M. Gratzel, *Angew Chem Int Edit* **2014**, *53*, 3151-3157; d) N. J. Jeon, J. H. Noh, W. S. Yang, Y. C. Kim, S. Ryu, J. Seo, S. I. Seok, *Nature* **2015**, *517*, 476-+.
- [6] Z. Yu, L. C. Sun, *Adv Energy Mater* **2015**, *5*.

- [7] U. Bach, D. Lupo, P. Comte, J. E. Moser, F. Weissortel, J. Salbeck, H. Spreitzer, M. Gratzel, *Nature* **1998**, 395, 583-585.
- [8] H. P. Zhou, Q. Chen, G. Li, S. Luo, T. B. Song, H. S. Duan, Z. R. Hong, J. B. You, Y. S. Liu, Y. Yang, *Science* **2014**, 345, 542-546.
- [9] N. J. Jeon, H. G. Lee, Y. C. Kim, J. Seo, J. H. Noh, J. Lee, S. I. Seok, *J Am Chem Soc* **2014**, 136, 7837-7840.
- [10] P. Gratia, A. Magomedov, T. Malinauskas, M. Daskeviciene, A. Abate, S. Ahmad, M. Gratzel, V. Getautis, M. K. Nazeeruddin, *Angew Chem Int Edit* **2015**, 54, 11409-11413.
- [11] J. H. Heo, S. H. Im, J. H. Noh, T. N. Mandal, C. S. Lim, J. A. Chang, Y. H. Lee, H. J. Kim, A. Sarkar, M. K. Nazeeruddin, M. Gratzel, S. I. Seok, *Nat Photonics* **2013**, 7, 487-492.
- [12] W. M. Zhang, J. Smith, R. Hamilton, M. Heeney, J. Kirkpatrick, K. Song, S. E. Watkins, T. Anthopoulos, I. McCulloch, *J Am Chem Soc* **2009**, 131, 10814+.
- [13] Y. K. Song, S. T. Lv, X. C. Liu, X. G. Li, S. R. Wang, H. Y. Wei, D. M. Li, Y. Xiao, Q. B. Meng, *Chem Commun* **2014**, 50, 15239-15242.
- [14] J. Kruger, R. Plass, L. Cevey, M. Piccirelli, M. Gratzel, U. Bach, *Appl Phys Lett* **2001**, 79, 2085-2087.
- [15] J. Burschka, A. Dualeh, F. Kessler, E. Baranoff, N. L. Cevey-Ha, C. Y. Yi, M. K. Nazeeruddin, M. Gratzel, *J Am Chem Soc* **2011**, 133, 18042-18045.
- [16] G. N. Lewis, D. Lipkin, *J Am Chem Soc* **1942**, 64, 2801-2808.
- [17] C. M. Cardona, W. Li, A. E. Kaifer, D. Stockdale, G. C. Bazan, *Adv Mater* **2011**, 23, 2367-2371.
- [18] D. M. deLeeuw, M. M. J. Simenon, A. R. Brown, R. E. F. Einerhand, *Synthetic Met* **1997**, 87, 53-59.

Chapter 6 Synthesis of Nanographene Networks by Electrochemistry

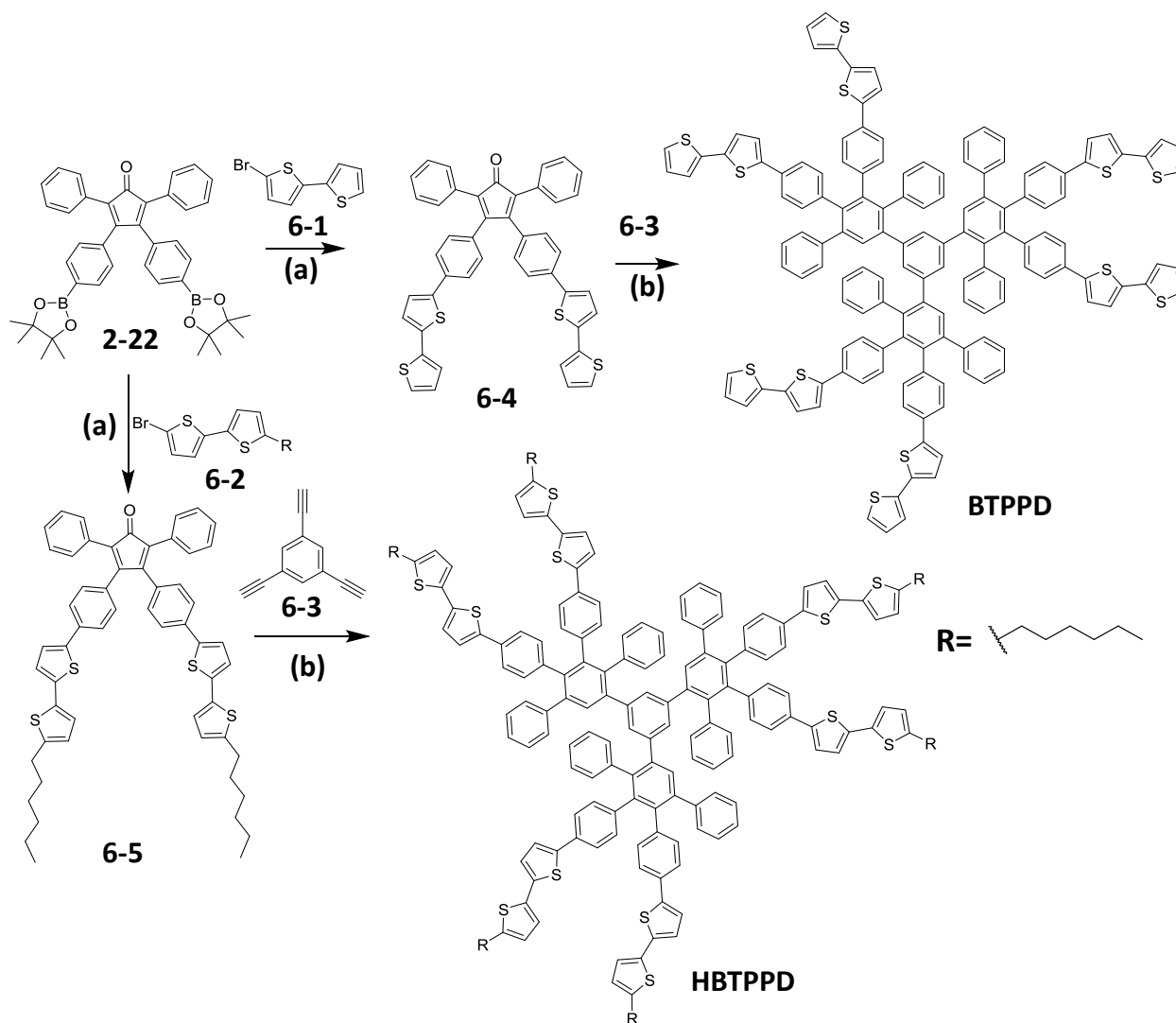
In this chapter, the synthesis and structural characterizations of several peripheral-oligothiophene-functionalized **PPDs** will be described. In addition, the formation process of nanographene networks (**NGNs**) and their characterizations will be included and discussed.

6.1 Bithiophene-functionalized dendrimers for NGNs

6.1.1 Synthesis of dendrimers

As an initial trial, the bithiophene-functionalized **PPDs** were designed and synthesized (Scheme 6.1). 1,3,5-Triethynylbenzene (**6-3**) was selected as the core for Diels-Alder reactions because the formed central polyphenylenes could potentially transfer into C₉₆ nanographene moieties after cyclodehydrogenations by electrochemistry.

To synthesize the dendrimers, bithiophene-functionalized **CPs** were prepared first (Scheme 6.1). Initially, a boronic ester-functionalized **CP** (**2-22**) was reacted with 5-bromo-2,2'-bithiophene (**6-1**) by a Suzuki coupling to form the bithiophene-functionalized **CP** (**6-4**) in high yield (94%). The 5-hexyl-2,2'-bithiophene-functionalized dendrimer (**HBTPPD**) was also produced to compare its electrochemical properties with the 2,2'-bithiophene-functionalized dendrimer (**BTPPD**). As a result, **CP** (**6-5**) was obtained similar as **CP** (**6-4**) by a reaction between compound **2-22** and 5-bromo-5'-hexyl-2,2'-bithiophene (**6-2**) in high yield (100%). With the **CPs** ready, **BTPPD** and **HBTPPD** were procured by a Diels-Alder reaction in high yields (68% and 65%, respectively).



Scheme 6.1: Synthetic routes for **BTPPD** and **HBTPPD**. (a) $\text{Pd}(\text{PPh}_3)_4$, K_2CO_3 , tetrabutylammonium bromide, toluene, H_2O , 24 h, $80\text{ }^\circ\text{C}$, 94% for **6-4**, 100% for **6-5**; (b) *o*-xylene, $145\text{ }^\circ\text{C}$, 12 h, 68% for **BTPPD**, $170\text{ }^\circ\text{C}$, 24 h, 65% for **HBTPPD**.

Both dendrimers were characterized by ^1H and ^{13}C NMR spectroscopy, MALDI-TOF Mass and HRMS spectrometry, UV-Vis absorption and photoluminescence spectroscopy and cyclic voltammetry. In the ^1H NMR spectra of **BTPPD** (Figure 6.1), except for the solvent peaks, all the proton signals were basically lined in the aromatic region. The aromatic signals were barely distinguished due to their strong overlaps. Because the chemical shifts of the β protons of thiophene moieties were usually located at higher field than those of other protons of thiophenes and the protons of benzene,^[1] the multiplet peak at around 6.71 pm corresponded to the β protons of the surface thiophene fragments. In addition, the relative intensities of all peaks correlated well with the number of protons of the molecule.

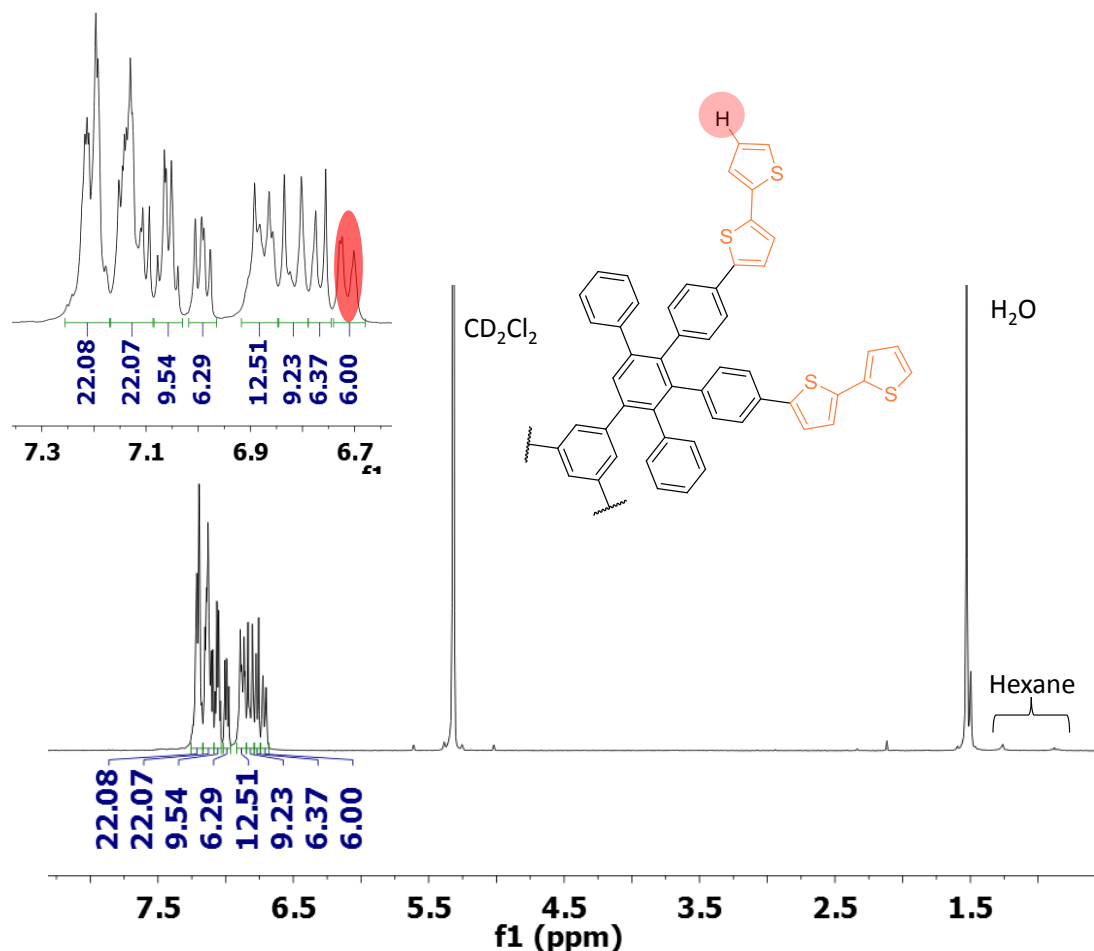


Figure 6.1: ^1H NMR spectra of **BTPPD** (solvent: CD_2Cl_2) (inset: enlarged image of aromatic area).

The MALDI-TOF mass spectra of each dendrimer showed a single peak of the molecule ions, consistent with the molecular masses of the dendrimers (Figure 6.2). In addition, the HRMS spectra of **BTPPD** displayed clear isotope patterns which were consistent with the calculated results. Therefore, the desired products were prepared.

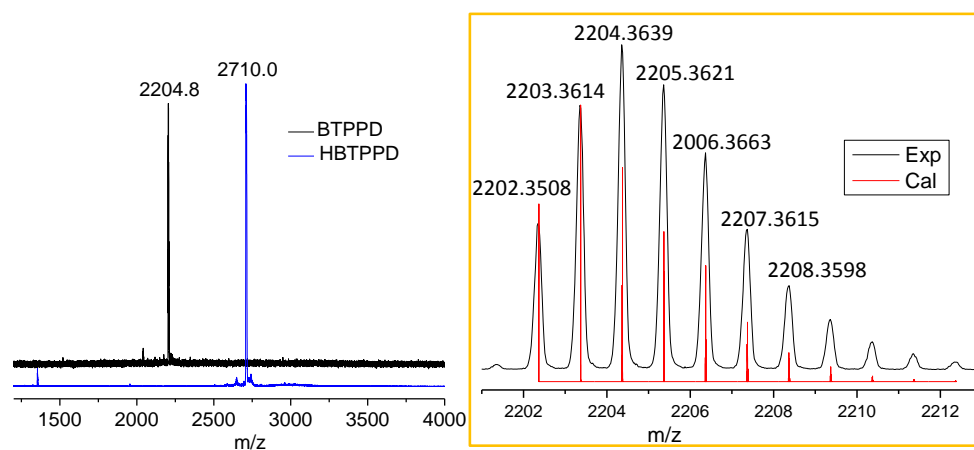


Figure 6.2: MALDI-TOF mass spectra of **BTPPD** and **HBTPPD** (left) and HRMS spectra of **BTPPD** (right).

6.1.2 Photophysical properties

As depicted in Figure 6.3 (a), both the absorption of **BTPPD** and **HBTPPD** possessed a broad band between 300 nm and 420 nm, centered at 352 nm and 360 nm respectively. This was due to the π - π^* transitions of 5-phenyl-2,2'-bithiophene moieties.^[2] In addition, **BTPPD** had higher extinction coefficient than **HBTPPD**. As depicted in Figure 6.3 (b), both dendrimers were deep-blue emissive with fine structures in solutions due to 5-phenyl-2,2'-bithiophenes as the chromophores in these dendrimers. The emission of **HBTPPD** was slightly bathochromic-shifted (λ_{em} : 423 and 439 nm) compared with that of **BTPPD** (λ_{em} : 416 and 436 nm), probably due to the electron donating effects of the hexyl groups in **HBTPPD**, which slightly decreased the energy gap of the molecule (Table 6.1).

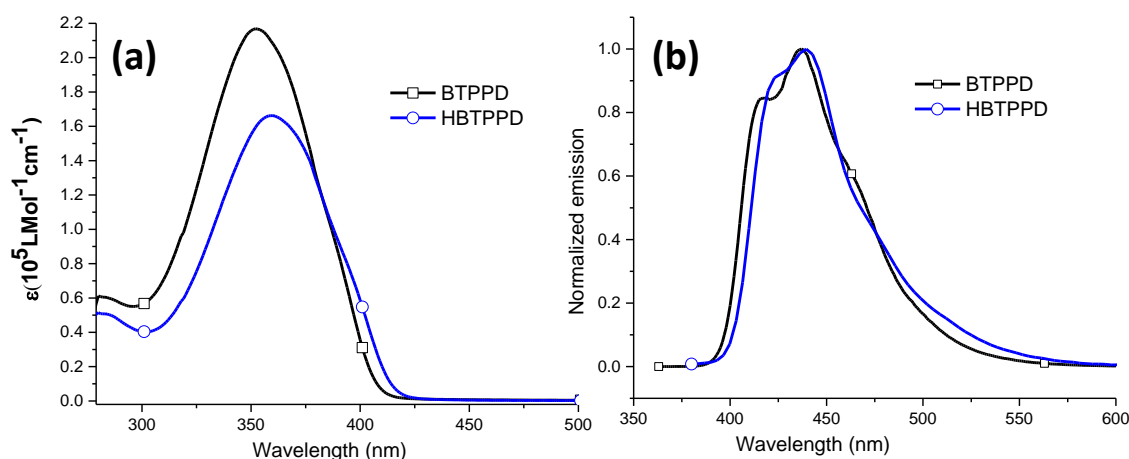


Figure 6.3: UV-vis absorption (a) and photoluminescence spectra (b) of **BTPPD** (ex: 352 nm) and **HBTPPD** (ex: 360 nm) (10^{-5} M, toluene).

Table 6.1: Photophysical and electrochemical properties of **BTPPD** and **HBTPPD**.

	λ_{ab} (nm)	λ_{em} (nm)	HOMO (eV) ^{a)}	LUMO (eV) ^{b)}	E_g (eV) ^{c)}
BTPPD	352	416, 436	-5.44	-2.40	3.04
HBTPPD	360	423, 439	-5.43	-2.45	2.98

^{a)} Calculated from CV by comparing the first redox onset of **PPDs** and the oxidation onset of ferrocene; ^{b)} calculated from the energy gap and HOMO level; ^{c)} calculated from the absorption edge of the longest wavelength band.

6.1.3 Electrochemical properties and Formation of NGNs

The electrochemistry of both dendrimers were measured by cyclic voltammetry. Standard one-component, three-electrodes setup was employed, in which a platinum disk covered with a solvent-resistant plastic body (\varnothing : 1 mm) was the working electrode, a platinum wire worked as the counter electrode and a silver wire served as the reference electrode. The sweeps were conducted in 0.1 M

TBAPF₆ electrolyte solution in DCM with scanning rate at 100 Mv/s and the concentrations of the dendrimers were controlled at approximate 10⁻³ M.

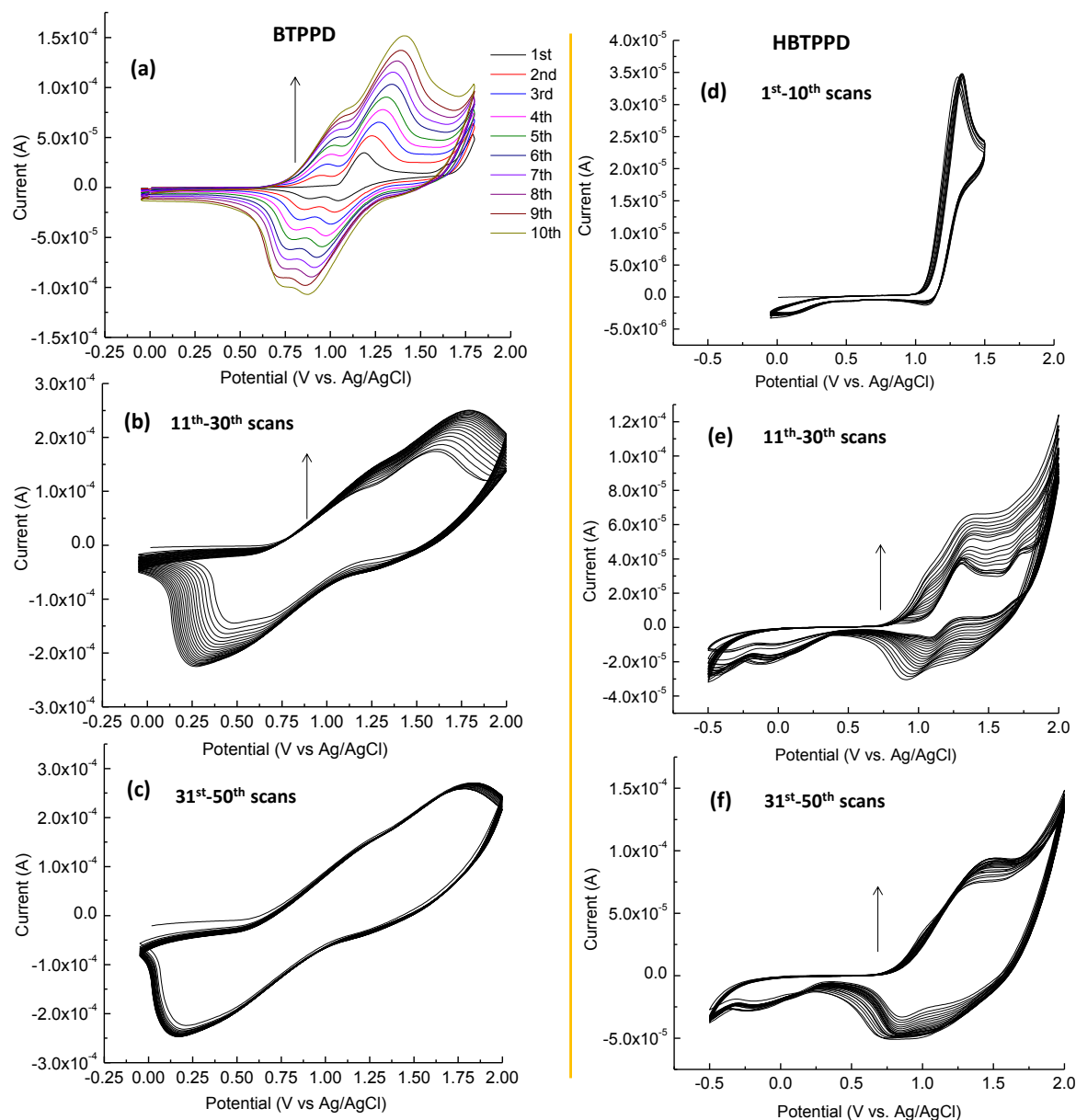


Figure 6.4: Multi-times CV curves of **BTPPD** (left) and **HBTPPD** (right) under different sweeps (note: the arrows stand for the scanning sequence).

As depicted in Figure 6.4 (a) in the first cycle, the oxidation of **BTPPD** started at around 1.05 V ($E_{pa} \sim 1.15$ V), corresponding to the oxidation of bithiophenes.^[3] In the reverse scan of the first cycle, there existed two reductive peaks. The one with a more positive potential ($E_{pc} = 1.04$ V) was the reduction of the bithiophene cations into their neutral forms and the other one ($E_{pc} = 0.88$ V) corresponded to the reduction of quaterthiophene cations into their neutral states, indicating the occurrence of intermolecular couplings between the bithiophene moieties.^[4] Starting from the second scan, the oxidation of quaterthiophene was observed at a lower potential than that of bithiophene. In addition, the current

increased notably after each sweep, suggesting that the film formed on the working electrode became more conductive with the sweeps due to the generation of quaterthiophene-bridged networks (Figure 6.5).^[5]

As depicted in Figure 6.4 (b, 11th scan), with the scanning extended to 2 V, another oxidation peak showed up centered around 1.61V with a higher current intensity than the oxidation of bithiophenes. This was attributed to the oxidation of benzene groups in the polyphenylene segment. This is consistent with the reported oxidation of phenyl moieties in HPB (onset: 1.5 V vs. Ag/AgCl)^[6] and in polyphenylene dendrimers (onset: 1.35 V, E_{pa} = 1.7 V, vs. Ag/AgCl)^[7]. In the reverse scan, a new emerging peak (~0.47 V) which was more negative than the reduction potential of quaterthiophene radical cation was due to the neutralization of intermediate arenium cations (partially cyclodehydrogenated **PPD** segments). Similar reductive potentials, e.g. 0.61, 0.49 and 0.29 V, were found in the CV curve of HPB.^[6] In addition, with subsequent sweeps, the current intensities increased considerably, suggesting that the film formed on the electrode became more conductive due to the intramolecular phenyl-phenyl couplings. From 31st to 50th scans, the current intensity was not increased notably, indicating the finish of **NGN1** formation (Figure 6.5).

As depicted in Figure 6.4(d), for **HBTPPD**, on the other hand, the oxidation waves kept almost the same with an onset potential at around 1.0 V and a strong anodic peak at around 1.3 V after multiple sweeps between -0.5 and 1.5 V. This was the oxidation of 5-phenyl-2,2'-bithiophene, similar as that in **BTPPD**. In the reverse scans, the reductive peaks looked much less noticeable than their oxidative parts indicating the instability of the 5-phenyl-2,2'-bithiophene radical cations. Due to the hexyl groups' protections of the α positions of bithiophenes in **HBTPPD**, the intermolecular couplings did not occur (Figure 6.5). However, when the scanning was enlarged to 2 V (11th scan), another oxidation wave appeared (E_{pa} : ~1.70 V) and was quasireversible with a shallow well at around 1.50 V in the reverse scan. This oxidation couple was attributed to the oxidation of benzene groups in the polyphenylene segment, consistent with that of **BTPPD** mentioned above. In addition, another oxidation process started at around 0.75 V which was more negative than the oxidation of 5-phenyl-2,2'-bithiophenes after the 11th scan, corresponding to the oxidation of the partially cyclodehydrogenated **HBTPPD** by intramolecular phenyl-phenyl couplings. Moreover, the current increased notably with the sweeps, elucidating that more and more intramolecular couplings occurred. As depicted in Figure 6.4 (f), as the scans continued further, the current enhancement slowed down and stopped eventually, which suggested the intramolecular couplings finished.

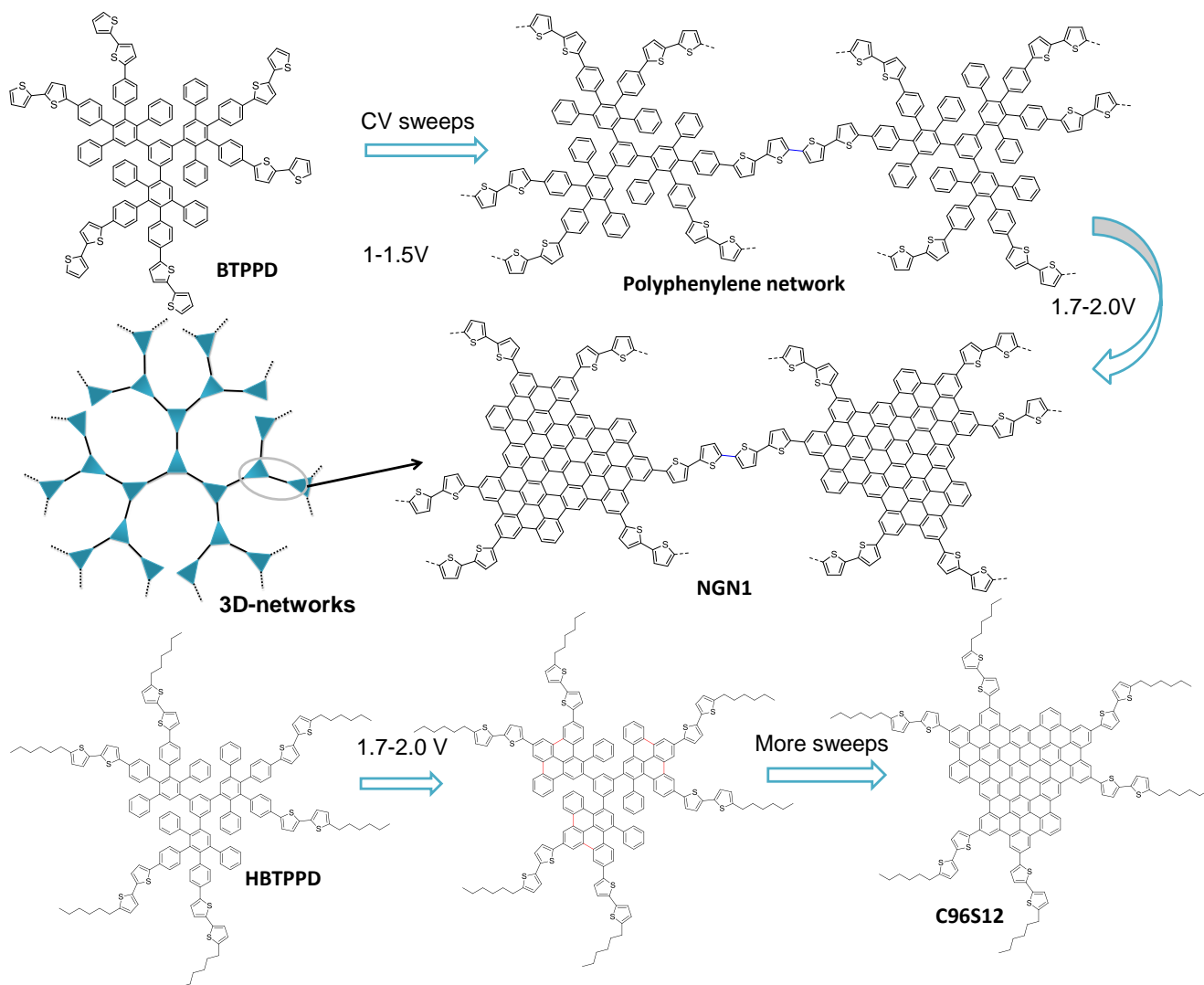


Figure 6.5: The process of **NGN1** and **C96S12** upon electrochemical oxidation.

6.1.4 Characterizations of nanographene network

The surface area of the platinum disk was so small that the film formed on the electrode was tiny amount. This rendered much difficulty to characterize it by IR, Raman and UV-vis absorption spectroscopy. As a result, much bigger working electrodes, i.e. a platinum foil and an ITO (both were rectangular-shaped with the sizes of approximate 1×2 cm) were utilized to prepare **NGN1**. They both demonstrated successful growth of **NGN1**.

The film grown on the platinum foil after 100 scans up to 2 V was obtained as a black solid with the thickness between 5 and 20 μm . It was very fragile and broke into small pieces quickly after the solvent evaporated, probably due to its high thickness. It was washed with DCM for at least three times before characterizations as there were **PPDs** and electrolytes left on the surface or inside the film. Similar as many other cross-linked materials, it was not soluble in common organic solvents, e.g. DCM, THF and toluene. After careful cleaning and drying the film, it was characterized with Raman and IR spectroscopy. Raman spectra were measured by Dr. Zongping Chen in our group with a 532 nm

excitation laser. As depicted in Figure 6.6, two characteristic sharp peaks referred to the D band and G band for graphites, graphenes and polycyclic aromatic hydrocarbons were observed.^[8] The D band located at around 1320 cm^{-1} and was due to the small conjugation domains in the C96-based **NGN1**.^[8f] G band was at around 1600 cm^{-1} . The nonexistence of other peaks, such as the band of monosubstituted benzene rings at 994 cm^{-1} suggested that polyphenylenes were transformed into nanographenes.^[9] Due to the different excitation wavelength of the reported Raman spectra of bare C96 nanographene from that of **NGN1** and the lack of calibration of the Raman spectrometer before measuring **NGN1**, their Raman spectra were not compared in detail.^{[8e][8f]}

In the IR spectra, as depicted in Figure 6.6 (d), **BTPPD** showed two major peaks above 3000 cm^{-1} due to the sp^2 C-H stretching. However, no notable peaks were in this area for **NGN1**, demonstrating considerable cyclodehydrogenations of polyphenylenes in the network. However, there remained three peaks between 2800 and 3000 cm^{-1} (2867 , 2926 and 2953 cm^{-1}). These peaks are usually correlated to sp^3 C-H stretching from alkyl chains. The possible TBAPF₆ doping in the film was ruled out due to the different absorption of TBAPF₆ IR spectra (2879 , 2937 and 2966 cm^{-1}). By in-depth analysis, the IR spectra of **BTPPD** also exhibited several tiny peaks between 2800 and 3000 cm^{-1} , correlating well with the ones observed in **NGN1** both in positions and structures. These peaks were finally aligned to the small amount of n-hexane molecule encapsulated in **BTPPD** (introduced during purification of this dendrimer), considering very similar IR absorption of n-hexane as those of **NGN1** and **BTPPD** in this area (2874 , 2929 and 2959 cm^{-1}).^[10] The existence of n-hexane in the dendrimer was supported by the ¹H NMR spectra of **BTPPD**. As depicted in Figure 6.1, there were indeed two tiny peaks at 1.27 and 0.87 ppm, corresponding to n-hexane.^[11]

As depicted in Figure 6.6 (c), the finger-print region of the IR spectra has several different features between **NGN1** and **BTPPD**. For **NGN1**, the peak at around 800 cm^{-1} corresponded to the α -quaterthiophene (C _{β} -H) vibration (literature value: 797.6 cm^{-1})^[12] and the C-H out-of-plane deformation from para-substituted phenyl ($\sim 795\text{ cm}^{-1}$)^[13] in **BTPPD** disappeared in **NGN1**, indicating considerable cyclodehydrogenations occurred in **NGN1**. Another strong peak at 785 cm^{-1} in **BTPPD**, characteristic in highly twisted polyphenylenes and due to C-H out-of-plane bending of mono-substituted phenyls bonding to multi-position-substituted benzene also vanished in the network.^[14] The peak at 698 cm^{-1} in the network was from C _{α} -H out of plane deformation of the non-reacted bithiophenes.^[15] The major peak at 694 cm^{-1} from the dendrimer was due to the C-H out-of-plane deformation of mono-substituted benzenes together with the C-H out-of-plane deformation of bithiophene groups.^[15-16] The peak at 754 cm^{-1} in **NGN1** was due to the C-H out of plane deformation from the benzene group with three adjacent protons.^[16a]

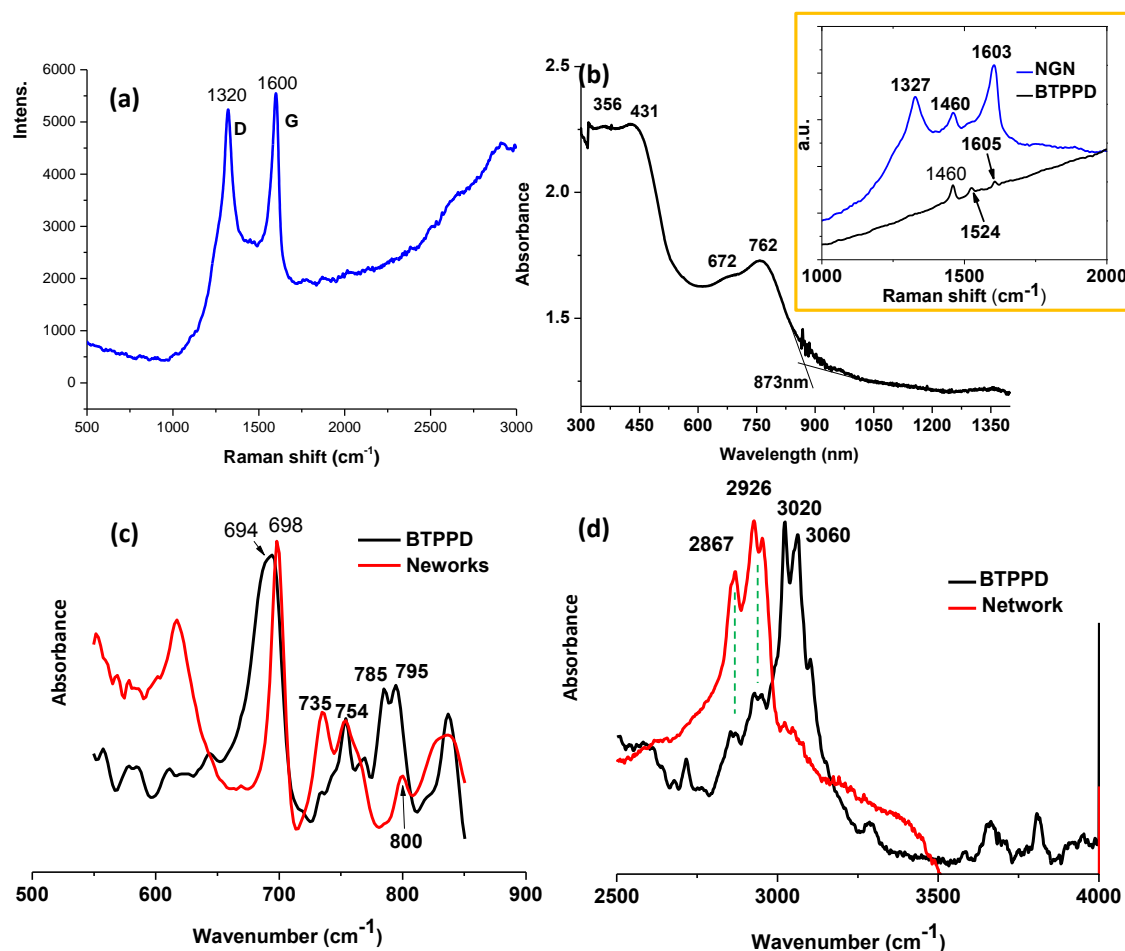


Figure 6.6: Raman (a), UV-vis absorption (b) (inset: the Raman signals of **NGN1** grown on ITO and Raman peaks of **BTPPD**) and IR spectra (c, d) of **NGN1**.

In addition, after 20 sweeps up to 2 V, a yellow-brown-colored thin film was obtained on the surface of ITO. It was taken out of the solution and a complete film was saved without cracks after solvent evaporation due to the relatively low film thickness. After that, Raman spectra were measured. As depicted in Figure 6.6 (b, inset), a D band (1327 cm^{-1}) and a G band (1603 cm^{-1}) were observed. In addition, another peak at 1460 cm^{-1} showed up between D and G band, consistent with the observed Raman band of 1460 cm^{-1} in **BTPPD**, probably due to some dendrimer molecules trapped inside the film. This film on ITO was used to measure the UV-vis absorption spectra. As depicted in Figure 6.6 (b), there were totally 4 absorption bands ranging between ultraviolet and infrared. The peak at around 356 nm was due to the absorption of the 5-phenyl-2,2'-bithiophene moieties from the dendrimers trapped in the film or from the unreacted bithiophenes in **NGN1**. The peak at 431 nm was attributed to the π - π^* transitions of 5,5''-diphenyl-2,2':5',2'':5'',2'''-quaterthiophene in **NGN1**.^[17] The notable band centered around 762 nm with a shoulder at around 672 nm corresponded to the π - π^* transitions of the whole conjugated system in **NGN1**. Compared with the published C96 nanographene (peak absorption in thin films: 491 nm),^[8f] the absorption of **NGN1** was bathochromically shifted by around 270 nm, indicating much increased conjugations in the C96-based, quaterthiophene-bridged network architecture. In

addition, the peak absorption of **NGN1** is very close to that of C222 nanographene (~765 nm).^[18] The absorption edge of **NGN1** was around 873 nm, corresponding to an energy gap of 1.42 eV.

HBTPPD was grown **C96S12** by a large-area Pt foil as the working electrode. After around 100 sweeps up to 2 V by CV. A thin and light-red-colored film was obtained on Pt surface. This film was thoroughly cleaned with DCM and dried before characterizations. It was characterized with Raman spectroscopy. Again two bands were observed with D band at 1328 cm⁻¹ and G band at 1607 cm⁻¹, suggesting that considerable cyclodehydrogenation occurred. The UV-vis absorption spectra was measured by dispersing small amount of the product inside N-Methyl-2-pyrrolidone (NMP) and sonication. The dispersion worked well as no particles was observed by the naked eyes after sonication. As depicted in Figure 6.7 (a), a strong band centered at 492 nm was identified and was bathochromically shifted by 10 nm compared with the reported C96 nanographene in dilute solutions,^[8f] due to the elongated conjugations of **C96S12** than C96 by bithiophenes. **C96S12** also represented the first known oligothiophene functionalized nanographene synthesized by electrochemistry.

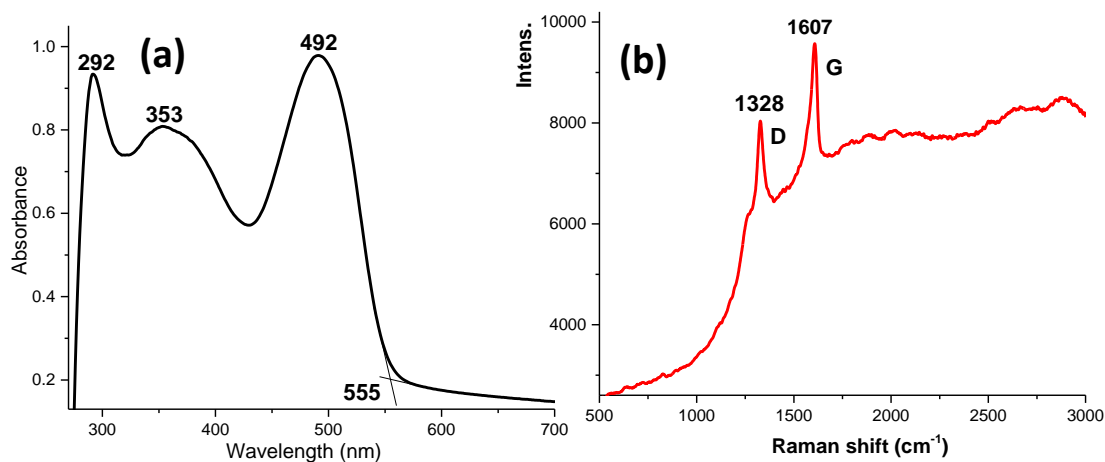


Figure 6.7: UV-vis absorption (a) and Raman spectra (b) of **C96S12** (note: the absorption spectra was measured by dispersing the sample in NMP solvent).

MALDI-TOF mass spectrometry is an important method to prove the existence of nanographene. For example, the molecular ion peaks of C60,^[19] C96,^[20] C132^[21] and C222^[18] were observed in MALDI-TOF mass spectra. It was attempted to detect **C96S12** using this method, however no desired signals were detected so far both from solid state and solution samples.

In addition, scanning electron microscopy (SEM) was used to explore the surface morphologies of the films produced by electrochemistry. The SEM measurements were conducted by Mr. Gunnar Glasser in our institute. As depicted in Figure 6.8, **NGN1** adopted a porous and 3-dimensional architecture, while the **C96S12** nanographene displayed a disk-like geometry (probably with column-like π - π stacks, similar

as functionalized HBCs^[22]). Consequently, the morphologies of **NGN1** and **C96S12** were consistent with the structures of the products.

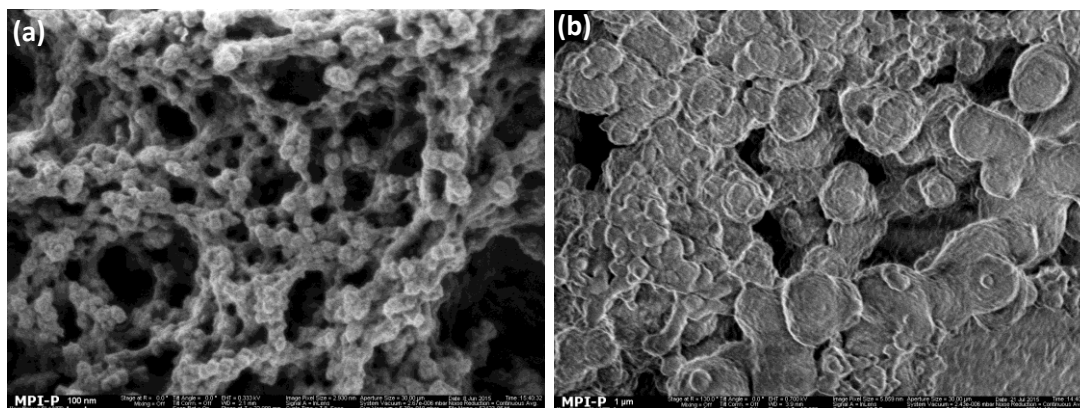


Figure 6.8: SEM images of **NGN1** (a) and **C96S12** (b).

6.1.5 Conductivity measurements

The conductivity measurement was carried out, using a similar setup reported by Zotti et al, in 2002 for in-situ conductivity of conducting polymers^[24]. As depicted in Figure 6.9, the working electrode was a two-Pt-foil assembly (5 mm × 10 mm) separated by a 30 μm-thick Teflon tape. The Pt foils and the Teflon tape were adhered together by epoxy resins. There was a 1 mm length of void between the two Pt foils at the bottom edge of the electrode. The complete electrode was embedded in a glass tube. The two-Pt-foil assembly had an open-circuit resistance of more than 40 MΩ which was beyond the detection limit of an ohm meter.

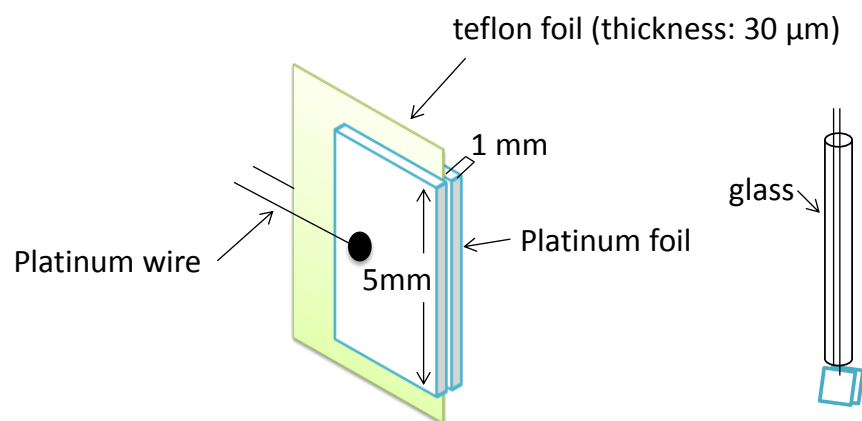


Figure 6.9: An overview of the conductivity setup.

In this case, **NGN1** was grown on this new working electrode by CV. A standard one-component, 3 electrode electrochemistry cell was employed, in which a silver wire worked as the reference electrode and a platinum wire was the counter electrode. The electrochemistry was conducted in a 0.1 MTBAPF₆ electrolyte solution in DCM (conc. of **BTTPD**: 2×10^{-3} M). As expected, after 100 sweeps between 0 and 2 V, the empty space between the two Pt foils was filled with **NGN1** as a black material (Figure 6.10).

After that, the electrolyte solution was decanted and a fresh electrolyte solution was added and an oxidation/p-doping of **NGN1** was carried out for three minutes with the potential controlled at 1.5 V.^[25] Then, the electrolytes were removed and the resistance was measured with an ohm meter with its each electrode touching one platinum wire on the two-Pt-foil assembly. The resistance (R) was around 1 M Ω , indicating some conductivity in p-doped **NGN1**. The thickness (L) of the black material was determined to be around 100 μm measured with an optical microscopy by Sheng Yang in our group. The area (A) of the film was calculated to be around $2.5 \times 10^{-6} \text{ m}^2$. Thus the conductivity was deduced to be $5 \times 10^{-7} \text{ S/cm}$ from the equation: $\sigma = L / (R \times A)$. This conductivity value was much lower than the reported nanographene network by Heinze et al, in 2005 ($\sim 10^{-1} \text{ S/cm}$).^[7] The big difference in conductivity largely depended on the measurement method (they use special in situ conductivity setup^[7]) and the doping levels of the sample^[25] Consequently, even though relatively low conductivity value was obtained, it provided a feasible method to measure the conductivities of nanographene networks without touching the film.

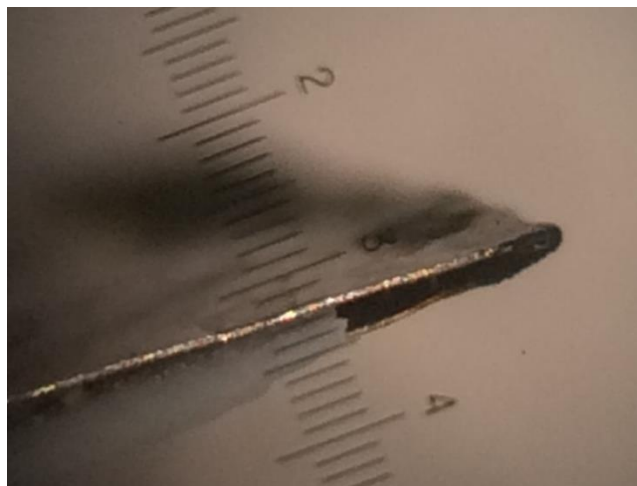


Figure 6.10: An optical microscopic image of **NGN1** within two Pt foils (the image was enlarged for 20 times).

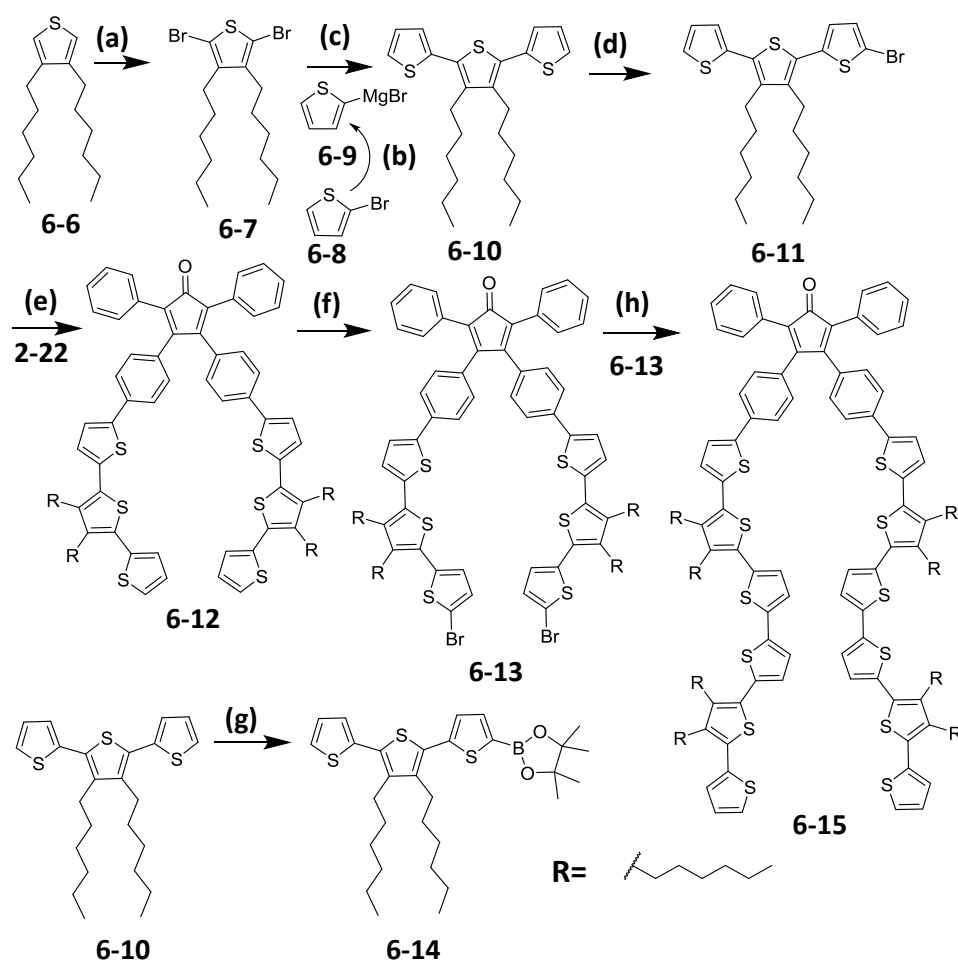
6.2 Synthesis of α -sexithiophene-functionalized PPDs

Higher NGN conductivities could probably be achieved with longer oligothiophenes as the bridges. As a result, as depicted in Scheme 6.3, α -sexithiophene functionalized **PPDs**, namely, **STPPD** and **STPPDG2** were designed and synthesized.

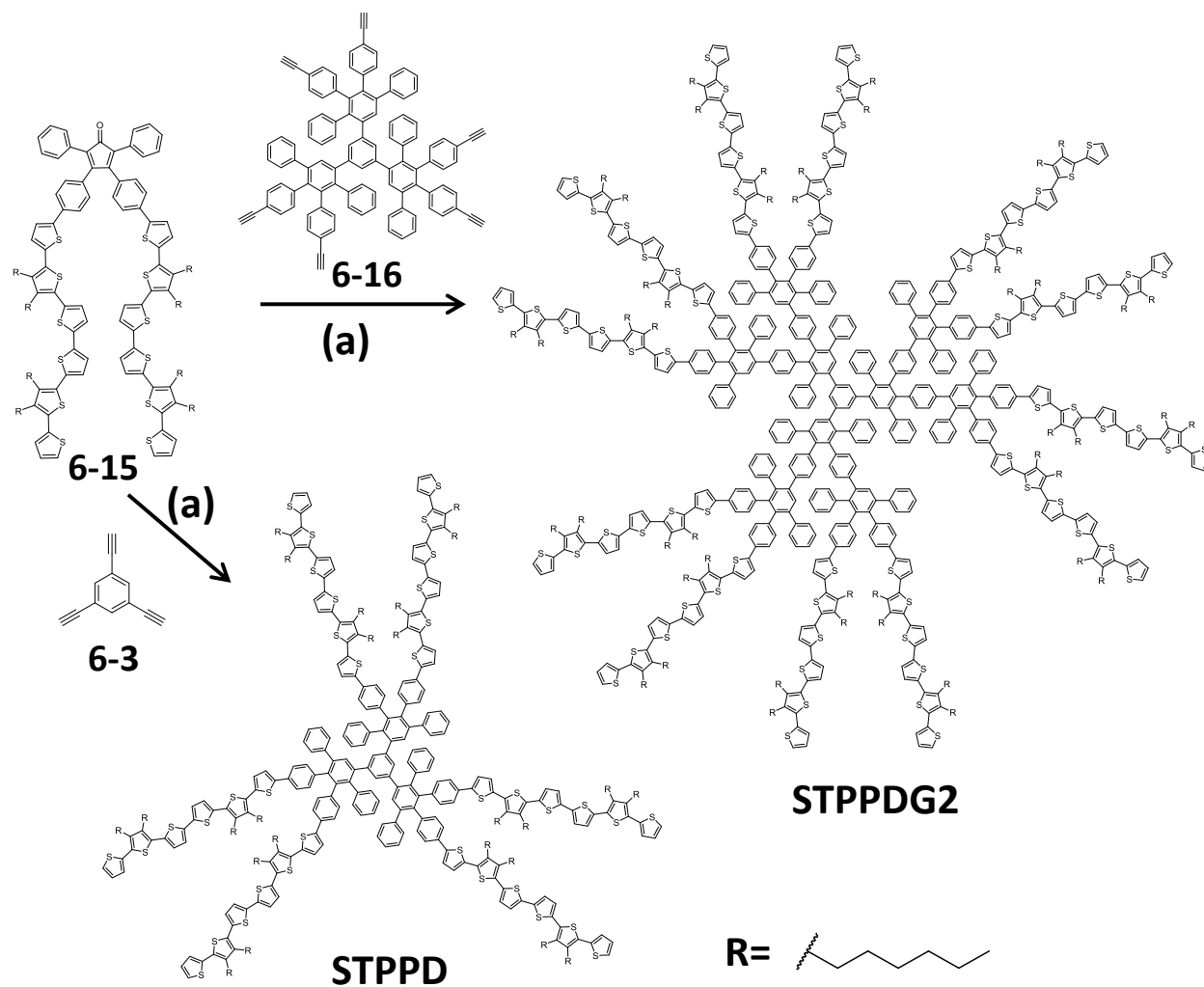
6.2.1 Dendrimer synthesis

To synthesize the dendrimers, **CPs** were prepared first. To ensure good solubilities of the dendrimers and to reduce the synthetic efforts, 3,4-dihexylthiophene (**6-6**) was employed as the starting material. The synthesis of sexithiophene-functionalized **CP** (**6-15**) took totally eight steps. As depicted in Scheme 6.2, first, compound **6-6** was brominated into 2,5-dibromo-3,4-dihexylthiophene (**6-7**) using N-bromosuccinimide (NBS) in high yield (91.7%). Then, 3',4'-dihexyl-2,2':5',2''-terthiophene (**6-10**) was

generated by a Kumada coupling in high yield (77.6%) between compound **6-7** and thiophene-2-magnesium bromide (**6-9**) which was obtained from 2-bromothiophene (**6-8**) in situ. After that, one bromine atom was introduced into one α position of compound **6-10** using NBS to form compound **6-11** in high yield (68%). Then the terthiophene-functionalized CP (**6-12**) was procured by a Suzuki coupling between compound **6-11** and diboronic-ester-functionalized CP (**2-22**) in high yield (74%). After that, compound **6-12** was brominated selectively at the two α positions of terthiophene segments using NBS to afford compound **6-13** in high yield (81%). At last, a Suzuki coupling between compound **6-13** and boronic-ester-functionalized terthiophene (**6-14**) gave birth to the sexithiophene-functionalized CP (**6-15**) in high yield (62%). In the last step, tri(*t*-butyl)phosphonium tetrafluoroborate ($[(t\text{-Bu})_3\text{PH}]\text{BF}_4$)^[26] worked as an efficient ligand for the palladium. Compound **6-14** was produced from 3',4'-dihexyl-2,2':5',2''-terthiophene (**6-10**) in 48% yield according the published procedure.^[27]



Scheme 6.2: Synthetic routes for α -sexithiophene-functionalized CP (**6-15**). (a) NBS, DMF, 0 °C, 72 h, 91.7 %; (b) Mg, diethyl ether, I₂, 40 °C, 1 h (c) (1) Pd(dppf)Cl₂, diethylether, -78 °C, (2) **5-9**, r.t., 24 h, 77.6%; (d) NBS, DMF, -20 °C, 72 h, 68%; (e) Pd(PPh₃)₄, K₂CO₃, tetrabutylammonium bromide, toluene, H₂O, 24 h, 105 °C, 74%; (f) NBS, DMF, 0 °C, 48 h, 81%; (g) (1) LDA, THF, -78 °C, 1 h, (2) 2-isopropoxy-4,4,5,5-tetramethyl-1,3,2-dioxaborolane, r.t., 12 h, 48%; (h) Pd₂(dba)₃, $[(t\text{-Bu})_3\text{PH}]\text{BF}_4$, K₂CO₃, THF, water, 60 °C, 12 h, 62.1%.



Scheme 6.3: Synthetic routes for **STPPD** and **STPPDG2**. (a) *o*-xylene, 160 °C, 3 days, 71.3% for **STPPD**, 165 °C, 14 days, 60.8% for **STPPDG2**.

With the **CP** available, as depicted in Scheme 6.3, the first generation dendrimer (**STPPD**) was obtained by a Diels-Alder reaction between compound **6-15** and 1,3,5-triethynylbenzene (**6-3**). Even though there were only three reactive points in compound **6-3**, the time needed to finish the reaction was much longer (3 days) than the first-generation dendrimers described in chapter 2 and **BTPPD** and **HBTPPD** mentioned above due to the much more bulkiness of the **CP** in this instance. Eventually, an orange-colored solid was received in high yield (71%) after purifications and drying under vacuum. **STPPDG2** was prepared from compound **6-15** and ethynyl-functionalized-1,3,5-benzene-based **PPD** (**6-16**) which was synthesized according to the reported procedures.^[28] Due to the doubled ethynyl groups in compound **6-16** compared with compound **6-3**, the time required to finish the reaction was much longer. Eventually, after stirring at 165 °C for 14 days, with argon protection and in the absence of light, the reaction was complete as proved by the observation of solely the product molecular ion peak without any side product peaks due to incomplete reactions, as monitored by MALDI-TOF mass spectrometry

and an orange-colored product was received in high yield (61%) after purifications and drying under vacuum.

Both dendrimers were readily soluble in some organic solvents, e.g. DCM, THF and toluene. This made them easily characterizable by ^1H and ^{13}C NMR spectroscopy, MALDI-TOF mass spectrometry, HRMS, UV-vis absorption and photoluminescence spectroscopy and cyclic voltammetry. As depicted in Figure 6.11, the aromatic protons signals in the ^1H NMR spectra of **STPPD** were not well resolved due to the strong overlaps. However, the signals of the hexyl groups were easily identified. For example, the protons which were closest to the thiophene groups (marked red) had the chemical shift of 2.74 ppm and those with the longest distance to the thiophene moieties showed a chemical shift of 0.93 ppm (marked yellow). The rest of hexyl proton signals were at around 1.50 ppm (marked green). In addition, the relative intensities of each signals correlated well with the number of respective protons in the molecule.

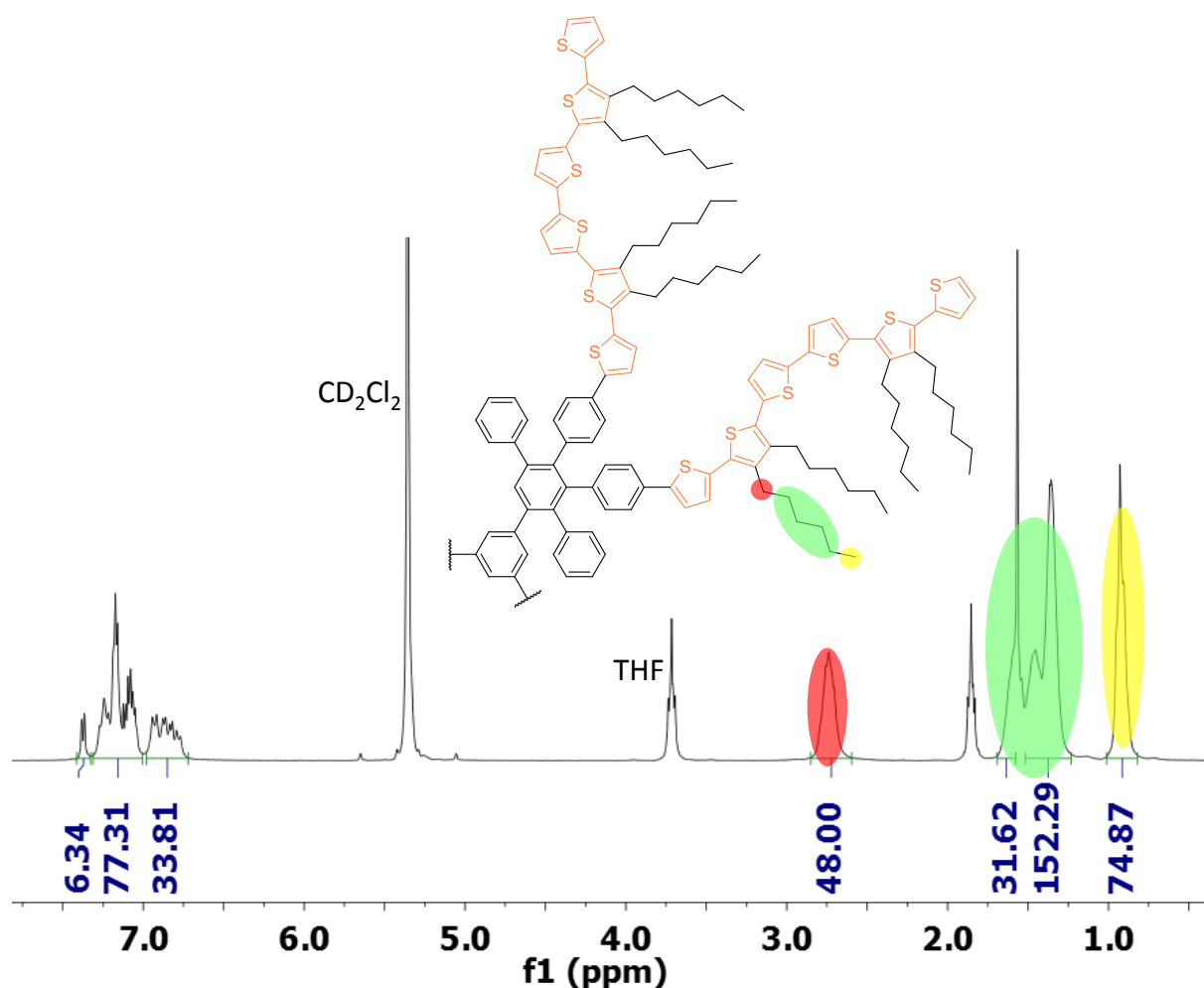


Figure 6.11: ^1H NMR spectra of **STPPD** (solvent: CD_2Cl_2).

The MALDI-TOF mass spectra of each dendrimer exhibited a single peak of the molecular ion. In addition, the HRMS spectra of **STPPD** displayed clear isotope patterns which were consistent with calculated results. Therefore, the desired products were synthesized (Figure 6.12).

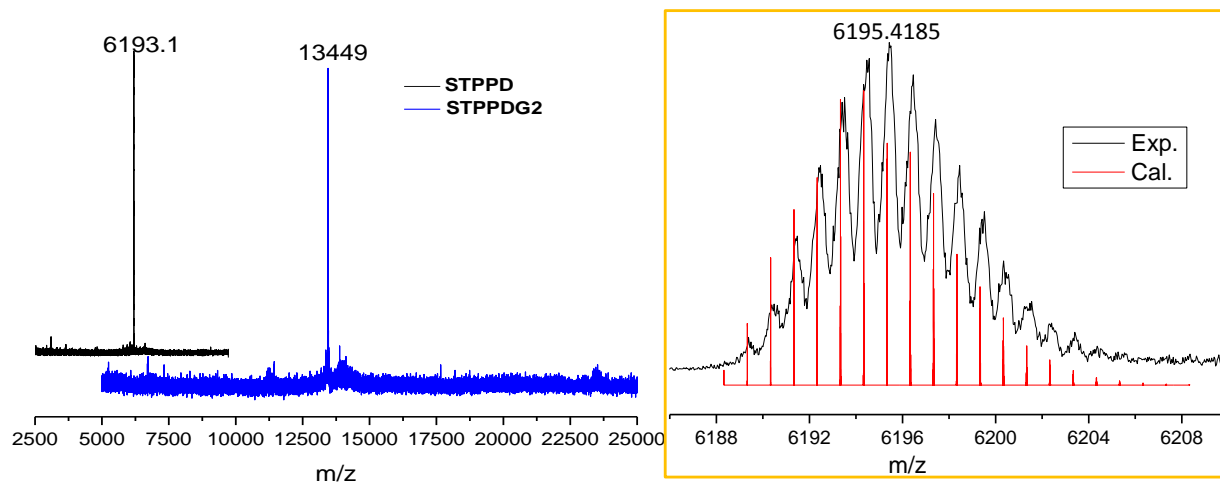


Figure 6.12: MALDI-TOF mass spectra of **STPPD** and **STPPDG2** (left) and HRMS spectra of **STPPD** (right).

6.2.2 Photophysical properties

As depicted in Figure 6.13, both dendrimers possessed a strong and broad absorption band centered around 421 nm) in solutions due to the π - π^* transitions of the α -phenyl-sexithiophenes.^[29] In addition, **STPPDG2** displayed much higher extinction coefficient ($\sim 6.5 \times 10^5 \text{ Lmol}^{-1} \text{ cm}^{-1}$) than **STPPD** ($\sim 2.5 \times 10^5 \text{ Lmol}^{-1} \text{ cm}^{-1}$) due to twice the number of surface chromophores in the former than the latter. Going to their emissions, they were both yellow-color emitters with nearly identical emission wavelengths and structures (λ_{max} : 531 nm and a shoulder: 562 nm) due to their same surface chromophores.

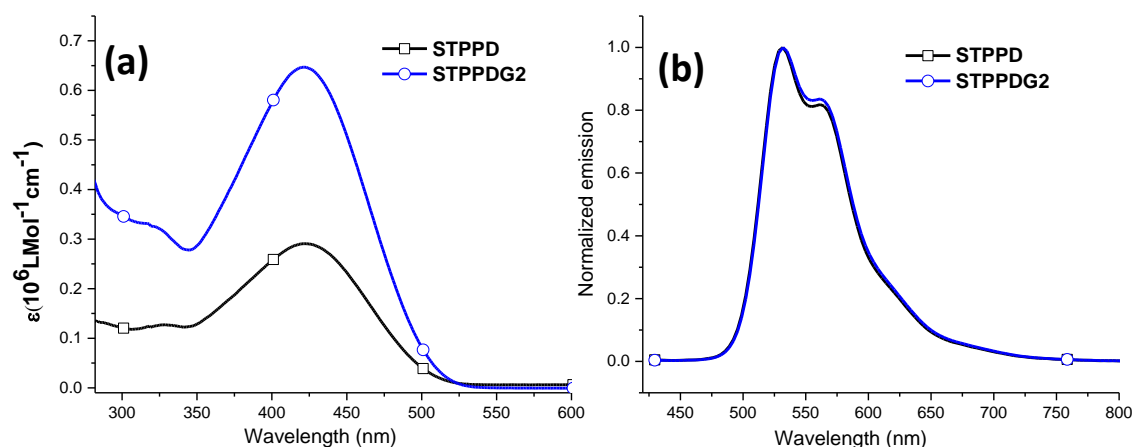


Figure 6.13: UV-vis absorption (a) and photoluminescence spectra (b, excited at 421 nm) spectra of **STPPD** and **STPPDG2** (10^{-6} M , toluene).

Table 6.2: Photophysical and electrochemical properties of **STPPD** and **STPPDG2**.

	$\lambda_{ab}(\text{nm})$ Sol.	$\lambda_{em}(\text{nm})$ Sol.	HOMO (eV) ^{a)}	LUMO (eV) ^{b)}	E_g (eV) ^{c)}
STPPD	421	531, 562	-5.06	-2.61	2.45
STPPDG2	421	531, 562	-5.05	-2.63	2.42

^{a)}Calculated from CV curves by comparing the first redox onset of **PYPPDs** and the oxidation onset of ferrocene; ^{b)}calculated from the band gap and HOMO level; ^{c)} calculated from the absorption edge of the longest wavelength band.

6.2.3 Electrochemical properties

The electrochemistry of these two dendrimers was investigated by CV using the same electrochemical setup as described before. As depicted in Figure 6.14, the oxidation of **STPPD** displayed three reversible oxidation couples between 0 and 1.4 V ($E_{1/2}$: 0.76 V, 0.85 V and 1.06 V respectively vs. Ag/AgCl), representing the three oxidation states of α -phenylsexithiophenes.^[30] **STPPD** was scanned up to 1.9 V for 10 cycles. There appeared another oxidation wave starting from around 1.56 V (E_{pa} : ~ 1.66 V). This was due to the oxidation of benzene moieties of the polyphenylene scaffold, consistent with the reported oxidation potentials of phenyl groups.^[6-7] The non-noticeable current enhancements and no new oxidation appearing at lower potentials after multiple sweeps demonstrated that no intermolecular couplings among sexithiophenes and no intramolecular cyclodehydrogenations occurred. This is probably related to the more stabilized sexithiophene as well as benzene radical cations by the much more resonant structures in sexithiophene backbone than the smaller oligothiophenes, e.g. bithiophene. This is consistent with the reported results that the longest oligothiophene undergoing self-couplings by CV was quaterthiophene.^[4b] These results also suggested that **STPPD** stayed quite stable after multiple scans up to 1.9 V and it could be a good hole transporting material. **STPPDG2** displayed similar oxidation properties as **STPPD**. In this instance, the scan was increased to 2.3 V, and another oxidation process occurred with peak potential at around 2.0 V due to overoxidation of this molecule,^[31] which destabilized the molecule as observed in subsequent sweeps. Their HOMO levels were calculated to be both around -5.05 eV by comparing their oxidation onsets with that of ferrocene and their LUMO levels were both around -2.45 eV by comparing their optical band gaps with their HOMO levels.

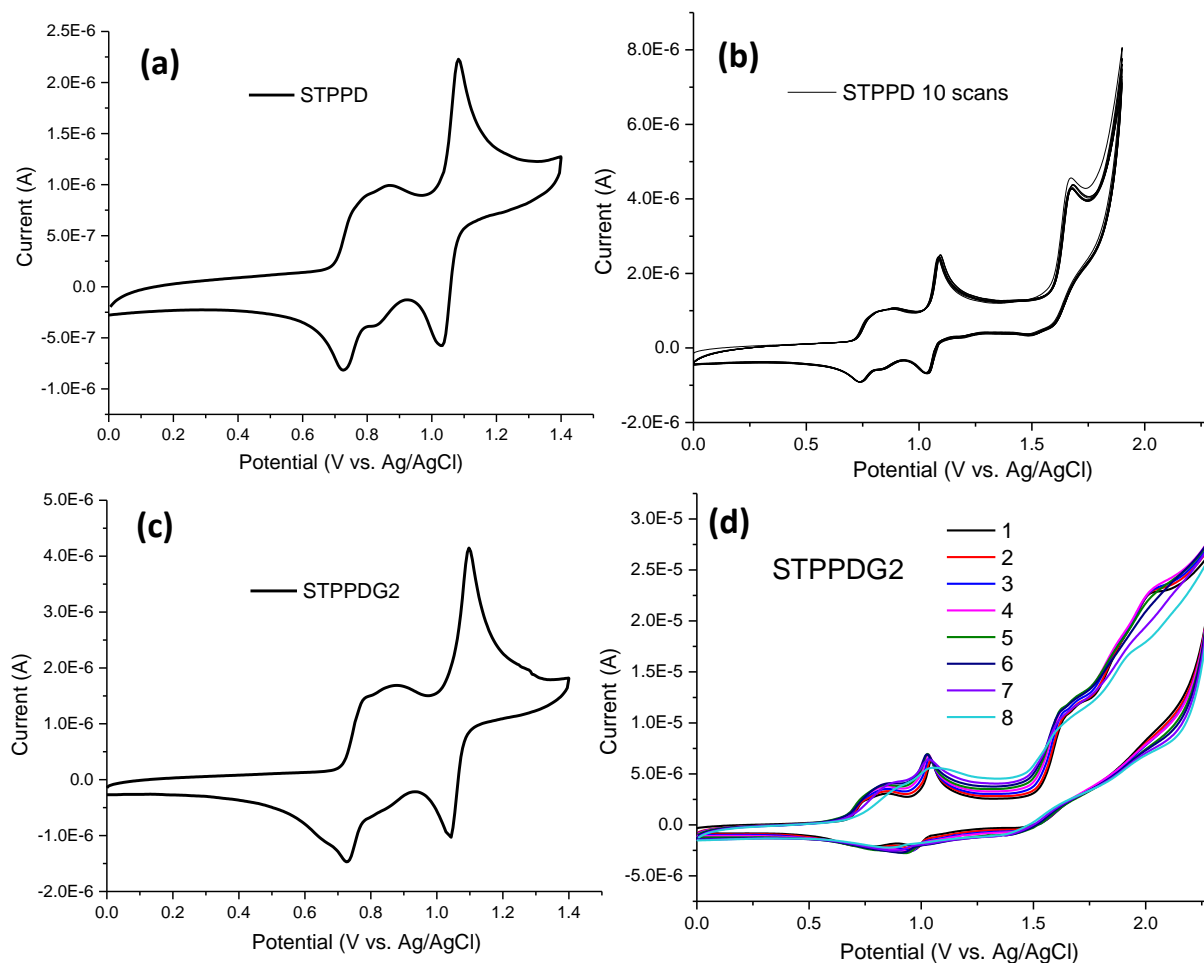


Figure 6.14: CV curves of STPPD and STPPDG2.

6.3 Summary

Bithiophene-functionalized **PPDs** were synthesized in two steps. **BTPPD** underwent intermolecular couplings between bithiophenes and cyclodehydrogenations of polyphenylene segments under CV sweeps. As a result, **NGN1** was formed after multiple scans. **NGN1** was characterized by Raman, IR, UV-vis absorption and SEM spectra. The Raman spectra showed the D and G band which were characteristic for graphene and PAH materials. IR spectra clearly demonstrated significant cyclodehydrogenations of polyphenylene segments. In addition, UV-vis absorption spectra demonstrated a large conjugated system in **NGN1** due to a strongly bathochromically shifted band compared with that of C96 nanographene. Moreover, SEM image of **NGN1** elucidated a 3-dimensional, cross-linked structure. The conductivity of the **NGN1** in the p-doped state provided a value of 10^{-7} S/cm using a two-Pt-foil assembly. This value could be improved by doping level control and measurement method (e.g. in situ conductivity method^[7]). **HBTTPD** was cyclodehydrogenated under multiple CV sweeps as proved by Raman and UV-vis absorption spectra. However, it is not determined whether the

cyclodehydrogenation is complete or not due to the absence of the desired molecular ion peak in MALDI-TOF mass spectra.

The sexithiophene-functionalized **PPDs** were synthesized successfully. They both displayed similar absorption and emission properties due to their same surface chromophores. However, they were not able to form nanographene networks by CV due to their more stabilized radical cations by the formation of more resonant structures along the sexithiophene backbones than smaller oligothiophenes, e.g. bithiophene.

Literature

- [1] a) NMR-thiophene, http://sdbs.db.aist.go.jp/sdbs/cgi-bin/direct_frame_top.cgi; b) NMR-benzene, http://sdbs.db.aist.go.jp/sdbs/cgi-bin/direct_frame_top.cgi.
- [2] a) M. Danko, A. Andicsova, P. Hrdlovic, D. Racko, D. Vegh, *Photoch Photobio Sci* **2013**, *12*, 1210-1219; b) A. Yokooji, T. Satoh, M. Miura, M. Nomura, *Tetrahedron* **2004**, *60*, 6757-6763.
- [3] C. C. You, P. Espindola, C. Hippus, H. Heinze, F. Wurthner, *Adv Funct Mater* **2007**, *17*, 3764-3772.
- [4] a) Z. G. Xu, D. Fichou, G. Horowitz, F. Garnier, *J Electroanal Chem* **1989**, *267*, 339-342; b) M. Barth, S. Guilerez, G. Bidan, G. Bras, M. Lapkowski, *Electrochim Acta* **2000**, *45*, 4409-4417.
- [5] C. C. You, C. R. Saha-Moller, F. Wurthner, *Chem Commun* **2004**, 2030-2031.
- [6] L. Q. Qin, Y. A. Zhang, X. Y. Wu, L. Nian, Z. Q. Xie, L. L. Liu, Y. G. Ma, *Small* **2015**, *11*, 3028-3034.
- [7] H. John, R. Bauer, P. Espindola, P. Sonar, J. Heinze, K. Mullen, *Angew Chem Int Edit* **2005**, *44*, 2447-2451.
- [8] a) C. Castiglioni, C. Mapelli, F. Negri, G. Zerbi, *J Chem Phys* **2001**, *114*, 963-974; b) C. Castiglioni, F. Negri, M. Rigolio, G. Zerbi, *J Chem Phys* **2001**, *115*, 3769-3778; c) F. Negri, C. Castiglioni, M. Tommasini, G. Zerbi, *J Phys Chem A* **2002**, *106*, 3306-3317; d) C. Mapelli, C. Castiglioni, E. Meroni, G. Zerbi, *J Mol Struct* **1999**, *481*, 615-620; e) M. Rigolio, C. Castiglioni, G. Zerbi, F. Negri, *J Mol Struct* **2001**, *563*, 79-87; f) J. S. Wu, Z. Tomovic, V. Enkelmann, Y. Mullen, *J Org Chem* **2004**, *69*, 5179-5186.
- [9] Z. B. Shifrina, M. S. Averina, A. L. Rusanov, M. Wagner, K. Mullen, *Macromolecules* **2000**, *33*, 3525-3529.
- [10] IR-n-hexane, http://sdbs.db.aist.go.jp/sdbs/cgi-bin/direct_frame_top.cgi.
- [11] G. R. Fulmer, A. J. M. Miller, N. H. Sherden, H. E. Gottlieb, A. Nudelman, B. M. Stoltz, J. E. Bercaw, K. I. Goldberg, *Organometallics* **2010**, *29*, 2176-2179.
- [12] J. O. Vogel, I. Salzmann, S. Duhm, M. Oehzelt, J. P. Rabe, N. Koch, *J Mater Chem* **2010**, *20*, 4055-4066.
- [13] L. W. Shacklette, R. R. Chance, D. M. Ivory, G. G. Miller, R. H. Baughman, *Synthetic Met* **1980**, *1*, 307-320.
- [14] a) R. C. Doss, P. W. Solomon, *J Org Chem* **1964**, *29*, 1567-1568; b) Y. Fujioka, S. Ozasa, K. Sato, E. Ibuki, *Chem Pharm Bull* **1985**, *33*, 22-29.
- [15] A. S. Matharu, S. J. Cowling, G. Wright, *Liq Cryst* **2007**, *34*, 489-506.
- [16] a) A. Centrone, L. Brambilla, T. Renouard, L. Gherghel, C. Mathis, K. Mullen, G. Zerbi, *Carbon* **2005**, *43*, 1593-1609; b) M. G. Schwab, A. Narita, Y. Hernandez, T. Balandina, K. S. Mali, S. De Feyter, X. L. Feng, K. Mullen, *J Am Chem Soc* **2012**, *134*, 18169-18172.
- [17] M. H. Yoon, A. Facchetti, C. E. Stern, T. J. Marks, *J Am Chem Soc* **2006**, *128*, 5792-5801.
- [18] C. D. Simpson, J. D. Brand, A. J. Berresheim, L. Przybilla, H. J. Rader, K. Mullen, *Chem-Eur J* **2002**, *8*, 1424-1429.
- [19] V. S. Iyer, K. Yoshimura, V. Enkelmann, R. Epsch, J. P. Rabe, K. Mullen, *Angew Chem Int Edit* **1998**, *37*, 2696-2699.
- [20] V. S. Iyer, M. Wehmeier, J. D. Brand, M. A. Keegstra, K. Mullen, *Angewandte Chemie-International Edition in English* **1997**, *36*, 1604-1607.
- [21] F. Morgenroth, E. Reuther, K. Mullen, *Angewandte Chemie-International Edition in English* **1997**, *36*, 631-634.

- [22] a) M. D. Watson, A. Fechtenkotter, K. Mullen, *Chem Rev* **2001**, *101*, 1267-1300; b) J. H. Wu, M. D. Watson, K. Mullen, *Angew Chem Int Edit* **2003**, *42*, 5329-5333.
- [23] a) J. D. Wood, G. P. Doidge, E. A. Carrion, J. C. Koepke, J. A. Kaitz, I. Datye, A. Behnam, J. Hewaparakrama, B. Aruin, Y. F. Chen, H. Dong, R. T. Haasch, J. W. Lyding, E. Pop, *Nanotechnology* **2015**, *26*; b) G. B. Barin, Y. Song, I. D. Gimenez, A. G. Souza, L. S. Barretto, J. Kong, *Carbon* **2015**, *84*, 82-90.
- [24] P. H. Aubert, L. Groenendaal, F. Louwet, L. Lutsen, D. Vanderzande, G. Zotti, *Synthetic Met* **2002**, *126*, 193-198.
- [25] M. C. Morvant, J. R. Reynolds, *Synthetic Met* **1998**, *92*, 57-61.
- [26] a) C. Q. Ma, E. Mena-Osteritz, M. Wunderlin, G. Schulz, P. Bauerle, *Chem-Eur J* **2012**, *18*, 12880-12901; b) M. R. Netherton, G. C. Fu, *Org Lett* **2001**, *3*, 4295-4298; c) C. Q. Ma, E. Mena-Osteritz, T. Debaerdemaeker, M. M. Wienk, R. A. J. Janssen, P. Bauerle, *Angew Chem Int Edit* **2007**, *46*, 1679-1683.
- [27] G. Zotti, S. Zecchin, B. Vercelli, M. Pasini, S. Destri, F. Bertini, *Chem Mater* **2006**, *18*, 3151-3161.
- [28] U. M. Wiesler, A. J. Berresheim, F. Morgenroth, G. Lieser, K. Mullen, *Macromolecules* **2001**, *34*, 187-199.
- [29] a) D. Fichou, G. Horowitz, B. Xu, F. Garnier, *Synthetic Met* **1992**, *48*, 167-179; b) M. Belletete, L. Mazerolle, N. Desrosiers, M. Leclerc, G. Durocher, *Macromolecules* **1995**, *28*, 8587-8597.
- [30] P. Bauerle, U. Segelbacher, K. U. Gaudl, D. Huttenlocher, M. Mehring, *Angewandte Chemie-International Edition in English* **1993**, *32*, 76-78.
- [31] a) C. Kvarnstrom, A. Ivaska, *Synthetic Met* **1991**, *43*, 2917-2921; b) B. Krische, M. Zagorska, *Synthetic Met* **1989**, *28*, C257-C262.

Chapter 7 Summary and Outlook

A major focus of this thesis was to produce efficient polyphenylene-dendrimer-based blue light emitting materials for **OLEDs**. The strategy involved specific surface and core functionalization of the dendrimers. First, the core was a fluorescent emitter, i.e. pyrene and the surfaces were decorated with hole and/or electron transporting moieties to decrease the charge injection barriers from the electrodes. Second, the core was replaced with phosphorescent emitters, i.e. iridium complexes. Besides using these materials in OLED applications, the triphenylamine-functionalized dendrimers were also employed as fluorescence sensors for TNT and Fe³⁺ detection. In addition, some dendrimers worked as hole transporting materials in Perovskite solar cells. The other task was generating nanographene networks from oligothiophene functionalized dendrimers by electrochemistry.

Chapter 2 presented the synthesis of a series of pyrene-based polyphenylene dendrimers with diverse surface functions. Due to the proper energy alignment between the emission of the surface chromophores and the absorption of the core, all the dendrimers showed pure blue emissions from the core through surface-to-core energy transfers. First-generation dendrimers demonstrated better performance in **OLEDs**, partially due to their more efficient FRETs than second-generation ones. In addition, judiciously tuning the HOMO/LUMO level of the peripheral chromophores of the dendrimers enhanced **OLED** performances by decreasing the charge injection barriers. For the bipolar-surface dendrimers, no significant device improvements were achieved compared with the **PYPPDs** with mono-component surfaces, possibly due to the reduced hole-electron recombination efficiency in the former, in which holes transport through donor moieties and electron transport through acceptor segments and their chances of recombination were reduced.

In the future, it will be beneficial to increase the charge transporting abilities of the dendrimer backbones by attaching conjugated oligofluorenes in the shell resulting in an enhanced electroluminescence.^{[1] [2] [3]} Furthermore, the periphery of the dendrimer may be functionalized with triphenylamines to reduce the hole injection barrier towards the pyrene emitting core. Therefore, Figure 7.1 illustrates a new core-shell surface functionalized dendrimer design.

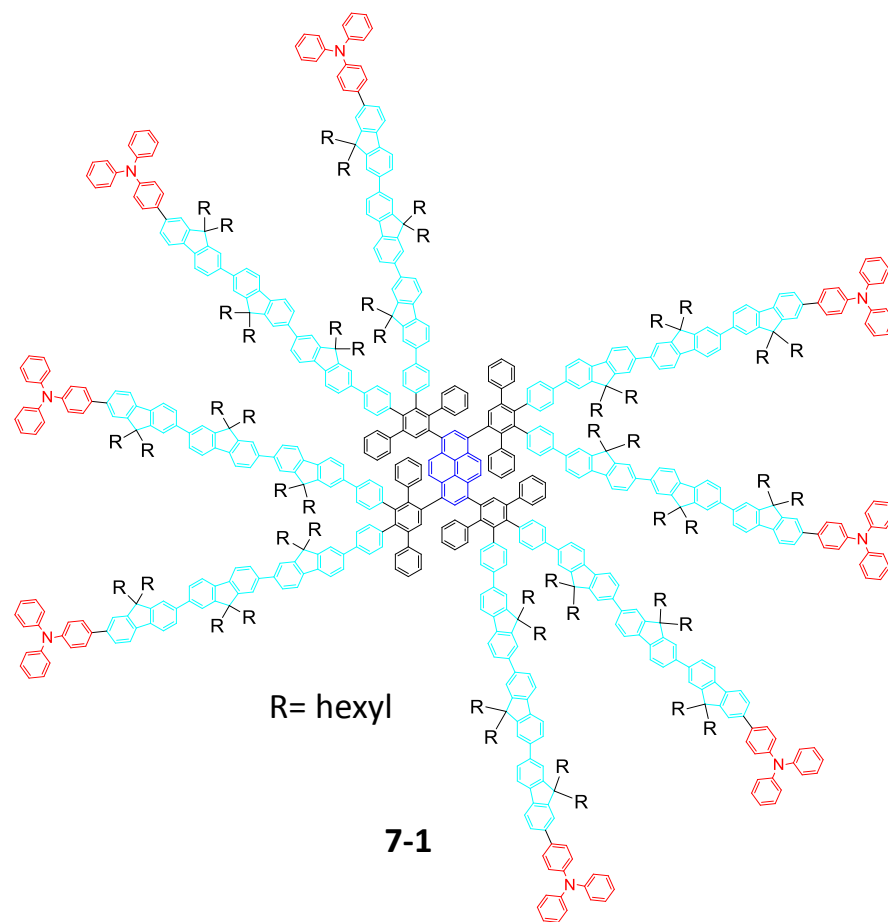


Figure 7.1: A proposed new blue-light-emitting dendrimer.

The iridium-complex-based polyphenylene dendrimers were synthesized as described in Chapter 3. However, the obtained dendrimers sometimes suffered from significant bathochromic shifts in emission and strong reduction in PLQYs compared with the bare core, probably due to the extended conjugation effects induced by polyphenylenes. The ligands bonded to polyphenylenes were calculated using the DFT method and considerable contributions by the polyphenylenes to the HOMO/LUMO level of the ligands were discovered. Therefore, it was deduced that direct bonding of polyphenylenes to the ligands of iridium complexes rendered modifications of the electronic structures of the ligands of the iridium-complex-based dendrimers and, as a result, the photoluminescence properties of the dendrimers were changed. Consequently, it is hard to make efficient polyphenylene-dendrimer-based phosphorescent blue emitters because there exist conjugation-induced bathochromic shifts by polyphenylenes, and it is not advised to carry out further investigations in this field.

As discussed in chapter 4, triphenylamine-functionalized dendrimers, especially the second-generation one, demonstrated high sensitivity and selectivity to Fe^{3+} detection in solutions and thin films due to the favorable coordinating between ferric ions and the surface “N” atoms of triphenylamines, which blocked the surface-to-core energy transfers. Even though thin films of the dendrimers exhibited minor responses to TNT explosive, the electropolymerized film obtained by intermolecular couplings among

triphenylamines under CV sweeps manifested significant fluorescence quenching toward TNT and much lower sensitivity towards other nitro-rich compounds due to their either lower vapor pressures or lower electron accepting abilities than TNT. The reason for the much enhanced sensitivity and selectivity of the electropolymerized film towards TNT was the microporous ($\text{\O}: \sim 1 \text{ nm}$) and cross-linked structure of the film, which created enough space for TNT vapors to penetrate inside the film and interact with pyrene moieties adequately, compared with the densely-packed films from spin coating.

In the future, more efficient fluorescence sensors can be prepared following two design principles: first, the dendrimer should be big enough to guarantee high selectivity, especially for Fe^{3+} ; second, the scaffold of the dendrimer should have more space for the analyte, e.g. TNT to penetrate inside. Therefore, as depicted in Figure 7.2, the core is decorated with 4 phenyl groups to enlarge the volume around the emitter and create more space around the core for better interaction with TNT molecules. Additionally, 4 more phenyl groups are placed in the shell to make more free-volume for the explosive units to pass through the scaffold.

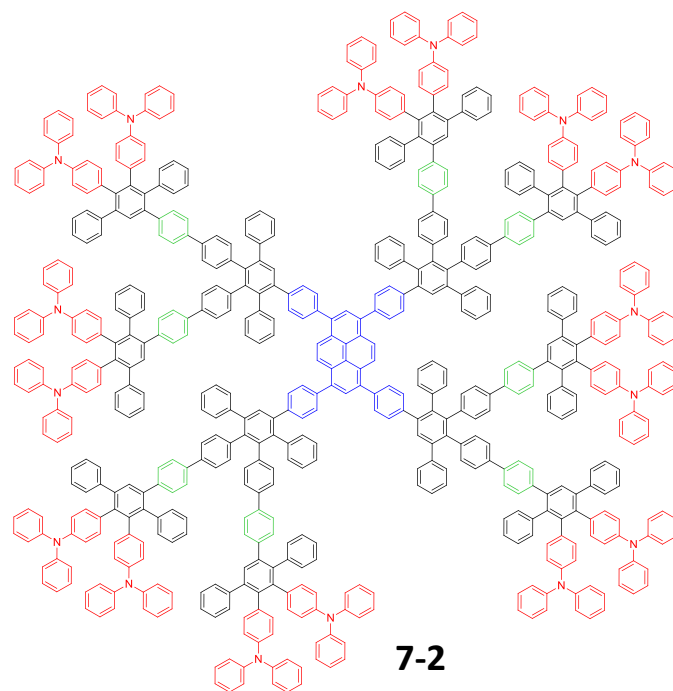


Figure 7.2: A proposed new dendrimer for efficient fluorescence sensor.

The first-generation dendrimers with hole transporting moieties in the periphery demonstrated promising applications as hole transporting materials in Perovskite solar cells which were covered in chapter 5. The dendrimer, **PYTPA** stored at ambient conditions for over 2 years promoted the power conversion efficiency up to 17 %, suggesting that this dendrimer was among the best performing hole transporting materials.^[4] However, the newly synthesized **PYTPA** displayed much lower efficiencies (1%). The difference between the first batch and the new one was that the former was partially oxidized by oxygen in air as confirmed by the tiny triphenylamine radical cation band in the UV-vis absorption spectra and

the radical peak in EPR spectra. In addition, the oxidation of triphenylamines could easily render intermolecular couplings among triphenylamines. As a result, the enhanced performances of the old sample should relate to the existence of radicals or the dendrimer-based and/or the cross-linked structure. However, the oxidation ratio was very small (~0.1%) as suggested from the absorbance. It is surprising that such a low doping level of the dendrimers induced such a large boost in device performance, though the exact reason is still under investigation.

In the future, more studies should focus on partially oxidizing or doping the newly **PYTPA** to try to reach the performance of the old sample. Then the compositions of the high-performance samples will be characterized and studied to find out the reason for the enhanced device performances and, lastly, new dendrimers with logical designs will be synthesized.

Oligothiophene-functionalized dendrimers were utilized to grow nanographene networks by electropolymerizations, as mentioned in chapter 6. The films obtained on the working electrode were characterized by Raman, IR and UV-vis absorption spectroscopies. Raman spectra exhibited the characteristic D and G bands of graphene materials. IR spectra demonstrated considerable cyclodehydrogenations of the polyphenylenes. UV-vis absorption spectra showed a strongly red-shifted band compared with that of C96 nanographene, indicating the formation of a large conjugated structure. As a result, it was determined that nanographene networks were formed.

However, the conductivity property of the nanographene network needs further studies before synthesizing more **NGNs**. As shown in chapter 6, the intrinsic **NGN1** was an insulator but it became conductive under p-doped state (10^{-7} S/cm was obtained). The conductivity of this material can be improved by controlling the doping level by electrochemistry or some oxidants, e.g. AsF_5 , I_2 and FeCl_3 .^[5] In addition, n-type doping can also be tried by electrochemistry or some reductants, e.g. sodium naphthalenide.^[5b]

Literature

- [1] C. Liu, Q. Fu, Y. Zou, C. L. Yang, D. G. Ma, J. G. Qin, *Chem Mater* **2014**, *26*, 3074-3083.
- [2] L. Wang, Y. Jiang, J. Luo, Y. Zhou, J. H. Zhou, J. Wang, J. Pei, Y. Cao, *Adv Mater* **2009**, *21*, 4854-+.
- [3] P. Moonsin, N. Prachumrak, S. Namuangruk, S. Jungstittiwong, T. Keawin, T. Sudyoadsuk, V. Promarak, *J Mater Chem C* **2014**, *2*, 5540-5552.
- [4] P. Gratia, A. Magomedov, T. Malinauskas, M. Daskeviciene, A. Abate, S. Ahmad, M. Gratzel, V. Getautis, M. K. Nazeeruddin, *Angew Chem Int Edit* **2015**, *54*, 11409-11413.
- [5] aL. W. Shacklette, R. R. Chance, D. M. Ivory, G. G. Miller, R. H. Baughman, *Synthetic Met* **1980**, *1*, 307-320; bC. K. Chiang, S. C. Gau, C. R. Fincher, Y. W. Park, A. G. Macdiarmid, A. J. Heeger, *Appl Phys Lett* **1978**, *33*, 18-20; cD. M. Deleeuw, *Synthetic Met* **1993**, *57*, 3597-3602.

Chapter 8 Experimental Part

8.1 Materials and methods

4,4'-Di(TIPSE)benzil (**1-1**),^[1] 3,4-bis(4-TIPSEphenyl)-2,5-diphenylcyclopentadienone (**1-3**),^[1] 3,4-bis(4-bromophenyl)-2,5-diphenylcyclopentadienone (**2-1**),^[2] 1,3,6,8-tetraethynylpyrene(**2-9**),^[3] TIPSE-functionalized first-generation **PYPPD** (**2-10**),^[3] peripheral-ethynyl-functionalized first-generation **PYPPD** (**2-11**),^[3] 2-bromophenyl-5-(p-tertbutyl-phenyl)-1,3,4-oxadiazole (**2-16**),^[4] 1-(4-bromophenyl)-2-(4-iodophenyl)ethyne (**2-19**),^[5] 2-(4-tert-butylphenyl)-5-(4-(4,4,5,5-tetramethyl-1,3,2-dioxaborolan-2-yl)phenyl)-1,3,4-oxadiazole (**2-17**),^[6] 3,4-bis[4-(4,4,5,5-tetramethyl-1,3,2-dioxaborolan-2-yl)phenyl]-2,5-diphenylcyclopentadienone (**2-22**)^[7], 1-bromo-4-TIPSEbenzene (**3-24**)^[8], 1,3,5-triethynylbenzene (**6-3**)^[9], 1,3,5-benzene-based first generation **PPD** (**6-16**)^[10] were synthesized according to the published procedures. All the other chemicals and solvents were used as received except where noted. They were generally purchased from Sigma-Aldrich, Acros Organics, Alfa Aesar, Fisher Scientific, Synthoix or TCI Europe companies. Unless otherwise stated, all the syntheses were carried out under argon atmosphere using standard schlenk techniques. The photochemistry was carried out in a photochemical reactor from Rayonet (16 UV lamps, 20 W for each lamp, shining wavelength: 365 nm).

Chromatography:

Silica gel flash columns were fabricated with the gel size in between 0.063 and 0.200 mm (from Merck). For the analysis of reactions by thin layer chromatography (TLC), substrates coated with silica gel 60 F254 from Merck were applied. Preparative gel permeation chromatography (GPC) columns were built by packing the gels formed by dispersing the cross-linked polystyrenes (based on Bio-Beads S-X1 from Bio-Rad Laboratories) in THF.

NMR spectroscopy:

¹H NMR, ¹³C NMR, ¹⁹F NMR and ¹H-¹H COSY spectra were acquired by Bruker DPX 250, Bruker AMX 300, Bruker DRX 500, Bruker DRX 700 or Bruker DRX 850. Chemical shifts were referenced by the deuterated solvents, e.g. CD₂Cl₂, THF-d₈ based on the NMR chemical shifts of organic solvents.^[10]

Mass spectrometry:

Field desorption (FD) mass spectra were recorded on a VG-Instruments ZAB 2-SE-FDP using 8 kV accelerating voltage. MALDI-TOF mass spectra were recorded by a Bruker Reflex II spectrometer with fullerene as the reference and dithranol as the matrix. High resolution-ESI mass spectra were recorded by an ESI Qtof Ultima 3 Micro Mass spectrometer from Waters.

UV-vis spectroscopy: UV-Vis absorption spectra were recorded by PERKIN ELMER UV/Vis spectrometer (Lambda 900).

Photoluminescence spectroscopy: Fluorescence spectra were acquired by a SPEX Fluorolog 2 spectrometer.

Raman spectroscopy: Raman spectra were obtained from a Bruker RFS 100/S spectrometer (laser wavelength 532 nm).

IR spectroscopy: IR spectra were obtained from Nicolet 730 FT-IR Spectrometer.

SEM spectroscopy: SEM images were obtained from Zeiss Gemini 1530 instrument.

EPR spectroscopy: EPR spectra were recorded with a Bruker x-band spectrometer ESP300 E, equipped with an NMR gauss meter (Bruker ER035) and a frequency counter (Bruker ER041XK).

Cyclic voltammetry:

CV measurements were conducted on a computer-controlled GSTAT12 workstation using a three electrodes system in which a Pt wire, a silver wire, and a glassy carbon electrode were counter, reference and working electrode respectively. The measurements were conducted in 0.1 M tetrabutylammonium hexafluorophosphate (TBAPF₆) solution under argon environment with a scan rate of 50 or 100 mV/s at room temperature. The solvents were anhydrous DCM for the oxidation part and anhydrous THF for the reduction part. Ferrocene/Ferrocenium (Fc/Fc⁺) worked as the internal reference throughout the measurements. The calculations of HOMO and LUMO using CV were based on the following equations, $E_{\text{HOMO}} \text{ (eV)} = - (E_{\text{ox}}^{\text{onset}} - E_{\text{Fc/Fc}^+}^{\text{onset}}).e - 4.80 \text{ eV}$ and $E_{\text{LUMO}} \text{ (eV)} = - (E_{\text{red}}^{\text{onset}} - E_{\text{Fc/Fc}^+}^{\text{onset}}).e - 4.80 \text{ eV}$, where $E_{\text{ox}}^{\text{onset}}$, $E_{\text{Fc/Fc}^+}^{\text{onset}}$ and $E_{\text{red}}^{\text{onset}}$ mean the onset oxidation potential of the sample, the onset oxidation potential of Ferrocene and the onset reduction potential of the sample, compared to Ag/Ag⁺ reference electrode.

Single crystal growth and structure identification:

Crystals suitable for single-crystal x-ray analysis were grown as follows:

Compound **2-3m** and compound **2-3p**: two phase slow dispersion between n-pentane and chloroform; **fac(2,6-difpy-5'-TMSpy)₃Ir** and **mer(2,6-difpy-5'-TMSpy)₃Ir**: two phase slow dispersion and evaporation between methanol and dichloromethane. Crystallographic data were collected from the diffractometer of STOE IPDS 2T or APEX II or Smart CCD (radiation: Mo-K_α Graphitmonochromator).

HOMO and LUMO level calculations:

The HOMO and LUMO levels of some small chromophores were calculated by Gaussian software based on density functional theory (DFT)/ B3LYP method and basis set of 6-31G.

OLED fabrication and characterizations:

For the fabrication of single- and multilayer-devices all indium tin oxide covered glass substrates were cleaned mechanically by the use of acetone and isopropanol. The substrates were subjected to subsequent supersonic cleaning steps in deionized water, toluene and isopropanol. Prior to the deposition of poly(3,4-ethylenedioxythiophene)–polystyrenesulfonic acid (Baytron P VPAI 4083) (PEDOT:PSS) from H. C. Starck as a first polymeric layer, to enhance the wettability of PEDOT:PSS on the substrate, the ITO substrates were subjected to a dry cleaning procedure in oxygen plasma. PEDOT:PSS was spin-cast onto the as prepared substrates under ambient conditions and dried according to the specifications under dynamic vacuum with a pressure less than 1×10^{-5} mbar. For single layer dendrimer-based light-emitting diodes (DLEDs) the emissive layer was spin cast from 8 mg mL^{-1} toluene solutions. After spin coating the samples were annealed for 1h under high vacuum ($p \leq 1 \times 10^{-5}$ mbar) at $70 \text{ }^\circ\text{C}$. The thicknesses of the emissive layers were determined to be 50 nm with a mean error of less than 10%. To fabricate triple-layer-OLEDs, TFB layers were deposited by spin-coating from a 15 mg mL^{-1} solution under inert conditions and dried in argon at $200 \text{ }^\circ\text{C}$ for 2h. Afterwards, the substrates were cooled to room temperature on a cold surface. To remove the soluble parts of the annealed polymer the TFB layer was spin-rinsed by pure toluene resulting in a final layer thickness of 5 nm with good reproducibility as long as annealing temperature and time were kept constant. Emissive layers were spin-cast onto prepared TFB films from an 8 mg mL^{-1} toluene solution and dried at $80 \text{ }^\circ\text{C}$ for 2h in vacuum ($p \leq 1 \times 10^{-5}$ mbar) resulting in layer thicknesses of 75 nm. Prior to depositing PEGPF in the case of triple-layer devices, the TFB/dendrimer-substrates were spin-rinsed by pure methanol. Afterwards PEGPF dissolved in methanol was applied by spin-coating at a polymer content of 1 mg mL^{-1} . The layer was annealed at $70 \text{ }^\circ\text{C}$ for 1h under high vacuum ($p \leq 1 \times 10^{-5}$ mbar) and exhibited a thickness of 10 nm, which was well controllable for spinning speeds above 1500 rpm. After polymer deposition 1 nm of Cs_2CO_3 and 100 nm Al as cathode materials were deposited thermally through a shadow mask forming a device area of 9 mm^2 in a custom made vapor deposition unit from tungsten boats at an initial base pressure less than 1×10^{-6} mbar. Current/luminance/voltage (I–L–V) characteristics were recorded in a customized setup. To determine the I–V characteristics a Keithley 2612A source measure unit was used and a Keithley 6485 Picoammeter using a calibrated photodiode was employed for recording the luminance.

Perovskite solar cell fabricaton and characterizations:

Fluorine-doped Tin Oxide (FTO) glass substrates with dimension of $2.0 \text{ cm} \times 2.0 \text{ cm}$ were patterned by etching with zinc powder and 2 M hydrochloric acid. The substrates were then sequentially washed in

ultrasonic baths of acetone, distilled water and ethanol. A compact TiO₂ blocking layer was spin-coated onto the cleaned FTO glass using 0.15 M titanium tetraisopropanolate in ethanol solution at 2000 rpm for 30 s. The substrate was heated at 120 °C for 15 min, and then annealed at 550 °C for 30 min. After cooling to the room temperature, the film was immersed into the 20 mM TiCl₄ solution at 70 °C for 30 min. After dried, a ~200 nm thick mesoporous TiO₂ film was deposited on the pre-treated FTO substrate by spin-coating of the TiO₂ paste (Dyesol DSL 18NR-T) with ethanol (1:3, mass ratio), which was followed by the heating at 550 °C for 30 min. For the perovskite layer, the as-prepared substrate was infiltrated with a hot solution of PbI₂ in N, N-dimethylformamide (462 mg/1 mL) by spin-coating at 4000 rpm for 30 s, and then dried at 120 °C for 5 min. After cooling to room temperature, the film was dipped into the solution of CH₃NH₃I in 2-propanol (10 mg/mL) for 30 s, which was spun at 4000 rpm for 20 s and then heated at 100 °C for 5 min. After the deposition of the perovskite layer, the TSHBC-R (TSHBC/graphene)/chlorobenzene (10 mg/mL) solution were coating by solution process at 4000 rpm for 30 s. Finally, a 80 nm thick Au counter electrode was deposited by thermal evaporation under reduced pressure of 2×10^{-7} Torr. The active area was 0.10 cm².

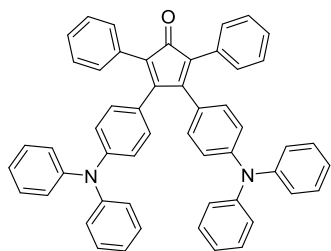
Current-voltage characteristics were recorded from a solar simulator equipped with a Keithley 2400 source meter and 300 W collimated Xenon lamp (Newport) calibrated with the light intensity to 100 mW cm⁻² at AM 1.5 G solar light condition by the certified silicon solar cell. Incident photon-to-electron conversion efficiency (IPCE) was measured on a computer-controlled IPCE system (Newport) containing a Xenon lamp, a monochromator and a Keithley multimeter. The system was calibrated with the certified silicon solar cell and the IPCE data were collected at DC mode. XRD patterns were analyzed by an X-ray diffractometer (Rigaku, RINT-2500) with a CuK α radiation source. The surface morphology of were recorded via a SEM-4800 field-emission scanning electron microscope (SEM). The UV-vis spectra were measured with the perovskite infiltrated mesoscopicTiO₂ films supported by FTO glass using a Cary-5000 UV-vis spectrophotometer. The Time-resolved photoluminescence (PL) spectra were measured using an Edinburgh Instruments FLS920 spectrometer. The electrochemical impedance spectroscopy (EIS) was carried out in the frequency range from 10⁶ to 0.1 Hz in the dark, in which the potential bias was applied from 400 to 900 mV. According to the simplified transmission line model, the arcs at high-intermediate frequency can be supposed to be charge-transport resistance.

8.2 Synthetic procedures

8.2.1 Synthesis of blue fluorescent dendrimers (Chapter 2)

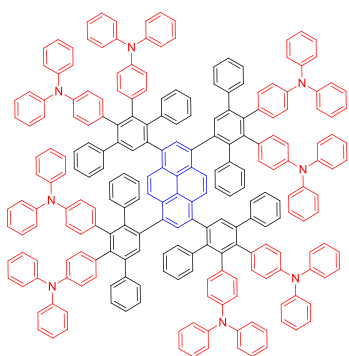
3,4-Bis(4-triphenylamino)-2,5-diphenylcyclopentadienone (2-3a)

Compound **2-3a** was synthesized with a modified procedure from a published article.^[12] The procedure is as follows:



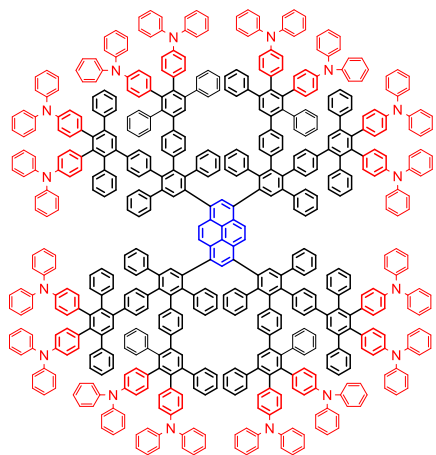
Compound **2-1** (4.00 g, 7.38 mmol) and diphenylamine (2.50 g, 14.75 mmol) were placed in a 100 ml round bottom flask. It was then transferred to a glove box, in which sodium tertbutoxide (2.13 g, 22.13 mmol), tris(dibenzylideneacetone)dipalladium (0.17 g, 0.18 mmol), tri(tertbutyl)phosphine (0.298 g, 1.48 mmol) and 40 ml of dry toluene were added sequentially. Then the mixture was stirred at 60 °C for 12 hours. The resulting mixture was extracted with DCM and dilute NH₄Cl solution, followed by a silica gel flash column (DCM/petroleum ether, 3/7). Eventually, 3.71 g dark-purple solid was received after drying under reduced pressure (70%). Spectra data were consistent with published date.^[12]

Pyrene-based, peripheral-triphenylamine polyphenylene dendrimer-G1 (PYTPA)



Compound **2-9** (15.0 mg, 0.05 mmol) and **2-3a** (180.7 mg, 0.25 mmol) were placed in a 10 ml round bottom flask and dissolved in 4ml anhydrous o-xylene. The mixture was stirred at 140 °C for 24 hours. Then the cooled mixture was poured into methanol to precipitate and filtered. The obtained crude product was purified by a silica gel flash column (1/1, DCM/hexane). The dendrimer fractions were further purified by a GPC column (toluene as the solvent). Eventually, 100 mg light yellow solid was received after drying under reduced pressure (65%). ¹H NMR(700MHz, CD₂Cl₂, 300K) δ H:7.97-7.80(m, 6H), H:7.62-7.47(m, 4H), 7.31-7.12(m, 52H), 6.97-6.60(m, 100H). ¹³C NMR(75MHz, CD₂Cl₂, 298K) δ 148.21, 145.87, 145.50, 142.15, 142.08, 142.01, 141.91, 141.26, 141.21, 141.02, 140.74, 140.63, 140.60, 140.55, 140.48, 140.42, 140.27, 139.92, 139.78, 139.75, 139.64, 139.61, 139.56, 139.50, 137.04, 136.85, 136.38, 136.25, 136.18, 135.71, 133.63, 133.44, 133.07, 132.95, 131.94, 131.75, 130.60, 130.52, 129.51, 129.42, 128.48, 128.23, 127.89, 127.23, 126.99, 126.69, 126.05, 125.72, 124.82, 124.07, 123.85, 123.70, 122.76, 122.58. MALDI-TOF: calculated for C₂₃₂H₁₆₂N₈: 3061.9, found: 3059.9. HR-ESI-MS: calculated for C₂₃₂H₁₆₂N₈: 3062.2830, found: 3062.2830 [M⁺].

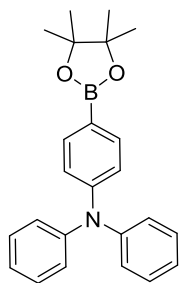
Pyrene-based, peripheral-triphenylamine polyphenylene dendrimer-G2 (PYTPAG2)



Compound **2-11** (80.0 mg, 0.042 mmol) and compound **2-3a** (450.2 mg, 0.626 mmol) were dissolved in 15 ml o-xylene in a round bottom flask. Then the mixture was heated at 160 °C for 2 days. The resulting mixture was precipitated in methanol, followed by filtration. Then the solid mixture was purified by a silica gel column (6/4, DCM/hexane). The resulting product was further purified by a GPC column (toluene as the solvent). Eventually, 150 mg light-

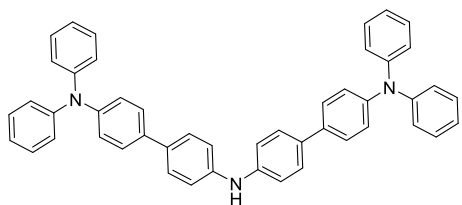
yellow-colored solid was received after drying under reduced pressure (50%). ^1H NMR(700MHz, CD_2Cl_2 , 300 K) δ 7.81-7.65(m, 6H), 7.48-7.36(m, 12H), 7.23-6.28(m, 376H). ^{13}C NMR(176 MHz, CD_2Cl_2 , 298 K) δ 148.04, 145.64, 145.29, 142.08, 141.99, 140.94, 140.89, 140.68, 140.61, 140.44, 139.54, 139.45, 139.34, 139.28, 139.14, 138.72, 138.55, 138.31, 136.88, 136.15, 135.51, 132.82, 132.01, 131.41, 131.15, 130.31, 129.33, 129.26, 128.94, 128.62, 128.31, 128.24, 128.20, 127.97, 127.80, 127.11, 126.54, 125.91, 125.80, 123.88, 123.66, 123.50, 122.57, 122.42. MALDI-TOF: calculated for $\text{C}_{568}\text{H}_{394}\text{N}_{16}$: 7443.1, found: 7440.8. HR-MALDI-TOF: calculated for $\text{C}_{568}\text{H}_{394}\text{N}_{16}$: 7443.1524, found: 7443.3420 [M^+].

4-(Diphenylamino)phenylboronic acid pinacol ester (2-6)



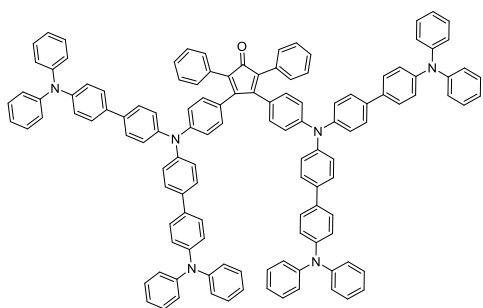
In a 100 ml flame-dried Schlenk flask was added 4-bromotriphenylamine (2.00 g, 6.17 mmol), degassed and added argon 3 times. Then 40 ml of dry THF was added and the mixture was put in dry ice/acetone bath and stirred to make it dissolve. Then 1.6 M n-BuLi in hexane (4.6 ml, 7.40 mmol) was added slowly and let it stirred in dry ice bath for 1 hour. Then 2-isopropoxy-4,4,5,5-tetramethyl-1,3,2-dioxaborolane (1.5 ml, 7.40 mmol) was added slowly and let the mixture stir overnight at room temperature. Then extraction was done with diethyl ether to collect the organic fraction which was condensed and dried under vacuum to receive 2.29 g yellow-brown-colored liquid (100%). The product was directly used for next step without further purification. ^1H NMR (250 MHz, CDCl_3 , 298 K) δ 7.67 (d, J = 8.0 Hz, 2H), 7.24 (d, J = 8.0 Hz, 2H), 7.07 (m, 10H), 1.33 (s, 12H). Spectral data were consistent with published date.^[13]

4,4'-Di(4-triphenylamino)diphenylamine (2-8)



Bis(4-bromophenyl)amine (0.820 g, 2.51 mmol), compound (2-6) (2.33 g, 6.27 mmol), Na_2CO_3 (1.66 g, 15.67 mmol), 30 ml of toluene and 10 ml of water were added in a 50 ml round bottom flask. Then the mixture was degassed and added argon for 3 times, followed by the addition of $\text{Pd}(\text{PPh}_3)_4$ (144 mg, 0.125 mmol). The mixture was then stirred at 110 °C for 24 hours. Then it was extracted by DCM and purified by a silica gel flash column (2/3, DCM/Petroleum ether). Eventually, 1.00 g of white-colored solid was received after drying under reduced pressure (60%). ^1H NMR (250 MHz, $\text{DMSO}-d_6$, 298 K) δ 8.43 (s, 1H), 7.55 (dd, J = 8.7, 3.1 Hz, 8H), 7.31 (dd, J = 8.5, 7.2 Hz, 8H), 7.17 (d, J = 8.6 Hz, 4H), 7.10 – 6.91 (m, 16H). The spectral data are consistent with the published result.^[14]

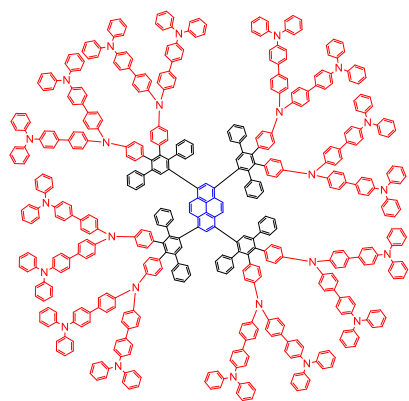
3,4-Bis-(4,4'-di(4-triphenylamino)triphenylamino)-2,5-diphenylcyclopentadienone (2-3c)



Compound **2-1** (0.206 g, 0.380 mmol) and compound **2-8** (0.498 g, 0.76 mmol) were placed in a 10 ml round bottom flask. It was then transferred to a glove box, in which sodium tert-butoxide (0.109 g, 1.14 mmol), tris(dibenzylideneacetone)dipalladium (9 mg, 9.0 μ mol), tri(tertbutyl)phosphine (15 mg, 76 μ mol) and 5 ml of dry toluene were added sequentially. Then the mixture was

stirred at 60 °C for 12 hours. The resulting mixture was extracted with DCM and dilute NH₄Cl solution, followed by a silica gel flash column (DCM/petroleum ether, 1/1). Eventually, 0.29 g black solid was received after drying under reduced pressure (20.5%). ¹H NMR (300 MHz, CD₂Cl₂, 300 K) δ 7.46 (d, *J* = 8.6 Hz, 8H), 7.39 (d, *J* = 8.7 Hz, 8H), 7.33 (m, 8H), 7.30 – 7.20 (m, 20H), 7.15 (d, *J* = 8.6 Hz, 8H), 7.10 – 7.00 (m, 30H), 7.00 – 6.95 (m, 4H), 6.88 (d, *J* = 8.7 Hz, 4H). ¹³C NMR (176 MHz, CD₂Cl₂, 298 K) δ 154.17, 147.32, 146.64, 133.85, 131.16, 129.99, 129.15, 127.97, 127.18, 127.06, 124.13, 123.86, 122.75, 99.79. MALDI-TOF: calculated for C₁₂₅H₉₀N₆O: 1691.7, found: 1691.0 [M]⁺.

Pyrene-based, periperal-4,4'-di(4-triphenylamino)triphenylamine polyphenylene dendrimer G1 (PYDTPA)

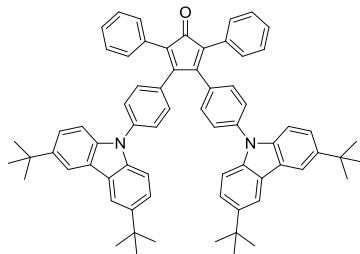


Compound **2-9** (5 mg, 0.05028 mmol) and compound **2-3c** (141.79 mg, 0.083 mmol) were put in a 10 ml round bottom flask and dissolved in 5ml anhydrous o-xylene. The mixture was stirred at 140 °C overnight. Then the cooled mixture was poured into MeOH to precipitate and then filtered, getting the solid which was purified over a GPC column (toluene as the solvent) two times and recovered 0.05g light yellow solid (43%). ¹H NMR (300 MHz, CD₂Cl₂, 300K) δ 8.07 – 7.79 (m, 6H), 7.66 – 7.47 (m, 4H), 7.42 – 7.11 (m, 167H), 7.09 – 6.67 (m,

221H). ¹³C NMR (176 MHz, CD₂Cl₂, 300K) δ 148.10, 147.10, 146.89, 145.56, 145.18, 141.98, 140.91, 140.54, 139.78, 137.08, 136.75, 136.35, 134.97, 134.83, 134.67, 133.26, 133.17, 130.69, 130.65, 130.04, 130.57, 129.63, 127.99, 127.59, 127.56, 124.68, 124.34, 123.99, 123.79, 123.23. MALDI-TOF: calculated for C₅₂₀H₃₇₀N₂₄: 6955.0 (100%), found: 6952.6. HR-MALDI-TOF: calculated for C₅₂₀H₃₇₀N₂₄: 6953.9858, found: 6954.1348 [M]⁺.

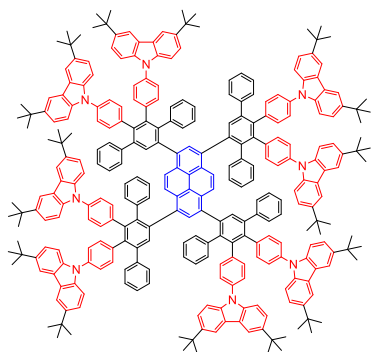
3,4-Bis-[4-(3,6-di-tert-butyl-carbazole)phenyl]-2,5-diphenylcyclopentadienone (2-3d)

Compound **2-1** (2.00 g, 3.69 mmol) and 3,6-di-tertbutyl-carbazole (2.06g, 7.38 mmol) were placed in a 100 ml round bottom flask. It was then transferred to a glove box, in which sodium tertbutoxide (1.06 g, 11.06 mmol), tris(dibenzylideneacetone)dipalladium (0.08 g, 0.09 mmol), tri(tertbutyl)phosphine (0.15 g,



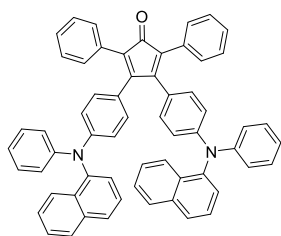
0.74 mmol) and 30 ml of dry toluene were added sequentially. Then the mixture was heated under reflux and stirred for 24 hours. The resulting mixture was extracted with DCM and dilute NH_4Cl solution, followed by a silica gel flash column (4/6, DCM/petroleum ether). Eventually, 2.36 g yellowish brown solid was received after drying under reduced pressure (68%). ^1H NMR (300 MHz, CD_2Cl_2 , 300 K) δ 8.14 (s, 4H), 7.50 (d, 4H), 7.43-7.32 (m, 18H), 7.26(d, 4H). ^{13}C NMR (75 MHz, CD_2Cl_2 , 298 K) δ 154.31, 143.78, 139.20, 138.86, 132.01, 131.41, 130.67, 128.61, 128.17, 126.27, 124.17, 123.96, 116.75, 109.59, 35.04, 32.14. FD-Mass: calculated for $\text{C}_{69}\text{H}_{66}\text{N}_2\text{O}$: 939.3, found: 939.9 $[\text{M}]^+$.

Pyrene-based, peripheral-9-phenyl-3,6-ditertbutyl-carbazole polyphenylene dendrimer-G1 (PYCAB)



Compound **2-9** (30.0 mg, 0.10 mmol), compound **2-3d** (472.0 mg, 0.50 mmol) and 25 ml of *o*-xylene were added in a 50ml Schlenk flask. It was heated at 145 °C for 3 days. The resulting mixture was condensed under reduced pressure and purified by a silica gel flash column (DCM). It was further purified by a GPC column (THF as the solvent). Eventually, 0.30 g light yellow solid was received after drying under reduced pressure (77%). ^1H NMR (300 MHz, CD_2Cl_2 , 300 K) δ 8.17-8.01(m, 22H), 7.82-7.69(m, 4H), 7.41-6.65(m, 104H), 1.40(s, 144H). ^{13}C NMR(75 MHz, CD_2Cl_2 , 298 K) δ 143.20, 143.14, 141.83, 141.42, 141.35, 141.32, 141.22, 141.19, 140.90, 140.82, 140.71, 140.40, 140.10, 140.02, 139.72, 139.60, 136.22, 135.87, 133.60, 131.87, 130.70, 130.64, 128.24, 127.63, 127.43, 127.38, 127.09, 126.48, 126.30, 126.18, 125.92, 125.67, 125.62, 125.26, 125.05, 124.90, 124.64, 123.99, 123.95, 123.61, 123.54, 116.60, 109.44, 35.00, 32.19. MALDI-TOF: calculated for $\text{C}_{296}\text{H}_{274}\text{N}_8$: 3943.2, found: 3941.1. HR-MALDI-TOF: calculated for $\text{C}_{296}\text{H}_{274}\text{N}_8$: 3943.1787, found: 3943.2048 $[\text{M}]^+$.

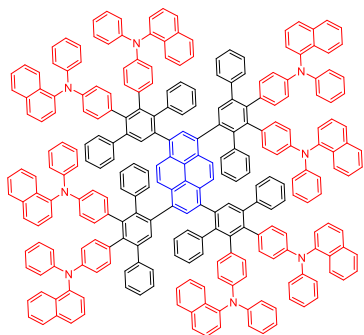
3, 4-Bis[4-(N-phenyl,N'-1-naphthylamino)phenyl]-2,5-diphenylcyclopentadienone (2-3e)



Compound **2-1** (2.00 g, 3.69 mmol) and N-phenyl-1-naphthalenamine (1.78 g, 8.11 mmol) were placed in a 50 ml round bottom flask. It was then transferred to a glove box, in which sodium tert-butoxide (1.06 g, 11.06 mmol), tris(dibenzylideneacetone)dipalladium (0.08 g, 0.09 mmol), tri(tertbutyl)phosphine (0.15 g, 0.74 mmol) and 20 ml of dry toluene were added sequentially. Then the mixture was stirred at 70 °C for 24 hours. The resulting mixture was extracted with DCM and dilute NH_4Cl solution, followed by a silica gel flash column (4/6-5/5, DCM/hexane). Eventually, 2.20 g black solid was received after drying under reduced pressure (73%). ^1H NMR (300 MHz, CD_2Cl_2 , 300 K) δ 7.88-7.73 (m, 6H), 7.49-6.98 (m, 28H), 6.72 (m, 8H). ^{13}C NMR (75 MHz,

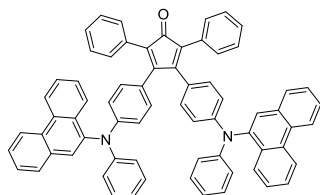
CD₂Cl₂, 298 K) δ 154.83, 149.10, 147.98, 143.35, 135.82, 132.04, 131.44, 131.07, 130.55, 129.63, 128.87, 128.30, 127.69, 127.52, 127.26, 126.75, 126.70, 126.64, 126.00, 124.74, 124.33, 123.33, 123.15, 119.80. FD-Mass: calculated for C₆₁H₄₂N₂O: 818.3, found: 818.5 [M]⁺.

Pyrene-based, peripheral-N, N-diphenyl-1-naphthylamine polyphenylene dendrimer-G1 (PYNPA)



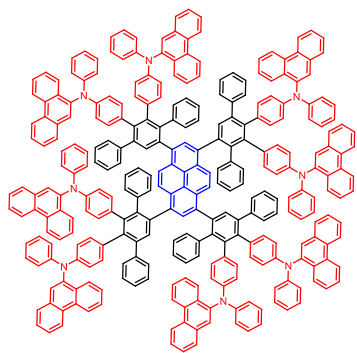
Compound **2-9** (30.0 mg, 0.10 mmol) and compound **2-3e** (362.4 mg, 0.44 mmol) were placed in a 25 ml round bottom flask and dissolved in 12 ml anhydrous o-xylene. The mixture was stirred at 150 °C for 24 hours. Then the cooled mixture was poured into methanol to precipitate and filtered. The obtained crude product was purified by a silica gel flash column (1/1, DCM/hexane). The dendrimer fractions were further purified by a GPC column (toluene as the solvent). Eventually, 0.10 g light yellow solid was received after drying under reduced pressure (29%). ¹H NMR (300 MHz, CD₂Cl₂, 300 K) δ 7.86-7.69(m, 30H), 7.45-6.52 (m, 148H). ¹³C NMR(75MHz, THF-d₈, 298 K) δ 167.18, 149.84, 149.79, 149.75, 147.18, 146.86, 144.79, 142.76, 141.34, 140.23, 136.45, 136.39, 135.55, 135.47, 135.11, 133.43, 131.94, 131.82, 130.90, 129.80, 129.72, 129.12, 129.05, 128.26, 127.46, 127.27, 126.83, 126.75, 125.20, 122.82, 122.73, 122.31, 122.18, 121.76. MALDI-TOF: calculated for C₂₆₄H₁₇₈N₈: 3461.4, found: 3459.7[M-H]⁺. HR-MALDI-TOF: calculated for C₂₆₄H₁₇₈N₈: 3461.4242, found: 3461.4447 [M]⁺.

3,4-Bis[4-(N-phenyl-9-phenanthrenamino)phenyl]-2,5-diphenylcyclopentadienone (2-3f)



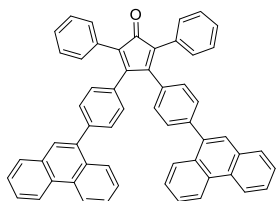
Compound **2-1** (800 mg, 1.48 mmol) and N-phenyl-9-phenanthrenamine (834 mg, 3.10 mmol) were placed in a 25 ml round bottom flask. It was then transferred to a glove box, in which sodium tert-butoxide (425 mg, 4.43 mmol), tris(dibenzylideneacetone)dipalladium (33 mg, 0.036 mmol), tri(tertbutyl)phosphine (60 mg, 0.29 mmol) and 15 ml of dry toluene were added sequentially. Then the mixture was stirred at 70 °C for 24 hours. The resulting mixture was extracted with DCM and dilute NH₄Cl solution, followed by a silica gel flash column (3/7-3/2, DCM/petroleum ether). Eventually, 0.908 g red-brown solid was received after drying under reduced pressure (66.8%). ¹H NMR (700 MHz, C₂D₂Cl₄, 298 K) δ 8.67 (dd, *J* = 8.5, 5.5 Hz, 4H), 7.84 (s, 2H), 7.71 (d, *J* = 7.8 Hz, 2H), 7.67 (t, *J* = 7.7 Hz, 2H), 7.58 (d, *J* = 8.4 Hz, 4H), 7.48 (d, *J* = 7.8 Hz, 2H), 7.33 – 7.22 (m, 16H), 7.18 (d, *J* = 8.0 Hz, 4H), 7.05 (t, *J* = 7.3 Hz, 2H), 6.81 (d, *J* = 8.3 Hz, 4H), 6.73 (d, *J* = 8.3 Hz, 4H). ¹³C NMR (176 MHz, C₂D₂Cl₄, 298 K) δ 200.58, 154.20, 148.11, 147.09, 141.21, 132.06, 131.87, 131.18, 130.71, 129.96, 129.84, 129.23, 128.16, 127.90, 127.55, 127.06, 126.91, 126.87, 126.69, 125.41, 125.11, 124.66, 123.94, 122.96, 122.79, 122.73, 122.49, 119.16. FD-Mass: calculated for C₆₉H₄₆N₂O: 918.4, found: 917.5 [M-H]⁺.

Pyrene-based, peripheral-N, N-diphenyl-9-phenanthrenamine polyphenylene dendrimer G1 (PYPPA)



Compound **2-9** (20.0 mg, 0.067 mmol) and compound **2-3f** (300 mg, 0.326 mmol) were placed in a 25 ml round bottom flask and dissolved in 7 ml anhydrous *o*-xylene. The mixture was stirred at 140 °C for 24 hours. Then the cooled mixture was poured into methanol to precipitate and filtered. The obtained crude product was purified by a silica gel flash column (1/1, DCM/hexane). The dendrimer fractions were further purified by precipitation in methanol. Eventually, 0.20 g light-yellow solid was received after drying under reduced pressure (77.2%). ¹H NMR (300 MHz, CD₂Cl₂, 300 K) δ 8.64 (m, 16H), 8.02 – 6.21 (m, 178H). ¹³C NMR (126 MHz, CD₂Cl₂, 298 K) δ 149.03, 146.37, 146.07, 142.75, 142.16, 141.82, 141.18, 140.92, 140.46, 139.72, 139.56, 137.01, 136.31, 135.13, 134.78, 132.94, 132.86, 132.45, 132.38, 130.62, 130.56, 130.42, 129.55, 129.48, 129.39, 128.44, 128.37, 128.12, 127.86, 127.36, 127.27, 127.20, 127.12, 127.08, 127.03, 126.73, 126.65, 125.52, 124.71, 123.39, 123.33, 122.88, 122.31, 122.23, 122.04, 121.91, 121.46, 121.37. MALDI-TOF: calculated for C₂₉₆H₁₉₄N₈: 3861.5, found: 3863.4. HR-MALDI-TOF: calculated for C₂₉₆H₁₉₄N₈: 3862.5527, found: 3862.5807 [M⁺].

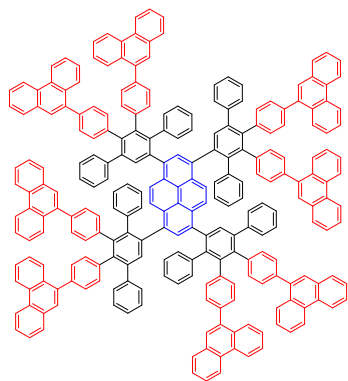
3, 4-Bis[4-(9-phenanthren)phenyl]-2,5-diphenylcyclopentadienone (2-3g)



9-Bromophenanthrene (0.500 g, 1.94 mmol), compound **2-22** (0.562 g, 0.884 mmol), tetrabutylammonium bromide (57 mg, 0.177 mmol), K₂CO₃ (0.611 g, 4.42 mmol), 35 ml of toluene and 15 ml of water were added in a 100 ml round bottom flask. Then the mixture was degassed and added argon for 3 times, followed by the addition of Pd (PPh₃)₄ (51 mg, 0.044 mmol). The mixture was then stirred at 80 °C for 48 hours. Then it was extracted by DCM and purified by a silica gel flash column (DCM/petroleum ether, 1/1). Eventually, 0.42 g of purple solid was received after drying under reduced pressure (60%). ¹H NMR (300 MHz, CD₂Cl₂, 300K) δ 8.76 (m, 4H), 7.88 (ddd, *J* = 11.5, 8.0, 1.5 Hz, 4H), 7.77 – 7.56 (m, 9H), 7.52 – 7.28 (m, 15H), 7.25 – 7.18 (m, 4H). ¹³C NMR (176 MHz, C₂D₂Cl₄, 353 K) δ 154.42, 140.93, 137.98, 132.39, 131.35, 130.85, 130.80, 130.55, 130.08, 129.94, 129.55, 129.26, 128.53, 127.96, 127.48, 127.26, 126.80, 126.64, 126.57, 126.39, 126.32, 125.43, 122.82, 122.41. FD-Mass: calculated for C₅₇H₃₆O: 736.3, found: 738.1.

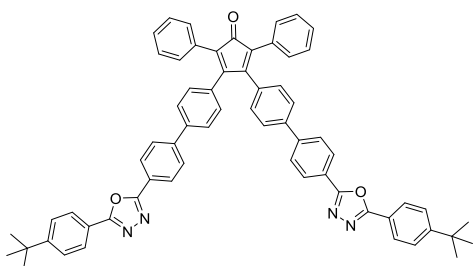
Pyrene-based, peripheral-9-phenylphenanthrene polyphenylene dendrimer-G1 (PYPAN)

Similar to procedure for **PYTPA**, 1,3,6,8-tetraethynylpyrene (20 mg, 0.067 mmol) and compound **2-3g** (227 mg, 0.308 mmol) were stirred in 8 ml *o*-xylene at 145 °C for 48 h. The product was purified by silica gel flash column (DCM/hexane, 7/3) and GPC column (THF as the solvent). Eventually, 0.12 g of



light-yellow solid was received after drying under reduced pressure (57%). ^1H NMR (300 MHz, CD_2Cl_2 , 300 K) δ 8.72 (m, 16H), 8.22 – 7.97 (m, 6H), 7.80 (m, 8H), 7.62 (m, 40H), 7.44 – 6.61 (m, 84H). ^{13}C NMR (126 MHz, CD_2Cl_2 , 298 K) δ 142.14, 141.31, 141.17, 141.01, 140.93, 140.78, 140.66, 140.63, 140.34, 140.10, 139.98, 139.88, 139.09, 139.03, 138.60, 138.28, 138.24, 137.16, 136.52, 132.17, 132.07, 132.05, 131.91, 131.67, 131.65, 131.61, 130.85, 130.82, 130.73, 130.69, 130.66, 130.24, 129.16, 128.94, 128.92, 128.82, 128.15, 128.11, 127.48, 127.35, 127.21, 127.17, 126.94, 126.90, 126.73, 123.12, 123.09, 122.85, 100.40. MALDI-TOF: calculated for $\text{C}_{248}\text{H}_{154}$: 3133.2, found: 3132.9 $[\text{M}]^+$. HR-MALDI-TOF: calculated for $\text{C}_{248}\text{H}_{154}$: 3133.2118, found: 3133.2304 $[\text{M}]^+$.

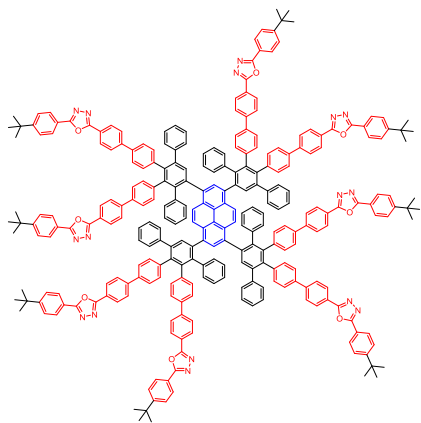
3,4-Bis[4-(2-tertbutylphenyl-5-phenyl-1,3,4-oxadiazolyl)phenyl]-2,5-diphenylcyclopentadienone (2-3h)



In a 250ml round bottom flask, compound **2-22** (0.809g, 1.27mmol), compound **2-16** (1.00g, 2.80mmol), potassium carbonate (0.879g, 6.36mmol), tetrabutylammonium bromide (82.5mg, 0.254mmol), 70ml toluene, and 30ml water were added sequentially. The mixture was degassed and added argon 3 times, then $\text{Pd}(\text{PPh}_3)_4$ (73.5mg, 0.0636mmol) was added. The system was degassed and added argon 3 times again and it was refluxed for 48 hours. The resulting mixture was extracted with $\text{DCM}/\text{H}_2\text{O}$ for 3 times and the organic layer was dried with MgSO_4 , then filtered, condensed with rotary evaporation and run a silica gel flash column with ethyl acetate/ DCM (10%-20%). Eventually, 1.03 g red brown solid was recovered after drying (86.6%). ^1H NMR (300 MHz, CD_2Cl_2 , 300K) δ 8.17(d, 4H), 8.05(d, 4H), 7.78(d, 4H), 7.59-7.54(m, 8H), 7.29(s, 10H), 7.12(d, 4H), 1.36(s, 18H). ^{13}C NMR (75MHz, CD_2Cl_2 , 300K) δ 200.44, 165.12, 164.54, 155.95, 154.36, 143.59, 140.16, 133.47, 131.36, 130.63, 130.58, 128.52, 128.08, 127.89, 127.69, 127.02, 126.57, 126.42, 123.73, 121.60, 35.38, 31.26. FD-Mass: calculated for $\text{C}_{65}\text{H}_{52}\text{N}_4\text{O}_3$: 937.13, found: 937.0 $[\text{M}]^+$.

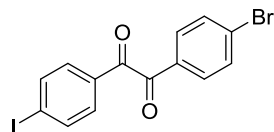
Pyrene-based, peripheral-2-bis(p-phenyl)-5-(4-tertbutylphenyl)-1, 3, 4-oxadiazole polyphenylene dendrimer-G1 (PYPBD)

Similar as procedure for **PYTPA**, compound **2-9** (20 mg, 0.067 mmol) and compound **2-3h** (276 mg, 0.294 mmol) were stirred in 10 ml o-xylene at 150 °C for 24h. The product was purified by silica gel flash column (EtAc/ DCM , 1/4) and GPC column (THF as the solvent). Eventually, 0.070 g of yellow solid was received after drying under reduced pressure (26.5%). ^1H NMR (250 MHz, CD_2Cl_2 , 300K) δ 8.20 – 7.81 (m, 38H), 7.75 – 7.49 (m, 36H), 7.43 – 6.42 (m, 72H), 1.35 (s, 72H). ^{13}C NMR (176 MHz, CD_2Cl_2 , 298K) δ 165.01, 164.62, 155.82, 143.92, 141.94, 141.05, 140.76, 140.28, 137.23, 136.90,



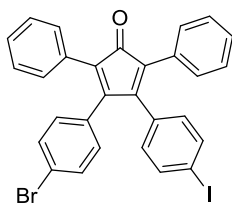
136.33, 132.75, 130.46, 130.39, 128.29, 128.11, 128.07, 127.63, 127.56, 127.52, 126.97, 126.53, 126.01, 125.68, 123.16, 123.10, 121.57, 100.41, 35.40, 31.25. MALDI-TOF: calculated for $C_{280}H_{218}N_{16}O_8$: 3933.7, found: 3935.4. HR-ESI-MS: calculated for $C_{280}H_{218}N_{16}O_8$: 3936.7397, found: 1968.3635 [$M^{2+}/2$].

1-(4-Iodophenyl)-2-(4-bromophenyl) diketone (2-20)



Compound **2-19** (4.0 g, 10.4 mmol), iodine (2.66 g, 10.44 mmol) and 130 ml of DMSO were added in a 250 ml flask. Then the mixture was degassed and added argon 3 times and stirred in 155 °C for 24 hours. Then it was filtered and washed with DCM, THF and acetone. Eventually, 3.86 g light yellow solid was received after drying under reduced pressure (89.1%). 1H NMR (300 MHz, THF- d_8 , 300 K) δ 7.95 (d, 8.7 Hz, 2H), 7.87 (d, 8.7 Hz, 2H), 7.73 (d, 8.7 Hz, 2H), 7.69 (d, 8.7 Hz, 2H). ^{13}C NMR (75 MHz, THF- d_8 , 300 K) 192.99, 182.76, 139.20, 133.10, 132.04, 131.63, 130.68, 104.07. FD-Mass: calculated for $C_{14}H_8BrIO_2$: 413.9 (100%), found: 414.4 [M] $^+$.

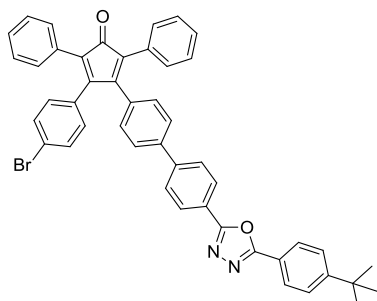
3-(4-Bromophenyl)-4-(4-iodophenyl)-2,5-diphenylcyclopentadienone (2-3i)



Compound **2-20** (3.0 g, 7.22 mmol), 1,3-diphenylacetone (1.51 g, 7.18 mmol) and 30 ml of ethanol were added in a 100 ml Schlenk flask. Then the mixture was degassed and added argon 3 times and heated to 85 °C to make the solids dissolved. Then, 0.2 g of potassium hydroxide in 5 ml ethanol was added. The mixture was stirred for another 1 hour, followed by cooling with ice bath. Then water was added to form precipitate which was filtered and washed with methanol. Eventually, 3.21 g pure-colored solid was received after drying under reduced pressure (76%). 1H NMR (300 MHz, CD_2Cl_2 , 300 K) δ 7.55 (d, 2H), 7.35 (d, 2H), 7.30-7.26 (m, 6H), 7.21-7.18 (m, 4H), 6.82 (d, 2H), 6.68 (d, 2H). ^{13}C NMR (75 MHz, CD_2Cl_2 , 300 K) 153.41, 137.79, 132.82, 132.28, 131.84, 131.45, 131.40, 130.90, 130.51, 128.56, 128.20, 123.37, 95.25. FD-Mass: calculated for $C_{29}H_{18}BrIO$: 588.0 (100%), found: 588.4 [M] $^+$.

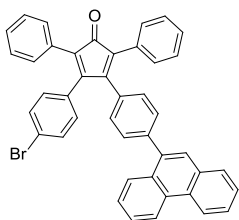
3-(4-Bromophenyl)-4-[4-(2-tertbutylphenyl-5-phenyl-1,3,4-oxadiazolyl)phenyl]-2,5-diphenylcyclopentadienone (2-3j)

Compound **2-17** (1.00 g, 2.47 mmol), compound **2-3i** (1.89 g, 3.22 mmol), tetrabutylammonium bromide (4 mg, 0.01 mmol), K_2CO_3 (0.68 g, 4.95 mmol), 60 ml of toluene and 20 ml of water were added in a 250 ml round bottom flask. Then the mixture was degassed and added argon for 3 times, followed by the



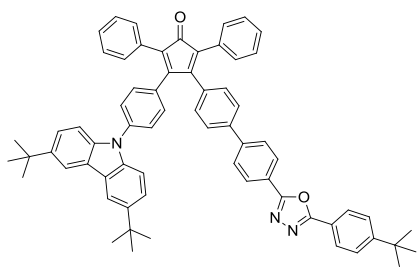
addition of Pd (PPh₃)₄ (143 mg, 0.12 mmol). The mixture was then stirred at 80 °C for 48 hours. Then it was extracted by DCM and purified by a silica gel flash column (first DCM, then ethyl acetate/DCM (5/95) as eluents). Eventually, 1.85 g of purple solid was received after drying under reduced pressure (100%). ¹H NMR (300 MHz, CD₂Cl₂, 300 K) δ 8.20 (d, J=8.5 Hz, 2H), 8.08 (d, J=8.6 Hz, 2H), 7.80 (d, J=8.6 Hz, 2H), 7.58 (dd, J=10.6, 8.5 Hz, 4H), 7.36 (d, J=8.5 Hz, 2H), 7.28-7.23 (m, 10H), 7.07 (d, J=8.4 Hz, 2H), 6.89 (d, J= 8.5 Hz, 2H), 1.38 (s, 9H). ¹³C NMR (75 MHz, CD₂Cl₂, 300 K) δ 165.16, 164.59, 155.94, 154.04, 153.58, 143.51, 140.23, 133.21, 132.53, 131.77, 131.52, 131.21, 131.04, 130.60, 130.55, 130.49, 129.40, 128.56, 128.53, 128.16, 128.10, 127.92, 127.71, 127.52, 127.09, 127.05, 126.58, 123.76, 123.30, 121.60, 35.44, 31.28. FD-Mass: calculated for C₄₇H₃₅BrN₂O₂: 738.2 (100%), found:738.1 [M]⁺.

3-(4-Bromophenyl)-4-[4-(9-phenanthren)phenyl]-2,5-diphenylcyclopentadienone (2-3k)



9-Phenanthracenylboronic acid (0.40 g, 1.80 mmol), compound **2-3i** (1.17 g, 1.98 mmol), tetrabutylammonium bromide (4 mg, 0.01 mmol), K₂CO₃ (0.50 g, 3.60 mmol), 40 ml of toluene and 15 ml of water were added in a 100 ml round bottom flask. Then the mixture was degassed and added argon for 3 times, followed by the addition of Pd (PPh₃)₄ (104 mg, 0.09 mmol). The mixture was then stirred at 80 °C for 48 hours. Then it was extracted by DCM and purified by a silica gel flash column, using Ethyl DCM/Hexane (6/4) as the eluent. Eventually, 0.91 g of purple solid was received after drying under reduced pressure (79%). ¹H NMR (300 MHz, THF-*d*₈, 300K) δ 8.85 (d, *J* = 9.0 Hz, 1H), 8.78 (d, *J* = 9.0 Hz, 1H), 7.92 (dd, *J* = 7.7, 1.6 Hz, 1H), 7.81 (dd, *J* = 8.2, 1.3 Hz, 1H), 7.72 (s, 1H), 7.69 – 7.51 (m, 4H), 7.47 – 7.41 (m, 4H), 7.37 – 7.19 (m, 10H), 7.14 (d, *J* = 8.1 Hz, 2H), 6.98 (d, *J* = 8.4 Hz, 2H). ¹³C NMR (75 MHz, THF-*d*₈, 300K) δ 154.88, 154.01, 142.15, 138.88, 133.55, 133.42, 132.56, 132.33, 132.20, 131.96, 131.78, 131.70, 131.10, 131.05, 130.75, 130.29, 129.50, 128.82, 128.74, 128.36, 128.33, 128.30, 127.69, 127.59, 127.35, 127.24, 126.61, 126.32, 123.96, 123.57, 123.43. FD-Mass: calculated for C₄₃H₂₇BrO: 638.1(100%), found: 639.9.

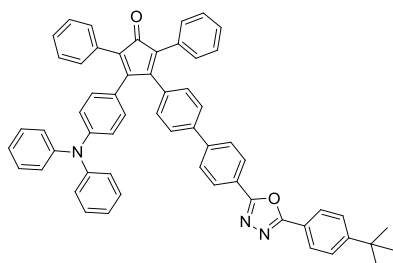
3-(4-(3,6-Di-tert-butyl-carbazole)phenyl)-4-[4-(2-tertbutylphenyl-5-phenyl-1,3,4-oxadiazolyl)phenyl]-2,5-diphenylcyclopentadienone (2-3m)



Compound **2-3j** (1.52 g, 2.06 mmol) and 3,6-ditertbutyl-carbazole (0.59 g, 2.13 mmol) were placed in a 50 ml round bottom flask. It was then transferred to a glove box, in which sodium tertbutoxide (0.29 g, 3.04 mmol), tris(dibenzylideneacetone)dipalladium (46 mg, 0.05 mmol), tri(tertbutyl)phosphine (82 mg, 0.41 mmol) and 20 ml of dry toluene were added sequentially. Then the mixture was heated under reflux and stirred for 24 hours.

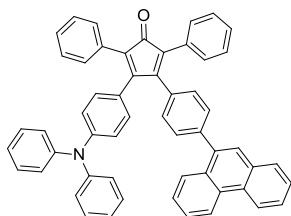
The resulting mixture was extracted with DCM and water, followed by a silica gel flash column, first using DCM then using ethyl acetate/DCM (2/98) as the eluent. It was further purified by recrystallization in ethanol. Eventually, 1.48 g of a yellowish brown solid was received after drying under reduced pressure (78%). ^1H NMR (300 MHz, CD_2Cl_2 , 300 K) δ 8.22 (d, J = 8.5 Hz, 2H), 8.14 (d, J = 1.6 Hz, 2H), 8.08 (d, J = 8.6 Hz, 2H), 7.83 (d, J = 8.5 Hz, 2H), 7.65 – 7.55 (m, 4H), 7.49 – 7.28 (m, 16H), 7.22 (d, J = 8.5 Hz, 2H), 7.17 (d, J = 8.4 Hz, 2H), 1.44 (s, 18H), 1.39 (s, 9H). ^{13}C NMR (75 MHz, CD_2Cl_2 , 300 K) δ 165.16, 164.59, 155.94, 154.39, 154.32, 143.73, 143.66, 140.26, 139.20, 138.74, 133.54, 132.06, 131.33, 130.64, 128.59, 128.56, 128.14, 128.10, 128.01, 127.72, 127.08, 127.05, 126.59, 126.28, 126.19, 126.12, 124.13, 123.93, 123.77, 121.61, 116.77, 109.60, 35.44, 35.05, 32.16, 31.30. FD-Mass: calculated for $\text{C}_{67}\text{H}_{59}\text{N}_3\text{O}_2$: 937.5, found: 937.8 $[\text{M}]^+$.

3-(4-Triphenylamino)-4-[4-(2-tertbutylphenyl-5-phenyl-1,3,4-oxadiazolyl)phenyl]-2,5-diphenylcyclopentadienone (2-3n)



Compound **2-3j** (1.00 g, 1.35 mmol) and diphenylamine (0.25 g, 1.49 mmol) were placed in a 50 ml round bottom flask. It was then transferred to a glove box, in which sodium tertbutoxide (0.19 g, 2.03 mmol), tris(dibenzylideneacetone)dipalladium (30 mg, 0.033 mmol), tri(tertbutyl)phosphine (55 mg, 0.27 mmol) and 15 ml of dry toluene were added sequentially. Then the mixture was heated at 75 °C and stirred for 24 hours. The resulting mixture was extracted with DCM and water, followed by a silica gel flash column, first using DCM then using ethyl acetate/DCM (3/97) as the eluent. It was further purified by recrystallization in ethanol. Eventually, 0.44 g of a red solid was received after drying under reduced pressure (39%). ^1H NMR (300 MHz, CD_2Cl_2 , 300 K) δ 8.22 (d, J = 8.4 Hz, 2H), 8.14 – 8.04 (m, 2H), 7.85 – 7.75 (m, 2H), 7.59 (dd, J = 8.5, 7.1 Hz, 4H), 7.37 – 7.20 (m, 14H), 7.18 – 7.00 (m, 8H), 6.81 (s, 4H), 1.38 (s, 9H). ^{13}C NMR (126 MHz, CD_2Cl_2 , 298 K) δ 200.48, 165.16, 164.63, 155.94, 155.04, 154.04, 148.71, 147.50, 143.74, 140.02, 133.82, 131.90, 131.69, 131.51, 131.02, 130.69, 130.63, 130.58, 129.77, 129.67, 128.45, 128.42, 127.94, 127.92, 127.73, 127.71, 127.06, 126.84, 126.59, 126.46, 126.37, 125.83, 125.67, 125.52, 124.91, 124.88, 124.12, 123.70, 123.62, 123.46, 121.92, 121.62, 121.53, 54.06, 35.45, 31.29. FD-Mass: calculated for $\text{C}_{59}\text{H}_{45}\text{N}_3\text{O}_2$: 827.3, found: 827.9 $[\text{M}]^+$.

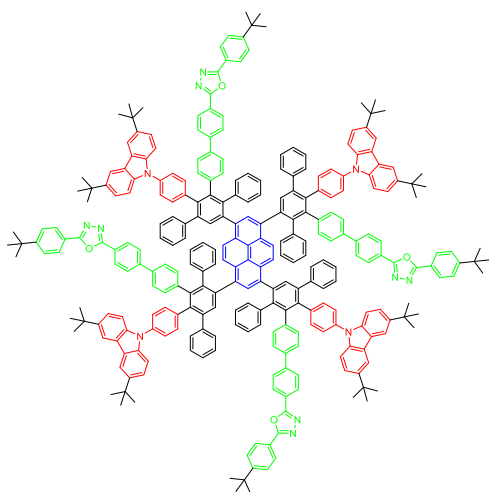
3-(4-Triphenylamino)-4-[4-(9-phenanthren)phenyl]-2,5-diphenylcyclopentadienone (2-3p)



Compound **2-3k** (0.50 g, 0.78 mmol) and diphenylamine (0.16 g, 0.94 mmol) were placed in a 50 ml round bottom flask. It was then transferred to a glove box, in which sodium tertbutoxide (0.11 g, 1.17mmol), tris(dibenzylideneacetone)dipalladium (17 mg, 0.019 mmol), tri(tertbutyl)phosphine (32 mg, 0.156 mmol) and 20 ml of dry toluene were added sequentially. Then the

mixture was heated at 75 °C and stirred for 24 hours. The resulting mixture was extracted with DCM and water, followed by a silica gel flash column, first using DCM/hexane (6/4) as the eluent. It was further purified by recrystallization in ethanol. Eventually, 0.42 g of a red solid was received after drying under reduced pressure (74%). ^1H NMR (300 MHz, CD_2Cl_2 , 300 K) δ 8.80 (dd, $J = 8.3, 1.2$ Hz, 1H), 8.75 (dd, $J = 8.2, 1.3$ Hz, 1H), 7.92 (dd, $J = 7.9, 1.6$ Hz, 1H), 7.82 (dd, $J = 8.4, 1.4$ Hz, 1H), 7.75 – 7.59 (m, 4H), 7.51 – 7.20 (m, 17H), 7.19 – 7.14 (m, 2H), 7.12 – 7.00 (m, 6H), 6.87 (s, 4H). ^{13}C NMR (75 MHz, CD_2Cl_2 , 300 K) δ 155.19, 154.56, 148.74, 147.54, 141.31, 138.57, 133.09, 131.96, 131.91, 131.60, 131.29, 131.12, 131.01, 130.67, 130.59, 130.39, 129.97, 129.92, 129.80, 129.07, 128.44, 127.89, 127.72, 127.39, 127.20, 127.10, 126.97, 126.50, 126.20, 125.50, 124.75, 124.08, 123.36, 122.95, 121.55. FD-Mass: calculated for $\text{C}_{55}\text{H}_{37}\text{NO}$: 727.3(100%), found: 728.3[M+H] $^+$.

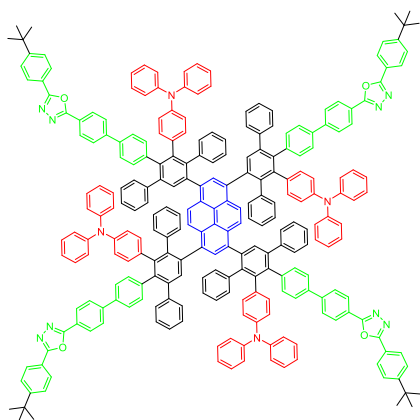
Pyrene-based, peripheral-carbazole-oxadiazole polyphenylene dendrimer-G1(PYCABPBD)



Compound **2-9** (15.0 mg, 0.05 mmol) and **2-3m** (217.0 mg, 0.231 mmol) were placed in a 25 ml round bottom flask and dissolved in 8 ml anhydrous *o*-xylene. The mixture was stirred at 130 °C for 24 hours. Then the cooled mixture was poured into hexane to precipitate and filtered. The obtained crude product was purified by a silica gel flash column (5/95, ethyl acetate/DCM). The dendrimer fractions were further purified by a GPC column (THF as the solvent). Eventually, 100 mg light yellow solid was received after drying under reduced pressure (50%).

^1H NMR (300 MHz, CD_2Cl_2 , 300 K) δ 8.20 (m, 8H), 8.09-8.06 (m, 20H), 7.82-6.61 (m, 110H), 1.39 (s, 36H), 1.36 (s, 72H). ^{13}C NMR (126 MHz, CD_2Cl_2 , 298 K) δ 165.03, 164.63, 155.87, 144.09, 144.04, 143.09, 143.04, 142.01, 141.92, 141.75, 141.84, 141.69, 141.41, 141.32, 141.06, 141.02, 140.91, 140.80, 140.75, 140.63, 140.56, 140.47, 140.43, 140.36, 140.32, 140.29, 140.25, 140.20, 140.14, 140.09, 140.02, 139.95, 139.86, 139.76, 139.71, 139.68, 139.63, 139.59, 137.28, 137.05, 136.92, 136.37, 136.16, 135.90, 135.58, 133.41, 133.35, 132.88, 131.89, 130.68, 130.59, 130.50, 128.21, 128.18, 127.87, 127.81, 127.64, 127.32, 127.00, 126.56, 126.14, 126.00, 125.78, 123.89, 123.40, 123.35, 123.29, 123.26, 121.60, 116.52, 109.33, 35.43, 34.94, 32.08, 31.27. MALDI-TOF: calculated for $\text{C}_{288}\text{H}_{246}\text{N}_{12}\text{O}_4$: 3937.9, found: 3939.5. HR-MALDI-TOF: calculated for $\text{C}_{288}\text{H}_{246}\text{N}_{12}\text{O}_4$: 3938.9516, found: 3939.0044 [M $^+$].

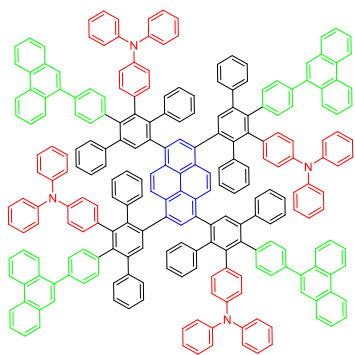
Pyrene-based, peripheral-triphenylamine-oxadiazole polyphenylene dendrimer-G1 (PYTPAPBD)



Compound **2-9** (15.0 mg, 0.05 mmol) and **2-3n** (187.3 mg, 0.23 mmol) were placed in a 25 ml round bottom flask and dissolved in 7 ml anhydrous *o*-xylene. The mixture was stirred at 130 °C for 24 hours. Then the cooled mixture was poured into hexane to precipitate and filtered. The obtained crude product was purified by a silica gel flash column (5/95, ethyl acetate/DCM). The dendrimer fractions were further purified by a GPC column (THF as the solvent). Eventually, 80 mg of a light yellow solid was received after drying under reduced

pressure (45.4%). ^1H NMR (300 MHz, CD_2Cl_2 , 300 K) δ 8.18 (m, 8H), 8.08 (m, 8H), 8.00-6.52 (m, 138H), 1.38 (s, 36H). ^{13}C NMR (126 MHz, CD_2Cl_2 , 298K) δ 165.06, 164.70, 155.85, 148.08, 145.83, 145.50, 144.16, 141.96, 141.35, 141.03, 140.73, 140.38, 139.95, 139.90, 137.17, 137.05, 137.02, 136.78, 136.33, 136.12, 136.04, 135.59, 132.97, 132.88, 131.92, 130.51, 129.39, 129.32, 128.10, 127.95, 127.69, 127.61, 127.01, 126.81, 126.56, 125.88, 125.54, 123.91, 123.71, 123.18, 123.12, 122.73, 122.58, 121.61. MALDI-TOF: calculated for $\text{C}_{256}\text{H}_{190}\text{N}_{12}\text{O}_4$: 3497.5, found: 3499.6. HR-ESI-MS: calculated for $\text{C}_{256}\text{H}_{190}\text{N}_{12}\text{O}_4$: 3499.5256, found 1749.7679 [$\text{M}^{2+}/2$].

Pyrene-based, peripheral-triphenylamine-phenanthrene polyphenylene dendrimer-G1 (PYTPAPAN)

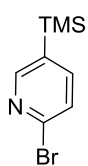


Compound **2-9** (30.0 mg, 0.10 mmol) and **2-3p** (329.4 mg, 0.45 mmol) were placed in a 25 ml round bottom flask and dissolved in 8 ml anhydrous *o*-xylene. The mixture was stirred at 120 °C for 24 hours. Then the cooled mixture was poured into methanol to precipitate and filtered. The obtained crude product was purified by a silica gel flash column (50/50, ethyl acetate/DCM). The dendrimer fractions were further purified by a GPC column (THF as the solvent). Eventually, 228 mg of a light yellow solid

was received after drying under reduced pressure (73%). ^1H NMR (300 MHz, CD_2Cl_2 , 300 K) δ 8.75 (m, 8H), 8.14-7.82 (m, 9H), 7.78-6.45 (m, 141H). ^{13}C NMR (126 MHz, CD_2Cl_2 , 298K) δ 148.16, 145.93, 145.58, 142.10, 141.99, 141.18, 141.02, 140.87, 140.63, 140.43, 140.34, 140.08, 139.99, 139.85, 139.73, 139.09, 138.51, 138.13, 137.12, 136.45, 136.20, 135.76, 133.13, 132.16, 132.10, 132.00, 131.94, 131.93, 131.80, 131.68, 131.66, 131.63, 130.88, 130.83, 130.67, 130.59, 130.26, 130.22, 129.46, 129.39, 129.04, 128.94, 128.91, 128.69, 128.03, 127.96, 127.47, 127.32, 127.25, 127.00, 126.93, 126.89, 126.80, 126.77, 126.16, 125.81, 123.99, 123.80, 123.78, 123.17, 123.11, 122.88, 122.71, 122.55. MALDI-TOF: calculated for $\text{C}_{240}\text{H}_{158}\text{N}_4$: 3097.3 (100%), found: 3096.4 [$\text{M}-\text{H}$] $^+$. HR-MALDI-TOF: calculated for $\text{C}_{240}\text{H}_{158}\text{N}_4$: 3097.2554, found: 3097.2707 [M^+].

8.2.2 Synthesis of iridium-complex-based polyphenylene dendrimers (Chapter 3)

2-Bromo-5-trimethylsilylpyridine (3-3)

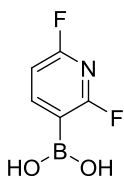


In a Schlenk flask was added 2,5-dibromopyridine (5.00g, 21.11 mmol), degassed and added argon 3 times. Then 200 ml of diethyl ether was added. The mixture was stirred at $-78\text{ }^{\circ}\text{C}$ in dry ice bath, followed by addition of 1.6 M n-BuLi (20.05 mmol, 12.53 ml). The mixture was stirred for 1h. Then TMSCl (4.00 ml, 31.66 mmol) was added. The mixture was stirred at room temperature overnight followed by quenching with dilute HCl solution and extraction with DCM. Finally the condensed organic crude material was purified by distillation at $170\text{ }^{\circ}\text{C}$ under vacuum to get 4.00 gram of colorless liquid (82%). ^1H NMR(250 MHz, CD_2Cl_2 , 292 K) δ 8.40 (d, 1H), 7.65 (dd, 1H), 7.46 (dd, 1H), 0.24 (s, 9H). ^{13}C NMR (75 MHz, CD_2Cl_2 , 298 K) δ 154.67, 143.87, 143.49, 134.74, 127.91, -1.38.

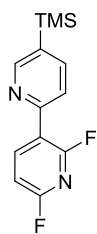
2,6-Difluoro-pyridine-5-boronic acid (3-5)

(1) Synthesis of LDA: In a Schlenk flask was added diisopropylamine (13.8 ml, 98.8 mmol) and 10 ml of dry THF. It was stirred in ice bath. Then 1.6 M n-butyllithium in hexane (58.7 ml, 93.9 mmol) was added slowly. The mixture was stirred at this temperature for 30 min and ready for use.

(2) In another Schlenk flask was added 2,6-difluoropyridine (9.4 ml, 103.8 mmol) and 30 ml of dry THF. The mixture was stirred at dry ice bath. Then LDA was added into the mixture slowly. The mixture was continually stirred for another 2 hours, followed by addition of triisopropylborate (34.2 ml, 148.2 mmol). The mixture was stirred at room temperature overnight. Then it was quenched by 1 M aqus. HCl and purified by extraction using ethyl acetate. Finally 15.70 g yellow-colored solid was received after drying under reduced pressure (100%). Spectra data were consistent with published date.^[15]

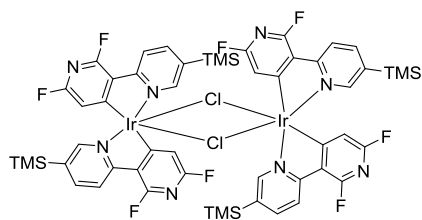


2,6-Difluoro-5'-trimethylsilyl-3,2'-dipyridine (3-4)



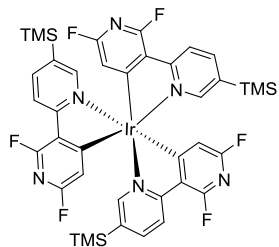
In a 100 ml round bottom flask were added compound **3-3** (2.00 g, 8.69 mmol), compound **3-5** (1.70 g, 10.69 mmol), K_2CO_3 (2.40 g, 17.38 mmol), 60 ml of THF and 5 ml of water sequentially. Then the mixture was degassed and added argon for 3 times, followed by the addition of Pd (PPh_3)₄ (502 mg, 434 mmol). The mixture was then stirred at $85\text{ }^{\circ}\text{C}$ for 24 hours. Then it was extracted by DCM and purified by a silica gel flash column (1/49, Ethyl acetate/DCM). Eventually, 1.2 g of a light yellow solid was received after drying under reduced pressure (50%). ^1H NMR (250 MHz, CD_2Cl_2 , 292 K) δ 8.78 (dd, 1H), 8.70 (dt, 1H), 7.92 (dd, 1H), 7.81 (ddd, 1H), 6.99 (ddd, 1H). ^{13}C NMR (75 MHz, CD_2Cl_2 , 298 K) δ 154.44, 150.81, 146.46, 142.40, 135.28, 123.37, 107.46, 107.00, -1.30. FD-Mass: calculated for $\text{C}_{13}\text{H}_{14}\text{F}_2\text{N}_2\text{Si}$: 264.1, found:263.7 $[\text{M}]^+$.

[(2,6-DiFpy-5'TMSpy)₂Ir(μ-Cl)₂] (3-6)



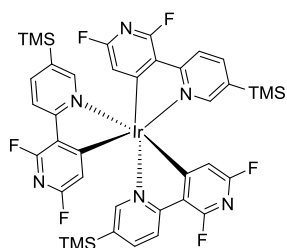
In a Schlenk flask was added compound **3-4** (0.25g, 0.946 mmol), IrCl₃.nH₂O (277 mg, 0.927 mmol) and 10 ml of 2-ethoxyethanol. The mixture was stirred at 140 °C under argon for 24 hours. Then water was added to precipitate the product, followed by centrifuge to get the solid. Eventually, 0.67g of a yellow solid was received after drying under reduced pressure (47.8%). It was directly used for next step without further purification. FD-Mass: calculated for C₅₂H₅₂Cl₂F₈Ir₂N₈Si₄: 1506.2, found: 1506.7 [M]⁺.

Mer(2,6-diFpy-5'TMSpy)₃Ir



In a round bottom flask were added compound **3-6** (0.67 g, 0.44 mmol), compound **3-4** (0.235 g, 0.89 mmol), K₂CO₃ (0.31 g, 2.22 mmol) and 16 ml of mesitylene. The mixture was degassed and added argon 3 times, followed by addition of silver trifluoromethanesulfonate (0.24 g, 0.92 mmol). The mixture was heated at 170 °C for 20 hours. Then it was extracted by DCM and purified by a silica gel flash column (DCM). Eventually, 0.46 g of a yellow solid was received after drying under reduced pressure (53%). ¹H NMR (250 MHz, CD₂Cl₂, 292 K) δ 8.33 (dt, 1H), 8.20 (ddt, 2H), 8.00 (m, 3H), 7.84 (ddd, 1H), 7.33 (dd, 1H), 6.45 (t, 1H), 5.95 (t, 1H), 5.74 (t, 1H), 0.13 (s, 9H), 0.11 (s, 9H), 0.04 (s, 9H). ¹⁹F NMR (471 MHz, CD₂Cl₂, 298 K) δ -68.56, -69.19, -69.63, -72.54, -72.73, -73.15. FD-Mass: calculated for C₃₉H₃₉F₆IrN₆Si₃: 982.2, found: 980.6.

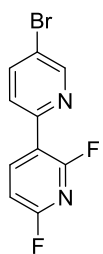
Fac(2,6-diFpy-5'TMSpy)₃Ir



In a quartz tube were mixed **mer(2,6-diFpy-5'TMSpy)₃Ir** (0.282 g, 0.287 mmol) and 15 ml of THF. The tube was degassed and added argon 3 times. Then the sealed tube was put in photochemical reactor and shined for 12 hours while the solution was stirred. After that, extraction was done using DCM and water. It was purified by a silica gel flash column (ethyl acetate/hexane, 2/3). Eventually, 0.254 g light-yellow-colored solid was received after drying under reduced pressure (90%). ¹H NMR (250 MHz, CD₂Cl₂, 300 K) δ 8.29 (d, *J* = 8.2 Hz, 1H), 7.95 (d, *J* = 8.2 Hz, 1H), 7.33 (s, 1H), 6.34 (s, 1H), 0.07 (s, 8H). ¹⁹F NMR (471 MHz, DMSO-*d*₆, 298 K) δ -68.62, -72.25. MALD-TOF: Calculated for C₃₉H₃₉F₆IrN₆Si₃: 982.2, found: 980.6 [M-H]⁺.

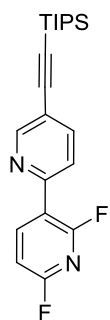
2,6-Difluoro-5'-bromo-3,2'-dipyridine (3-11)

In a 250 ml round bottom flask were added compound **3-5** (3.00 g, 18.9 mmol), 2-iodo-5-bromopyridine (6.43 g, 22.7 mmol), K₂CO₃ (5.22 g, 37.7 mmol), 150 ml of THF and 50 ml of water. The



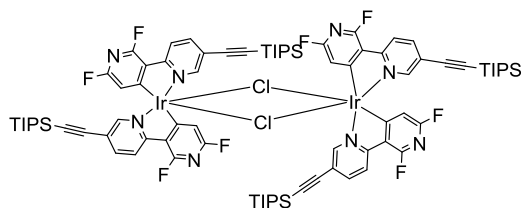
mixture was degassed and added argon 3 times. Then, Pd(PPh₃)₄ (436 mg, 0.38 mmol) was added. The mixture was stirred at 80 °C for 24 hours. Then extraction was done with DCM and water. It was purified by a silica gel flash column (DCM). Eventually, 2.00 g white-colored solid was received after drying under reduced pressure. ¹H NMR (300 MHz, CD₂Cl₂, 300 K) δ 8.77 (d, 1H), 8.68 (dd, 1H), 7.95 (dd, 1H), 7.77 (dd, 1H), 7.00 (dd, 1H). ¹⁹F NMR (470 MHz, CD₂Cl₂, 298 K) δ -68.50, -69.53. FD-Mass: calculated for C₁₀H₅BrF₂N₂: 270.0 (100%), found: 270.3 [M]⁺.

2,6-Difluoro-5'-TIPSE-3,2'-dipyridine (3-13)



In a Schlenk flask was added compound **3-11** (1.71 g, 6.31 mmol), PPh₃ (165 mg, 0.63 mmol), Pd(PPh₃)₂Cl₂ (221 mg, 0.31 mmol), CuI (60 mg, 0.31 mmol) and 80 ml of triethylamine. The mixture was bubbled argon for 10 min. Then (triisopropyl)acetylene (1.6 ml, 6.94 mmol) was added by cannula. The mixture was stirred at 80 °C for 24 hours. Then the mixture was extracted with DCM and water. It was purified by a silica gel flash column (DCM). Eventually, 2.0 g orange sticky liquid was received after drying under reduced pressure (85 %). ¹H NMR (300 MHz, CD₂Cl₂, 300 K) δ 8.77 (d, 1H), 8.71 (dd, 1H), 7.88-7.81 (m, 2H), 7.00 (dd, 1H), 1.15 (s, 21H). ¹³C NMR (75 MHz, CD₂Cl₂, 300 K) δ 152.98, 149.49, 149.40, 146.59, 146.54, 146.48, 146.43, 139.93, 123.31, 123.16, 120.26, 107.62, 107.54, 107.16, 107.09, 103.59, 96.46, 18.76, 11.64. FD-Mass: calculated for C₂₁H₂₆F₂N₂Si: 372.2(100%), found: 372.0 [M]⁺.

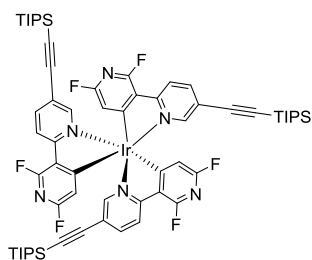
[(2,6-Difluoro-5'-ethynyl-3,2'-bipy)₂Ir(μ-Cl)₂] (3-15)



In a round bottom flask were added IrCl₃ (0.718 g, 2.40 mmol), compound **3-13** (1.84 g, 4.93 mmol) and 24 ml of 2-ethoxyethanol. The mixture was degassed and was added argon 3 times and stirred at 140 °C for 24 hours. Then water was added to precipitate it. After filtration and washing with water, 1.34 g of a yellow-brown solid was received after drying under reduced pressure (57.5%). It was directly used for next step without further purification. But it can do be purified by silica gel flash column (DCM). ¹H NMR (300 MHz, CD₂Cl₂, 300 K) δ 9.11 (d, 4H), 8.25 (dd, 4H), 8.06 (dd, 4H), 1.20 (s, 84H). FD-Mass: calculated for C₈₄H₁₀₀C₁₂F₈Ir₂N₈Si₄: 1938.6 (100%), found: 1942.2.

Mer(2,6-difluoro-5'-ethynyl-3,2'-bipy)₃Ir (3-17)

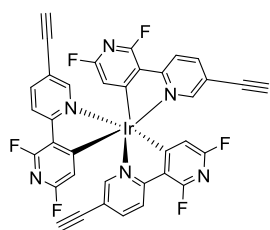
In a round bottom flask were added compound **3-15** (1.20 g, 0.62 mmol), compound **3-13** (0.46 g, 1.24 mmol), K₂CO₃ (0.43 g, 3.09 mmol), Silver trifluoromethanesulfonate (0.33 g, 1.28 mmol) and 24 ml of 1,3,5-trimethylbenzene. The reactor was degassed and added argon 3 times and stirred at 170 °C for 24 hours. The resulting mixture was extracted with DCM and water. It was purified by a silica gel flash



column (DCM) and a GPC column afterwards. Eventually, 0.49 g of a yellow solid was received after drying under reduced pressure (25%). ^1H NMR (300 MHz, CD_2Cl_2 , 300 K) δ 8.33 (dd, 1H), 8.23 (dd, 1H), 8.16 (dd, 1H), 8.00 (d, 1H), 7.95 (d, 1H), 7.87 (dd, 1H), 7.82 (dd, 1H), 7.77 (dd, 1H). ^{19}F NMR (470 MHz, CD_2Cl_2 , 298 K) δ -67.62, -68.35, -68.98, -71.21, -71.52, -71.86. FD-

Mass: calculated for $\text{C}_{63}\text{H}_{75}\text{F}_6\text{IrN}_6\text{Si}_3$: 1306.5 (100%), found: 1305.4 $[\text{M-H}]^+$.

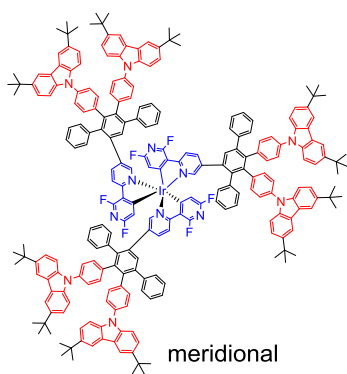
Mer(2,6-difluoro-5'-ethynyl-3,2'-bipy) $_3$ Ir (**3-19**)



In a round bottom flask were added compound **3-17** (420 mg, 0.32 mmol), tetrabutylammonium fluoride (0.25 g, 0.96 mmol) and 50 ml of THF. The reactor was degassed and added argon 3 times and stirred at room temperature overnight. Then it was extracted with DCM and water for several times to remove TBAF. Then it was purified by a silica gel flash column (Ethyl acetate/ hexane, 45/55).

Eventually, 120 mg of a light yellow solid was received after drying under reduced pressure (46%). ^1H NMR (300 MHz, CD_2Cl_2 , 300 K) δ 8.39 (dd, 1H), 8.27 (ddd, 1H), 8.21 (ddd, 1H), 7.99 (d, 1H), 7.98 (s, 1H), 7.96 (d, 1H), 7.89 (dd, 1H), 7.86 (dd, 1H), 6.33 (t, 1H), 5.97 (t, 1H), 5.71 (t, 1H), 3.33 (s, 1H), 3.30 (s, 1H), 3.28 (s, 1H). ^{19}F NMR (470 MHz, CD_2Cl_2 , 298 K) δ -66.93, -67.67, -68.48, -70.62, -71.07, -71.37. FD-Mass: calculated for $\text{C}_{36}\text{H}_{15}\text{F}_6\text{IrN}_6$: 838.1 (100%), found: 836.8 $[\text{M-H}]^+$.

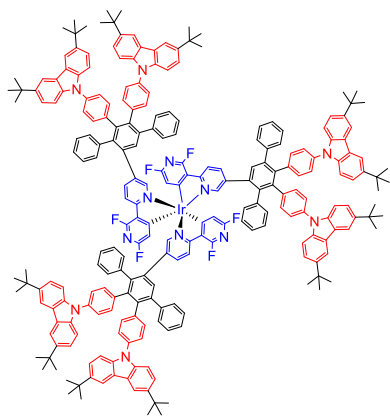
Mer(2,6-difluoro-3,2'-bipy) $_3$ Ir-based-5'-dendronized, peripheral-carbazole polyphenylene dendrimer G1 (mer(dfppy) $_3$ -CAB-G1)



In a round bottom flask were added compound **3-19** (68 mg, 0.081 mmol), compound (**2-3d**) (0.27 g, 0.28 mmol) and 12 ml of *o*-xylene. The reactor was degassed and added argon 3 times. Then it was heated at 150 °C for 24 hours. After that, the mixture was purified by a silica gel flash column (DCM/Hexane, 1/1~4/1). The product was further purified by a GPC column. Eventually, 160 mg yellow-colored solid was received after drying under reduced pressure (55%). ^1H NMR (300 MHz, CD_2Cl_2 , 300 K) δ 8.25

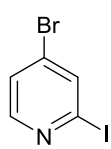
(m, 2H), 8.09-8.06 (m, 12H), 8.03 (d, 2H), 7.93 (dd, 1H), 7.72 (dd, 1H), 7.58 (dd, 3H), 7.45 (d, 2H), 7.36-6.72 (m, 79H), 5.98(t, 1H), 5.74 (t, 1H), 5.19 (t, 1H), 1.41-1.34 (m, 108H). ^{19}F NMR (470 MHz, CD_2Cl_2 , 298 K) δ -68.02, -68.86, -70.32, -71.36, -71.81, -72.72. MALD-TOF: Calculated for $\text{C}_{240}\text{H}_{213}\text{F}_6\text{IrN}_{12}$: 3571.6 (100%), found: 3571.1 $[\text{M}]^+$.

Fac(2,6-difluoro-3,2'-bipy) $_3$ Ir-based-5'-dendronized, peripheral-carbazole polyphenylene dendrimer G1 (fac(dfppy) $_3$ -CAB-G1)



In a quartz tube were added 120 mg mer-dendrimer, and 20 ml of THF. The tube was degassed and added argon 3 times. Then the sealed tube was put in photochemical reactor and shined for 12 hours while the solution was stirred. After that, extraction was done using DCM and water. It was purified by a silica gel flash column (DCM). Eventually, 100 mg yellow-colored solid was received after drying under reduced pressure (83%). ^1H NMR (300 MHz, CD_2Cl_2 , 300 K) δ 8.13 (d, 3H), 8.07 (d, 6H), 8.03 (d, 6H), 7.32-6.65 (m, 84H), 7.52 (d, 3H), 5.91 (t, 3H), 1.36 (s, 54H), 1.30 (s, 54H). ^{19}F NMR (470 MHz, CD_2Cl_2 , 298 K) δ -68.98, -72.98. MALD-TOF: calculated for $\text{C}_{240}\text{H}_{213}\text{F}_6\text{IrN}_{12}$: 3571.6 (100%), found: 3572.3 $[\text{M}+\text{H}]^+$. HR-MALDI-TOF: calculated for $\text{C}_{240}\text{H}_{213}\text{F}_6\text{IrN}_{12}$: 3571.6637, found: 3571.6842 $[\text{M}]^+$.

2-Iodo-4-bromopyridine (3-10)



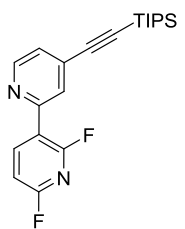
2-amino-4-bromopyridine (4.00 g, 23.12 mmol), CuI (4.40 g, 23.12 mmol), iodine (5.87 g, 23.12 mmol) and tertbutylnitrite (8.25 ml, 69.36 mmol) were added into a 50 ml two-neck Schlenk flask sequentially. After that, 25 ml of diiodomethane was added. The system was heated at 50 °C for 12 hours with one outlet connecting with reflux tube and open for nitrogen going and the other opening sealed. After that, extraction was done with K_2CO_3 and $\text{Na}_2\text{S}_2\text{O}_3$ solution. After that, a silica gel flash column was done with DCM as eluent. Eventually, 4.00 g of a light-yellow solid was received after drying under reduced pressure. ^1H NMR (300 MHz, DMSO-d_6 , 298 K) δ 8.25 (d, $J = 5.3$ Hz, 1H), 8.19 (d, $J = 1.8$ Hz, 1H), 7.72 (dd, $J = 5.3, 1.8$ Hz, 1H). ^{13}C NMR (75 MHz, CD_2Cl_2 , 298 K) δ 151.45, 137.70, 133.31, 127.03, 118.17.

2,6-Difluoro-4'-bromo-3,2'-dipyridine (3-12)



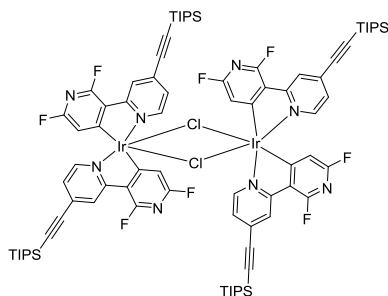
In a 250 ml round bottom flask were added compound **3-5** (1.27 g, 7.99 mmol), 2-iodo-4-bromo-pyridine (2.50 g, 8.79 mmol), K_2CO_3 (2.21 g, 15.99 mmol), 50 ml of THF and 20 ml of water. The mixture was degassed and added argon 3 times. Then, $\text{Pd}(\text{PPh}_3)_4$ (318 mg, 0.27 mmol) was added. The mixture was stirred at 80 °C for 24 hours. Then extraction was done with DCM and water. It was purified by a silica gel flash column (DCM). Eventually, 0.738 g of a yellow solid was received after drying under reduced pressure (34%). ^1H NMR (300 MHz, CD_2Cl_2 , 300 K) δ 8.69 (dt, $J = 9.7, 8.0$ Hz, 1H), 8.53 (dd, $J = 5.2, 0.6$ Hz, 1H), 8.05 (td, $J = 1.7, 0.6$ Hz, 1H), 7.51 (dd, $J = 5.3, 1.8$ Hz, 1H), 7.01 (ddd, $J = 8.3, 3.0, 0.9$ Hz, 1H). ^{19}F NMR (470 MHz, CD_2Cl_2 , 298 K) δ -68.08, -69.52. FD-Mass: calculated for $\text{C}_{10}\text{H}_5\text{BrF}_2\text{N}_2$: 270.0 (100%), found: 270.2 $[\text{M}]^+$.

2,6-Difluoro-4'-TIPSEcetyl-3,2'-dipyridine (3-14)



In a Schlenk flask were added compound **3-12** (0.10 g, 0.369 mmol), PPh₃ (9 mg, 36.9 μmol), Pd(PPh₃)₂Cl₂ (13 mg, 18.4 μmol), CuI (10 mg, 52.6 μmol) and 5 ml of triethylamine. The mixture was bubbled argon for 10 min. Then (triisopropyl)acetylene (74 mg, 0.406 mmol) was added by syringe. The mixture was stirred at 80 °C for 24 hours. Then the mixture was extracted with DCM and water. It was purified by a silica gel flash column (DCM). Eventually, 131 mg of a yellow sticky liquid was received after drying under reduced pressure (96 %). ¹H NMR (300 MHz, CD₂Cl₂, 300 K) δ 8.73 – 8.58 (m, 1H), 7.86 (dt, *J* = 2.3, 1.2 Hz, 1H), 7.34 (dd, *J* = 5.0, 1.5 Hz, 1H), 7.05 – 6.92 (m, 1H), 1.15 (s, 21H). ¹⁹F NMR (470 MHz, CD₂Cl₂, 298 K) δ -68.79, -69.83. FD-Mass: calculated for C₂₁H₂₆F₂N₂Si: 372.2(100%), found: 372.3 [M]⁺.

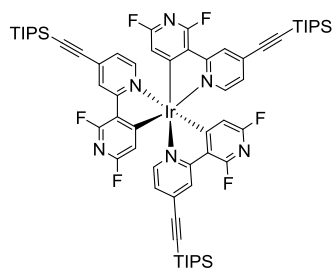
[(2,6-DiFpy-4'-TIPSEpy)₂Ir(μ-Cl)₂] (3-16)



In a round bottom flask were added IrCl₃ (19 mg, 63.6 μmol), compound **3-14** (50 mg, 0.134 mmol) and 1 ml of 2-ethoxyethanol. The mixture was degassed and added argon 3 times and stirred at 140 °C for 24 hours. Then water was added to precipitate it. After filtration and washing with water, 30 mg of a yellow-brown solid was received after drying under reduced pressure (24.4%). It was directly

used for next step without further purification. FD-Mass: calculated for C₈₄H₁₀₀C₁₂F₈Ir₂N₈Si₄: 1938.6 (100%), found: 1941.1.

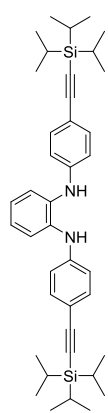
Mer(2,6-diFpy-4'-TIPSEpy)₃Ir (3-18)



In a round bottom flask was added compound **3-16** (30 mg, 0.015 mmol), compound **3-14** (11 mg, 0.031 mmol), K₂CO₃ (10 mg, 0.077 mmol), Silver trifluoromethanesulfonate (8 mg, 0.032 mmol) and 1 ml of 1,3,5-trimethylbenzene. The reactor was degassed and added argon 3 times and stirred at 170 °C for 24 hours. The resulting mixture was extracted with DCM and water. It was purified by a silica gel flash column (DCM) and a

GPC column afterwards. Eventually, 4 mg of a yellow solid was received after drying under reduced pressure (20%). ¹H NMR (300 MHz, CD₂Cl₂, 300 K) δ 8.34 (s, 1H), 8.28 – 8.19 (m, 2H), 7.85 (d, *J* = 6.1 Hz, 1H), 7.82 – 7.75 (d, *J* = 5.7 Hz, 1H), 7.49 – 7.43 (m, 1H), 7.08 (dd, *J* = 5.8, 1.7 Hz, 1H), 6.95 (ddd, *J* = 6.3, 5.1, 1.8 Hz, 3H), 6.31 (t, *J* = 2.8 Hz, 1H), 6.00 (t, *J* = 2.7 Hz, 1H), 5.81 (t, *J* = 2.0 Hz, 1H), 1.13 (s, 63H). ¹⁹F NMR (470 MHz, CD₂Cl₂, 298 K) -67.80, -68.39, -69.09, -71.64, -72.10, -72.22. FD-Mass: calculated for C₆₃H₇₅F₆IrN₆Si₃: 1306.5 (100%), found: 1305.9 [M]⁺.

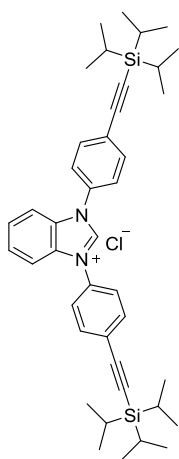
1,2-Di[(4-triisopropylsilylethynyl)amino]benzene (3-25)



1,2-diaminobenzene (1.56 g, 14.43 mmol) and 1-bromo-4-[(triisopropylsilyl)ethynyl]benzene (9.75 g, 28.90 mmol) were placed in a 100 ml Schlenk flask. It was then transferred to a glove box, in which sodium tertbutoxide (4.16 g, 43.28 mmol) and 20 ml of toluene were added. In another flask, Pd₂(dba)₃ (295 mg, 0.289 mmol), 2,2'-bi(diphenylphosphino)-1,1'-dinaphthalene (864 mg, 1.39 mmol) and 20 ml of dry toluene were added sequentially to make it totally dissolved. Then the catalyst solution was added into the Schlenk flask. Then the mixture was heated at 90 °C and stirred for 13 hours.

The resulting mixture was quenched with aq. NH₄Cl solution and extracted with DCM and dilute NH₄Cl solution, followed by a silica gel flash column (DCM/hexane, 1/1). Eventually, 8.00 g of a white-brown solid was received after drying under reduced pressure (89.2%). ¹H NMR (300 MHz, CD₂Cl₂, 300 K) δ 7.41 – 7.26 (m, 6H), 7.04 (dd, *J* = 6.0, 3.2 Hz, 2H), 6.84 (d, *J* = 8.9 Hz, 4H), 5.78 (s, 2H), 1.11 (s, 42H). ¹³C NMR (75 MHz, CD₂Cl₂, 300 K) δ 144.64, 134.69, 133.58, 124.19, 121.65, 116.34, 115.16, 107.92, 88.85, 18.87, 11.81. FD-Mass: calculated for C₄₀H₅₆N₂Si₂: 620.4 (100%), found: 621.7 [M+H]⁺.

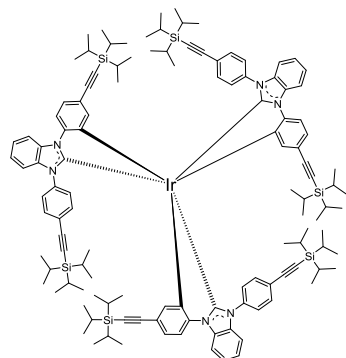
1,3-Di[(4-triisopropylsilylethynyl)phenyl]benzimidazonium chloride (3-26)



Compound **3-25** (7.26 g, 11.69 mmol) and 70 ml of triethyl orthoformate were placed in a Schlenk flask, stirred to make it dissolve. Then the system was degassed and added argon 3 times. Then conc. HCl (1.5 ml, 22.83 mmol) was added quickly. It was stirred at room temperature for 30 minutes. Then it was heated at 80 °C for 14 hours. After the mixture was cooled down, 40 ml of Et₂O was added to precipitate it. Then filtration was done to get 4.4 g of a white solid after drying (85.5%). ¹H NMR (250 MHz, DMSO-*d*₆, 298K) δ 10.62 (s, 1H), 8.06 – 7.76 (m, 12H), 1.14 (s, 42H). ¹³C NMR (75 MHz, DMSO-*d*₆, 300K) δ 143.10, 133.65, 132.95, 131.07, 127.98, 125.89, 124.55, 113.88, 105.61, 93.08, 64.96, 18.55, 10.74. FD-Mass: calculated for C₄₁H₅₅N₂Si₂:631.4,

found: 632.1 [M+H]⁺.

1,3-Di[(4-triisopropylsilylethynyl)phenyl]benzimidazonium carbene-chealated Ir complex (3-27)

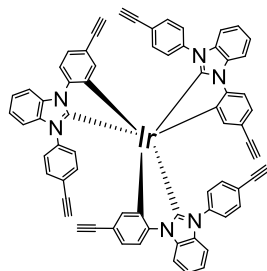


IrCl₃.*n*H₂O (500 mg, 1.67 mmol), compound **3-26** (3.58 g, 5.36 mmol), Ag₂CO₃ (739 mg, 2.68 mmol), Na₂CO₃ (284 mg, 2.68 mmol) and 80 ml of 2-ethoxyethanol were added in a Schlenk flask. Then the mixture was degassed and added argon 3 times. It was stirred at 145 °C for 20 hours. After the mixture was cooled down, water was added to precipitate it. Then filtration was done to get pale-white-colored solid after drying. After that, the solid was further purified by recrystallization by hexane and 2 gram of

light-yellow-colored solid product was obtained after drying under reduced pressure (57%). The

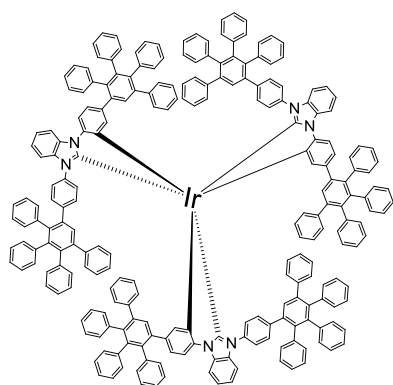
obtained product could be used for next step reaction directly. To characterize the product, part of the product was further purified by a silica gel flash column (DCM/hexane, 1/4) to get 80 mg of a light-yellow solid after drying under reduced pressure (22%). ^1H NMR (250 MHz, CD_2Cl_2 , 300 K) δ 8.14 (d, $J = 8.3$ Hz, 3H), 7.88 (d, $J = 8.2$ Hz, 3H), 7.40 (dd, $J = 8.2, 1.9$ Hz, 3H), 7.40 (dd, $J = 8.1, 1.8$ Hz, 3H), 7.32 (dd, $J = 7.4, 7.4$ Hz, 3H), 7.23 (dd, $J = 8.2, 1.9$ Hz, 3H), 7.06 (dd, $J = 7.8, 7.6$ Hz, 3H), 6.73 (d, $J = 1.9$ Hz, 3H), 6.52 (dd, $J = 8.3, 3.7$ Hz, 3H), 6.42 (dd, $J = 8.2, 2.3$ Hz, 3H), 6.28 (dd, $J = 8.2, 1.9$ Hz, 3H), 6.11 (dd, $J = 8.1, 2.2$ Hz, 3H), 1.11 (s, 63H), 1.04 (s, 63H). ^{13}C NMR (176 MHz, CD_2Cl_2 , 300 K) δ 187.96, 148.74, 148.21, 140.82, 137.98, 137.55, 132.54, 132.12, 131.80, 128.90, 127.22, 126.14, 123.79, 123.61, 123.39, 119.72, 112.41, 111.22, 110.61, 110.08, 105.69, 92.53, 88.44, 18.88, 18.86, 11.85, 11.65. FD-Mass: calculated for $\text{C}_{123}\text{H}_{159}\text{IrN}_6\text{Si}_2$: 2082.1, found: 2082.2 $[\text{M}]^+$.

1,3-Di[(4-ethynyl)phenyl]benzoimidazonium carbene-chealated Ir complex (3-28)



Compound **3-27** (1.66 g, 0.795 mmol) was added into a Schlenk flask. Then it was degassed and added argon 3 times. Then, 65 ml of THF was added to dissolve it and stirred under ice bath. Then TBAF (1.22 g, 4.66 mmol) dissolved in 20 ml of THF was added dropwise. Then the mixture was stirred for 1 hour at 0 °C. After that, THF was evaporated to get solid. Then a silica gel flash column was run (DCM/hexane, 4/1) to get 0.34 g of a light-yellow solid after drying under reduced pressure (37.4%). ^1H NMR (300 MHz, CD_2Cl_2 , 300 K) δ 8.12 (d, $J = 8.3$ Hz, 3H), 7.91 (d, $J = 8.2$ Hz, 3H), 7.47 – 7.23 (m, 9H), 7.10 (t, $J = 7.8$ Hz, 3H), 6.72 (d, $J = 2.0$ Hz, 3H), 6.66 (dd, $J = 8.2, 2.2$ Hz, 3H), 6.54 (d, $J = 8.1$ Hz, 3H), 6.46 (dd, $J = 8.1, 2.0$ Hz, 3H), 6.14 (dd, $J = 8.2, 2.3$ Hz, 3H), 2.97 (s, 1H), 2.91 (s, 1H). ^{13}C NMR (63 MHz, CD_2Cl_2 , 300 K) δ 187.49, 149.17, 148.30, 140.51, 137.88, 137.75, 132.55, 132.37, 131.97, 129.05, 127.06, 126.68, 124.12, 123.48, 122.51, 118.11, 112.61, 111.31, 110.71, 85.71, 82.06, 78.86, 75.75. FD-Mass: calculated for $\text{C}_{69}\text{H}_{39}\text{IrN}_6$: 1144.3 (100%), found: 1143.7 $[\text{M-H}]^+$.

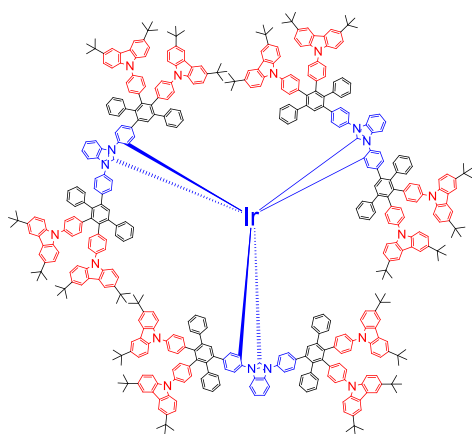
Fac(dpbic)₃Ir-based polyphenylene dendrimer G1 (fac(dpbic)₃Ir-PPD-G1)



Compound **3-28** (5.8 mg, 5.07 μmol), 2,3,4,5-tetraphenylcyclopentadienone (20 mg, 52 μmol) and 0.5 ml of o-xylene were added into a Schlenk flask. Then the mixture was degassed and was added argon 3 times. Then, it was heated at 145 °C for 18 hours. After the mixture was cooled down, 10 ml of hexane was added to precipitate the product and filtration was done to get the solid. Then, the product was purified by silica gel flash column (DCM/hexane, 1/1 to 7/3) to get 6 mg of a white solid (36.1%). ^1H NMR (300 MHz, CD_2Cl_2 , 300 K) δ 7.71 (d, $J = 8.2$ Hz, 3H), 7.40 (d, $J = 8.2$ Hz, 3H), 7.35 – 7.24 (m, 9H), 7.18 – 7.10 (m,

10H), 7.10 – 6.96 (m, 16H), 6.96 – 6.64 (m, 86H), 6.58 (s, 3H), 6.52 (dd, $J = 8.1, 2.1$ Hz, 3H), 6.44 – 6.21 (m, 22H), 6.02 (d, $J = 8.0$ Hz, 3H), 5.86 (s, 3H), 5.69 (d, $J = 8.2$ Hz, 3H). ^{13}C NMR (176 MHz, CD_2Cl_2 , 300 K) δ 188.98, 147.48, 143.03, 142.35, 142.07, 141.75, 141.63, 141.30, 141.24, 141.10, 140.93, 140.75, 140.64, 140.45, 140.29, 140.12, 139.88, 139.81, 139.75, 138.59, 138.45, 138.19, 137.43, 135.89, 132.39, 132.10, 132.00, 131.82, 131.61, 130.52, 130.11, 129.90, 128.60, 127.87, 127.62, 127.23, 127.13, 127.05, 126.97, 126.92, 126.79, 126.68, 126.58, 126.26, 126.05, 125.84, 125.69, 125.37, 125.13, 123.53, 123.12, 122.15, 111.19, 110.81, 110.19. MALDI-TOF: calculated for $\text{C}_{237}\text{H}_{159}\text{IrN}_6$: 3283.2 (100%), found: 3283.2 $[\text{M}]^+$. HR-ESI-MS: calculated for $\text{C}_{237}\text{H}_{159}\text{IrN}_6$: 3284.2412, found: 3284.2383 $[\text{M}^+]$.

Fac(dpbic)₃Ir-based peripheral-carbazole polyphenylene dendrimer G1 (fac(dpbic)₃Ir-CAB-G1)



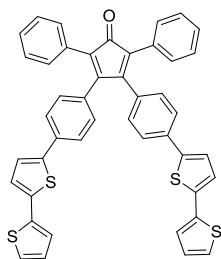
Compound **3-28** (36 mg, 31.5 μmol), compound **2-3d** (300 mg, 319.4 μmol) and 7 ml of *o*-xylene were added into a Schlenk flask. Then it was degassed and added argon 3 times. Then, it was heated at 150 $^\circ\text{C}$ for 48 hours. After the mixture was cooled down, methanol was added to precipitate the product and filtration was done to get the solid. Then, the product was purified by silica gel flash column (DCM/hexane, 2/3) to get solid product. Then a GPC column (THF as eluent) was done to get 0.185g of a white solid (88.9%).

^1H NMR (300 MHz, CD_2Cl_2 , 298 K) δ 8.07 (m, 24H), 7.91 (d, $J = 8.3$ Hz, 3H), 7.59 (d, $J = 8.2$ Hz, 3H), 7.52 – 7.39 (m, 12H), 7.38 – 7.32 (m, 7H), 7.29 – 6.88 (m, 131H), 6.82 (s, 5H), 6.75 – 6.61 (m, 13H), 6.51 (m, 12H), 6.28 (d, $J = 8.0$ Hz, 3H), 6.16 (s, 3H), 5.95 (d, $J = 8.1$ Hz, 3H), 1.36 (m, 216H). ^{13}C NMR (214 MHz, CD_2Cl_2 , 298 K) δ 149.08, 147.80, 143.44, 143.18, 143.14, 143.02, 142.98, 142.03, 141.84, 141.77, 141.43, 141.31, 141.11, 140.67, 140.64, 140.41, 140.33, 140.16, 139.99, 139.75, 139.65, 139.57, 139.54, 139.51, 139.27, 138.65, 138.39, 138.23, 137.46, 136.21, 136.18, 135.95, 135.85, 135.51, 133.54, 133.37, 133.33, 133.26, 132.60, 132.10, 131.94, 131.97, 130.79, 130.76, 130.53, 130.23, 129.95, 128.87, 128.22, 127.99, 127.51, 127.45, 127.37, 126.75, 126.32, 126.26, 125.82, 125.73, 125.70, 125.67, 125.62, 125.54, 125.42, 125.28, 123.94, 123.89, 123.84, 123.56, 123.52, 123.50, 123.45, 122.43, 116.59, 116.51, 111.54, 111.13, 110.42, 109.44, 109.41, 109.39, 109.34, 34.98, 34.95, 34.92, 32.16, 32.15. MALDI-TOF: calculated for $\text{C}_{477}\text{H}_{435}\text{IrN}_{18}$: 6612.4 (100%), found: 6611.4 $[\text{M}-\text{H}]^+$. HR-MALDI-TOF: calculated for $\text{C}_{477}\text{H}_{435}\text{IrN}_{18}$: 6612.4389, found: 6612.5690 $[\text{M}^+]$.

8.2.3 Synthesis of oligothiophene-functionalized dendrimers (Chapter 6)

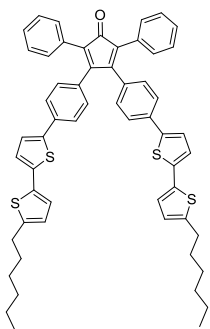
2,5-Diphenyl-3,4-di-[4-(2,2'-bithiophen-5-yl)phenyl]cyclopentadienone (6-4)

5-bromo-2,2'-bithiophene (0.49 g, 2.00 mmol), compound **2-22** (0.580 g, 0.911 mmol), tetrabutylammonium bromide (59.1 mg, 0.18 mmol), K_2CO_3 (0.63 g, 4.56 mmol), 40 ml of toluene and



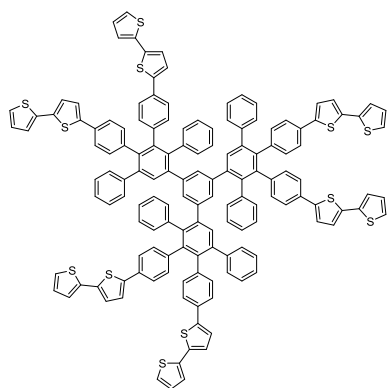
20 ml of water were added in a 100 ml round bottom flask. Then the mixture was degassed and added argon for 3 times, followed by the addition of $\text{Pd}(\text{PPh}_3)_4$ (90.8 mg, 0.078 mmol). The mixture was then stirred at 80 °C for 24 hours. Then it was extracted by DCM and purified by a silica gel flash column (DCM/petroleum ether, 1:1). Eventually, 0.61 g of a red solid was received after drying under reduced pressure (94%). ^1H NMR (300 MHz, CD_2Cl_2 , 300K) δ 7.49 – 7.40 (m, 4H), 7.30 – 7.24 (m, 14H), 7.22 (dd, $J = 3.6, 1.2$ Hz, 2H), 7.16 (d, $J = 3.8$ Hz, 2H), 7.06 – 6.95 (m, 6H). ^{13}C NMR (176 MHz, CD_2Cl_2 , 300 K) δ 154.11, 142.51, 137.66, 137.50, 134.52, 132.61, 131.38, 130.59, 128.49, 128.37, 127.97, 126.18, 125.18, 125.10, 124.80, 124.26. FD-Mass: calculated for $\text{C}_{45}\text{H}_{28}\text{OS}_4$: 712.1(100%), found: 713.6 $[\text{M}+\text{H}]^+$.

2,5-Diphenyl-3,4-di-[4-(5-hexyl-2,2'-bithiophen-5'-yl)phenyl]cyclopentadienone (6-5)



5-bromo-5'-hexyl-2,2'-bithiophene (0.171 g, 0.519 mmol), compound **2-22** (0.15 g, 0.236 mmol), tetrabutylammonium bromide (3.8 mg, 0.012 mmol), K_2CO_3 (0.228 g, 1.65 mmol), 15 ml of toluene and 7 ml of water were added in a 50 ml round bottom flask. Then the mixture was degassed and added argon for 3 times, followed by the addition of $\text{Pd}(\text{PPh}_3)_4$ (13 mg, 0.012 mmol). The mixture was then stirred at 110 °C for 14 hours. Then it was extracted by DCM and purified by a silica gel flash column (DCM/petroleum ether, 1:1). Eventually, 0.22 g of a red-brown solid was received after drying under reduced pressure (100%). ^1H NMR (250 MHz, Chloroform- d_1 , 300K) δ 7.45 (d, $J = 8.4$ Hz, 4H), 7.30 – 7.20 (m, 12H), 7.06 (d, $J = 3.8$ Hz, 2H), 7.03 – 6.96 (m, 6H), 6.70 (d, $J = 3.6$ Hz, 2H), 2.79 (t, $J = 7.6$ Hz, 4H), 1.74 – 1.59 (m, 4H), 1.30 (m, 12H), 0.88 (t, $J = 3.5$ Hz, 6H). ^{13}C NMR (176 MHz, CD_2Cl_2 , 298 K) δ 154.14, 146.44, 141.75, 138.30, 134.80, 134.63, 132.43, 131.41, 130.58, 128.48, 127.94, 126.13, 125.34, 125.07, 124.75, 124.28, 123.95, 32.00, 31.96, 30.52, 29.15, 22.99, 14.25. FD-Mass: calculated for $\text{C}_{57}\text{H}_{52}\text{OS}_4$: 880.3 (100%), found: 881.9 $[\text{M}+\text{H}]^+$.

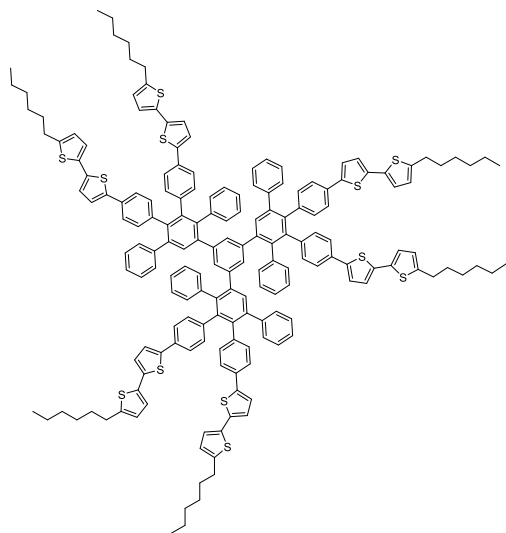
1,3,5-Benzene-based, peripheral-bithiophene polyphenylene dendrimer-G1 (BTPPD)



1,3,5-triethynylbenzene (10.0 mg, 0.067 mmol) and compound **6-4** (190 mg, 0.266 mmol) were added in a 10 ml round bottom flask and dissolved in 4 ml anhydrous *o*-xylene. The mixture was stirred at 145 °C for 12 hours. Then, the mixture was added into methanol to precipitate, followed by filtration to get the solid mixture. Then it was purified by a silica gel flash column (DCM/hexane, 1/1) and it was further purified by GPC column using THF as the eluent. Finally precipitation was formed by adding concentrated THF solution into methanol and solid was received by filtration. Eventually, 100 mg of a light-yellow solid was received

after drying under reduced pressure (68%). ^1H NMR (300 MHz, CD_2Cl_2 , 300 K) δ 7.24 – 7.17 (m, 22H), 7.16 – 7.09 (m, 22H), 7.08 – 7.03 (m, 9H), 6.99 (dd, $J = 5.1, 3.6$ Hz, 6H), 6.91 – 6.85 (m, 12H), 6.82 (d, $J = 9.8$ Hz, 9H), 6.77 (d, $J = 5.8$ Hz, 6H), 6.73 – 6.69 (m, 6H). ^{13}C NMR (176 MHz, CD_2Cl_2 , 300 K) δ 143.11, 141.85, 141.30, 141.17, 140.92, 140.85, 140.30, 140.25, 139.92, 139.55, 138.83, 137.68, 136.64, 136.57, 132.50, 132.45, 132.09, 132.00, 131.60, 131.32, 130.41, 130.12, 128.25, 127.95, 127.54, 126.82, 126.39, 124.88, 124.76, 124.26, 123.95, 123.89, 123.80. MALD-TOF: calculated for $\text{C}_{144}\text{H}_{90}\text{S}_{12}$: 2203.4 (100%), found: 2204.8 $[\text{M}+\text{H}]^+$. HR-ESI-MS: calculated for $\text{C}_{144}\text{H}_{90}\text{S}_{12}$: 2205.3789, found: 2205.3789.

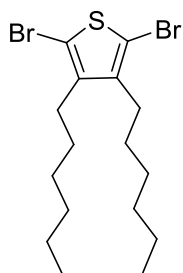
1,3,5-Benzene-based, peripheral-5-hexyl-bithiophene polyphenylene dendrimer-G1 (HBTPPD)



1,3,5-triethynylbenzene (8.5 mg, 0.057 mmol) and compound **6-5** (199 mg, 0.226 mmol) were added in a 10 ml round bottom flask and dissolved in 3 ml anhydrous *o*-xylene. The mixture was stirred at 170 °C for 24 hours. Then it was purified by a silica gel flash column (DCM/hexane, 1/1) and it was further purified by GPC column using THF as the eluent. Finally Precipitation was formed by adding concentrated THF solution into methanol and solid was received by filtration. Eventually, 100 mg of a light-yellow solid was received after drying under reduced pressure (65%). ^1H NMR (300 MHz, CD_2Cl_2 , 300 K) δ 7.26 – 7.16 (m, 16H), 7.15 – 7.10 (m, 12H),

7.06 (dd, $J = 9.0, 3.8$ Hz, 6H), 6.99 – 6.92 (m, 12H), 6.91 – 6.81 (m, 16H), 6.78 (dd, $J = 11.4, 3.0$ Hz, 10H), 6.73 – 6.69 (m, 6H), 6.66 (d, $J = 3.6$ Hz, 6H), 2.77 (t, $J = 7.6$ Hz, 12H), 1.65 (h, $J = 7.6, 6.9$ Hz, 12H), 1.31 (m, 36H), 0.93 – 0.82 (m, 18H). ^{13}C NMR (176 MHz, CD_2Cl_2 , 298 K) δ 146.03, 142.39, 141.88, 141.30, 141.20, 140.92, 140.28, 140.15, 139.78, 139.56, 138.86, 137.26, 137.19, 135.00, 132.50, 132.12, 131.72, 131.44, 130.43, 130.14, 127.95, 127.55, 126.80, 126.39, 125.21, 124.19, 124.07, 123.90, 123.84, 123.75, 123.61, 31.99, 31.95, 29.88, 29.14, 22.98, 14.23. MALD-TOF: calculated for $\text{C}_{180}\text{H}_{162}\text{S}_{12}$: 2707.9 (100%), found: 2710.0. HR-ESI-MS: calculated for $\text{C}_{180}\text{H}_{162}\text{S}_{12}$: 2708.9369, found: 2708.9011 $[\text{M}^+]$.

2,5-Dibromo-3,4-dihexylthiophene (6-7)



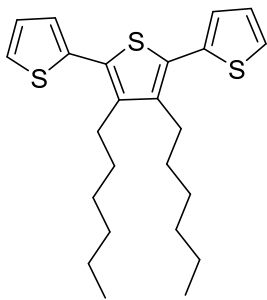
In a 100 ml round Schlenk flask were added 3,4-dihexylthiophene (5.0 g, 19.8 mmol) and 50 ml of DMF. The flask was degassed and added argon 3 times and the mixture was stirred under ice bath. Then NBS (4.12 g, 41.6 mmol) in 20 ml DMF was added dropwise. It was stirred overnight from 0 °C to room temperature. Checked TLC the next day, and found incomplete conversion, then another 2.0 g NBS in 10 ml DMF was

added dropwise while the mixture was stirred under ice bath. The next day, checked TLC again and found still incomplete conversion. Then, 1.0 g NBS in 5 ml DMF was added again with the same process as before. The next day checked TLC again and found complete conversion. Then the mixture was extracted with DCM and 5% aqu. HCl solution for 4 times to get rid of DMF, followed by a silica gel flash column (Hexane) to get 7.45 g colorless liquid after drying under reduced pressure (91.7%). ^1H NMR (250 MHz, CD_2Cl_2 , 292 K) δ 2.53 (t, 4H), 1.48-1.32 (m, 16H), 0.89 (t, 6H). Spectra data were consistent with the published data.^[16]

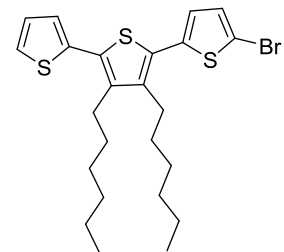
3',4'-Dihexyl-2,2':5',2''-terthiophene (6-10)

(1). **Grignard reagent:** In a 50 ml 2-neck flask (flame dried) were added Mg (polished by dilute HCl and dried before use) (1.79 g, 73.6 mmol) and a piece of I_2 . The flask was degassed and added argon 3 times. Then 2-bromothiophene (10.0 g, 61.3 mmol) in 20 ml diethyl ether was added. It was stirred at 40 °C for 1 hour and then cooled down for next step use.

(2). **Kumada coupling:** In another 100 ml 2-neck flask (flame dried) were added $\text{Pd}(\text{dppf})\text{Cl}_2$ (3.0 g, 4.10 mmol) and 15 ml of diethyl ether and compound **6-7** (5.78 g, 14.1 mmol) and the mixture was stirred at -78 °C. Then 19 ml Grignard reagent was added slowly. After that, the mixture was stirred at room temperature for 24 hours. Then the mixture was extracted with diethyl ether and water. The condensed organic fraction was purified by a silica gel flash column (hexane). Eventually, 5.46 g of a yellow oil was received after drying under reduced pressure (77.6%). ^1H NMR (250 MHz, CDCl_3 , 292 K) δ 7.31 (dd, 2H), 7.13 (dd, 2H), 7.06 (dd, 2H), 2.69 (t, 4H), 1.60-1.31 (m, 16H), 0.90 (t, 6H). Spectra data were consistent with the published data.^[16]



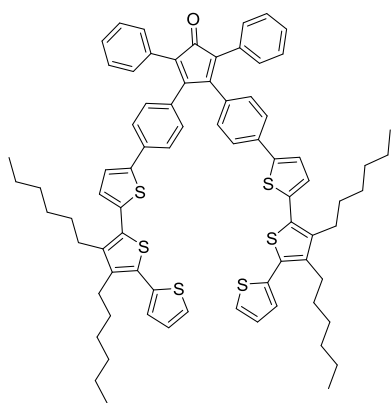
2-Bromo-3',4'-dihexyl-5,2':5',2''-terthiophene (6-11)



In a 250 ml Schlenk flask were added 3',4'-dihexyl-2,2':5',2''-terthiophene (5.47 g, 13.1 mmol) and 50 ml DMF. The flask was degassed and was added argon 3 times and stirred at -20 °C. Then NBS (1.0 g, 5.6 mmol) in 10 ml DMF was added dropwise and the mixture was stirred overnight from -20 °C to room temperature. Then 0.5 g NBS in 10 ml DMF was added again following the previous procedure and stirred for 5 hours at dry ice bath. Then, 0.3 g NBS in 5 ml DMF was added again and let it go overnight. Checked TLC and found big conversion. Finally, another 0.33 g NBS in 5 ml DMF was added again while the mixture was stirred at -20 °C for 5 hours. Then the mixture was extracted with DCM/ 5% aqu. HCl to get rid of DMF and it is further purified by a silica gel flash column (hexane) to get 4.64 g of a yellow liquid (68%). ^1H NMR (250 MHz, CD_2Cl_2 , 292 K) δ 7.35 (dd, 1H), 7.14 (dd, 1H), 7.06 (m, 2H), 6.89 (dd, 1H), 2.67 (m, 4H), 1.43-1.32 (m, 16H), 0.89 (m, 6H). ^{13}C

NMR (75 MHz, CD₂Cl₂, 300 K) δ 141.3, 140.7, 138.2, 136.3, 130.7, 129.1, 127.8, 126.6, 126.4, 126.0, 118.6, 112.0, 31.9, 31.2, 29.9, 28.5, 23.0, 14.3. FD-Mass: calculated for C₂₄H₃₁BrS₃: 494.1 (100%), found: 494.5[M⁺].

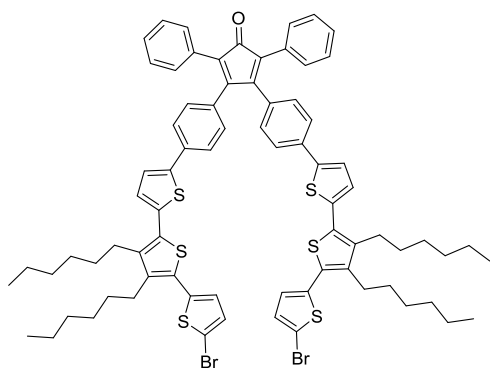
2,5-Diphenyl-3,4-di-[4-(3',4'-dihexyl-2,2':5',2''-terthiophen-5'''-yl)phenyl]cyclopentadienone (6-12)



Compound **6-11** (3.27 g, 6.60 mmol), compound **2-22** (2.0 g, 3.14 mmol), tetrabutylammonium bromide (101.3 mg, 0.31mmol), K₂CO₃ (2.17 g, 15.7 mmol), 400 ml of toluene and 100 ml of water were added in a 1000 ml round bottom flask. Then the mixture was degassed and added argon for 3 times, followed by the addition of Pd (PPh₃)₄ (181.6 mg, 0.16 mmol). The mixture was then stirred at 105 °C for 24 hours. Then it was extracted by DCM and purified by a silica gel flash column (DCM/hexane, 1:1). Eventually, 3.2 g of a dark-brown solid was

received after drying under reduced pressure (74%). ¹H NMR (250 MHz, CD₂Cl₂, 300K) δ 7.49 (d, 4H), 7.34 (dd, 2H), 7.32 (d, 2H), 7.28 (d, 10H), 7.15 (dd, 2H), 7.11 (d, 2H), 7.08 (dd, 2H), 7.02 (d, 4H), 2.72 (m, 8H), 1.58 (m, 8H), 1.42 (m, 8H), 1.32 (m, 16H), 0.89 (m, 12H). ¹³C NMR (75 MHz, CD₂Cl₂, 300 K) δ 200.25, 154.14, 143.25, 140.94, 140.86, 136.67, 136.42, 134.61, 132.57, 131.41, 130.61, 130.38, 130.02, 128.50, 127.97, 127.84, 127.12, 126.32, 126.17, 125.87, 125.17, 124.45, 31.91, 31.10, 30.99, 30.12, 29.94, 28.61, 28.49, 23.05, 14.28. FD-Mass: calculated for C₇₇H₈₀OS₆: 1212.5, found: 1212.8 [M]⁺.

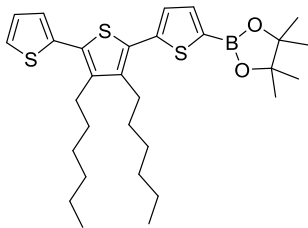
2,5-Diphenyl-3,4-di-[4-(5-bromo-3',4'-dihexyl-2,2':5',2''-terthiophen-5'''-yl)phenyl]cyclopentadienone (6-13)



In a 250 ml 2-neck flask were added compound **6-12** (2.19 g, 1.81 mmol) and 200 ml of DMF. The system was degassed and added argon 3 times and stirred at 0 °C. Then NBS (0.67g, 3.54 mmol) in 10 ml DMF was added dropwise. After addition, the mixture was continuously stirred for 2 days and the temperature was slowly increased to room temperature. Then it was poured into 2 liter of water and stirred to make precipitation form and followed by filtration and washing with methanol to get orange-

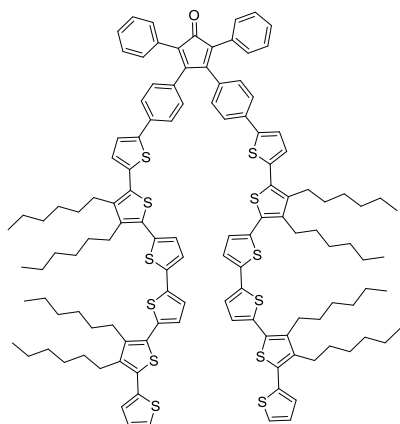
brown colored solid after dry. It was further purified by recrystallization under ethanol. Eventually, 2.0 g of a orange-brown solid was received after drying under reduced pressure (81%). ¹H NMR (250 MHz, CD₂Cl₂, 300 K) δ 7.48 (d, 4H), 7.31 (d, 2H), 7.23 (m, 10H), 7.11 (d, 2H), 7.05 (d, 2H), 7.02 (d, 4H), 6.90 (d, 2H), 2.69 (m, 8H), 1.56-1.31 (m, 32H), 0.90 (m, 12H). FD-Mass: calculated for C₇₇H₇₈Br₂OS₆: 1370.3 (100%), found: .1372.0.

3',4'-Dihexyl-5,2':5',2''-terthiophene-2-pinacol boronic ester (6-14)



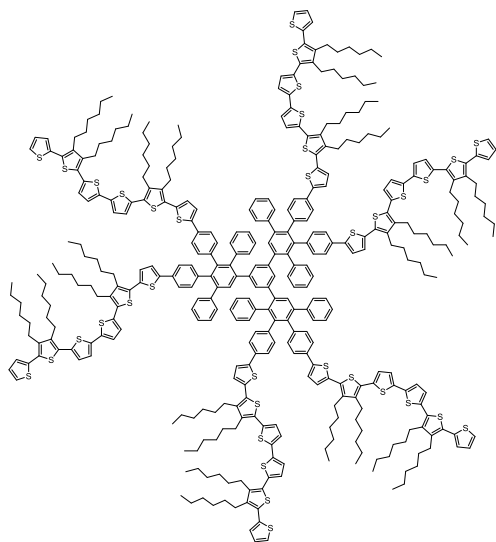
In a Schlenk flask (flame-dried) was added compound **6-10** (4.0 g, 9.60 mmol), degasing and adding argon 3 times and followed by addition of 40 ml of dry THF. Then it was stirred at $-78\text{ }^{\circ}\text{C}$ under argon environment. Then lithium diisopropylamine (8.8 ml, 9.60 mmol) was added slowly within 40 minutes. After 1 hour, 2-isopropoxy-4,4,5,5-tetramethyl-1,3,2-dioxaborolane (2.4 ml, 11.76 mmol) was added quickly. The mixture was then stirred overnight at room temperature. Then, it was extracted by DCM/water and dried with MgSO_4 . The condensed organic fraction was purified by a silica gel flash column (DCM/Hexane, 3/7). Eventually, 2.5 g of a dark green solid was received (48%). ^1H NMR (250 MHz, CD_2Cl_2 , 300K) δ 7.53 (d, 1H), 7.35 (dd, 1H), 7.21 (d, 1H), 7.15 (dd, 1H), 7.08 (dd, 1H), 2.72 (m, 4H), 1.58-1.27 (m, 16H), 0.89 (m, 6H). ^{13}C NMR (75 MHz, CD_2Cl_2 , 298 K) δ 143.42, 141.14, 140.86, 137.84, 136.39, 130.62, 130.06, 127.83, 127.35, 126.36, 125.88, 84.58, 31.90, 31.09, 30.92, 29.92, 28.49, 24.97, 23.04, 14.26. FD-Mass: calculated for $\text{C}_{30}\text{H}_{43}\text{BO}_2\text{S}_3$: 542.2 (100%), found: 542.8 $[\text{M}]^+$.

2,5-Diphenyl-3,4-di-[4-(3',3''',4',4''''-tetrahexyl-2,2':5',2'':5'',2''':5''',2''''':5''''',2''''':5''''')-phenyl]cyclopentadienone (6-15)



In a Schlenk flask were added compound **6-13** (2.00 g, 1.46 mmol), compound **6-14** (1.98 g, 3.65 mmol), K_2CO_3 (1.01 g, 7.29 mmol), 240 ml of THF and 40 ml of water. Then the mixture was bubbled argon for 10 minutes, followed by addition of $\text{Pd}_2(\text{dba})_3\cdot\text{CHCl}_3$ (74.5 mg, 0.073 mmol) and tri(*t*-butyl)phosphonium tetrafluoroborate (42.3 mg, 0.145 mmol) quickly. Then the mixture was stirred at $60\text{ }^{\circ}\text{C}$ for 12 hours. Then it was extracted with DCM and water. The condensed organic fraction was purified by 3 times recrystallization using ethyl acetate as the solvent. Eventually, 1.85 g of a black solid was received after drying under reduced pressure (62.1%). ^1H NMR (300 MHz, CD_2Cl_2 , 300 K) δ 7.50 (d, 4H), 7.35-7.32 (m, 4H), 7.28 (m, 10H), 7.16 (m, 6H), 7.13 (d, 2H), 7.08 (m, 6H), 7.02 (d, 4H), 2.74 (m, 16H), 1.58 (m, 16H), 1.45 (m, 48H), 0.90 (m, 24H). ^{13}C NMR (75 MHz, CD_2Cl_2 , 300 K) δ 200.24, 154.12, 143.31, 141.09, 141.05, 140.90, 140.85, 137.09, 136.92, 136.56, 136.42, 135.72, 135.52, 134.56, 132.56, 131.39, 130.60, 130.33, 130.21, 130.11, 129.83, 128.49, 127.97, 127.84, 127.16, 126.83, 126.75, 126.28, 126.14, 125.84, 125.16, 124.48, 124.32, 31.90, 31.00, 29.94, 28.61, 23.05, 14.29. FD-Mass: calculated for $\text{C}_{125}\text{H}_{140}\text{OS}_{12}$: 2041.8 (100%), found: 2044.0.

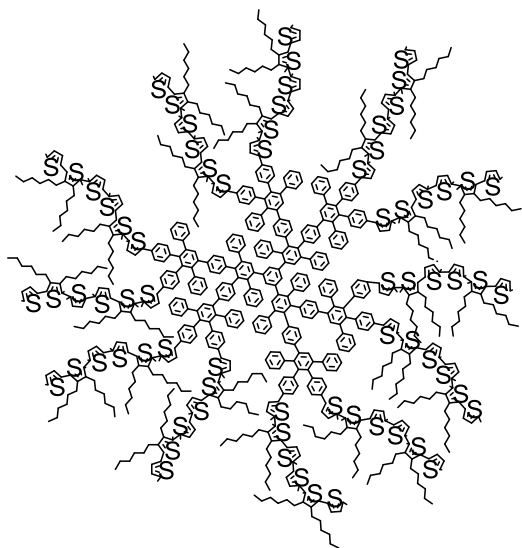
1,3,5-Benzene-based, peripheral-sexithiophene polyphenylene dendrimer-G1 (STPPD)



1,3,5-Triethynylbenzene (7.0 mg, 0.046 mmol) and compound (**6-15**) (333 mg, 0.163 mmol) were added in a 25 ml round bottom flask and dissolved in 14 ml anhydrous *o*-xylene. The mixture was stirred at 160 °C for 3 days. Then, the mixture was added into 100 ml of ethanol to precipitate, followed by filtration to get the solid mixture. Then it was purified by a silica gel flash column (DCM/hexane, 1/1) and it was further purified by GPC column using THF as the eluent. Finally Precipitation was formed by adding concentrated THF solution into ethanol and solid was received by centrifuge. Eventually,

206 mg of a orange solid was received after drying under reduced pressure (71.3%). ^1H NMR (300 MHz, CD_2Cl_2 , 300 K) δ 7.34 (dd, 6H), 7.25-7.13 (m, 48H), 7.09-7.02 (m, 24H), 6.95-6.73 (m, 32H), 2.72 (t, 48H), 1.56 (m, 48), 1.41-1.31 (m, 144H), 0.89 (m, 72H). ^{13}C NMR (126 MHz, CD_2Cl_2 , 298 K) δ 143.95, 141.87, 141.32, 141.23, 140.96, 140.88, 140.78, 140.31, 139.92, 139.55, 138.90, 136.98, 136.95, 136.45, 135.72, 135.65, 132.56, 132.16, 131.40, 130.43, 130.31, 129.88, 129.83, 127.98, 127.82, 126.73, 126.26, 125.81, 124.26, 31.91, 31.89, 31.08, 31.00, 30.95, 29.94, 29.91, 28.61, 28.49, 23.05, 14.28, 14.26. MALD-TOF: calculated for $\text{C}_{384}\text{H}_{426}\text{S}_{36}$: 6194.3 (100%), found: 6193.1 $[\text{M}-\text{H}]^+$. HR-MALDI-TOF: calculated for $\text{C}_{384}\text{H}_{426}\text{S}_{36}$: 6194.3372, found: 6194.4707 $[\text{M}]^+$.

1,3,5-Benzene-based, peripheral-sexithiophene polyphenylene dendrimer-G2 (STPPDG2)



Compound **6-16** (51 mg, 0.037 mmol) and compound **6-15** (529 mg, 0.259 mmol) were added in a 50 ml round bottom flask and dissolved in 20 ml anhydrous *o*-xylene. The mixture was stirred at 165 °C for 14 days. Then, the mixture was added into 150 ml of ethanol to precipitate, followed by filtration to get the solid mixture. Then it was purified by a silica gel flash column (DCM/hexane, 1/1) and it was further purified by a GPC column using THF as the eluent. Finally Precipitation was formed by adding concentrated THF solution into ethanol and solid was received by centrifuge.

Eventually, 300 mg of a orange solid was received after drying under reduced pressure (60.8 %). ^1H NMR (300 MHz, CD_2Cl_2 , 300 K) δ 7.45-6.42 (m, 282H), 2.70 (m, 96H), 1.56-1.31 (m, 384H), 0.88 (m, 144H). ^{13}C NMR (176 MHz, CD_2Cl_2 , 298 K) δ 144.01, 142.11, 141.68, 141.47, 141.28, 140.96, 140.85, 140.81, 140.50, 140.25, 140.03, 139.65, 138.97, 136.97, 136.46, 135.65, 135.47, 132.56, 131.93, 131.82, 131.68, 131.39, 130.44, 130.32, 129.88, 128.11, 127.83,

127.38, 127.01, 126.73, 126.28, 125.82, 124.27, 123.99, 123.61, 123.53, 31.91, 31.08, 30.96, 29.94, 28.62, 28.49, 23.05, 14.29. MALD-TOF: Calculated for C₈₅₂H₉₀₆S₇₂: 13455, found: 13449.

Literature

- [1] F. Morgenroth, K. Mullen, *Tetrahedron* **1997**, *53*, 15349-15366.
- [2] F. Morgenroth, E. Reuther, K. Mullen, *Angewandte Chemie-International Edition in English* **1997**, *36*, 631-634.
- [3] S. Bernhardt, M. Kastler, V. Enkelmann, M. Baumgarten, K. Mullen, *Chem-Eur J* **2006**, *12*, 6117-6128.
- [4] K. T. Kamtekar, C. S. Wang, S. Bettington, A. S. Batsanov, I. F. Perepichka, M. R. Bryce, J. H. Ahn, M. Rabinal, M. C. Petty, *J Mater Chem* **2006**, *16*, 3823-3835.
- [5] aA. Orita, K. Miyamoto, M. Nakashima, F. Ye, J. Otera, *Adv Synth Catal* **2004**, *346*, 767-776; bA. Orita, H. Taniguchi, J. Otera, *Chem-Asian J* **2006**, *1*, 430-437.
- [6] K. E. Linton, A. L. Fisher, C. Pearson, M. A. Fox, L. O. Palsson, M. R. Bryce, M. C. Petty, *J Mater Chem* **2012**, *22*, 11816-11825.
- [7] I. Oesterling, K. Mullen, *J Am Chem Soc* **2007**, *129*, 4595-4605.
- [8] J. Burdynska, Y. C. Li, A. V. Aggarwal, S. Hoger, S. S. Sheiko, K. Matyjaszewski, *J Am Chem Soc* **2014**, *136*, 12762-12770.
- [9] M. I. Mangione, R. A. Spanevello, A. Rumbero, D. Heredia, G. Marzari, L. Fernandez, L. Otero, F. Fungo, *Macromolecules* **2013**, *46*, 4754-4763.
- [10] U. M. Wiesler, A. J. Berresheim, F. Morgenroth, G. Lieser, K. Mullen, *Macromolecules* **2001**, *34*, 187-199.
- [11] G. R. Fulmer, A. J. M. Miller, N. H. Sherden, H. E. Gottlieb, A. Nudelman, B. M. Stoltz, J. E. Bercaw, K. I. Goldberg, *Organometallics* **2010**, *29*, 2176-2179.
- [12] J. Q. Qu, N. G. Pschirer, D. J. Liu, A. Stefan, F. C. De Schryver, K. Mullen, *Chem-Eur J* **2004**, *10*, 528-537.
- [13] Y. T. Tsoi, Z. Y. Zhou, W. Y. Yu, *Org Lett* **2011**, *13*, 5370-5373.
- [14] M. R. Zhu, J. H. Zou, X. He, C. L. Yang, H. B. Wu, C. Zhong, J. G. Qin, Y. Cao, *Chem Mater* **2012**, *24*, 174-180.
- [15] D. Cheng, L. Croft, M. Abdi, A. Lightfoot, T. Gallagher, *Org Lett* **2007**, *9*, 5175-5178.
- [16] R. B. K. Siram, K. Tandy, M. Horecha, P. Formanek, M. Stamm, S. Gevorgyan, F. C. Krebs, A. Kiriy, P. Meredith, P. L. Burn, E. B. Namdas, S. Patil, *J Phys Chem C* **2011**, *115*, 14369-14376.

List of Publications

1. Zhang, G.; Baumgarten, M.; Auer, M.; Trattnig, R.; List-Kratochvil, E. J. W.; Mullen, K., Core-and-Surface-Functionalized Polyphenylene Dendrimers for Solution-Processed, Pure-Blue Light-Emitting Diodes Through Surface-to-Core Energy Transfer. *Macromol Rapid Comm* **2014**, *35*, 1931-1936.
2. Ma, H.; Li, F.; Li, P.; Wang, H.; Zhang, M.; Zhang, G.; Baumgarten, M.; Muellen, K., A Dendrimer-Based Electropolymerized Microporous Film: Multifunctional, Reversible, and Highly Sensitive Fluorescent Probe. *Adv Funct Mater* **2016**, *26*, 2025-2031.
3. Li, P.; Zhang, M.; Sun, X.; Guan, S.; Zhang, G.; Baumgarten, M.; Muellen, K., A Dendrimer-based Highly Sensitive and Selectivity Fluorescence-quenching Sensor for Fe³⁺ Both in Solution and As Film. *biosensors and bioelectronics* **2016**. (accepted)
4. Zhang, G.; Auer-Berger, M.; Gehrig, D. W.; Blom, P. W.; Baumgarten, M.; Schollmeyer, D.; List-Kratochvil, E. J. W.; Muellen, K., Bipolar dendrimers: one with pure core emission and the other with dual emissions. **2016**. (in preparation)